



# IVIM : modélisation, validation expérimentale et application à des modèles animaux

Gabrielle Fournet

## ► To cite this version:

Gabrielle Fournet. IVIM : modélisation, validation expérimentale et application à des modèles animaux. Medical Physics [physics.med-ph]. Université Paris Saclay (COMUE), 2016. English. NNT : 2016SACLS367 . tel-01533421

**HAL Id: tel-01533421**

**<https://theses.hal.science/tel-01533421>**

Submitted on 6 Jun 2017

**HAL** is a multi-disciplinary open access archive for the deposit and dissemination of scientific research documents, whether they are published or not. The documents may come from teaching and research institutions in France or abroad, or from public or private research centers.

L'archive ouverte pluridisciplinaire **HAL**, est destinée au dépôt et à la diffusion de documents scientifiques de niveau recherche, publiés ou non, émanant des établissements d'enseignement et de recherche français ou étrangers, des laboratoires publics ou privés.

NNT : 2016SACLS367

Thèse de doctorat de l'Université Paris-Saclay soutenue à  
l'Université Paris-Sud

Ecole doctorale n° 575

Electrical, Optical, Bio-physics and Engineering

Spécialité de doctorat: Imagerie et physique médicale

Par :

**Mme Gabrielle Fournet**

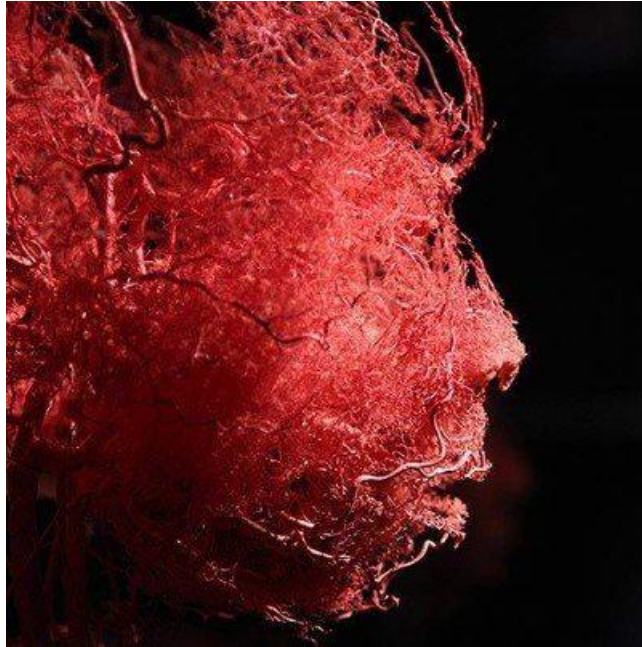
IVIM: modeling, experimental validation and application to  
animal models

Thèse présentée et soutenue à Gif-sur-Yvette le 10 novembre 2016.

**Composition du jury :**

M. E. Sigmund	Professeur associé, New York University Langone Medical Center, Bernard and Irene Schwartz Center for Biomedical Imaging	Rapporteur
Mme I. Vignon- Clementel	Chargée de recherche, INRIA Paris	Rapporteur
Mme L. Ciobanu	Ingénieur E5, Neurospin, CEA Saclay	Directeur de thèse
Mme J-R. Li	Chargée de recherche, INRIA Saclay	Codirecteur de thèse
M. D. Le Bihan	Directeur de recherche, Neurospin, CEA Saclay	Examineur
M. X. Maître	Chargé de recherche, IR4M	Examineur
M. E. Barbier	Directeur de recherche, Grenoble – Institut des Neurosciences	Examineur
Mme S. Salmon	Professeur, Laboratoire de Mathématiques, Université de Reims	Examineur, président du jury





*“All beauty comes from beautiful blood and a beautiful brain.”*

*- Walt Whitman (from the preface to Leaves of Grass, 1855)*

(Picture: Plastinated blood vessels of a human face shown during a media viewing for the exhibition “The Human Body” in Ostend in 2012)



# Acknowledgments

When I first came to Neurospin for an interview with Luisa Ciobanu after my PhD application, I was immediately impressed by all the MRI scanners available at Neurospin and I still consider myself lucky to have conducted my PhD in such a high level laboratory. Yet, my time as a PhD student has been full of ups and downs. During these three years, I have been greatly dependent on the support from people around me. The friendly environment at Neurospin has enabled me to put up with all the stress and difficulties I encountered during the PhD and I am grateful to all of you! If I forget to thank anyone during this period of intense work and short nights, please forgive me.

My deepest thanks go to Luisa Ciobanu, the best supervisor I could have dreamed for! She is a great person, always available, very dedicated to her students. I am grateful to have benefited from her extensive knowledge of MRI in general, her MRI debugging skills and her positivism in every situation. She has taught me to never give up and keep up with the hard work, showing me that, in the end, it pays off!

How could I have found my way through the mathematical modelling and the numerical simulations without Jing-Rebecca Li, my co-supervisor at INRIA Saclay. Her guidance was essential to me and I would like to thank her a lot for her patience and the pieces of advice that helped me overcome many obstacles I thought unsurmountable.

I would never have been able to work on IVIM imaging without its creator, Denis Le Bihan. Its interest and implication in my work despite his very busy schedule has inspired me to be more involved and work even harder during these three years. I realize the chance I had to be able to discuss my subject with him and get his useful input on my work. Thank you very much!

I would like to thank Drs. Eric Sigmund and Irène Vignon-Clementel for accepting to review this manuscript and Drs. Denis Le Bihan, Xavier Maître, Emmanuel Barbier and Stéphanie Salmon for being part of the jury.

Our project was in collaboration with Brad Sutton and Alex Cerjanic from the Beckman Institute in the University of Illinois Urbana-Champaign, USA. I had the chance to go to their institute only

once but it was an interesting experience and I would like to thank them for the stimulating discussions we had on the project and their useful comments and corrections on my abstracts and posters.

The experiments would never have been so successful without the help of Boucif Djemai and Erwan Selingue, our two animal experimentation technicians. Boucif taught me a lot and both were always there to give me a hand whenever I needed it.

I didn't get the opportunity to do a lot of histology although it would have pleased me. However, even if they were not concretely used in this project, I helped to embed a few rat brains in an epoxy resin on the expert advice of Françoise Geffroy. I would like to thank her for that and all the pleasant talks we had during lunch or at breaks in the afternoon when she would bring one of her delicious cakes!

Special thanks to Tomokazu Tsurugizawa for his kind help with my experiments when something was going wrong or whenever I had a question. Thanks also for the tip on the Sake and Japanese drinks fair ;)

Next is Benoit Larrat. What to say, he is a very funny guy! I really enjoyed coming back with him by car from Neurospin to Paris. At lunch, he was always making jokes together with Erwan making the day more enjoyable. Also, if he had not decided to start breeding APP/PS1 mice together with Erwan, I would not have had the chance to scan them and add the study on Alzheimer's disease to this thesis. Again, thanks a lot!

I cannot go on like this without thanking my flat-mate Alfredo Lopez-Kolkovsky who moved in with me at the beginning of my third year and had to support my everyday moods and was always willing to help in every matter. Thank you Dr. Alfredo!

One person who was always alongside me during these past years and with whom I exchanged a lot on the difficulties of the PhD is Marianne Boucher. I want to thank her for the long talks we had on the PhD experience and everything else.

A person who holds a special place is Allegra Conti. She only arrived a bit before my third year began but we are now very good friends and she helped me a lot with her unlimited support on

every matter, scientific as well as personal. Great many thanks to you Allegra and I hope we continue this friendship after I am gone!

Neurospin has a PhD student association called the Neurobreakfast team. With them, we organized multiple “Neurobreakfasts” to talk about the great science we make at Neurospin around breakfast, social events to have fun together outside of Neurospin and the first one-day spindating meeting to federate all persons in Neurospin and make them better know each other. Thanks to the team: Valentina, Arthur, Marianne, Carole and Benoit M.

My desk at Neurospin was surrounded by great people in the sometimes freezing, sometimes boiling open space 1025 A: Rémi, Guillaume, Khieu, Pavel, Matthieu, Jacques. I would also like to thank people from the other open spaces or offices I enjoyed talking to when they were passing by: David, Hermes, Yoshi, Tanguy, Gaël, Lisa, Achille, Cyrille, Justine, Delphine, Amaury, Morgan, Antoine, Elodie P., Elodie G., Aude, ...

Next, I would like to thank the other senior researchers I had the opportunity to talk to during these three years: Cyril, Fawzi, Sébastien, Béchir, Alexandre, ...

Although I did not do any experiments on a clinical scanner, I got to know Chantal Ginisty and am very grateful about it! Thank you for driving me home at the time we played badminton together next to the CEA and for the long talks we had about every possible matter and the pieces of advice you gave me about a particular matter. Thanks again!

I am finally very grateful to my friends and family, especially to my parents, who were very present and supportive at every step. I would not be there if that were not for them, thank you for caring about me and being always there for me.





## Résumé de la thèse en français

Cette thèse de doctorat est centrée sur l'étude de la technique d'imagerie par résonance magnétique (IRM) de mouvement incohérent intravoxel (IVIM), sa modélisation, validation expérimentale et application à un modèle animal. La technique d'imagerie IVIM permet d'obtenir des informations sur la structure des microvaisseaux sanguins à l'intérieur des tissus de manière non-invasive et sans utiliser d'agents de contraste.

### Introduction sur les vaisseaux sanguins du cerveau

Le sang est le fluide le plus important du corps humain. Il a pour fonction de transporter l'oxygène et les nutriments jusqu'à toutes les cellules de l'organisme. Sans oxygène, les cellules meurent très rapidement. Le cerveau a besoin d'une grande quantité d'énergie pour fonctionner mais est incapable de la stocker. Cette thèse est focalisée sur l'étude d'une fraction particulière du système vasculaire du cerveau : les microvaisseaux. Ce terme inclut les artérioles, capillaires et veinules. Pour pouvoir les observer directement, des méthodes d'imagerie optique sont généralement privilégiées. D'autres techniques comme la micro IRM ou le micro scanner à rayons X peuvent également être utilisées mais sur des tissus déjà fixés. Les réseaux microvasculaires peuvent être extraits des images obtenues à l'aide de ces techniques en utilisant des méthodes de segmentation pour extraire des paramètres morphologiques tels que le diamètre et la longueur des vaisseaux. Les capillaires ont un diamètre moyen d'environ  $4.2\ \mu\text{m}$  chez le rat et de  $6.2\ \mu\text{m}$  chez l'homme avec une longueur moyenne d'environ  $50\ \mu\text{m}$ . Des techniques d'imagerie optique permettent aussi la mesure de la vitesse du flux à l'intérieur des vaisseaux sanguins qui est d'environ  $1.6\ \text{mm/s}$  pour les capillaires chez le rat. Néanmoins, la reconstruction de réseaux microvasculaires à partir de ces images dans le but de modéliser l'hémodynamique du sang ou le transport de l'oxygène par les vaisseaux peut être laborieuse. C'est pourquoi des modélisations simplifiées de ces réseaux obtenues à partir de simulations où une structure de type arbre vasculaire est privilégiée pour les artérioles et les veinules et une structure de type maillage vasculaire est généralement choisie pour les capillaires ont été développées. Elles sont faciles à manipuler et représentent des modélisations acceptables du réseau microvasculaire.

## Introduction sur l'IRM des réseaux vasculaires

Pour mener à bien cette thèse, l'IRM a été utilisée pour étudier les réseaux microvasculaires. Cette technique permet de réaliser des images des tissus mous avec un bon contraste et de façon non-invasive. L'IRM est basée sur les mêmes principes physiques que la résonance magnétique nucléaire. Des bobines de gradients sont ajoutées pour encoder spatialement la position des spins des molécules d'eau et construire des images. Différents contrastes qui dépendent des caractéristiques de la séquence d'impulsions radiofréquence (RF) et des paramètres d'acquisition peuvent être obtenus. Pour être sensible seulement aux groupes de spins en mouvement dans les vaisseaux sanguins, des gradients de diffusion sont ajoutés avant et après l'impulsion RF de  $180^\circ$  d'une séquence d'écho de spin (SE) standard (séquence SE à gradients pulsés (PGSE)) comme sur la Figure 1R.

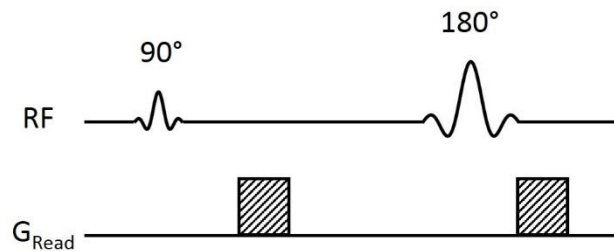


Figure 1R. Diagramme de la séquence d'impulsions PGSE. Elle est basée sur la séquence SE qui se compose d'une impulsion RF de  $90^\circ$  suivie d'une impulsion RF de  $180^\circ$ . Deux gradients de diffusion sont ajoutés à cette séquence sur la direction du gradient de lecture ( $G_{\text{Read}}$ ) avant et après l'impulsion de  $180^\circ$  (blocs hachurés).

Le premier gradient de diffusion applique le même déphasage à tous les spins. Le second gradient de diffusion applique le même déphasage mais avec le signe inversé (négatif) à cause de l'impulsion de  $180^\circ$ , ainsi compensant et annulant le déphasage induit par le premier gradient pour les spins statiques. Par contre, les spins en mouvement dans les tissus ou dans le système vasculaire auront accumulé une phase non-nulle et donneront donc lieu à une atténuation du signal IRM (sauf cas particulier où le moment magnétique au premier ordre est nul, i.e. séquences compensées en flux). En réalisant des mesures répétées à différentes amplitudes du gradient de diffusion, l'évolution de l'atténuation du signal peut être obtenue et affichée en fonction d'un paramètre dérivé de l'amplitude du gradient de diffusion appelée valeur de  $b$ . La composante du signal IRM,  $S(b)$ , correspondant aux spins qui diffusent dans le

tissu,  $F_{diff}(b)$ , peut être séparée de celle qui fait référence aux spins en mouvement dans les vaisseaux sanguins qui est appelée signal IVIM,  $F_{IVIM}(b)$ ,

$$S(b) = S_0(1 - f_{IVIM})F_{diff}(b) + S_0f_{IVIM}F_{IVIM}(b)$$

où  $S_0$  représente le signal total à  $b = 0$ .

Ces deux composantes sont pondérées par  $(1 - f_{IVIM})$  et  $f_{IVIM}$ , respectivement, où  $f_{IVIM}$  représente la fraction volumique de sang à l'intérieur du tissu. D'autres techniques utilisant l'IRM permettent aussi d'étudier les vaisseaux sanguins. La première catégorie de techniques appelée angiographie IRM (ARM) permet seulement l'étude des gros vaisseaux sanguins, les artères et les veines. La seconde catégorie dont fait partie la technique IVIM est focalisée sur l'imagerie des microvaisseaux et se nomme imagerie IRM de perfusion. Parmi elles, on trouve l'IRM dynamique de contraste de susceptibilité magnétique et l'IRM dynamique rehaussée par agent de contraste qui nécessitent l'injection d'un agent de contraste, ce qui est l'un de leurs inconvénients majeurs. Par contre, la technique IVIM et le marquage de spin artériel (ASL) n'en ont pas besoin. L'ASL est le plus proche compétiteur de la technique IVIM. Cependant, la technique ASL utilise une impulsion RF d'inversion qui est plutôt caractérisée par sa longueur ( $180^\circ$ ) pour réaliser le marquage qui nécessite beaucoup de puissance et peut chauffer le tissu ou le sujet d'étude, ce qui rend l'ASL moins approprié chez les enfants et les patients fragiles que la technique IVIM, pour laquelle ce n'est pas un problème.

### **Différentes modélisations possibles du signal IVIM**

Plusieurs expressions mathématiques ont été proposées pour modéliser le signal IVIM. Le premier modèle qui a été développé par Le Bihan et al. en 1988 est un modèle mono-exponentiel

$$F_{IVIM}(b) = e^{-b(D_b + D^*)},$$

caractérisé par le coefficient de pseudo-diffusion,  $D^*$ , et le coefficient de diffusion de l'eau dans le sang,  $D_b$ .  $D_b$  n'est pas considéré comme un paramètre IVIM et est supposé constant pour toutes les expériences réalisées pendant cette thèse. Ce modèle mono-exponentiel est basé sur le fait que les groupes de spins traversent plusieurs segments de capillaires pendant le temps de

diffusion comme illustré sur la Figure 2R.A. Le temps d'encodage de diffusion est défini comme le temps pendant lequel les spins peuvent diffuser avant l'acquisition du signal IRM. Ce temps débute à partir de l'application du premier gradient de diffusion et se termine à la fin du deuxième gradient de diffusion.

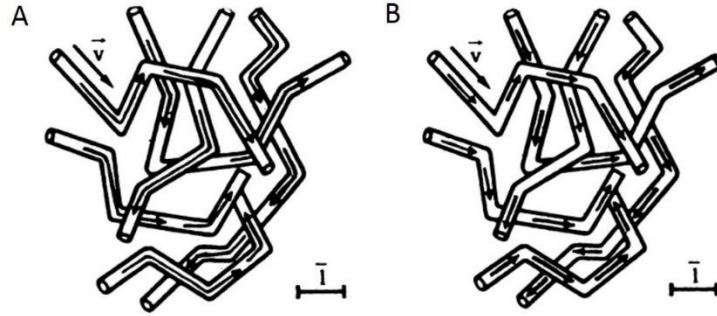


Figure 2R. Représentation de groupes de spins entraînés par le flux sanguin à l'intérieur d'un réseau de capillaires dans le cas (A) où ils changent de segments de capillaires plusieurs fois pendant le temps de diffusion et dans le cas (B) où ils restent dans le même segment de capillaire pendant le temps de diffusion. Adapté de Le Bihan et al [1].

Ce type de mouvement est proche du mouvement Brownien mais il provient des groupes de spins en mouvement à l'intérieur d'un réseau de segments de capillaires orientés de façon aléatoire. Ce n'est pas à proprement parlé un phénomène de diffusion mais d'écoulement donc on parle généralement de pseudo-diffusion. Un autre modèle dans lequel les groupes de spins restent dans le même segment de capillaire pendant le temps de diffusion (Figure 2R.B) peut être défini par une fonction sinus cardinal

$$F_{IVIM}(c) = e^{-bD_b} \text{sinc}(cV)$$

où  $c$  est un paramètre qui, comme  $b$ , dérive de l'amplitude du gradient de diffusion et  $V$  est la norme du vecteur vitesse du flux sanguin.

D'autres modèles plus complexes ont également été proposés dans la littérature. Certains auteurs remettent en question le fait que la technique IVIM permette d'être seulement sensible aux groupes de spins à l'intérieur des capillaires sanguins mais soit au contraire sensible au réseau microvasculaire entier. Nous proposons un modèle IVIM bi-exponentiel pour tenir compte de ce dernier point. Ce modèle a deux composantes : une composante lente caractérisée par  $f_{slow}$  et  $D_{slow}^*$  qui correspondrait au modèle IVIM initial qui ne prend en

compte que les capillaires et une composante rapide caractérisée par  $f_{fast}$  et  $D_{fast}^*$  qui correspondrait à des vaisseaux plus gros comme des artérioles et veinules de taille moyenne

$$F_{IVIM}(b) = e^{-bD_b} \left( f_{slow} e^{-bD_{slow}^*} + f_{fast} e^{-bD_{fast}^*} \right),$$

avec  $f_{slow} + f_{fast} = 1$ .

### **Validation expérimentale du modèle bi-exponentiel du signal IVIM**

Pour valider ce nouveau modèle, onze rats ont été scannés sous anesthésie à l'isoflurane sur un scanner IRM à 7T avec la séquence PGSE et les paramètres d'acquisition suivants : 30 valeurs de  $b$  allant de 7 à 2500 s/mm<sup>2</sup>, 3 directions de gradient de diffusion [1,1,1], [0,1,0] et [0,0,1], la durée d'un gradient de diffusion,  $\delta = 3$  ms, l'intervalle entre les deux gradients de diffusion,  $\Delta = 14, 24$  et 34 ms, une résolution spatiale de 250 x 250  $\mu\text{m}^2$ , temps d'écho/temps de répétition (TR) = 45/1000 ms et 6 répétitions. Deux régions d'intérêt ont été sélectionnées sur le cortex gauche et le thalamus gauche. Après avoir moyenné le signal IRM sur les différentes répétitions, directions de diffusion (la diffusion est ici supposée isotrope) et régions d'intérêt, la composante de diffusion du signal IRM a été retirée du signal total pour ne garder que le signal IVIM en ajustant le signal IRM à grandes valeurs de  $b$  sur le modèle de diffusion Kurtosis puis en extrapolant ce modèle pour les petites valeurs de  $b$  et en le soustrayant au signal IRM total. Le critère d'information d'Akaike a été utilisé pour comparer et déterminer le meilleur modèle du signal IVIM pour décrire les données expérimentales entre les modèles mono-, bi- et tri-exponentiels et un autre modèle développé par Kennan et al. qui est supposé mieux décrire le signal IVIM que le modèle mono-exponentiel standard. Le modèle bi-exponentiel a été évalué comme étant le meilleur modèle pour décrire ces données par ce critère pour les deux plus petites valeurs de  $\Delta = 14$  et 24 ms, mais pas pour tous les rats pour la plus grande valeur de  $\Delta = 34$  ms, ce qui suggère que les deux modèles convergent aux grandes valeurs de  $\Delta$ .

### **Simulations du signal IVIM pour extraire des informations structurales sur les réseaux de vaisseaux sanguins**

Pour obtenir plus d'informations sur les caractéristiques des deux composantes du modèle IVIM bi-exponentiel, des simulations du signal IVIM ont été réalisées. Des trajectoires de groupes de

spins composées de segments de vaisseaux modélisés par des segments mis bout à bout et caractérisés chacun par la longueur du segment et la vitesse du flux à l'intérieur du segment ont été générées. Le diamètre des segments et le branchement d'un segment avec plusieurs autres segments n'ont pas été considérés. Des calculs mathématiques ont été réalisés pour extraire le signal IVIM de groupes de spins se déplaçant suivant ces trajectoires. Le modèle analytique obtenu nous a permis de générer un dictionnaire de signaux IVIM en faisant varier les longueurs et vitesses du flux sanguins associées aux segments des trajectoires suivant des distributions Gaussiennes,  $L_{mean} \pm \sigma_L$  et  $V_{mean} \pm \sigma_V$ , respectivement. En s'inspirant du modèle bi-exponentiel, des paires de signaux du dictionnaire ont été combinées. Chacun des deux signaux correspond à une des deux composantes du modèle bi-exponentiel,  $e^{-bD_{slow}^*}$  ou  $e^{-bD_{fast}^*}$ , et est appelé,  $F_{Sim/slow}(L_{slow}, V_{slow})$  ou  $F_{Sim/fast}(L_{fast}, V_{fast})$

$$F_{IVIM/Sim}(L_{slow}, V_{slow}, L_{fast}, V_{fast}) \\ = f_{slow}F_{Sim/slow}(L_{slow}, V_{slow}) + f_{fast}F_{Sim/fast}(L_{fast}, V_{fast})$$

où  $f_{slow}$  et  $f_{fast}$  prennent les valeurs calculées précédemment en réalisant le fit bi-exponentiel des données expérimentales.

Toutes les paires possibles de signaux du dictionnaire ont été combinées et comparées aux signaux expérimentaux pour en extraire une longueur moyenne des segments,  $L_{mean}$ , et la vitesse moyenne du flux à l'intérieur des segments,  $V_{mean}$ , pour chaque composante, lente et rapide. Cette comparaison nous a permis d'obtenir une gamme de valeurs possibles pour  $V_{mean}$  pour chaque composante avec  $V_{slow}$  autour de 1.6 mm/s et  $V_{fast}$  autour de 4.5 mm/s. Ces valeurs de  $V_{mean}$  sont cohérentes avec des valeurs trouvées dans la littérature pour les capillaires et les artérioles de taille moyenne. Cependant, il n'a pas été possible de déterminer  $L_{mean}$ , ce qui suggère que les deux composantes du signal IVIM sont plus proches du régime sinc que du régime exponentiel car, dans ce régime, comme les spins restent dans le même segment pendant le temps d'encodage de diffusion, il n'est pas possible de déterminer la longueur réelle du segment dans lequel ils sont.

### Etude de l'évolution du signal IVIM avec les paramètres d'acquisition

Par la suite, l'évolution des paramètres IVIM avec des paramètres d'acquisition a été étudiée. Pour chaque paramètre varié, quatre rats ont été scannés. Dans un premier temps, le temps de répétition, TR, a été varié entre 1000 et 3000 ms avec une séquence PGSE standard. Une très forte baisse de  $f_{IVIM}$ , et une baisse également de  $f_{fast}$  ont été observées. Ces diminutions ne peuvent pas être expliquées seulement par la variation de TR et sont cohérentes avec l'effet d'entrée de coupe ou inflow. A court TR, le signal provenant du tissu n'a pas assez de temps pour retrouver son aimantation complète entre chaque TR et des spins frais présents dans les vaisseaux entrant dans la coupe imagée apparaissent avoir plus de signal que le tissu augmentant artificiellement  $f_{IVIM}$  comme montré sur la figure 3R.

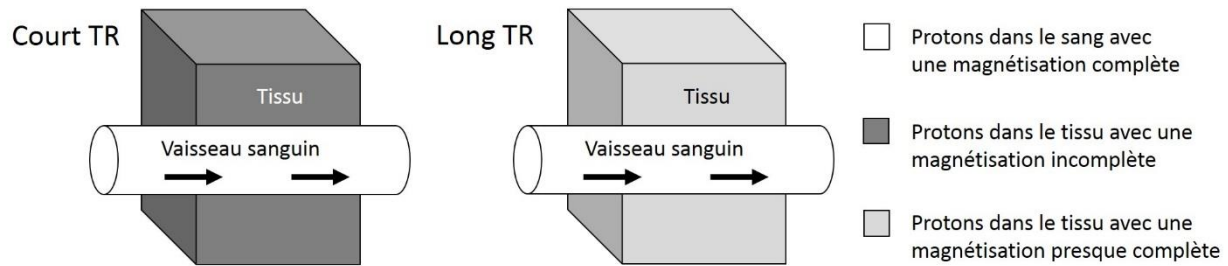


Figure 3R. Schéma expliquant l'effet d'entrée de coupe ou inflow à court et long temps de répétition (TR). Les protons des molécules d'eau présents dans les vaisseaux sanguins entrent dans le voxel avec une magnétisation complète (en blanc) alors qu'à court TR les protons situés à l'intérieur du tissu n'ont pas assez de temps pour retrouver leur magnétisation complète (gris foncé). Cela augmente la contribution du signal provenant des vaisseaux sanguins comparée à celle du tissu. Au contraire, à long TR, les protons situés dans le tissu ont plus de temps pour retrouver une magnétisation complète (gris clair) ainsi donnant une moins grande différence entre le signal provenant des spins situés dans le sang.

Cet effet impacte plus les vaisseaux où le flux sanguin est important menant à une augmentation de  $f_{fast}$ . Dans un deuxième temps, l'effet d'utiliser la séquence d'écho stimulé, STE, qui permet d'accéder à des temps de diffusion plus longs au lieu de la séquence SE a été étudié. La séquence STE est moins sensible à l'effet inflow que la séquence SE car elle est moins sensible aux flux dans les larges vaisseaux, ce qui donne des valeurs de  $f_{IVIM}$  et de  $f_{fast}$  moins élevées que pour la séquence SE. Cette étude a été réalisée à deux TRs différents, 1000 et 3500 ms. Le signal IVIM est devenu mono-exponentiel à TR = 3500 ms suggérant que la composante rapide n'est plus visible aux longs TRs. Enfin, la variation du temps de diffusion a été étudiée sur



une séquence STE en modifiant la valeur de  $\Delta$  :  $\Delta = 14, 30$  et  $60$  ms. Aux longs temps de diffusion, nous avons confirmé que le comportement bi-exponentiel du signal IVIM tendait à disparaître.

### **Application de la technique IVIM à l'étude d'un modèle animal de la maladie d'Alzheimer**

Enfin, la technique IVIM a été appliquée à l'étude de la maladie d'Alzheimer. C'est une maladie neurodégénérative affectant particulièrement les personnes âgées de plus de 65 ans. Les personnes atteintes de cette maladie perdent progressivement leur capacité à se rappeler, penser, apprendre et vivre de façon indépendante. Avant l'apparition de ces symptômes cliniques, des changements se produisent aussi au niveau biologique. Des agrégats anormaux de protéines forment des plaques dites amyloïdes dans le cerveau. Des neurones perdent leur connexion avec le réseau neuronal et finissent par mourir aboutissant à une diminution du volume cérébral. Les capillaires cérébraux sont aussi affectés dans les premières phases de la maladie car leur membrane basale s'épaissit et des plaques amyloïdes se forment à l'intérieur de leur paroi. Ces changements induisent des distorsions de la lumière des capillaires provoquant une diminution de la microcirculation. Comme des symptômes précoces de la maladie sont liés à des dérèglements de la microcirculation, IVIM pourrait jouer un rôle dans son diagnostic précoce. Pour le montrer, un modèle de souris de la maladie d'Alzheimer, la souris APP/PS1, a été utilisé. Six souris contrôles et six souris APP/PS1 ont été scannées à 6 mois sur l'IRM à 11.7T. Cependant, aucune différence dans les paramètres de diffusion ou IVIM n'a été trouvée entre les deux populations. Nous pensons que les souris étaient trop jeunes pour détecter un éventuel effet dû au développement de plaques amyloïdes dans la paroi des vaisseaux. 5 souris APP/PS1 entre 22 et 24 mois ont aussi pu être scannées. Cependant, aucune souris contrôle du même âge n'a pu être obtenue. Néanmoins, elles ont été comparées avec les souris APP/PS1 scannées à l'âge de 6 mois. Des différences ont été observées dans les paramètres de diffusion suggérant une diffusion plus restreinte en fin de maladie. Ce résultat n'est pas en complet accord avec des résultats publiés précédemment dans la littérature qui montrent au contraire une augmentation de la diffusion au sein des tissus suite à la disparition des barrières naturelles qui limitent normalement la diffusion. Aucune différence significative n'a été observée entre les paramètres IVIM avec l'âge des souris APP/PS1. Peut-être les résultats auraient été différents si

les souris APP/PS1 âgées avaient été comparées à des souris contrôles du même âge. Une analyse plus poussée et une comparaison avec des souris contrôles du même âge seraient souhaitables pour vraiment pouvoir estimer si la technique IVIM pourrait être utilisée pour étudier la maladie d'Alzheimer.

## **Conclusion**

Pour conclure, les expériences et simulations réalisées pendant cette thèse ont permis de mieux comprendre comment le signal IVIM peut être modélisé et comment il est influencé par les paramètres d'acquisition. Son application à l'étude de la maladie d'Alzheimer a donné des résultats qui ont besoin d'être confirmés et il serait intéressant de continuer les expériences commencées pendant cette thèse à ce sujet. En perspectives, il serait intéressant d'étudier l'influence de différents types d'anesthésie pour sélectionner la meilleure anesthésie qui permette la plus grande stabilité dans l'estimation des paramètres IVIM. La technique IVIM pourrait également être éprouvée sur un fantôme microfluidique. Les simulations numériques pourraient aussi être améliorées en prenant en compte le diamètre des vaisseaux et en simulant directement le signal IVIM à partir de réseaux microvasculaires directement extraits d'images histologiques. L'étude d'autres maladies neurodégénératives devrait aussi être considérée.



# Table of contents

Acknowledgments.....	5
Résumé de la thèse en français.....	9
Table of contents.....	19
Abbreviations and notations.....	25
General introduction.....	29
Chapter 1: Blood vessels in the brain.....	31
1.1 Blood content .....	31
1.1.1 Plasma .....	31
1.1.2 Red blood cells .....	32
1.1.3 White blood cells.....	33
1.1.4 Platelets.....	33
1.2 The brain vascular system .....	34
1.2.1 Why does the brain need a constant vascular input?.....	34
1.2.2 Vasculogenesis and angiogenesis mechanisms .....	35
1.2.3 Similarities between vascular and nervous systems.....	36
1.2.4 Anatomy of the brain vascular system.....	37
1.2.5 Characteristics of the vessels .....	38
1.3 The brain microvasculature .....	39
1.3.1 Methods to observe and extract information from the microvasculature .....	40
1.3.1.1 Staining of the blood vessels .....	40
1.3.1.2 Imaging after staining of the blood vessels .....	42
1.3.2 Structural characteristics of the microvessels .....	44

1.3.3	Flow inside blood vessels .....	48
1.3.3.1	Measure of the blood velocity .....	48
1.3.3.2	Velocity profiles .....	51
1.3.4	Simulated microvascular networks .....	53
1.3.4.1	Limitations of using real microvascular networks .....	53
1.3.4.2	Models of the microvascular network .....	54
Chapter 2:	MRI of the vasculature .....	59
2.1	History of MRI .....	59
2.2	Basic physical concepts of MRI .....	59
2.2.1	Spins and Larmor frequency .....	59
2.2.2	Magnetization vector and Bloch equations .....	61
2.2.3	Relaxation types .....	62
2.2.4	Image generation .....	65
2.2.4.1	Spatial encoding using magnetic field gradients .....	65
2.2.4.2	Modified Bloch equations .....	66
2.2.4.3	K-space and image reconstruction .....	66
2.2.5	Basic MR pulse sequences .....	67
2.2.5.1	Gradient echo sequence .....	67
2.2.5.2	Spin echo and stimulated echo sequences .....	68
2.2.5.3	Echo planar imaging sequence .....	71
2.2.5.4	Diffusion weighted imaging .....	72
2.3	MRI of the blood vessels .....	76
2.3.1	Imaging of the large blood vessels: MR angiography .....	76
2.3.2	Imaging of the microvasculature: perfusion imaging .....	79

2.3.2.1	Techniques with injection of contrast agent .....	79
2.3.2.2	Technique free from contrast agent injection .....	81
2.3.2.3	Emphasis on intravoxel incoherent motion imaging .....	83
Chapter 3: Impact of the diffusion encoding time on IVIM signal modelling .....		87
3.1	IVIM signal models.....	87
3.1.1	Two models for two limit cases.....	87
3.1.1.1	The standard mono-exponential model .....	87
3.1.1.2	The sinc model .....	89
3.1.2	Other models proposed in the literature.....	90
3.1.2.1	Models accounting for the intermediate regime .....	90
3.1.2.2	Other strategies to directly obtain and model the IVIM signal .....	91
3.1.3	The bi-exponential model .....	94
3.2	Evaluation of the best model for the IVIM signal at short diffusion encoding time .....	96
3.2.1	Material and methods.....	96
3.2.1.1	Animal procedures.....	96
3.2.1.2	MRI experiments.....	96
3.2.1.3	Data processing.....	97
3.2.1.4	Statistical analysis .....	101
3.2.2	Model comparison .....	102
3.2.3	Interpretation of the bi-exponential IVIM model .....	107
3.2.4	Evolution of the model parameters with the diffusion encoding time .....	109
Chapter 4: Numerical simulations of the IVIM signal .....		113
4.1	Introduction .....	113
4.1.1	Method combining perfusion MRI with simulations of the MR signal .....	113

4.1.2	Approach chosen for this thesis .....	114
4.2	Modelling of the IVIM signal in a microvascular network.....	115
4.2.1	Simplified spin trajectories and isochromat magnetization .....	115
4.2.2	Assumption 1: Uniform distribution of segment orientations .....	118
4.2.3	Assumption 2: Gaussian distribution of segment lengths and flow velocity.....	119
4.2.4	The average magnetization of trajectories in two limit cases .....	120
4.2.4.1	Trajectories containing only one segment .....	120
4.2.4.2	Trajectories containing many segments.....	121
4.2.5	Influence of the Gaussian distribution of the blood velocity on the total magnetization.....	122
4.2.6	Taking into account starting position of spins in the trajectory .....	123
4.3	Simulation results and discussion.....	124
4.3.1	Simulation parameters.....	124
4.3.2	The transition from sinc to exponential regime .....	127
4.3.3	Influence of imposing a Gaussian distribution for the segment length and the blood velocity .....	129
4.3.3.1	Gaussian distribution for the segment length .....	130
4.3.3.2	Gaussian distribution for the blood velocity .....	131
4.3.4	Influence of the diffusion encoding time .....	132
4.3.5	The two pool hypothesis .....	133
Chapter 5:	Extraction of vascular structural characteristics and influence of the acquisition parameters on the IVIM outputs .....	136
5.1	Comparison of IVIM data with the numerical simulations .....	136
5.1.1	Generation of a dictionary of simulated signals .....	136
5.1.2	Comparison of the experimental data with the dictionary of simulated signals ..	137

5.1.3	Interpretation of the shape of the contour plots .....	139
5.1.4	Extraction of structural parameters for the two pools .....	143
5.2	Influence of the repetition time: inflow effect.....	144
5.2.1	Explanation of the inflow effect.....	145
5.2.2	Impact on the IVIM outputs .....	145
5.3	Influence of the pulse sequence: spin echo versus stimulated echo.....	147
5.3.1	Phantom experiment .....	147
5.3.2	Physical explanation.....	150
5.3.3	Impact on the IVIM outputs .....	153
5.3.3.1	At short repetition time .....	153
5.3.3.2	At long repetition time.....	154
5.3.3.3	Discussion.....	154
5.4	Influence of the diffusion encoding time .....	156
Chapter 6:	Application of IVIM imaging to the study of Alzheimer's disease .....	159
6.1	Alzheimer's disease .....	159
6.1.1	Description of the disease.....	159
6.1.2	Current imaging techniques used in clinics to diagnose and follow the disease ..	160
6.1.3	Potential of IVIM in the study of Alzheimer's disease .....	161
6.2	Material and methods .....	162
6.2.1	Animal model .....	162
6.2.2	MRI experiments and data processing.....	163
6.2.3	Statistical analysis.....	164
6.3	Results and discussion .....	164
6.3.1	Comparison of 6-month APP/PS1 and control mice .....	164



6.3.2	Comparison of young and old APP/PS1 mice.....	165
6.4	Conclusion .....	168
Chapter 7:	Summary and conclusion .....	169
7.1	Summary.....	169
7.2	Limitations and possible improvements .....	170
7.2.1	Experimental protocol: anesthesia .....	170
7.2.2	Data analysis: diffusion coefficient of water in blood.....	172
7.2.3	Improvements of the numerical simulations.....	172
7.3	Future work .....	173
7.4	General conclusion .....	174
Bibliography.....		175
List of relevant publications .....		188

# Abbreviations and notations

## Imaging techniques

ASL	Arterial spin labeling
CASL	Continuous arterial spin labeling
CE	Contrast enhanced
DCE	Dynamic contrast enhanced
DKI	Diffusion kurtosis imaging
DSC	Dynamic susceptibility contrast
DWI	Diffusion weighted imaging
EPI	Echo planar imaging
fMRI	Functional magnetic resonance imaging
GE	Gradient echo
IVIM	Intra-voxel incoherent motion
KESM	Knife-edge scanning microscopy
LSM	Light sheet microscopy
MOST	Micro-optical sectioning tomography
MRA	Magnetic resonance angiography
MRI	Magnetic resonance imaging
PASL	Pulsed arterial spin labeling
PCA	Phase contrast angiography
pCASL	Pseudo-continuous arterial spin labeling
PET	Positron emission tomography
PGSE	Pulsed gradient spin echo
SE	Spin echo
SEM	Scanning electron microscopy
STE	Stimulated echo
TOF	Time of flight
TPLSM	Two-photon laser scanning microscopy

### Parameters

$ADC$	Apparent diffusion coefficient (mm <sup>2</sup> /s)
AICc	Corrected Akaike information criterion
AIF	Arterial input function
AW	Akaike weight
$B_0$	Static magnetic field (T)
$B_1$	Oscillating magnetic field (T)
BP	Bayesian probability
(r)CBF	(Relative) cerebral blood flow
(r)CBV	(Relative) cerebral blood volume
$D^*$	Pseudo-diffusion coefficient (mm <sup>2</sup> /s)
$D_{fast}^*$	Pseudo-diffusion coefficient of the fast pool (mm <sup>2</sup> /s)
$D_{slow}^*$	Pseudo-diffusion coefficient of the slow pool (mm <sup>2</sup> /s)
$D_b$	Diffusion coefficient of water in blood (mm <sup>2</sup> /s)
$f_{fast}$	Fractional volume occupied by spins flowing in the fast pool in a voxel (%)
FID	Free Induction Decay
$f_{IVIM}$	Fractional volume occupied by groups of spins flowing in the microvasculature in a voxel (%)
$f_{slow}$	Fractional volume occupied by spins flowing in the slow pool in a voxel (%)
$G_{Phase}$	Phase encoding gradient
$G_{Read}$	Frequency encoding gradient
$G_{Slice}$	Slice selection gradient
KM	Kurtosis model
$\lambda$	Brain-blood partition coefficient
$L$	Length
MEM	Mono-exponential model
$MSE$	Mean squared error
MT	Magnetization transfer
MTT	Mean transit time

$M_{xy}$	Transverse magnetization
$M_z$	Longitudinal magnetization
$N_b$	Number of b-values
NLLS	Non-linear least squares
$N_M$	Number of mice
$N_R$	Number of rats
PFC	Perfluorocarbon
RF	Radiofrequency
ROI	Region of interest
SAR	Energy deposited in the tissue
SNR	Signal-to-noise ratio
$T_1$	Longitudinal relaxation time (s)
$T_{1b}$	Longitudinal relaxation time of blood (s)
$T_{1t}$	Longitudinal relaxation time of tissue (s)
$T_2$	Transversal relaxation time (s)
$T_2^*$	“Observed” $T_2$ in the presence of magnetic field inhomogeneities (s)
TE	Echo time (s)
TM	Mixing time (s)
TR	Repetition time (s)
Tukey’s HSD	Tukey’s Honest Significant Difference
$V$	Blood velocity
VENC	Velocity encoding

### Structure

$^{19}\text{F}$	Fluorine
$^1\text{H}$	Proton
BBB	Blood brain barrier
Ctx	Cortex
Gd	Gadolinium
GM	Grey matter
Hp	Hippocampus
ICA	Internal carotid arteries
LC	Left cortex
LT	Left thalamus
RBC	Red blood cell
St	Striatum
WM	White Matter

### Others

AD	Alzheimer's disease
APP	Amyloid precursor protein
FITC	Fluorescein isothiocyanate
NMR	Nuclear magnetic resonance
NSF	Nephrogenic systemic fibrosis
$\text{O}_2$	Dioxygen
PO2	Intravascular oxygen level
PS1	Presenilin 1
s.c.	Subcutaneous

# General introduction

The brain is one of the most important organs in the human body. Its structural and functional integrity requires a continuous supply of energy, oxygen and glucose, mediated by circulating blood flow. The microvasculature, particularly the capillary network, is directly responsible for oxygen transport to the tissue and the regulation of local blood flow. A good understanding of the microcirculation is an essential aspect necessary to obtain the perfusion patterns in healthy and diseased tissues. The microcirculation can be visualized and studied using medical imaging.

The term medical imaging refers to techniques and processes that create images of the inside of the body which can help the medical staff to diagnose a disease, follow the evolution of a treatment, guide the surgeon during a medical intervention and help study tissues and organs in vivo. Several types of imaging techniques exist. Compared to other imaging techniques able to image the whole body, computed tomography and positron emission tomography, magnetic resonance imaging (MRI) uses no ionizing radiation and is relatively non-invasive. MRI can study hydrogen as well as other nuclei such as carbon 13, sodium 23, etc. The nucleus the most commonly studied is however hydrogen because of its abundance in the human body. Several MRI techniques gathered under the term MRI angiography can be used to observe the large blood vessels such as arteries and veins. However, to study microvessels, the spatial resolution of MRI does not allow for their direct visualization. Nevertheless, with a well-chosen design of the pulse sequence, MRI can be made sensitive only to protons in motion inside the body. This motion is restricted by natural barriers such as cell membranes, vessel walls and macromolecules. One particularly interesting MRI technique to extract information from the microvasculature is the IntraVoxel Incoherent Motion (IVIM) technique. It is able to differentiate between water protons inside the tissue and inside the microvasculature. IVIM is capable of giving macroscopic information about microscopic processes, namely flow inside the microvessels. Moreover, it has numerous substantial advantages over other similar techniques as it is free from contrast agent injection, completely noninvasive and easy to implement on a clinical scanner as based on a standard MRI sequence available on every clinical scanner from any manufacturer.

However, although it has been proven that IVIM is sensitive to flow in the microvasculature, it is not clear if it is sensitive only to the capillary network or to a larger part of the microvasculature. If the second hypothesis is correct, it could enlarge the scope of the applications opened to IVIM. The goal of this thesis is to better understand from where the IVIM signal originates, validate our hypothesis experimentally and apply the IVIM technique to the study of an animal model of Alzheimer's disease.

The first chapter of this manuscript provides a brief description of the blood content and the brain microvasculature. In Chapter 2, the basics of MR physics are presented and applied to define and compare the MRI techniques which can be used to study blood flow in the brain. The advantages of the IVIM technique over the other MRI techniques are exposed at the end of this chapter. The validity of the standard IVIM signal model is challenged in Chapter 3 and a bi-exponential IVIM model accounting for two distinct vascular pools is found to better describe the IVIM signal experimentally at short diffusion times. Mathematical modelling of the IVIM signal is then performed in Chapter 4 to design numerical simulations of the IVIM signal. These simulations are used in Chapter 5 to create a dictionary of simulated signals which is then compared to the signals obtained experimentally in order to extract structural information about the two vascular pools of the proposed bi-exponential IVIM model. The influence of acquisition parameters on the IVIM signal is also investigated in Chapter 5. IVIM is then applied to the study of an animal model of Alzheimer's disease in Chapter 6. The final chapter, Chapter 7, contains the conclusions, possible improvements and future work of this thesis.

# Chapter 1: Blood vessels in the brain

This chapter introduces the brain vasculature, first by defining blood constituents, then introducing the brain vascular architecture before focusing on the brain microvasculature. Finally, the last section describes how the microvascular network can be modelled and simulated.

## 1.1 Blood content

Blood is the most important fluid in the human body. This section presents the main functions of blood by going through its main constituents. As shown in Figure 1.1.A, the major components of blood are plasma (~ 55 %), red blood cells (RBCs) (~ 45 %), white blood cells and platelets (< 1 %).

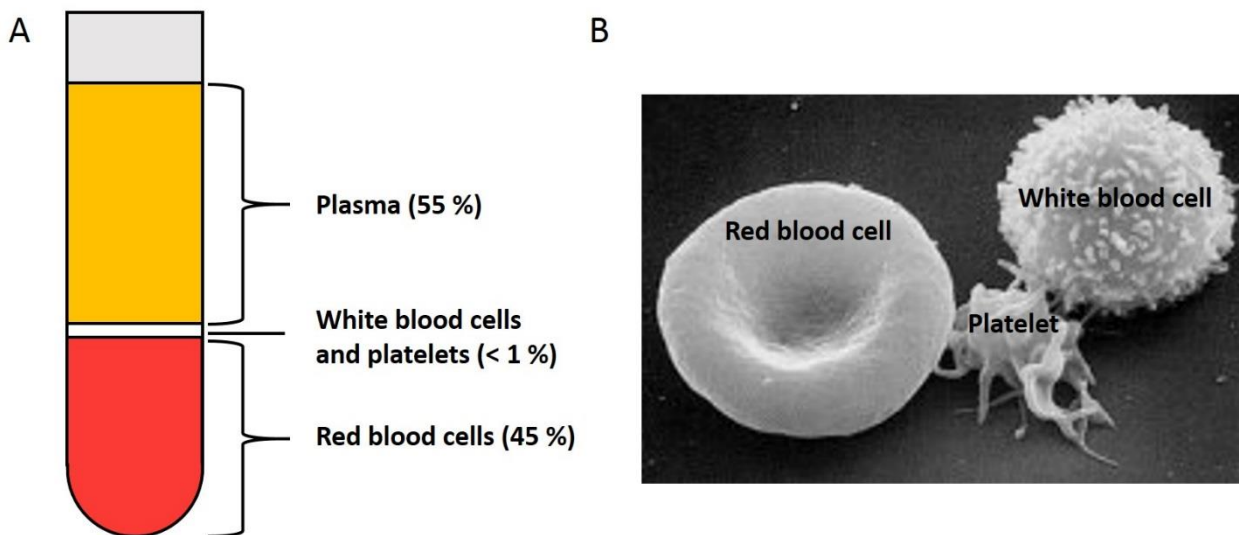


Figure 1.1. (A) Blood content represented in a centrifuged tube of blood sample. The heavier components, the red blood cells, pack at the bottom of the tube. Just above are the white blood cells and platelets. Finally, the principal component of blood, plasma, stays on top. (B) Scanning electron microscopy image of a red blood cell, platelet and white blood cell. Image taken at the Electron Microscopy Facility at the National Cancer Institute at Frederick, Maryland, USA.

### 1.1.1 Plasma

Plasma is the yellow fluid that remains after centrifuging a blood sample. It carries all the blood constituents to the cells. Apart from RBCs, white blood cells and platelets, it also contains sugars, lipids, vitamins, minerals, hormones, enzymes, antibodies and other proteins.



### 1.1.2 Red blood cells

RBCs, also called erythrocytes, account for 45 % of the blood content. As shown in the scanning electron microscopy image in Figure 1.1.B, they look like flattened biconcave discs of about 7  $\mu\text{m}$  in diameter. They have no nucleus. Their purpose is the transport of dioxygen,  $\text{O}_2$ , from the lungs to every cell in the body and of carbon dioxide from the cells back to the lungs. To accomplish that, RBCs have each around 280 million hemoglobin proteins. Hemoglobin consists of 4 hems, each containing one iron atom. Hems are arranged to leave a caveat at the center of the protein. The quaternary structure of the hemoglobin is important for the capture of  $\text{O}_2$  or its release. Figure 1.2 shows the two possible conformation states of the hemoglobin protein in quaternary structure: state T (for tensed) and state R (for relaxed).

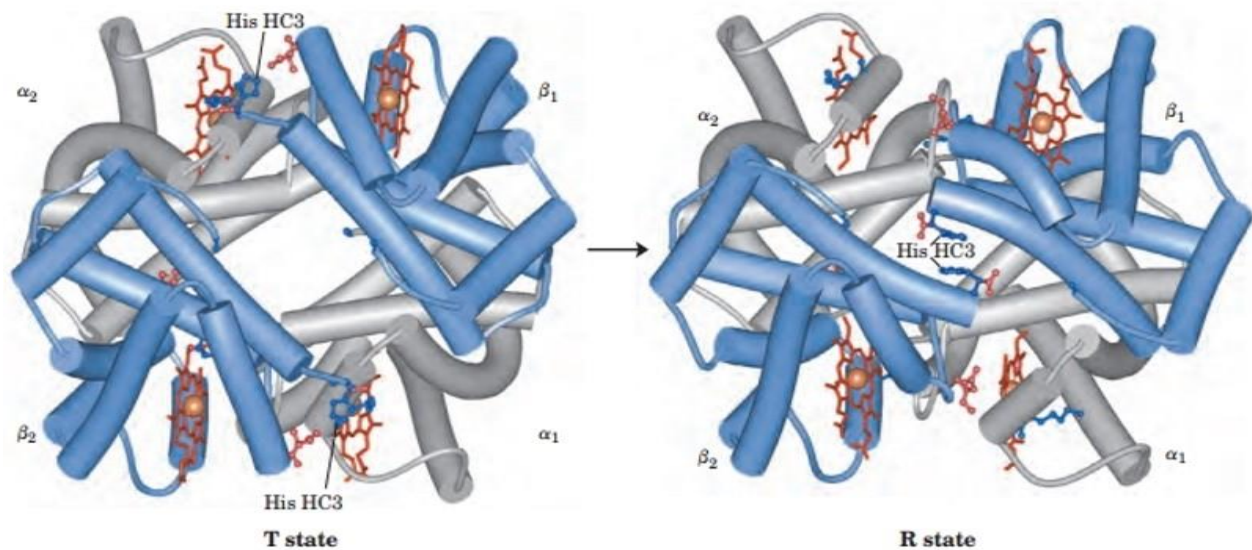


Figure 1.2. Transition between T and R states of hemoglobin in quaternary structure representation. The 4 hems of hemoglobin are also called subunits:  $\alpha_1$ ,  $\alpha_2$ , here in grey and  $\beta_1$  and  $\beta_2$ , here in blue. Histidine residues (His HC3) located at one end of the  $\beta$  subunits rotate between T and R states to the center of the caveat. This and other mechanisms result in a narrowing of the caveat of the hemoglobin in R state. This state is preferred when binding  $\text{O}_2$ . From Leningher [2].

At low pH and concentration of  $\text{O}_2$ , the protein is preferably in T conformation which has low affinity for  $\text{O}_2$ . Thus, if an  $\text{O}_2$  molecule was attached to the protein, it is released. On the contrary, if the pH is high as well as the  $\text{O}_2$  concentration, the R conformation with more affinity to  $\text{O}_2$  is preferred and hemoglobin is able to bind to  $\text{O}_2$ . In fact, the T conformation is more

stable than the R conformation but, when O<sub>2</sub> is present, it stabilizes the R conformation. Patients suffering from anemia lack of RBCs and feel fatigued due to a shortage of oxygen. When oxygen binds to iron atoms in hemoglobin, hemoglobin is called oxyhemoglobin and iron oxides are what gives blood its red color.

### 1.1.3 White blood cells

White blood cells, also called leukocytes, are about 600 times fewer than RBCs and represent less than 1% of the blood content with platelets. They are part of the immune system. Figure 1.1.B shows a scanning electron microscopy image of a white blood cell. Unlike RBCs, leukocytes have a nucleus. There are three types of leukocytes. The most abundant are granulocytes which have small particles called granules inside their cytoplasm. They include basophils which are involved in inflammatory reactions and eosinophils and neutrophils which digest, phagocytize, complexes formed by antibodies-antigens and bacteria, respectively. The second most numerous type of leukocytes is lymphocytes, small cells with a large round nuclei and a small cytoplasm, which are responsible for killing viruses and produce antibodies. The last category is monocytes which are precursors to macrophages which digest bacteria as well as viruses. Thus, blood also has the function to transport these cells of the immune system quickly to the location of an infection. White blood cells do not always stay inside the blood vessels and can easily cross the vessel walls by amoeboid motion. They are able to pass through holes in the vessel walls smaller than themselves by extending a small part of the cell called a pseudopodium through the vessel wall. The cell's cytoplasm and content progressively stream to that pseudopodium and finally arrive in the surrounding tissue.

### 1.1.4 Platelets

Platelets are the smallest elements in blood and are actually fragments of larger cells found in the bone marrow. They have no nucleus. Resting platelets are smooth discs of 2-4 μm in diameter while upon activation they have an irregular shape with protruding pseudopodia as the one shown in Figure 1.1.B. In that state, they are capable of the same amoeboid motion as white blood cells. The role of platelets is to start the clotting when a blood vessel is damaged and they constitute the major mass of the clot. In some circumstances, platelets can also produce a circulating clot also called thrombosis which, if located in one of a major arteries, can

prevent blood from flowing into one part of the heart or the brain and cause a heart attack or a stroke, respectively.

As a conclusion, all blood constituents have their own function: blood, oxygen and nutrients transportation, infection fighting and blood clotting. They contribute to the well-being of the organs and any change in the blood content can have tremendous consequences on the viability of the organ.

## 1.2 The brain vascular system

### 1.2.1 Why does the brain need a constant vascular input?

The brain is the most complex organ of the body. In the early eighteenth century, it was discovered to consist of two different parts: the white matter (WM) and the grey matter (GM) [3]. The WM, which represents more than half of the brain [4], mainly consists of myelinated axons and very few neuronal cell bodies. Its function is to ensure electrical connections between neurons. The GM includes all neurons, dendrites, microglia, astrocytes and blood vessels and represents less than 50 % of the brain. The function of neurons is to process information received through dendrites or axons. Dendrites have the same role as axons but are not surrounded by myelin and are shorter than axons. Microglial cells are part of the immune system and fight against foreign materials. Astrocytes, located between neurons and blood vessels, transport nutrients from the blood vessels to the neurons and also support endothelial cells that form the blood brain barrier (BBB). The BBB is a physiological barrier designed to protect the brain by regulating the crossing of particles from the blood stream at the capillary level to the brain tissue.

The brain consumes 20 % of the total energy of the body even though it represents only 2 % of the total body weight [5]. However, this organ is not able to store energy. This is why the brain needs a constant vascular input. Figure 1.3 shows the brain vasculature with a brain for which the tissues surrounding the vessels have been dissolved. The brain is not the organ receiving the most part of the cardiac output at rest. The kidneys, liver, spleen, gastrointestinal tract and skeletal muscles are more vascularized than the brain.



Figure 1.3. Cerebral blood vessels obtained by injecting the blood vessels with a plastic emulsion and dissolving the brain parenchyma. From Zlokovic et al [6].

Blood vessels have the important function to provide organs with energy supplies and remove the waste products. A constant regulation of the supply and removal of these materials in the brain is needed otherwise a cascade of events is initiated which leads to neuronal deaths and irreversible damages [7].

### 1.2.2 Vasculogenesis and angiogenesis mechanisms

The first process to occur in vascular network generation is vasculogenesis. In the embryo, endothelial precursor cells (angioblasts) migrate and differentiate into endothelial cells to create a first network of blood vessels. Then angiogenesis takes place. This process is shown in Figure 1.4.A: perivascular cells detach from the vessel walls and the vessel membrane is degraded to allow migration of endothelial cells creating new vessel buds and sprouts. These buds and sprouts elongate and form branches before being stabilized by the recruitment of perivascular cells and the production of extracellular matrix compounds.

Vasculogenesis was thought to be only a pre-natal process but it can also occur in the adult organism by recruitment of circulating angioblasts as shown in Figure 1.4.B. For example, post-natal vasculogenesis is involved in wound healing [8], limb ischemia [9] and tumor growth [10].

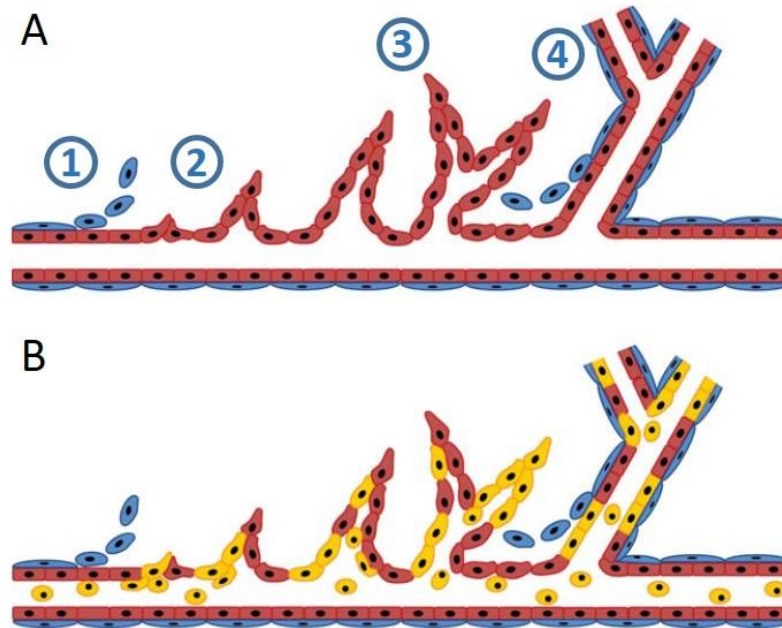


Figure 1.4. Mechanisms of blood vessel formation. (A) Angiogenesis: 1) upon activation by pro-angiogenic growth factors, perivascular cells (in blue) detach from the vascular wall and endothelial cells (in red) release proteases, which degrades their basement membrane. 2) It allows for endothelial cells migration and the formation of vessel buds or sprouts. 3) These sprouts further elongate and make branches and interconnections. 4) The new blood vessels are stabilized by the recruitment of perivascular cells and the production of extracellular matrix compounds. (B) Post-natal vasculogenesis: vessels form from the recruitment of circulating angioblasts (in yellow), their proliferation and finally differentiation into mature endothelial cells. From Laschke et al [11].

### 1.2.3 Similarities between vascular and nervous systems

As blood vessels act as supply vessels for the neurons, their geometry is not random. Nerve fibers and blood vessels follow an orderly pattern, often alongside each other. They can influence each other's development. Similarities have been found between the molecules involved in the guidance of nerve fibers and blood vessels and the growth factors directing angiogenic sprouting and those regulating terminal axon arborization [12]. Zheng et al. showed that there is a regional organization of the microvessels corresponding to the underlying organization of the neurons inside the primate visual cortex. They also suggest that this pattern can be generalized to other animals [13]. There is a close connection between the vascular and neuronal networks. The study of the vascular network can allow for a better understanding of

the organization of the neurons. Abnormalities in the nervous system most probably result or come from abnormalities in the vascular system.

#### 1.2.4 Anatomy of the brain vascular system

The human brain has approximately 400 miles of blood vessels. As it is the most important organ in the human body, its vascular system is the one which develops first in the embryo [14]. Blood arrives to the brain mainly from the two internal carotid arteries (ICA). It can also arise from the vertebral arteries which merge to form the basilar artery and join the ICA at the circle of Willis shown in Figure 1.5. Even if one artery is blocked or damaged, the circle of Willis enables to still provide normal cerebral perfusion as the arteries are all connected through that circle also called polygon. However, only about a half of the human population has a complete Willis polygon [15]. An incomplete polygon can condition the appearance and severity of cerebrovascular disorders such as aneurysms and infarctions.

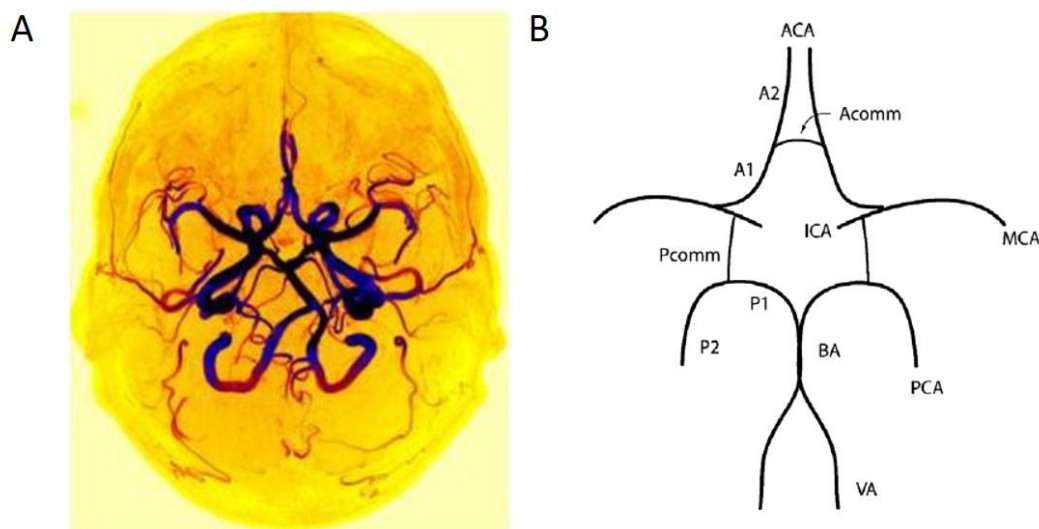


Figure 1.5. (A) Axial maximum intensity projection time-of-flight (TOF) images of a complete circle of Willis from one patient. The TOF technique will be presented later in section 2.3.1. (B) Arteries comprising the circle of Willis. ICA: internal carotid artery; ACA: anterior cerebral artery; MCA: middle cerebral artery; PCA: posterior cerebral artery; BA: basilar artery; VA: vertebral artery; Acomm: anterior communicating artery; Pcomm: posterior communicating artery; A1, A2, P1, P2: branches of the anterior and posterior cerebral arteries. From Ezzatian-Ahar et al. [16] and Cucchiara et al [17].

From the circle of Willis, the anterior, middle and posterior cerebral arteries supply the brain with  $O_2$  and nutrients (Figure 1.5.B). If we focus for example on the cortex, the arteries which



are mapping the surface of the cortex are called pial arteries. Smaller diameter arteries are named arterioles. When arterioles perforate the surface of the cortex, they are called penetrating arterioles and as they divide and their diameter decreases, they become deep microvessels or capillaries. Then capillaries merge to become venules which in turn merge to give veins which finally go back to the heart as the vena cava. Figure 1.6 shows a 3D reconstruction of a part of the cortex with the vascular network going from pial arterioles to pial venules.

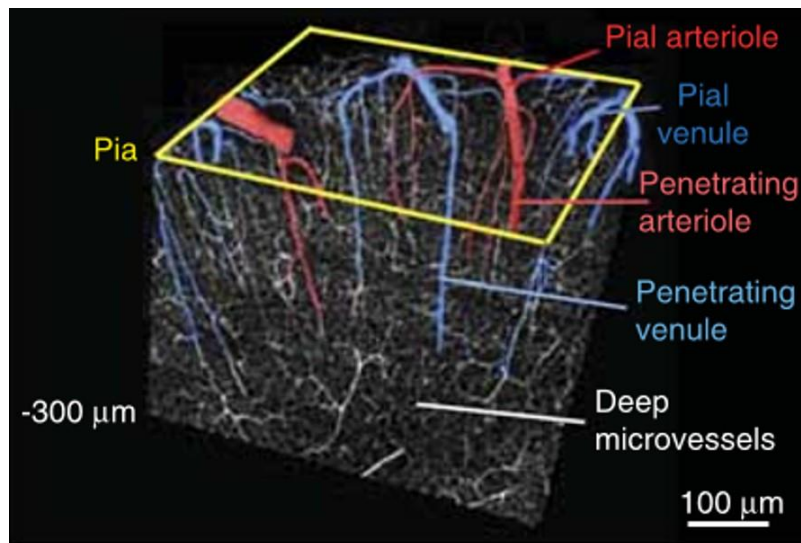


Figure 1.6. 3D-reconstruction of a block of tissue collected by in vivo two-photon laser scanning microscopy from the upper layers of the mouse cortex. Penetrating vessels plunge into the depth of the cortex, bridging flow from surface vascular networks to capillary beds. From Shih et al [18].

### 1.2.5 Characteristics of the vessels

The two main parameters measured when studying the brain vascular network are the cerebral blood flow (CBF) and cerebral blood volume (CBV). These two parameters can be broken up at the vessel scale into three other parameters: the vessel diameter, the vessel length and the blood velocity. Table 1.1 gives estimates of these three parameters and the wall thickness for the different vessel types. In this table, arterioles, capillaries and venules have been gathered under the term microvessels. They will be described in more details in the next section.

<b>Vessel type</b>	<b>Vessel diameter (mm)</b>	<b>Wall thickness (<math>\mu\text{m}</math>)</b>	<b>Vessel length (cm)</b>	<b>Blood velocity (mm/s)</b>
Aorta	25	1500	40	630
Large arteries	6.5	1000	20	200-500
Main artery branches	2.4	800	10	/
Terminal artery branches	1.2	125	1	50
Microvessels	0.008-0.15	1-20	0.1-0.2	0.2-5
Terminal veins	1.5	10	1	/
Main venous branches	5	100	10	/
Large veins	14	200	20	/
Vena cava	30	400	40	135

Table 1.1. Characteristics of the human blood vessels categorized by vessel type: vessel diameter, wall thickness, vessel length and blood velocity. From Freitas [19].

The vessel diameter displayed in Table 1.1 is the lumen diameter. Arteries have a smaller lumen diameter than veins because their wall thickness is thicker than the one of veins. Indeed, arteries' membranes must resist high blood pressure changes. Then, pressure drops when blood passes through the capillaries and is very low inside the veins which thus have thinner vessel walls. The values provided for the vessel length and blood velocity in Table 1.1 are mean values.

### 1.3 The brain microvasculature

This thesis is centered on the study of the microvasculature which consists of the smallest vessels: capillaries, arterioles and venules (Figure 1.7).

First, techniques to extract structural information from the microvasculature are presented. Then, information about the geometry, structure and flow in the microvessels are summarized. Finally, methods to simulate the microvascular network are described.





Figure 1.7. 3D volume rendering of a selected zone of the cortex by scanning electron microscope showing the microvasculature: pial, penetrating arterioles and venules and capillaries. From Schoonover [20].

### 1.3.1 Methods to observe and extract information from the microvasculature

The main techniques having enough spatial resolution to visualize and extract structural parameters from the microvessels are performed postmortem, ex-vivo. These techniques involve two steps. Microvessels are usually labelled to enhance their contrast compared to the surrounding tissue before being imaged. Techniques to measure the blood velocity are different as they require in-vivo access. They will be presented in section 1.3.3.1.

#### 1.3.1.1 Staining of the blood vessels

Labeling of the microvessels is an important step to facilitate their visualization in the imaging step. Different strategies can be used.

A low viscosity resin like methyl methacrylate can be injected into the vessels replacing blood. After some time, it solidifies. Then, potassium hydroxide can be used to completely dissolve the surrounding tissue leaving the resin intact and yielding a cast of vessels [21]. The advantage of this technique is that the vessels are completely separated from the tissue and they are not deformed so precise measurements of the lumen diameter can be obtained. However, as the vessels are no longer supported by nervous tissue, they are more difficult to identify.

The other staining techniques rely on histological methods. The most common method involves injection of india ink and gelatin [21], [22]. This method has the advantage to completely fill the microvascular network and allows for the precise identification and detailed study of arteries and veins. However, vascular rupture can happen in superficial vessels masking them. Also, the fixation and dehydration of the tissue following the injection of india ink can deform the vessels to a large extent making the measure of the vessel diameter not fully reliable. In addition to this, when some vessels are ruptured consequently to a disease, the ink can diffuse outside of the vessel.

Another strategy consists in injecting gelatin and fluorescein conjugated to albumin [23]. Crosslinking of the albumin to the gelatin skeleton prevents diffusion of the fluorophore in the extravascular space, even in exposed vessels. A derivative of the fluorescein, the fluorescein isothiocyanate (FITC), is often used in combination with dextran [24]. The india ink and fluorescein methods also permit simultaneous staining of other structures than the vessels. For example, if information about the location of the neurons compared to the vessels is sought, a fluorescent stain, DAPI, can be added to label all cell nuclei along with  $\alpha$ -NeuN antibody which allows for the differentiation of neuronal versus non-neuronal cells [23].

The two histological methods presented previously fill the vessels with a substance to label them. Another approach is to directly label endothelium cells of the vessel walls. This can be achieved by incubating the fixed tissue of interest with the calcium cobalt method to label alkaline phosphatase activity in the endothelium of blood vessels [25]. However, this type of staining is not homogeneous throughout the vascular tree [26]. In particular, venous capillaries are poorly stained. Other dyes use similar labeling strategies. Nissl targets the rough endoplasmic reticulum and free polyribosomes in neurons, glia and endothelial cells [27]. Von Willebrand factor specifically marks endothelial cells using specific antibodies [28]. And Dil efficiently stains the vessel membrane due to its lipophilic characteristics [29].

An interesting strategy is to combine staining of the perfused capillaries using for example FITC-dextran dyes with staining of the membranes of all capillaries by labeling alkaline phosphatase

activity in the endothelium of the vessels [30]. This allows for the comparison of perfused and non-perfused capillaries at the same time.

### 1.3.1.2 Imaging after staining of the blood vessels

Several imaging techniques can be used to visualize the blood vessels after that they have been stained. Two-photon laser scanning microscopy (TPLSM) allows for the observation of fluorescent dyes such as fluorescein or FITC. Figure 1.8.A shows a TPLSM image of the mouse brain cortex with different fluorescent stains: DAPI, fluorescein and  $\alpha$ -NeuN. Blinder et al. managed to image the cortex with a 1  $\mu$ m resolution [31]. However, this technique is limited by the imaging field and penetration depth of two-photon imaging.

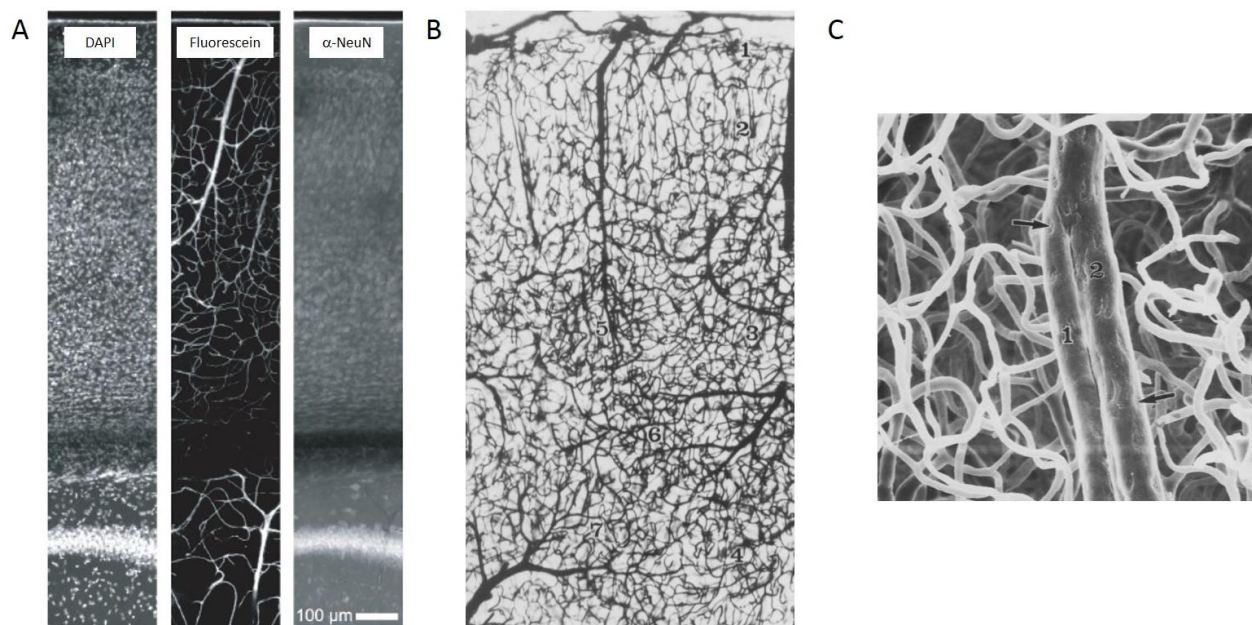


Figure 1.8. (A) Maximal projection of two-photon laser scanning microscopy image data of a 2 mm region of the mouse brain cortex from the bregma. DAPI, fluorescein and  $\alpha$ -NeuN are fluorescent dyes of all cell nuclei, blood vessels and neuronal cells, respectively. (B) Light sheet microscopy image after india ink staining of a section of the human brain cortex showing the four cortical vascular layers (1-4) and examples of bush-like venous network (5-7) (x 64). (C) Scanning electron microscopy image of a cast of vessels of the human brain cortex. (1) Recurrent branch coupled with the parent vessel (2). Arrows indicate impressions of endothelial cell nuclei on the arterial cast (x 440). From Tsai et al. [23] and Duvernoy et al [21].

Light sheet microscopy (LSM) is generally used to image tissues stained with india ink or Nissl [22]. Figure 1.8.B is an example of a light sheet microscope image after injection of india ink and fixation of the sample. This optical method has the same limitations as TPLSM. However, a

technique to improve the penetration depth called optical clearing aiming to make the surrounding tissue transparent is more and more used [32]. For example, by adding liquid paraffin to a sample already stained with india ink, Hashimoto et al. managed to get whole mouse brain images with a 5  $\mu\text{m}$  resolution [33].

To obtain LSM images, first the sample needs to be cut in very thin slices using a microtome. Techniques have been developed to perform this step at the same time as collecting the images. Li et al. created the micro-optical sectioning tomography (MOST) [34]. Using Nissl staining coupled with MOST, Wu et al. imaged the whole mouse brain at one micron voxel resolution with high image quality [35]. Xue et al. managed to get even better resolution with india ink perfusion:  $0.35 \times 0.4 \times 2 \mu\text{m}^3$  [36]. Another similar technique developed approximately at the same time is knife-edge scanning microscopy (KESM) [37]. It allows to cut sections as thin as 0.5  $\mu\text{m}$  from tissues embedded in resin with india ink or Nissl staining [38].

Casts of vessels obtained by dissolving tissues after filling the blood vessels with a resin are imaged with scanning electron microscopy (SEM) [21], [39]. Figure 1.8.C shows a SEM image of a vessel cast of the human brain cortex. Nuclei of endothelial cells are pointed at by arrows. SEM has higher resolution than light sheet microscopy and the depth of focus is high enough to get a large field of view enabling to reliably trace individual vessels either over very short or over extremely long distances.

Other strategies not using optical methods but MRI and CT can also be employed. Instead of injecting gelatin doped with gadolinium chelates to enhance the contrast in MRI images, an inert silicon rubber can be used. This other contrast agent causes vessels to appear dark on MRI and bright on CT. The low viscosity of the inert silicone rubber allows for complete filling of the vasculature and its hydrophobicity restricts itself from crossing the vessel membrane. By combining MRI and CT images, Dorr et al. created a whole brain mouse vascular atlas with a 30  $\mu\text{m}$  resolution [40]. This staining is also suitable for optical imaging as the silicon rubber is optically opaque. Pathak et al. thus compared MRI and CT images with LSM images of the same mouse brain to show that good agreement can be obtained between the three techniques (Figure 1.9) [41].

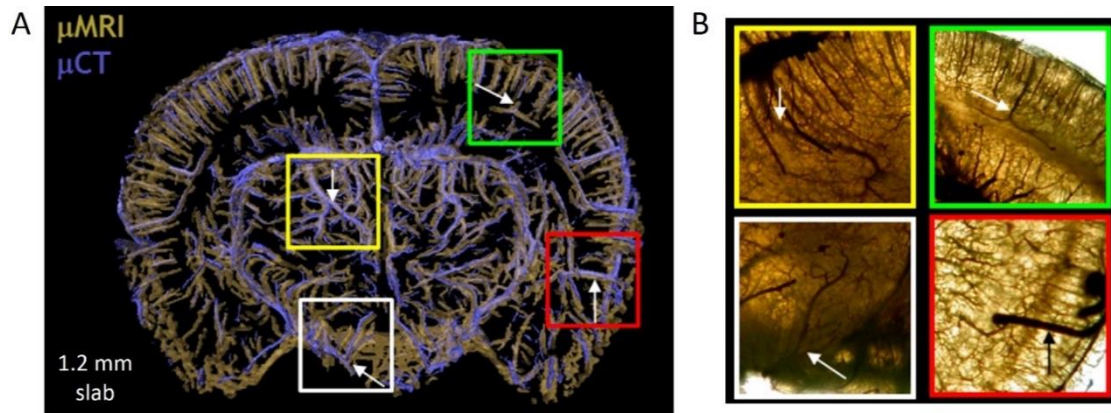


Figure 1.9. Comparison between  $\mu$ MRI,  $\mu$ CT and bright-field images. (A) 1.2 mm slab of a mouse brain in which the  $\mu$ MRI-derived vasculature (gold) is overlaid on that acquired using  $\mu$ CT (purple). (B) Bright-field images of ROIs corresponding to the colored squares in Figure 1.9.A. White arrows indicate major vessels that are visible in both Figure 1.9.A and B. From Pathak et al [41].

### 1.3.2 Structural characteristics of the microvessels

To detail the different characteristics of the microvessels, the work of Cassot et al. is going to be detailed.

Based on Duvernoy et al.'s images of the cortex of an india ink-injected human brain (Figure 1.10.a), Cassot et al. segmented all vessels in two sections of about 300  $\mu$ m thick to extract quantitative structural parameters of the microvessels (Figure 1.10.d) [42].

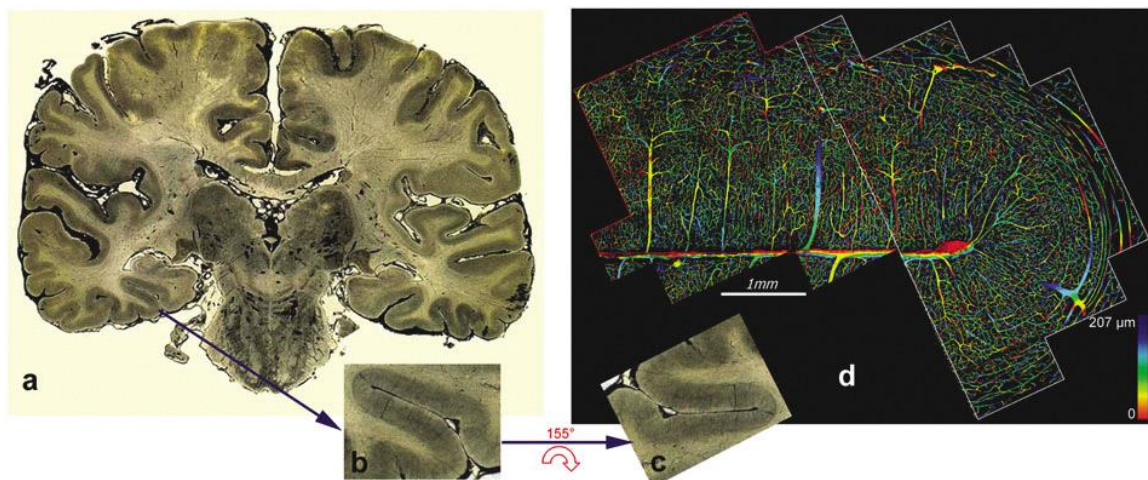


Figure 1.10. (a) Section of india ink-injected human brain imaged with confocal microscopy from Duvernoy et al.'s collection. (b-c) Image and flipped image zoomed from image (a) on the collateral sulcus in the temporal lobe. (d) Depth coded projection of the vessels in image divided in two mosaics outlined in red and white (c). From Cassot et al [42].



From this analysis, they were able to extract frequency distributions for the diameter and the vessel length of the microvascular network which are shown in Figure 1.11.

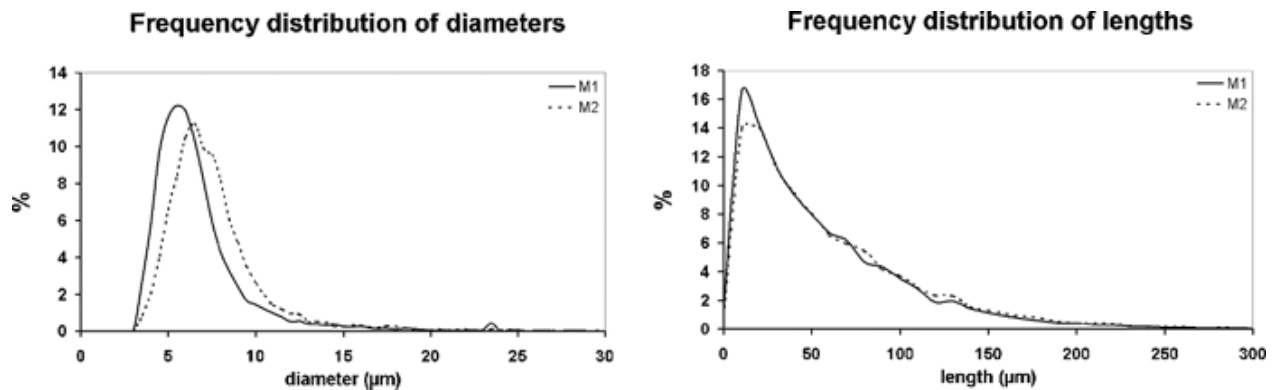


Figure 1.11. Histograms of diameters (left) and lengths (right) of the microvascular networks for the two mosaics in Figure 1.10.d (solid and dotted lines). From Cassot et al [42].

They also measured for the two sections a stable vascular density of 2.44 %. The vessels are preferentially forming bifurcations (94 %). A bifurcation is defined when one parent vessel splits into two daughter vessels at a branching node as shown in Figure 1.12.

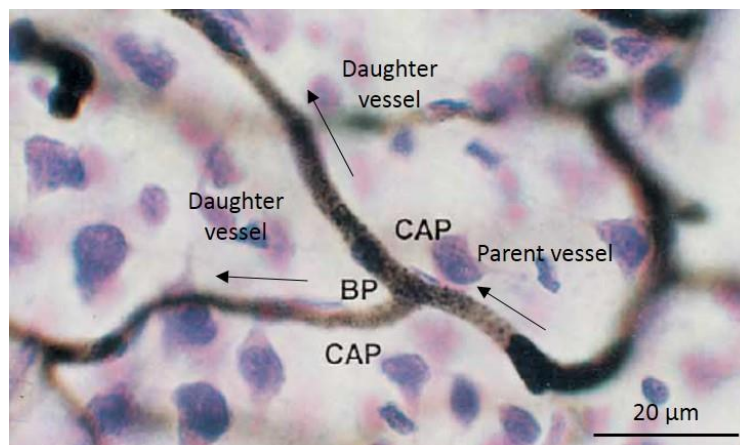


Figure 1.12. LSM image of a tissue perfused with india ink and stained with cresyl violet. Capillaries (CAP) perfused with india ink appear in black. A branching point (BP) can be seen in the middle of the image. The neurons stained with cresyl violet appear in violet. Adapted from Tata et al [22].

The arterial and venous networks can also be separated from the capillary network. Generally, the delimitation between arterioles, venules and capillaries is made by putting a diameter upper limit for the capillaries. Arterioles and venules are then defined as vessels with a larger diameter than this limit. To set the diameter limit, for example, Pawlik et al. took all vessels with a

diameter smaller than 15  $\mu\text{m}$  in their images and measured the goodness of fit of a normal distribution to a sample of 300 mean diameters while progressively decreasing this diameter limit [43]. The best fit was obtained for a diameter limit of 7  $\mu\text{m}$  (Figure 1.13) and with that limit they found that capillaries have diameters ranging from 4.2 to 7  $\mu\text{m}$  with a mean vessel length of 110  $\mu\text{m}$ . This diameter limit varies between studies and is generally between 6 and 10  $\mu\text{m}$ .

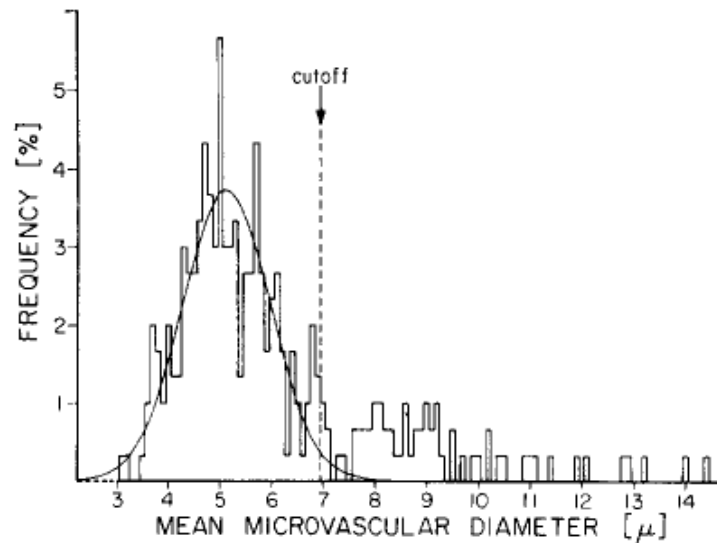


Figure 1.13. Frequency distribution of the microvascular mean diameters in cat cerebral cortex and maximum likelihood normal distribution of intracortical capillary mean diameters. From Pawlik et al [43].

In Cassot et al.'s paper, they first performed an analysis of the arterial and venous trees defining 4 levels of vessels for these two trees, the fourth level corresponding to a large vein and level 0 to a precapillary venule. The threshold for the capillaries was fixed to the mean diameter of level 0 which was 9  $\mu\text{m}$ . With this threshold, the capillary mean diameter and vessel length were found to be not so different from the mean diameter and vessel lengths of the entire microvascular network:  $5.9 \pm 1.30 \mu\text{m}$  and  $57.4 \pm 50.98 \mu\text{m}$  compared to  $6.91 \pm 3.85 \mu\text{m}$  and  $56.65 \pm 51.66 \mu\text{m}$  for the mean vessel diameter and length, respectively.

As there is no real consensus on what a capillary really is, anatomically, histologically or hemodynamically [44] and with the large of possible imaging methods, many different values for the capillary diameter and length have been reported in the literature. Some of them are gathered in Table 1.2.

Authors	Year	Subject	Method	Diameter (μm)	Length (μm)	Reference
Craigie et al.	1932	rat	India ink staining + LSM	2.3-3		[45]
Hunziker et al.	1974	cat	Alkaline phosphatase activity markers + SEM	4.8	280.4	[46]
Laursen et al.	1977	rat	Alkaline phosphatase activity markers + SEM	4.9	344.5	[25]
Meier-Ruge et al.	1980	human	Alkaline phosphatase activity markers + SEM	6.3		[47]
Ivanov et al.	1980	rat	Intravital microfilming	2-5	60-200	[48]
Pawlik et al.	1981	cat	High-speed microcinéphotography	4.2-7	110	[43]
Duvernoy et al.	1981	human	India ink staining + LSM and vascular corrosion cast + SEM	6	/	[21]
Weiss et al.	1982	rat	FITC-dextran staining + TPLSM	6.1	/	[30]
Ben Hamida et al.	1983	cat	Nissl staining + LSM	2-7	/	[49]
Villringer et al.	1994	rat	Fluorescein staining + TPLSM	5.3	/	[50]
Tata et al.	2002	rat	Nissl staining + LSM	4	32.2-51.2	[22]
			India ink staining + LSM	3.5	42.5-51.6	
Lu et al.	2004	rat	FITC-dextran staining + TPLSM	< 7.5	< 200 μm	[51]
Hauck et al.	2004	rat	Intravital microscopy	4.1	/	[52]
Cassot et al.	2006	human	India ink staining + LSM and vascular corrosion cast + SEM	5.9	57.4	[42]
Michaloudi et al.	2006	rat	India ink staining + LSM	4.1	/	[53]
Lauwers et al.	2008	human	India ink staining + LSM and vascular corrosion cast + SEM	6.5	53	[44]
Tsai et al.	2009	mouse	FITC-gelatin, DAPI, α-NeuN staining + TPLSM	4.1	/	[23]
Blinder et al.	2013	mouse	Fluorescein-conjugated-albumin gel staining + TPLSM	< 7	50	[31]
Wu et al.	2014	mouse	Nissl staining + MOST	3-6	/	[35]
Xue et al.	2014	mouse	India ink staining + MOST	4.6	/	[36]

Table 1.2. Reported capillary diameter and length in the literature in chronological order.



The mean capillary diameter ranges between 2.5 and 6.5  $\mu\text{m}$ . The mean value of all these estimates for each subject is very close between the rat (4.2  $\mu\text{m}$ ), the mouse (4.4  $\mu\text{m}$ ) and the cat (4.5  $\mu\text{m}$ ) but is a bit higher in humans (6.2  $\mu\text{m}$ ). The range of mean vessel length is also large from 32.2 to 344.5  $\mu\text{m}$ . The more recent values are around 50  $\mu\text{m}$  in humans as well as in mice.

Arterioles and venules being larger diameter vessels, it is easier to identify them and measure their structural characteristics. In humans, Freitas reports diameters for the arterioles between 25 and 100  $\mu\text{m}$  [19]. Venules have pretty much the same range transposed slightly to higher diameters up to 150  $\mu\text{m}$ . For the vessel length, they report the same for both types of vessels: on average, 2 mm.

### 1.3.3 Flow inside blood vessels

#### 1.3.3.1 Measure of the blood velocity

Contrary to the previous section, imaging techniques suitable for the study of microvessels *in vivo* are needed to obtain estimations of the blood velocity.

Optical methods like intra-vital microscopy allow for the measure of parameters related to the blood velocity. In the first section, we saw that RBCs are giving blood its red color and that plasma is more of a yellow color. Taking advantage of this color difference and knowing that, with the small capillary diameter, RBCs can travel only one behind each other in capillaries, researchers have developed optical methods to track the plasma gaps between RBCs inside the capillaries [48]. Figure 1.14 shows the shift of a plasma gap in two images separated by 0.1 s.

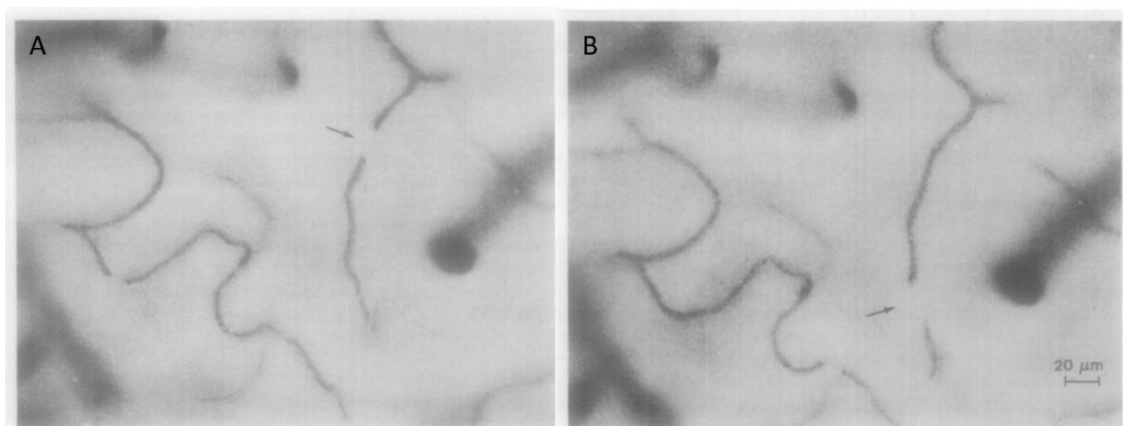


Figure 1.14. Brain capillaries at depth 40  $\mu\text{m}$  with arrows showing the shift of the plasma gap. Images A and B are separated by 0.1 s. Scale bar: 20  $\mu\text{m}$ . Adapted from Ivanov et al [48].

However, this technique can lead to measurement errors as plasma gaps can also correspond to slowly moving white blood cells.

A more reliable imaging technique is the tracking of fluorescently labeled RBCs [54]. After labeling of RBCs typically with FITC-dextran, the brain is imaged using a high speed camera laser scanning confocal microscope through a cranial window. In this technique, the movement of RBCs is directly recorded avoiding the problem of plasma gaps corresponding to white blood cells. However, Unekawa et al. pointed out a limitation of this method regarding the frame rate of the camera used [55]. As illustrated in Figure 1.15.A, the frequency distribution function of RBC velocities that is obtained highly depends on the frame rate. At short frame rate, high velocities are not measurable and a part of the RBCs present in the capillaries are not taken into account. Thus, a too short frame rate introduces errors in the RBCs velocity measurements. Only RBC velocity measurements with high frame rate are reliable.

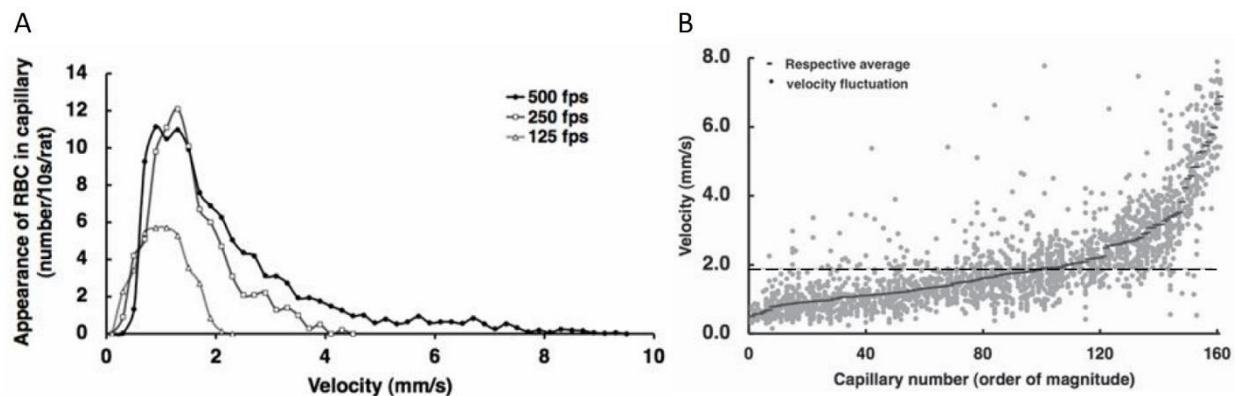


Figure 1.15. (A) Frequency distribution functions of RBC velocities obtained at different frame rates per second (fps): 500 fps (closed circles,  $n = 37$ ), 250 fps (open squares,  $n = 10$ ) and 125 fps (open triangles,  $n = 6$ ) for 10 s. (B) Fluctuation (small dots) and respective averages (small bars) of RBC velocities in individual capillaries detected 5 or more times at 500 fps for 10 s against the capillary number. The mean of individual averages, 1.96 mm/s, is shown by the horizontal dotted line. From Unekawa et al [55].

Figure 1.15.B shows the values of repeated measures of the RBC velocity for 161 individual capillaries with a high frame rate (500 frames per second). The average RBC velocity in capillaries was found to be  $1.96 \pm 1.26$  mm/s.

However, the RBC velocity is not the same as the blood velocity but it can be approximated from the RBC velocity. The RBCs' diameter being close if not larger than the diameter of microvessels, they should not be able to get inside capillaries but they still need to travel through capillaries to deliver oxygen and nutrients. To achieve that, their cell membrane has the capacity to deform as shown in Figure 1.16. Instead of a biconcave disc-shape, they can adopt a parachute shape by decreasing their length,  $L_{RBC}$ , and increase their width,  $W_{RBC}$ .

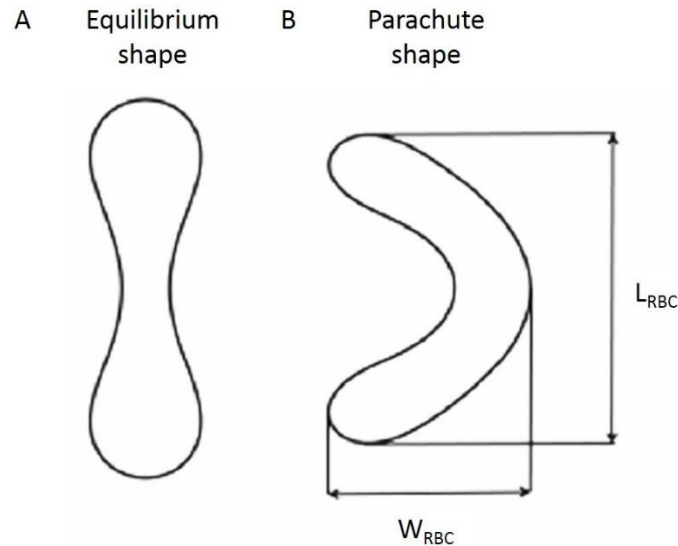


Figure 1.16. RBC shape in two cases: (A) without flow, equilibrium shape and (B) under flow in a capillary: parachute shape.  $L_{RBC}$  and  $W_{RBC}$  represent the length and width of the RBC, respectively. Adapted from Wang et al [56].

If the capillary diameter is approximated to  $5 \mu\text{m}$  and the RBC diameter to  $7 \mu\text{m}$ , the ratio between the RBC diameter and the vessel diameter is 1.4. If this ratio is around 1.3, it has been demonstrated that the blood velocity is 20 % smaller than the RBC velocity [57]. This approximates the mean blood velocity to 1.57 mm/s.

For the blood velocity of arterioles, Freitas gives a mean velocity of 5 mm/s [19]. Fernandez-Klett et al. differentiate between precapillary, penetrating and pial arterioles in the mouse brain with blood flow velocities between 2 and 4 mm/s, no estimation and between 6 and 8.5 mm/s, respectively [58]. Vennemann et al. report much higher values of 50 mm/s for the arterioles and 10 mm/s for the venules in the human vascular network [59]. However, they considered vessels with a much larger diameter, from 25 to  $100 \mu\text{m}$ , compared to 7 to  $15 \mu\text{m}$  for Fernandez-Klett et al. This difference in diameters explains the higher velocities they find.

The two methods described here to measure the RBC velocity are indirect measures of the blood velocity and have many limitations among which the small penetration depth of optical methods. Furthermore, in clinics, the applications of optical-based methods are limited to superficial areas such as the skin [60]. There is thus a need for a measurement method of the blood velocity suitable for in-vivo experiments and not relying on RBCs for its measure.

A new method has recently been developed by Demené et al [61]. By combining ultrasound ultrafast Doppler with tomographic reconstruction for 3D imaging, they are able to image the microvasculature in 4D. They achieve a 4D resolution of  $100\ \mu\text{m} \times 100\ \mu\text{m} \times 100\ \mu\text{m}$  and 10 ms. This technique is sensitive to flow in small vessels down to 1 mm/s. However, the transposition of this technique to clinics will be difficult as the human skull reduces transcranial propagation of the ultrasounds. However, it could be used to image newborns who have a fontanelle much thinner than the human skull.

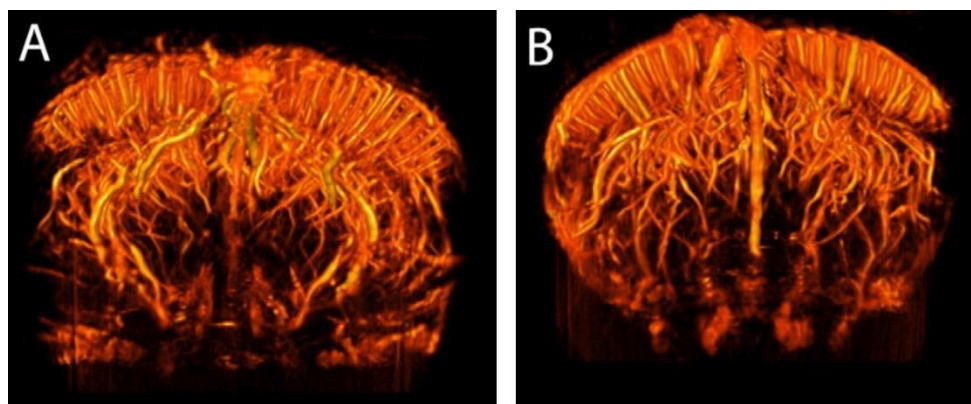


Figure 1.17. Back view (A) and front view (B) of the complete rat vascular network acquired with the ultrafast Doppler tomography technique. From Demené et al [61].

#### 1.3.3.2 Velocity profiles

Three types of velocity profiles can be defined to model blood flow: plug or bulk flow, laminar flow and turbulent flow (Figure 1.18).

Inside a vessel, blood flows in straight lines with each layer of blood staying at the same distance from the vessel wall throughout the vessel length.

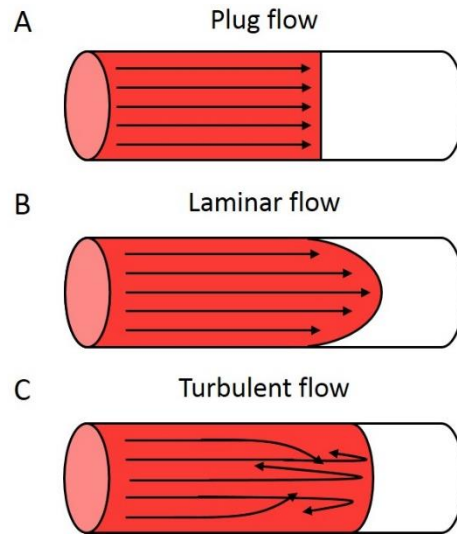


Figure 1.18. Flow velocity profiles in a blood vessel: plug (A), laminar (B) and turbulent (C) flow.

In plug flow, the flow is constant along the diameter of the pipe. Plug flow is an ideal model for blood flow. However, it is suitable for vessels with very small diameters like capillaries [62]. In these vessels, RBCs take a parachute shape and leave a cell-free layer of blood between the vessel wall and the RBCs [56]. No viscosity effects can slow down the velocity of the blood layers close to the vessel wall and the vessel diameter being also small, the velocity can be considered constant across the vessel diameter and be modelled by plug flow.

For vessels with a larger diameter, laminar flow occurs [62]. It appears when layers of blood closer to the vessel wall barely move and adhere to it making the other layers of blood slip over it. The result is a parabolic velocity profile. The blood velocity is maximum at the center of the vessel and 0 at the vessel walls. It is a more realistic model for the blood velocity.

Finally, when the velocity is very high, blood can encounter an obstacle or make a sharp turn, the flow can become turbulent. When it occurs, blood flows crosswise in the vessel as well as along the vessel and whorls can appear. This usually takes place in large arteries after a stenosis.

A dimensionless quantity can be calculated to define the limit between laminar and turbulent flow, it is called the Reynolds number,  $Re$  [63],[64]:

$$Re = \frac{\rho dV}{\mu} \quad 1.1$$

where  $\rho$  is the blood density,  $d$  the vessel diameter,  $V$  the vessel blood velocity and  $\mu$  the blood dynamic viscosity.

$Re$  represents the ratio of the inertial forces aiming to keep the fluid flowing to the viscosity forces aiming to slow down the fluid motion. For laminar flow,  $Re$  is small and viscosity forces prevail. For  $Re > 2000$ , the inertial forces are more important than the viscosity forces, the flow is no longer laminar and progressively becomes turbulent. For the diameter and blood flow velocities displayed in Table 1.1,  $\rho = 1.05 \text{ g/cm}^3$  and  $\mu = 0.03 \text{ P}$ ,  $Re$  varies between 0.0003 and 0.26 in the microvessels. These values are far from the turbulent flow limit. Blood flow can be modelled as plug flow in the capillaries and as laminar flow in larger vessels of the microvascular network, i.e. in arterioles and venules.

#### 1.3.4 Simulated microvascular networks

To extract more than morphological information from the microvascular networks, it can be interesting to simulate these networks. First, reasons to simplify realistic constructions of microvascular networks are exposed. Then, several simulations strategies are proposed.

##### 1.3.4.1 Limitations of using real microvascular networks

It would clearly be ideal to generate microvascular structures from real brain tissue and to run simulations on such networks. However, this process is extremely complex and time consuming as it involves sample preparation, scanning and image processing as well as being very difficult to do in-vivo. Yet, Duvernoy et al. acquired a collection of human brain cortex images making them available for the whole community [21]. For morphological studies, Lauwers et al. used part of this collection [44]. Working with the whole collection would mean to deal with a very large number of data so only pieces of it are processed at a time. After segmenting the vessels, he was able to obtain central morphometric features of the microcirculation. With the same method, Lorthois et al. measured the tortuosity of cortex blood vessels [65]. Using their own acquired data, other groups studied the relation between the microvascular topology [31] and the cortical columns or else the correlation between neuronal and microvascular densities [23].

These networks are handy when seeking morphological data only. Indeed, if studying different challenges, such as different levels of hypercapnia or hypoxia, it would be difficult to get images of a brain in the precise level of each condition.

Yet, when studying varying parameters, these networks can form a structural basis for modelling. For example, Linninger et al. took part of Duvernoy et al.'s collection, added and propagated blood supply into the segmented network to then predict oxygen exchange between the microvasculature and brain cells [66].

However, usually when studying more complex parameters such as hemodynamics, researchers are looking for simpler models of the vascular network. This is why having models of the microvascular network is needed.

#### 1.3.4.2 Models of the microvascular network

Two types of structures are generally proposed when modelling microvascular networks: mesh-like and symmetric tree-like structures [67]. Figure 1.19.A and B give representations of such networks.

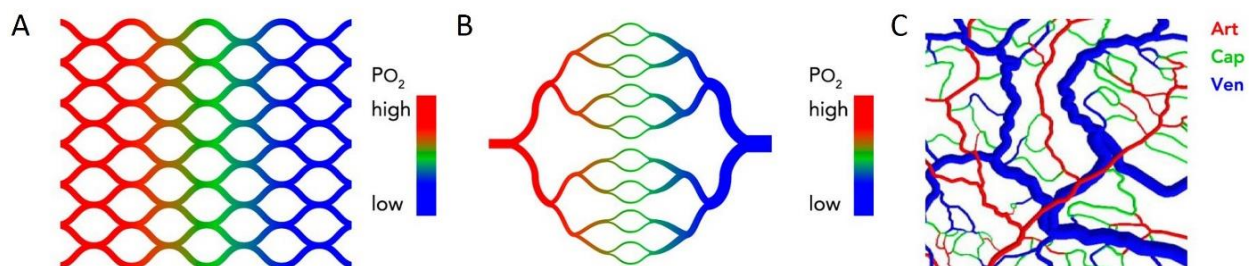


Figure 1.19. Representations of vascular networks. (A-B) Mesh-like and symmetric tree-like structures. The colors indicate the intravascular oxygen levels (PO<sub>2</sub>). PO<sub>2</sub> is higher in the arterioles and decreases progressively in the capillaries to be the lowest in the venules. (C) Real network extracted from the rat mesentery. The colors refer to the vessel type, red, green and blue for arterioles, capillaries and venules, respectively. Based on Pries et al [67].

To be efficient, a vascular network should be arranged to ensure effective transport of the oxygen and nutrients. Two mechanisms contribute to this transport: diffusive transport which depends on the random thermal motion of individual transported molecules and convective transport in which the transported molecules are carried by a flowing fluid, here blood.

The mesh-like structure is a simple structure that has short and homogenous distances between vessels and tissue cells. This structure is efficient for diffusive transport. However, the vessels in this structure are very thin and have relatively short lengths making convective transport ineffective. In the symmetric tree-like structure, on the contrary, the resistance to blood flow is lower due to changes in the blood flow along the tree. This structure is thus more effective for convective transport. Yet, it is only efficient for diffusive transport in the capillary region. Figure 1.19.C shows the representation of a real microvascular network. Capillaries can be found everywhere in the tissue, close and far from the arterioles and venules. This real structure can be seen as a combination of the tree-like structure for the arterioles and venules and a mesh-like structure for the capillaries. However, the capillaries are not oriented in a regular pattern as assumed by the mesh-like structure. Their orientation seems randomly distributed along the three directions.

For example, Boas et al. used a tree-like network model built up from a branching series of individual arterioles, going through the capillaries and then on to a converging series of venules [68]. Each series of vessels has its own structural properties related to real vascular networks. With it, they modelled the hemodynamic response to neuronal activity.

With a similar approach, Zagzoule et al. proposed a simplified model for which all important vessels are represented individually by a number in Figure 1.20 [69]. Then, they formulated a mathematical expression for blood flow which they applied to this model of the vasculature to study autoregulation during arterial hypotension.



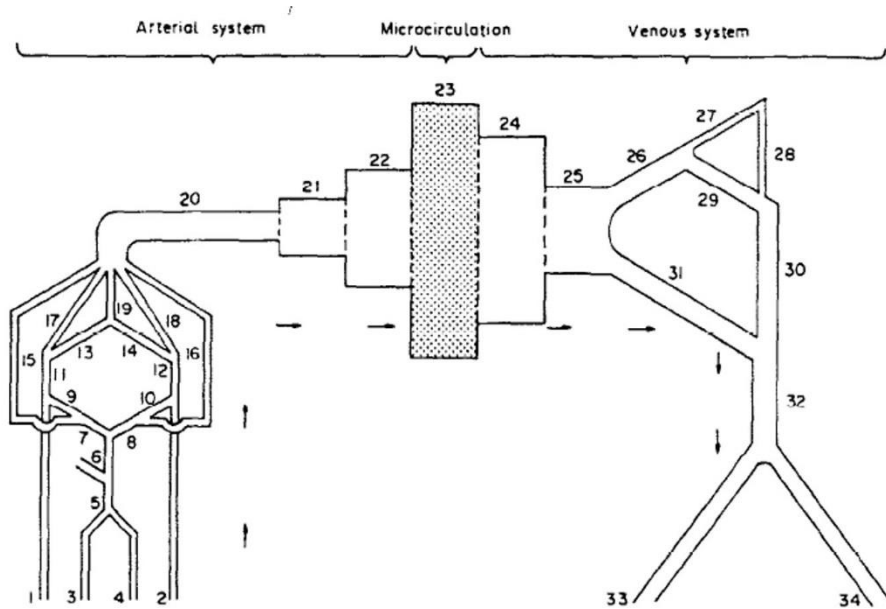


Figure 1.20. Schematic diagram of the vasculature. The numbers correspond to important vessels. For more details, see Zagzoule et al [69].

More complex structures have been proposed to model just the capillary network like the modified spanning tree method [70]. This approach first creates an incomplete small network using the minimum spanning tree method with Prim's algorithm [71] connecting a small number of nodes at random coordinates in a cube (Figure 1.21.A). Then, more nodes are added to the cube and branches are generated from a node to the closest node until a terminal node located on the sides of the cube is reached (Figure 1.21.B). In a third step, more branches are created between terminal nodes (Figure 1.21.C). Finally, vessels of specific lengths are added and removed to match the length distribution of the capillaries obtained with experimental data by Cassot et al. [42] and the radius distribution of the vessels likewise (Figure 1.21.D).

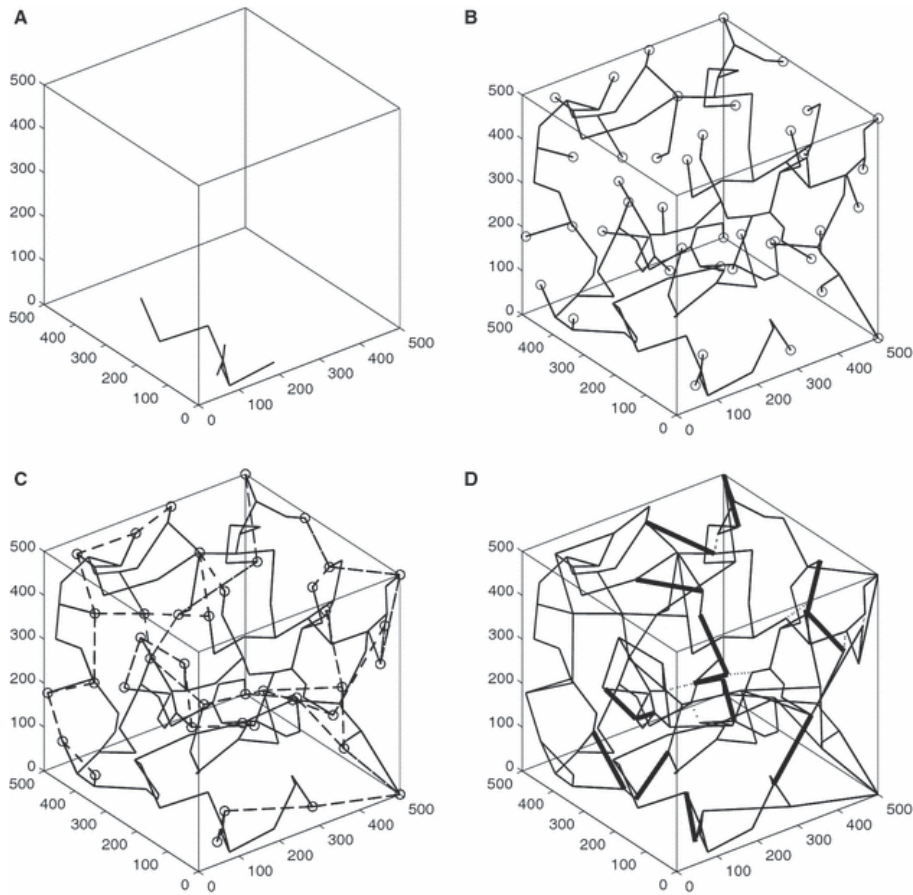


Figure 1.21. Modified spanning tree method. (A) Creation of a small network from nodes connected using the minimum spanning tree method with Prim's algorithm [71]. (B) More nodes are randomly added to the cube and branched from one node to the closest node until reaching a terminal node on one side of the cube highlighted by circles. (C) Segments are formed between terminal nodes (dotted lines). (D) In a final step, branches are added (bold solid lines) and subtracted (dotted lines) to match the vessel lengths and diameter distributions observed by Cassot et al [42]. From Su et al [70].

This simulated network is closer to a real capillary network as it matches the vessel lengths and diameter distributions observed in real tissues. This is a good model to simulate blood flow, oxygen and nutrients transport and, for hypercapnia or hypoxia challenges, the mean lengths and diameters of the distributions can be varied to mimic the changes occurring in the capillary network under such conditions.

As a conclusion to this chapter, the microvascular network is extensively described in the literature although with some differences depending on the labeling and imaging technique used. These characteristics can then be used to elaborate models to simulate the variation of

hemodynamic parameters after a challenge. As the goal of this thesis is to extract vascular parameters from the MRI signal, such simulated networks will be useful as a basis to model the evolution of the MRI signal with different vascular characteristics of the network. The next chapter introduces the MRI technique used in this thesis.

## Chapter 2: MRI of the vasculature

In this chapter, the history and basic physical concepts of MRI will be presented. The last section will focus on the MRI techniques able to probe characteristics of the blood vessels.

### 2.1 History of MRI

MRI is an imaging technique capable of producing images of the inside of the body in a noninvasive way and without the use of ionizing radiations.

The development of MRI comes from a long series of discoveries rewarded by Nobel Prizes which put all together made MRI possible. It began with the discovery of nuclear magnetic resonance (NMR) in 1939 by Isidor Rabi [72] who obtained the Nobel Prize in Physics for his work in 1944. Then, simultaneously, Felix Bloch at Harvard University [73] and Edward Purcell at Stanford University [74] demonstrated the potential of NMR to decipher the chemical composition and structure of materials. They won the Nobel Prize in Physics together in 1952. It is not until 1973 that Paul Lauterbur had the idea to add linear magnetic field gradients to the MR system to produce images and invented what is now called MRI [75]. He received the Nobel Prize in Medicine with Peter Mansfield [76] in 2003.

During the past 15 years, many different pulse sequences and contrast types have been designed and discovered making MRI a versatile technique suitable to study and diagnose a large number of pathologies and especially to better understand how the brain works.

### 2.2 Basic physical concepts of MRI

This section covers the basics needed to understand the physical concepts of MRI.

#### 2.2.1 Spins and Larmor frequency

NMR and thus MRI are limited to the study of specific atomic nuclei that have the capacity to rotate about an axis and generate their own magnetic field. Only nuclei which have an unpaired proton and therefore a half integer nuclear spin belong to this category. The most abundant atom in the human body is hydrogen and it happens to have an isotope with only one proton which obeys to this rule:  $^1\text{H}$ . Almost all atoms have an isotope that can fulfill this condition. However, as the MR signal scales with the amount of studied isotope in the sample and the

value of its gyromagnetic ratio,  $\gamma$ , only a small number of atoms are eligible for MRI. For  $^1\text{H}$  for example,  $\gamma = 267.51 \times 10^6 \text{ rad.s}^{-1}.\text{T}^{-1}$ . On top of being the most abundant isotope in the human body,  $^1\text{H}$  has the highest  $\gamma$ -value. It has therefore the highest MR sensitivity.  $^1\text{H}$  is thus the most commonly used atom but specific MRI techniques have been developed to study also  $^{13}\text{C}$ ,  $^{31}\text{P}$ ,  $^{19}\text{F}$ ,  $^7\text{Li}$  and  $^{23}\text{Na}$ ,  $^3\text{He}$ ,  $^{129}\text{Xe}$ ,  $^{83}\text{Kr}$ , etc.

A spin can create a tiny magnetic field on a microscopic level. However, in the absence of a strong external magnetic field, all the spins are randomly oriented and cancel each other's magnetic field resulting in a zero net magnetization (Figure 2.1.A). In the presence of a strong external static magnetic field  $\vec{B}_0$ , the collection of spins tend to align with it creating a net magnetization (Figure 2.1.B).

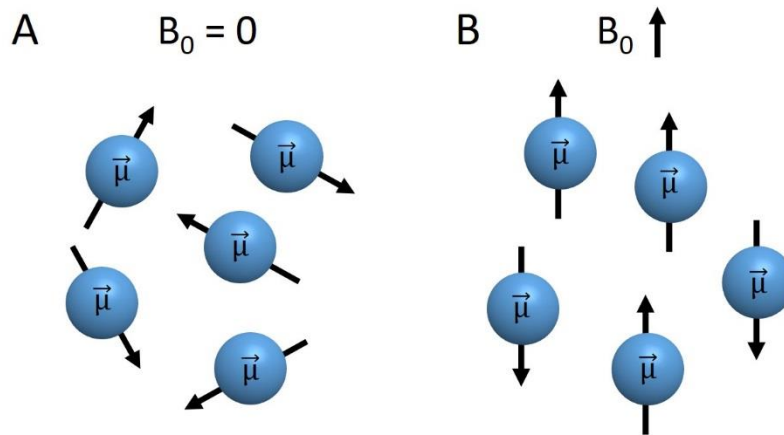


Figure 2.1. (A) Un-aligned collection of spins in the absence of a magnetic field. There is no net magnetization. (B) Aligned collection of spins in the presence of an external magnetic field,  $\vec{B}_0$ , creating a net magnetization;  $\vec{\mu}$  is the magnetic moment of a spin.

What comes next follows the semi-classical description of NMR. For the rigorous quantum description, interested readers can refer to more specialized literature such as Haacke et al [77].

An important parameter to define, the Larmor precession, the precession of the magnetic moment of a collection of spins about an external magnetic field, here  $\vec{B}_0$ , can be expressed as

$$\omega_0 = \gamma B_0 \quad 2.1$$

In Figure 2.1, the magnetic moments have been represented in a static way to simplify the figure.

$\omega_0$  is the Larmor frequency for a constant field  $B_0$ . If  $B = B(t) \neq B_0$ , the Larmor frequency associated with  $B(t)$  is  $\omega(t) = \gamma B(t)$ .

Instead of representing spin magnetic moments in a reference frame where the spins are precessing at  $\omega_0$ , it is sometimes more convenient to represent them in a reference frame rotating at  $\omega_0$ . In this frame, the spin axis is not moving anymore.

### 2.2.2 Magnetization vector and Bloch equations

In the previous section, spins have only been considered individually. We now introduce the local magnetic moment per unit volume also called magnetization,  $\vec{M}$ . Considering a volume element or voxel with volume  $V_x$ , the magnetization can be expressed as:

$$\vec{M} = \frac{1}{V_x} \sum_{\text{protons in } V_x} \vec{\mu}_j \quad 2.2$$

A microscopic group of spins in  $V_x$  which resonate at the same frequency and are in the same chemical environment are referred to as an isochromat.

With only a static magnetic field  $B_0$ , the magnetization stays aligned to  $B_0$ . In NMR and MRI, another magnetic field oscillating at  $\omega_0$  in the transverse plane,  $B_1$ , is added to tip the magnetization into the transverse plane.  $B_1$  is called the radiofrequency (RF) field as  $\omega_0$  is in the radiofrequency range (9 kHz to 300 GHz). Typically, for proton,  $\omega_0 = 300$  MHz at 7T and 500 MHz at 11.7T. A RF coil, the transmit coil, produces the RF pulse.

Commonly,  $\vec{B}_0$  is defined along the z-direction,  $\vec{B}_0 = B_0 \vec{e}_z$ . When the  $B_1$  field is applied to an isochromat, the longitudinal magnetization along  $\vec{B}_0$ ,  $M_z$ , is flipped toward the x-y plane. This process is called excitation and the magnetization in the x-y plane is labelled as  $M_{xy}$ . After  $B_1$  is turned off, the total magnetic moment relaxes back to its equilibrium state along the z-axis, generating a signal called free induction decay (FID). This signal is recorded by an RF coil, the receiver coil. The transmit and receiver coils can be the same coil or two different coils. The recorded signal is what we call the MR signal.

After the application of an RF pulse, the time variation of  $\vec{M}$  can be written as

$$\frac{d\vec{M}}{dt} = \gamma \vec{M} \times \vec{B}_0 \quad 2.3$$

This equation is known as the Bloch equation neglecting relaxation effects [74]. These effects will be explained in the next section. The Bloch equation can then be explicitly written for the three orthogonal components of the magnetization,  $M_x$ ,  $M_y$  and  $M_z$ , as

$$\begin{cases} \frac{dM_x}{dt} = \gamma M_y B_0 \\ \frac{dM_y}{dt} = -\gamma M_x B_0 \\ \frac{dM_z}{dt} = 0 \end{cases} \quad 2.4$$

### 2.2.3 Relaxation types

When the transverse magnetization goes back to equilibrium after the  $B_1$  field has been turned off, two types of relaxation occur simultaneously.

As shown in Figure 2.2.A, spins loose coherence and dephase in the x-y plane due to a transverse or spin-spin relaxation characterized by the relaxation time  $T_2$ . The return to equilibrium of the longitudinal component illustrated in Figure 2.2.B is caused by longitudinal or spin-lattice relaxation characterized by the relaxation time  $T_1$ .

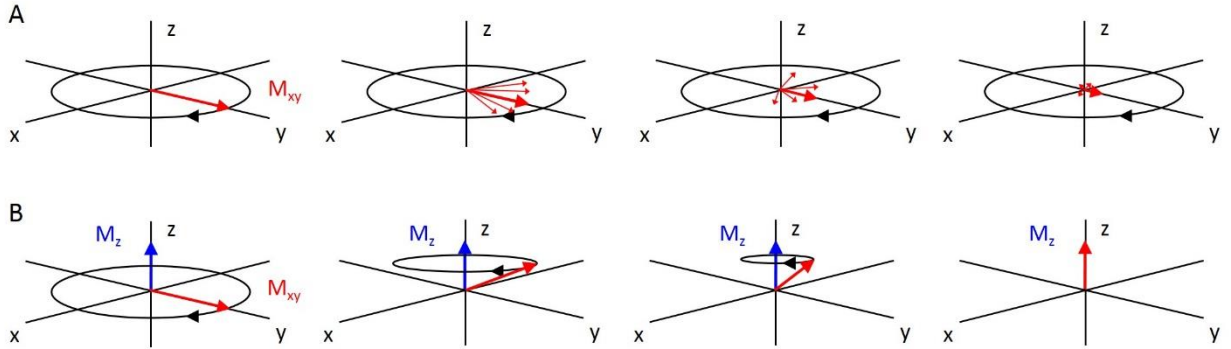


Figure 2.2. (A)  $T_2$  relaxation, dephasing of the transverse magnetization in the x-y plane. (B)  $T_1$  relaxation, recovery of the longitudinal component of the signal.

$T_1$  and  $T_2$  depend on the chemical and physical properties of the spin environment.  $T_1$  increases whereas  $T_2$  decreases with increasing magnetic field strength  $B_0$ . Figure 2.3 gives examples of the evolution of  $T_1$  and  $T_2$  with the magnetic field strength in different media.

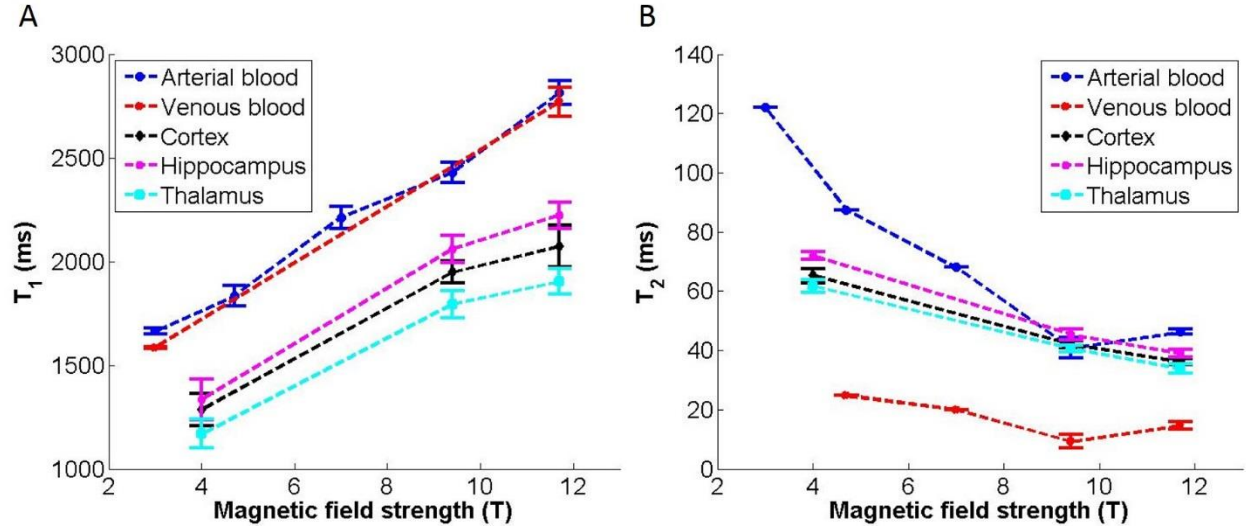


Figure 2.3. Variation of  $T_1$  (A) and  $T_2$  (B) against the magnetic field strength. Data citation: for arterial blood  $T_1$ : 3T [24], 4.7, 7T and 9.4T [78], 11.7T [79] ; for arterial blood  $T_2$ : 3T [80], 4.7T [81], 7T [82], 9.4T [83], 11.7T [79] ; for venous blood  $T_1$ : 3T [24], 11.7T [79] ; for venous blood  $T_2$ : 4.7T [81], 7T [82], 9.4T [83], 11.7T [79] ; for the cortex, hippocampus and thalamus  $T_1$  and  $T_2$  at 4T, 9.4T and 11.7T [84].

There is a significant gap between the  $T_1$  values of blood (arterial and venous) and tissue (cortex, hippocampus and thalamus). Indeed,  $T_1$  depends on the spin mobility. As it is higher in blood,  $T_1$  is higher for blood compared to tissue. Whereas  $T_1$  is very similar between arterial and venous blood,  $T_2$  is much smaller for venous blood than arterial blood. This is because  $T_2$  highly depends on the oxygenation level which is lower in venous blood.

In practice, an additional dephasing of the magnetization due to field inhomogeneities produces an additional decay of the signal. The signal decreases with a time constant shorter than  $T_2$  called  $T_2^*$ .

When taking into account the relaxation effects, the Bloch equations become

$$\begin{cases} \frac{dM_x}{dt} = \gamma M_y B_0 - \frac{M_x}{T_2} \\ \frac{dM_y}{dt} = -\gamma M_x B_0 - \frac{M_y}{T_2} \\ \frac{dM_z}{dt} = -\frac{M_z - M_0}{T_1} \end{cases} \quad 2.5$$

where  $M_0$  is the magnetization at  $t = 0$ .



In an MR experiment, we record the transverse complex magnetization,  $M_{xy}(t)$ , which is a combination of  $M_x(t)$  and  $M_y(t)$ ,  $M_{xy}(t) = M_x(t) + iM_y(t)$ . The Bloch equations become

$$\begin{cases} \frac{dM_{xy}}{dt} = -i\gamma M_{xy}B_0 - \frac{M_{xy}}{T_2} \\ \frac{dM_z}{dt} = -\frac{M_z - M_0}{T_1} \end{cases} \quad 2.6$$

To solve these equations, we assume that, at  $t = 0$ , the magnetization is only present in the z-direction. This gives initial conditions for the magnetization:  $M_{xy}(t = 0) = 0$  and  $M_z(t = 0) = M_0$ . Solving the Bloch equations with these initial conditions, we get

$$\begin{cases} M_{xy}(t) = M_0 e^{-\frac{t}{T_2}} e^{-i\omega_0 t} \\ M_z(t) = M_0 \left(1 - e^{-\frac{t}{T_1}}\right) \end{cases} \quad 2.7$$

As shown in Figure 2.4,  $M_{xy}(t)$  precesses at the Larmor frequency  $\omega_0$  within an envelope that decays with a time constant  $T_2$  (grey curves). If the static field  $B_0$  is not completely homogenous, the signal decays with  $T_2^*$  instead (red curves). The time constant,  $T_2$  or  $T_2^*$ , can be determined as it corresponds to the intersection of  $M_{xy}(t)$  with  $e^{-\frac{t}{T_2}}$  or  $e^{-\frac{t}{T_2^*}}$  when  $M_{xy} = \frac{1}{e} M_0$  represented by the violet solid line.

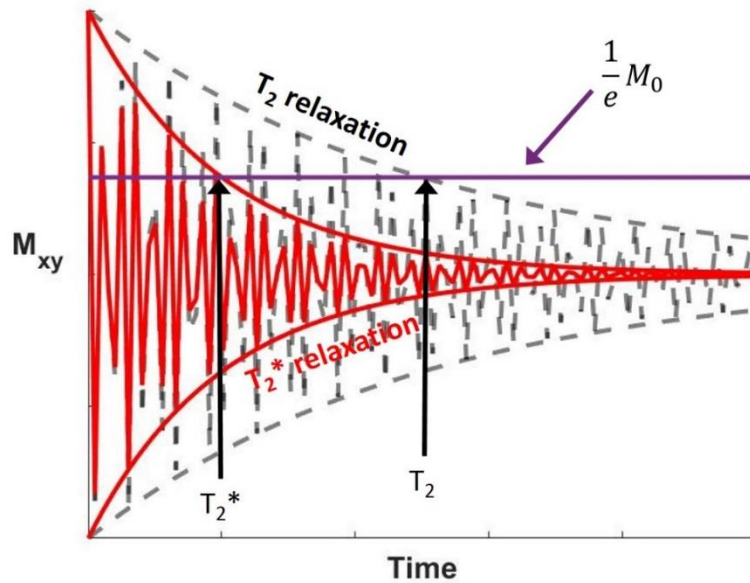


Figure 2.4. Time evolution of the complex transverse magnetization  $M_{xy}$  with  $T_2$  relaxation for the dotted grey curves and  $T_2^*$  relaxation for the solid red curves. The signal envelope is

characterized by a  $T_2$  or a  $T_2^*$  decay for the grey and red curves, respectively. The violet solid line corresponds to  $M_{xy} = \frac{1}{e} M_0$ .

Another useful definition of the complex transverse magnetization can be introduced, not in terms of real and imaginary parts but in terms of magnitude,  $|M_{xy}(t)|$ , and phase,  $\phi(t)$ :

$$M_{xy}(t) = |M_{xy}(t)|e^{-i\phi(t)} \quad 2.8$$

with  $|M_{xy}(t)| = M_0 e^{-\frac{t}{T_2}}$  and  $\phi(t) = \omega_0 t$  for which we assume that  $\phi(t = 0) = 0$ .

## 2.2.4 Image generation

All equations described in the previous subsections apply to both NMR and MRI. The present subsection introduces the main difference between NMR and MRI which allows MRI to produce images: the addition of spatial encoding gradients.

### 2.2.4.1 Spatial encoding using magnetic field gradients

In a complex sample as the human body, it is interesting to be able to localize where the MR signal comes from. This is typically done by adding spatial encoding gradients. To differentiate these gradients, they are named slice selection, frequency and phase encoding gradients.

At the beginning of all MR sequences, an excitation RF pulse is needed to flip the magnetization in the transverse plane. If this RF pulse is associated with a gradient in one of the directions, x, y or z, what will result is a selective excitation of the magnetization in one slice of the sample characterized by the two other directions. This process is called slice selection. The slice thickness,  $thk$ , can be controlled by varying the strength of the slice selection gradient,  $G_{slice}$ , and the RF pulse bandwidth,  $BW$ , as

$$thk = \frac{BW}{\gamma G_{slice}} \quad 2.9$$

After the slice selection gradient, a rephasing gradient is generally applied in the same direction. It has the function to correct for the accumulation of phase making the spins dephase. Consequently, the spins are all at zero phase after the end of the rephasing gradient.

After the selective excitation pulse, a gradient is applied along one of the other two directions. As spins in different positions will experience different magnetic field strengths, their phase will

be modified introducing a phase shift between  $t = 0$  and the recording of the signal. This process is called phase encoding.

By adding a gradient in the last direction, the Larmor frequency of spins is also varied according to their location along this direction. This gradient only affects spins inside the excited slice and changes their Larmor frequency with spins on one side of the chosen direction precessing faster than those on the other side, generating a frequency spectrum. This process is called frequency encoding.

#### 2.2.4.2 Modified Bloch equations

Now that the complex transverse magnetization has been introduced, its time evolution in the presence of imaging gradients will be considered. The Bloch equation associated with  $M_{xy}$  is

$$\frac{dM_{xy}}{dt} = -i\omega_0 M_{xy} - \frac{M_{xy}}{T_2} \quad 2.10$$

Magnetic field gradients modify the Larmor frequency as such

$$\omega = \omega_0 + \gamma \overrightarrow{G_{Im}(t)} \cdot \vec{x} \quad 2.11$$

where  $\overrightarrow{G_{Im}}$  is the imaging gradients vector and  $\vec{x}$  the position vector of the observed isochromat.

Replacing  $\omega_0$  by  $\omega$  in Eq. 2.10 gives:

$$\frac{dM_{xy}}{dt} = -i\omega_0 M_{xy} - \frac{M_{xy}}{T_2} - i\gamma \overrightarrow{G_{Im}(t)} \cdot \vec{x} M_{xy} \quad 2.12$$

The solution to this equation is straightforward:

$$M_{xy}(t) = M_0 e^{-\frac{t}{T_2}} e^{-i\omega_0 t} e^{-i \int_0^t \gamma \overrightarrow{G_{Im}(t')} \cdot \vec{x} dt'} \quad 2.13$$

#### 2.2.4.3 K-space and image reconstruction

The slice, frequency and phase information put together give the spatial location of a voxel. By combining information about many adjacent voxels, we now show how to obtain an image.

When neglecting the relaxation effects and working in the rotating frame, the solution to the Bloch equation for  $M_{xy}(t)$  in the presence of imaging gradients is:

$$M_{xy}(t) = M_0 e^{-i \int_0^t \gamma \overline{G_{Im}(t')} \cdot \vec{x} dt'} \quad 2.14$$

The phase accumulated during a pulse sequence for a given voxel is thus:

$$\phi(t) = \int_0^t \gamma \overline{G_{Im}(t')} \cdot \vec{x} dt' = 2\pi \vec{k} \cdot \vec{x} \quad 2.15$$

The encoding vector  $\vec{k}$  summarizes the information given by the encoding gradients. A space of spatial frequencies called k-space can then be defined for which the location information is stored in  $\vec{k}$ . In k-space, the total magnetization of the sample can be expressed as:

$$M_{xy}(\vec{k}) = \int |M_{xy}(\vec{x})| e^{-i\phi(\vec{x})} d\vec{x} = \int |M_{xy}(\vec{x})| e^{-i2\pi \vec{k} \cdot \vec{x}} d\vec{x} \quad 2.16$$

The magnitude of the magnetization,  $|M_{xy}(\vec{x})|$ , can be obtained by applying an inverse Fourier transformation to  $M_{xy}(\vec{k})$ :

$$|M_{xy}(\vec{x})| = FT^{-1}[M_{xy}(\vec{k})] = \int M_{xy}(\vec{k}) e^{i2\pi \vec{k} \cdot \vec{x}} d\vec{k} \quad 2.17$$

So, after applying the Fourier transformation, the MR image is obtained. Points located at the center of the k-space generate image contrast while those located toward the edges enable a higher resolution of the image.

## 2.2.5 Basic MR pulse sequences

This subsection introduces some of the basic MR pulse sequences: the gradient echo (GE), spin echo (SE) and stimulated echo (STE), echo planar imaging (EPI) and diffusion-weighted imaging (DWI) sequences.

### 2.2.5.1 Gradient echo sequence

The first sequence to be presented is the GE sequence. As stated by its name, the echo is formed by using gradients. It occurs when  $\int G_{Read}(t) dt = 0$  at  $t = TE$ , the echo time. This is typically achieved by applying successively a negative and a positive frequency encoding gradient as shown in Figure 2.5.A. This sequence has only one excitation pulse for which the flip angle,  $\alpha$ , can be less than 90°. As the rephasing lobe of the slice selection gradient, the phase encoding gradient and the negative lobe of the read gradient can be turned on at the same time, the GE sequence allows for rather short TE.

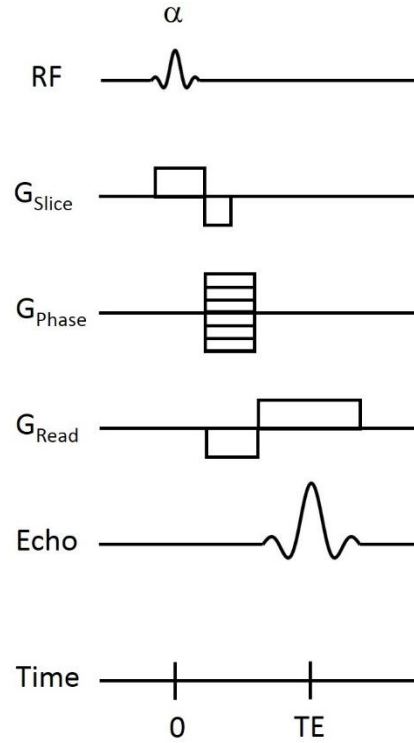


Figure 2.5. Sequence diagram of the GE sequence.

As nothing is done to correct for field inhomogeneities, this sequence is  $T_2^*$  and not  $T_2$ -weighted. The expression of the signal for this sequence in the rotating frame is

$$S_{GE} = \frac{S_0 \sin(\alpha) \left(1 - e^{-\frac{TR}{T_1}}\right) e^{-\frac{TE}{T_2^*}}}{1 - \cos(\alpha) e^{-\frac{TR}{T_1}}} \quad 2.18$$

where  $S_0$  is the signal at  $t = 0$ .

### 2.2.5.2 Spin echo and stimulated echo sequences

This sequence was first introduced by Erwin Hahn in 1950 [85]. As shown in Figure 2.6.A, the SE sequence uses a  $90^\circ$  selective excitation pulse. After a time delay  $\tau$  during which the spins are dephasing, a  $180^\circ$  refocusing pulse is applied. At  $t = 2 \times \tau$ , an echo forms and this time is defined as the echo time. Thanks to the  $180^\circ$  refocusing pulse, this sequence is not sensitive to field inhomogeneities and  $T_2$  can be used instead of  $T_2^*$ . Indeed, the phase shift induced by field inhomogeneities is constant in time and nulled by the refocusing pulse at the echo time. This sequence is commonly used to produce  $T_2$ -weighted images.

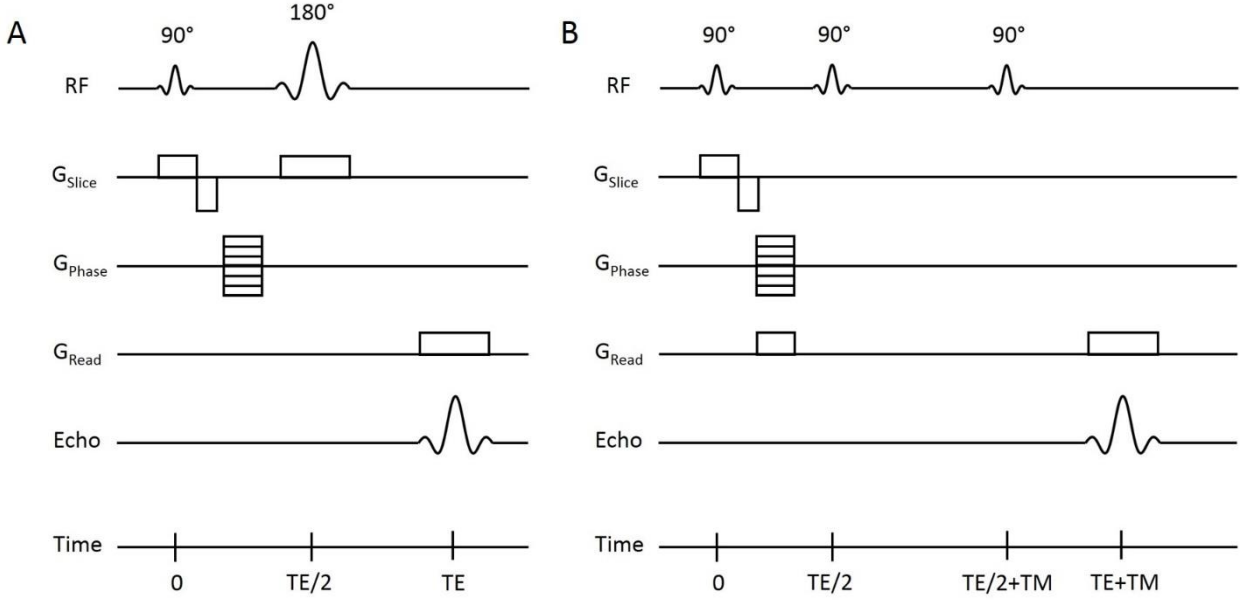


Figure 2.6. Sequence diagrams of the SE (A) and STE (B) sequences.

The expression of the signal for this sequence in the rotating frame is

$$S_{SE} = S_0 \left( 1 - e^{-\frac{TR}{T_1}} \right) e^{-\frac{TE}{T_2}} \quad 2.19$$

For this thesis, the STE sequence, which derives from the SE sequence, was also used. Its sequence diagram is displayed in Figure 2.6.B. Instead of a 180° pulse, two successive 90° pulses are applied. A new time delay between the second and third 90° pulses called the mixing time,  $TM$ , is defined. Several signals are produced during this sequence: three FIDs, three primary SEs, one secondary SE and one STE [86]. They are all shown in Figure 2.7.

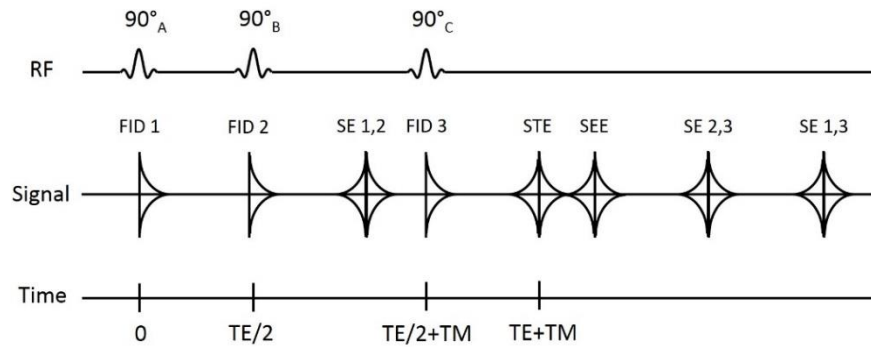


Figure 2.7. Signals generated by the STE sequence: three FIDs (FID 1 to 3) corresponding to the three pulses, (90° A to C), three primary SEs (SE 1,2, SE 2,3 and SE 1,3), one secondary SE (SEE) and one stimulated echo (STE).

When employing the STE sequence, the STE is the only signal we want to record. To suppress part of the unwanted signals, phase cycling can be used. The STE sequence is repeated a few times with the phases of the RF pulses varied at each repetition. The phases are carefully chosen so that the desired signals add up and the undesired signals cancel. To explain further how these values are chosen, the notion of coherence transfer pathway has to be introduced. This can only be explained with a quantum description so an exception regarding the semi-classical description is made here. The transverse magnetization is a type of coherence and can be classified according to a coherence order,  $p$ , which can take the values -1, 0 or 1. The conventions are that before the first pulse, the magnetization is at equilibrium so  $p = 0$  and that only signals with  $p = -1$  after the last pulse can be recorded. RF pulses induce transfers from a coherence order to another. The phase shift obtained after a RF pulse  $i$  is then  $\Phi_i = -\Delta p_i \phi_i$  where  $\Delta p_i$  is the difference in  $p$  before and after pulse  $i$ . A coherence transfer pathway can be built for a series of pulses. An example of such a pathway for the STE in the STE sequence and the values of  $\Delta p$  for all signals generated by the STE sequence are gathered in Figure 2.8.

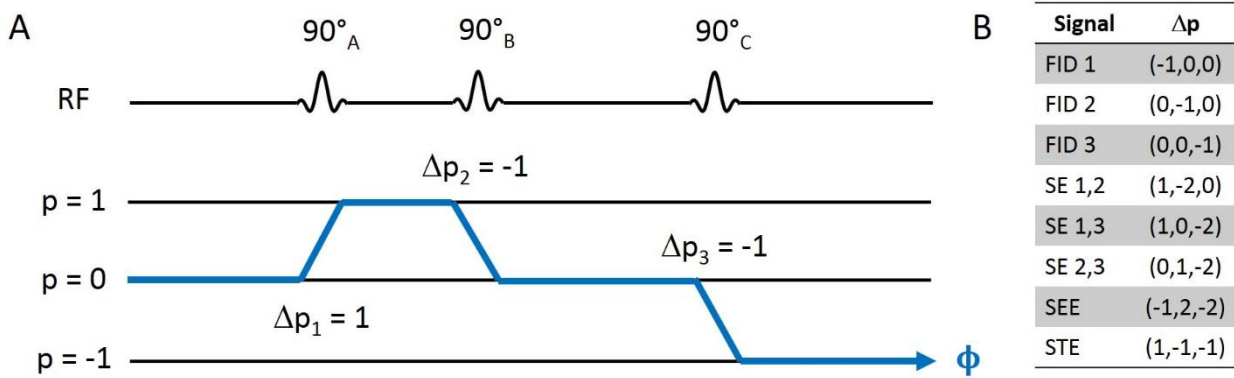


Figure 2.8. (A) Coherence transfer pathway of the STE in the STE sequence. (B) Table giving the values of  $\Delta p$  for all signals generated by the STE sequence. Based on Fauth et al. [87] and Kingsley [86].

The phases of the three pulses (A to C) and the receiver phase (D) in the phase cycling scheme of the STE sequence applied in this thesis are gathered in Table 2.1 [88]. This scheme allows only to keep signals with  $\Delta p_1 = 1$ , i.e. SE 1,2, SE 1,3 and STE. To get rid of the remaining primary SEs, a spoiler gradient can be applied between the second and third RF pulses. Only the first two repetitions of the phase cycling scheme are needed to select the STE signal but two more

repetitions were added to suppress artifacts related to longitudinal magnetization recovery during the time between the first and second pulses.

Repetition	A	B	C	D
1	0°	0°	0°	0°
2	270°	0°	0°	90°
3	180°	0°	0°	180°
4	90°	0°	0°	270°

Table 2.1. Four-step phase cycling used for the STE sequence in this thesis. A to C represent the three RF pulses of the sequence and D the receiver phase. Based on Sattin et al [88].

The signal amplitude of the STE sequence is half that of the SE sequence so more averages and repetitions are needed to obtain comparable signal-to-noise ratio (SNR) than with the SE sequence. Despite this drawback, there is a major advantage of this sequence. This advantage is that the mixing time can be extended without increasing TE and loosing signal due to  $T_2$  relaxation. The signal is  $T_2$ -weighted between the first and second pulses and between the second and third pulses but  $T_1$ -weighted during  $TM$ , thus

$$S_{STE} = \frac{S_0}{2} \left( 1 - e^{-\frac{TR}{T_1}} \right) e^{-\frac{TM}{T_1}} e^{-\frac{TE}{T_2}} \quad 2.20$$

### 2.2.5.3 Echo planar imaging sequence

The EPI sequence was pioneered by Peter Mansfield in 1977 [89]. It is mostly used in diffusion weighted imaging (DWI) and functional MRI (fMRI). The sequence diagram displayed in Figure 2.9 shows a version of the EPI sequence based on a SE sequence but it can also be applied to a STE or a GE sequence.



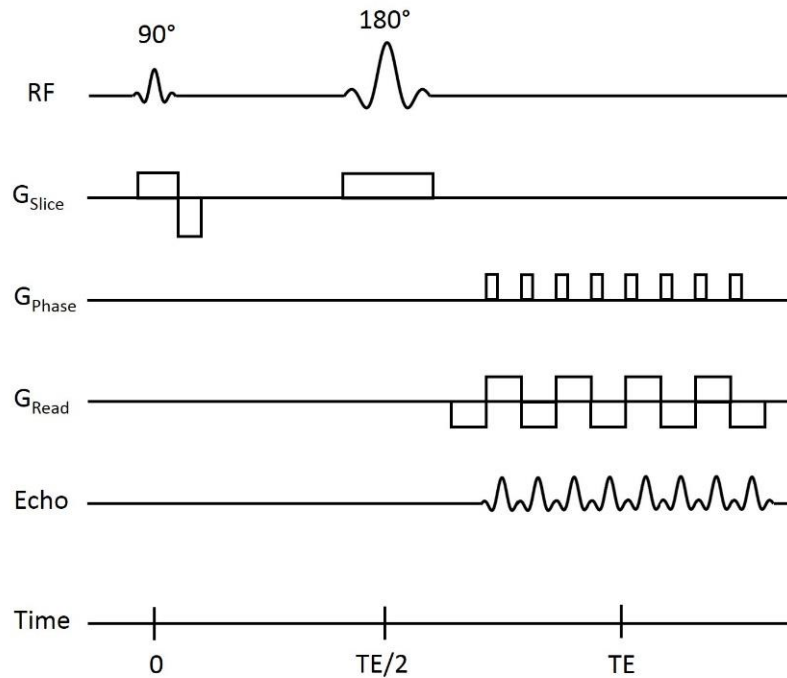


Figure 2.9. Sequence diagram of the EPI sequence based on a SE sequence.

The EPI-SE based sequence uses a train of gradient echoes to acquire all the desired part of k-space in one spin echo and TE. EPI thus enables fast and motion robust data acquisition.

#### 2.2.5.4 Diffusion weighted imaging

##### 2.2.5.4.1 Diffusion phenomenon

In 1828, Robert Brown studied the motion of small particles inside a fluid and found a similar random-walk type motion common to all particles in this particular state [90]. Figure 2.10 illustrates the possible course of a particle in a random-walk type motion.

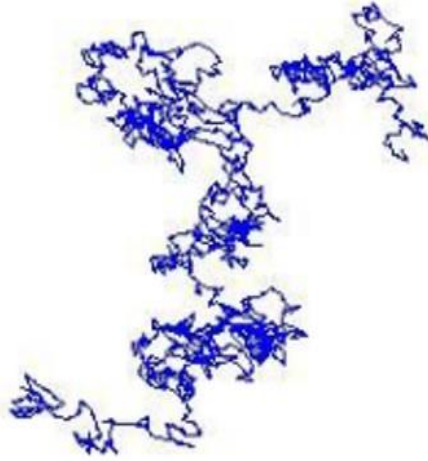


Figure 2.10. Random walk of a particle also called Brownian motion.

The term Brownian motion was assigned much later in honor to Robert Brown's work. Brownian motion is the microscopic description of the diffusion phenomenon. About a century later, in 1905, Albert Einstein formulated a mathematical definition for the diffusion coefficient of a particle experiencing Brownian motion [91]:

$$D = \frac{\langle R^2 \rangle}{2nT} \quad 2.21$$

where  $\langle R^2 \rangle$  is the mean squared displacement of a particle diffusing during a time  $T$  and  $n$  the dimension of the displacement. This equation has been generalized for any dimension of the displacement compared to Einstein's equation which was for 1D only.

This expression of the diffusion coefficient is only valid in free diffusion cases. Diffusion can be restricted for example for water molecules in the intracellular space. Their motion is limited to the inside of the cell and by the other constituents of the cell. In those cases, the diffusion coefficient is reduced and depends on the diffusion time and the geometry of the limiting space.

#### 2.2.5.4.2 Application to the design of an MR pulse sequence

MRI is able to probe the microstructure of a tissue non-invasively by using the diffusion phenomenon. Water molecules inside a tissue encounter many natural barriers such as vessel walls, cells, fibers or macromolecules which alter their diffusion coefficient. Hahn was the first to recognize the potential of the SE sequence to measure the diffusion coefficient [85]. Then, in 1965, Stejskal and Tanner proposed the pulsed gradient SE (PGSE) sequence, in which they

added two diffusion gradients, one before and one after the  $180^\circ$  pulse (Figure 2.11) [92]. The diffusion gradients allow this sequence to differentiate between static spins and spins in motion in the studied voxel as the dephasing induced by the first gradient will be completely compensated by the second gradient for static spins whereas it is not compensated for moving spins.

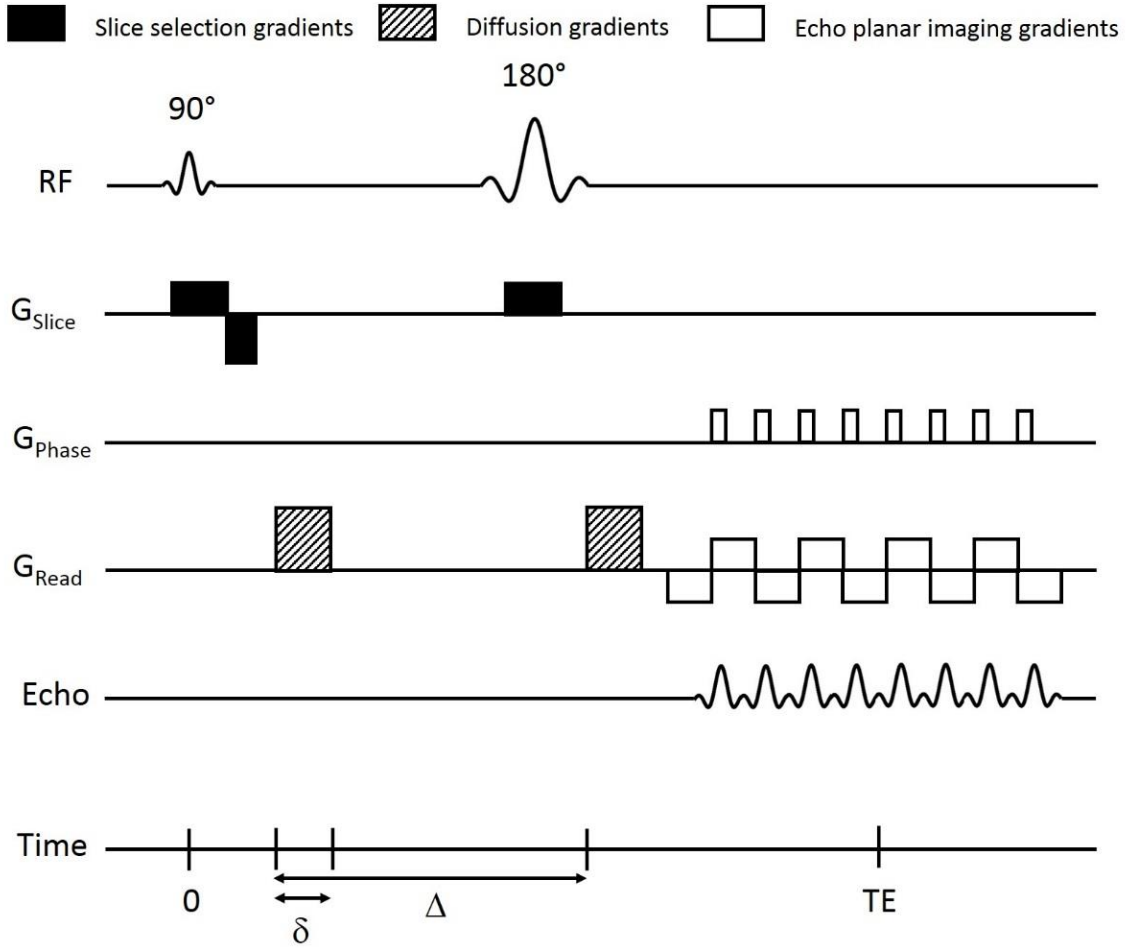


Figure 2.11. Sequence diagram of a PGSE sequence with EPI readout.

Apart from TE, two other time parameters are defined in the PGSE sequence: the pulse diffusion gradient duration,  $\delta$ , and the time delay between the two diffusion encoding gradients,  $\Delta$ .

To take the effects of diffusion into account in the Bloch equations, two terms need to be added. The first term accounts for the effects of the diffusion encoding gradients,  $\overrightarrow{G(t)}$ . Based on Fick's law [93], the second term can be expressed as  $D\nabla^2 M_{xy}$  giving the Bloch-Torrey equation [94]

$$\frac{dM_{xy}}{dt} = -i\omega_0 M_{xy} - \frac{M_{xy}}{T_2} - i\gamma \overrightarrow{G_{Im}(t)} \cdot \vec{x} M_{xy} - i\gamma \overrightarrow{G(t)} \cdot \vec{x} M_{xy} - D \nabla^2 M_{xy} \quad 2.22$$

The solution to this equation for a PGSE sequence in the rotating frame neglecting the effects of relaxation and the imaging gradients is then

$$S_{PGSE} = S_0 e^{-(\gamma \delta G)^2 \left(\Delta - \frac{\delta}{3}\right) D} \quad 2.23$$

where  $G$  is the diffusion encoding gradient strength.

When this technique was first applied to biological tissues, Le Bihan proposed to simplify the term in the exponential by gathering all parameters only linked to the sequence or the type of nucleus studied into one single parameter [95]

$$S_{PGSE}(b) = S_0 e^{-bD} \quad 2.24$$

where  $b = (\gamma \delta G)^2 \left(\Delta - \frac{\delta}{3}\right)$  is called the b-value. This expression of the b-value is only valid for the type of gradients used in this sequence but it can be calculated for any gradient waveform using

$$b = \int_0^{TE} |k(t)|^2 dt \quad 2.25$$

with  $k(t) = \gamma \int_0^t G(t') dt'$  where the sign of  $G(t')$  is reversed for  $t > \frac{TE}{2}$  in a SE sequence.

$T_{Diff} = \Delta - \frac{\delta}{3}$  is the diffusion time and represents the time isochromats diffuse inside the tissue. The factor  $D$  can be calculated from Eq. 2.24. However, it is usually called “apparent” diffusion coefficient ( $ADC$ ) and not simply diffusion coefficient

$$ADC = \frac{\ln\left(\frac{S_{PGSE}(b_2)}{S_{PGSE}(b_1)}\right)}{b_1 - b_2} \quad 2.26$$

The adjective “apparent” was added because the term diffusion alone is given only when free diffusion occurs. Within a tissue, diffusion is hindered by cell membranes, macromolecules, etc., so the term diffusion alone was not adequate.

Thanks to the diffusion gradients, the PGSE sequence is sensitive to diffusion but also to bulk motions such as cardiac-cycle-related pulsations, physical movements or flow of cerebrospinal

fluid. Applying fast EPI-readout allows to acquire an entire dataset in less than 0.1 ms and thus correct for this unwanted sensitivity [96].

There is a limit to the longest diffusion time achievable with the PGSE sequence. A longer diffusion time implies a longer TE and thus a larger signal loss due to  $T_2$ -relaxation. One way to get longer diffusion times without this limitation is to replace the SE sequence with a STE sequence. In this sequence, the time between the two diffusion gradients mainly depends on  $TM$  and can thus be increased without increasing TE. This PGSTE sequence is less dependent on  $T_2$ -relaxation and allows for longer diffusion times than with the PGSE sequence. However, it needs more averages and repetitions as the signal in this sequence is about half that of the PGSE sequence.

## 2.3 MRI of the blood vessels

Many imaging techniques allow for the visualization of blood vessels but, in this work, we will focus only on the ones using MRI. First, distinction needs to be made between imaging of large blood vessels, i.e. arteries and veins, and small vessels, i.e. capillaries, arterioles and venules.

### 2.3.1 Imaging of the large blood vessels: MR angiography

This section presents MRI techniques of the large blood vessels also called MR angiography (MRA): time-of-flight (TOF) MRA, phase contrast angiography (PCA) and contrast-enhanced (CE) MRA.

In TOF MRA, the signal coming from static tissue in the slice of interest is first “saturated” and thus gives low intensity signal. However, blood outside of this slice remains unsaturated. When unsaturated blood flows inside the slice of interest, signal coming from blood appears bright compared to the surrounding tissue. This TOF or inflow approach allows for the visualization of blood vessels without the need of contrast agents. As illustrated in Figure 2.12, the TOF signal depends on the blood velocity. Fast flowing blood gives a higher signal compared to the surrounding tissue than slow flowing blood, such as in tortuous vessels.

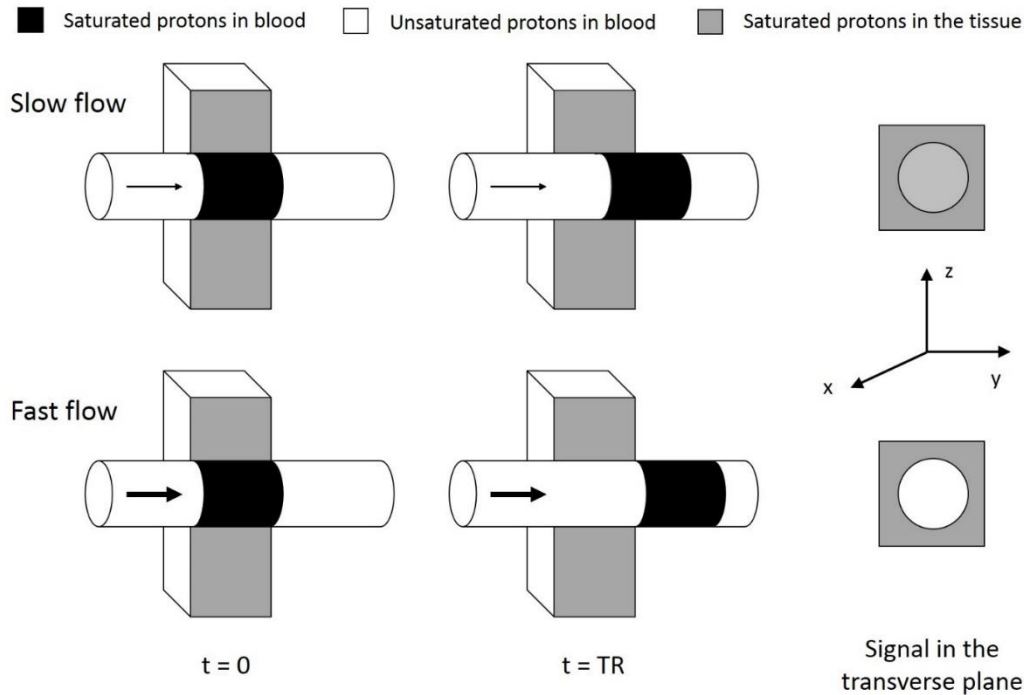


Figure 2.12. Schematic representation of TOF or inflow effects for slow and fast flowing blood and resulting signal in the transverse plane. At  $t = 0$ , the slice of interest represented here by a rectangle is saturated, the tissue has been put in dark grey color and the saturated blood in black color to better distinguish them. At  $t = TR$ , for slow flowing blood, unsaturated blood enters the slice but does not have the time to cross its entire thickness. The resulting signal in the transverse plane is in light grey, not much different from the signal from the tissue. On the contrary, fast flowing blood goes further inside the slice and maybe even outside of it, yielding a much higher contrast compared to the surrounding tissue represented by a white circle for the signal in the transverse plane.

The TOF signal is also affected by the slice orientation. It is maximal when the slice is oriented perpendicular to the vessels imaged. To avoid slice dependence, the solution is to use 3D-TOF MRA. It is however time-consuming and only applicable to structures non subject to strong motions such as the head and neck regions [97].

The second main technique used in MRA is PCA. The spatial phase encoding of the signal assumes that the sample imaged stays relatively still during the acquisition. It is true for static tissue but not for blood vessels and that can generate ghosting in the images. PCA takes advantage of these artefacts. PCA images are generated by taking the difference between flow-weighted images and flow-compensated images. The phase shift measured is between  $0^\circ$  and  $360^\circ$  and is related to the blood velocity of the vessels. Before acquiring data, a parameter

called velocity encoding (VENC) representing the maximum blood velocity expected in a sample needs to be defined. Values of the blood velocity can then be retrieved directly from the images. Phase shifts between  $0^\circ$  and  $180^\circ$  correspond to ranges of blood flow velocities from 0 to VENC while between  $180^\circ$  and  $360^\circ$ , they relate to the same range of blood velocities but flowing in the opposite direction. PCA can not only give quantitative values of the blood velocity but is also able to tell the flow direction. However a careful adjustment of VENC is crucial to avoid misinterpretation of the images. Also, turbulent flow which can be seen in some diseases or after a stenosis also causes intravoxel phase dispersion and signal loss in PCA.

In CE MRA, a Gd-based- $T_1$ -shortening contrast agent is injected intravenously. A GE sequence is then acquired with a TR as short as possible to get the highest contrast from the contrast agent located in the vessel lumen. The delay between the injection and the acquisition needs to be adjusted carefully not to have contamination from venous blood. Figure 2.13 shows an example of a time-resolved CE MRA of the head and neck of a healthy volunteer.

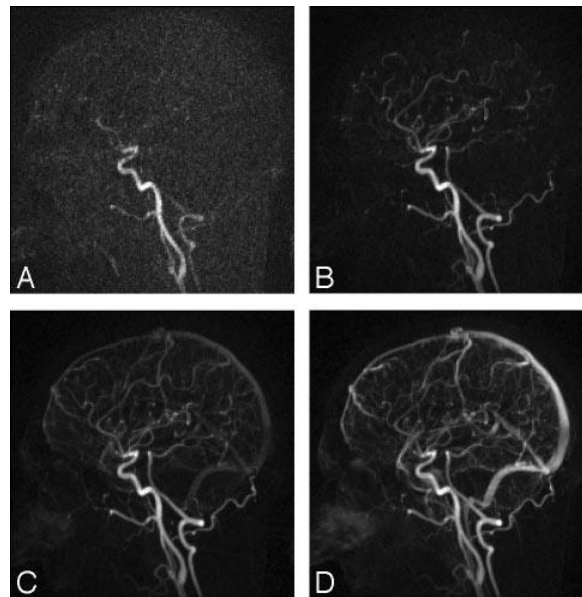


Figure 2.13. Time-resolved sagittal MRA at 3T of a healthy volunteer. Consecutive timeframes are shown with temporal resolution of 2.5 seconds/frame and spatial resolution of  $1 \times 1 \times 2.5$  mm. From Cashen et al [98].

This technique has the advantage to image in a more accurate way stenosis than the previously presented methods. It is also very fast and can be acquired within one breath-hold. It allows for what can be called dynamic or time-resolved MRA. Scans can be repeated in time and the

contrast agent path inside the vessels followed giving directional as well as anatomical information about the vessels.

CE MRA benefits from high SNR, high spatial resolution and is relatively free from flow-related artefacts. The main drawback of this method is the contrast agent itself which has a cost and may not be supported by all patients.

The three techniques presented in this section are able to image large blood vessels, i.e. arteries and veins. Information about their blood velocity and orientation can be retrieved, even the passage of a contrast agent inside these vessels can be followed. However, they are not suitable for the study of smaller vessels such as capillaries, arterioles and venules because they are limited in spatial resolution and by the gradient performances.

### 2.3.2 Imaging of the microvasculature: perfusion imaging

Because of its limited spatial resolution, MRI is not able to directly image the microvasculature. However, MRI methods that are sensitive to macroscopic parameters of the microvasculature can be designed. These techniques are known under the term perfusion imaging. Perfusion usually refers to the dynamic mechanism of blood supply allowing the delivery of nutrients and oxygen to an organ. It is measured in units of milliliters per 100 grams per minute. The study of the macrovasculature (arteries, veins) would not be sufficient to describe this phenomenon because these exchanges mainly take place at the capillary level.

This section goes through the perfusion imaging techniques splitting them into two categories: dynamic susceptibility contrast (DSC) and dynamic contrast enhanced (DCE) MRI which need a contrast agent injection and arterial spin labeling (ASL) which is contrast agent free. IVIM imaging falls also in the same category as ASL but, as it is the focus of this thesis, IVIM is presented in a separate section.

#### 2.3.2.1 Techniques with injection of contrast agent

DSC and DCE MRI are based on the injection of a paramagnetic contrast agent to generate a bolus. This tracer is typically a gadolinium (Gd) chelate. Paramagnetic contrast agents shorten both  $T_1$  and  $T_2$  relaxation times.



DSC MRI takes advantage of the  $T_2$ -shortening effects of the Gd-based paramagnetic agents. To mainly be sensitive to the  $T_2$ -relaxation, a high contrast agent infusion rate is used. GE or SE sequences can be applied. With a GE sequence, field inhomogeneities are not compensated and  $T_2^*$ -relaxation is observed. Furthermore, these inhomogeneities being more important in the large vessels, there is contamination of the signal by the large vessels. When a SE sequence is used, signal loss is reduced because of the refocusing  $180^\circ$  pulse and the large vessel contamination is limited. DSC MRI images are acquired before, during and after the bolus injection and three main quantitative physiological parameters can be extracted from DSC images: relative cerebral blood volume (rCBV), mean transit time (MTT) and relative cerebral blood flow (rCBF). Figure 2.14 shows how to retrieve these parameters from the DSC signal curve.

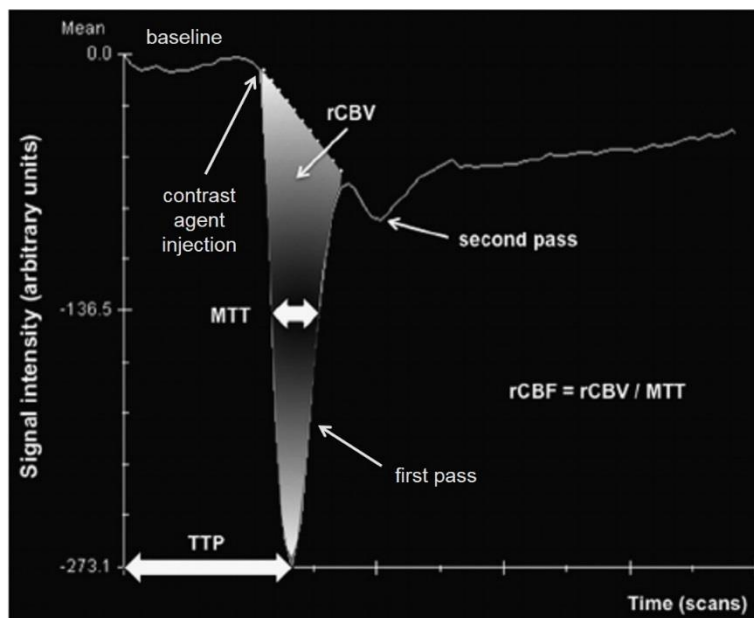


Figure 2.14. Parameters that can be calculated based on DSC perfusion imaging. The time-to-peak, TTP, is the time interval between contrast agent administration and minimum signal intensity. MTT is the width of the curve at half minimum value. rCBV corresponds to the area under curve. Then we directly have  $rCBF = rCBV / MTT$ . Based on Haller et al [99].

DSC MRI is the most widely used perfusion technique in clinics because post-processing of the data is fairly easy. However, only relative quantitative parameters can be obtained. It is also possible to get absolute estimates of CBF by deconvolution of the arterial input function (AIF) with the signal curve. The AIF needs to be carefully evaluated otherwise it can lead to many

artefacts [100]. DSC MRI is also subject to susceptibility artefacts from bone, air and blood which can be another source of error.

On the contrary, DCE MRI takes advantage of the  $T_1$ -shortening effects of the Gd-chelates which enable it to probe different properties of the vasculature. The tracer is chosen small enough to diffuse through the vessel membrane and permeability parameters can be measured. To obtain primarily  $T_1$ -shortening effect, a slower contrast agent infusion rate than in DSC MRI is used. Quantitative parameters can be extracted from DCE MRI images such as volume fractions of blood and the extravascular-extracellular space in the tissue and exchange constants between the blood and the tissue. These parameters are obtained by fitting the concentration curve to a model first developed by Tofts et al. [101] and then modified to take into account all of these parameters [102]. However, this equation depends on the diffusion properties of the contrast agent through the vessel membrane and on blood flow. Different vessel populations can be probed by varying the diffusion properties of the contrast agent. DCE MRI is very interesting in the sense that it allows to probe different quantitative parameters than the other perfusion techniques. However, the complexity of the kinetic modelling which depends on the diffusion properties of the contrast agent across the vessel membrane has made it less used in clinics than DSC MRI.

#### 2.3.2.2 Technique free from contrast agent injection

In ASL, the longitudinal magnetization of blood in the large arteries is inversed in what is called the labeling plane creating a bolus of magnetically tagged spins. After a time delay, tagged blood reaches the imaging volume and the acquisition is performed (Figure 2.15.B). The labeling image obtained is subtracted to a control image for which blood has not been tagged (Figure 2.15.A). The resulting image has very few signal as only 1 % of water molecules in blood is tagged during the allocated time delay. Images also need to be averaged and spatial resolution decreased to increase SNR (Figure 2.15.C). Generally, ASL uses single-shot GE EPI sequences to acquire multi-slice images with short TE to maximize SNR and relatively long TR to allow tagged spins to reach the slice of interest and exchange with the tissue. The main perfusion parameter measured with ASL is the CBF which is directly proportional to the ASL signal (Figure 2.15.C).

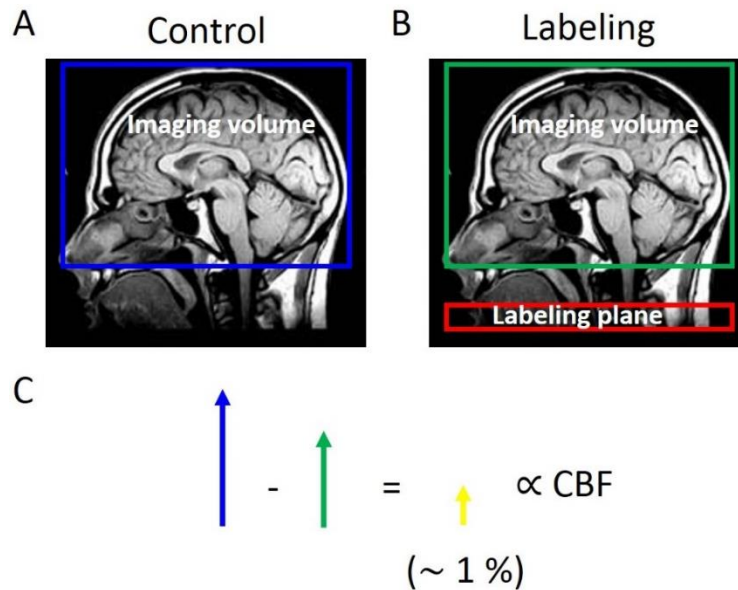


Figure 2.15. ASL imaging principles. (A) Acquisition of a control image in the imaging volume. (B) Labeling of blood ahead of the volume of interest and image acquisition after a time delay in the imaging volume. (C) The difference between control and labeled signals is very small as only 1 % of the blood is tagged but it is proportional to CBF.

There are three main types of ASL sequences [103]: continuous ASL (CASL) [104], pseudo-continuous ASL (pCASL) [105],[106] and pulsed ASL (PASL) [107]. They differ only in the labeling strategy. pCASL is the more recent ASL technique and derives from CASL, the first proposed ASL method. It is intermediate between CASL and PASL, combining the high labelling efficiency of PASL with the higher SNR of CASL. pCASL is the ASL method that was recommended in 2014 by Alsop et al. for use in clinics [108]. ASL can be used in repeated measurements and in patients where an intravenous injection is problematic because it does not need a contrast agent injection. However, it suffers from very low SNR and thus needs long acquisition time to increase the SNR which increases its sensitivity to motion artifacts. This can become a problem in uncooperative patients such as in stroke or neurodegenerative diseases. This is why this technique less used than DSC and DCE MRI in clinics.

Another MRI technique also free from contrast agent injection is IVIM imaging. As it is the technique used throughout this thesis, it is highlighted in a different section.

### 2.3.2.3 Emphasis on intravoxel incoherent motion imaging

The concept of diffusion imaging can be extended to the study of other intravoxel incoherent motions (IVIM). Indeed, capillaries have random orientations and blood flowing in the capillary network yields to a similar motion as the Brownian motion like shown in Figure 2.16.

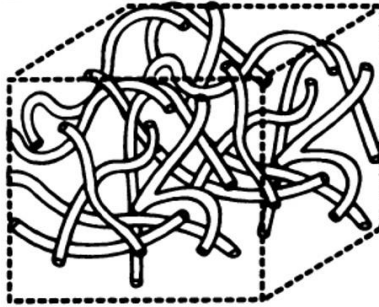


Figure 2.16. Representation of a capillary network in a voxel. Water molecules travelling inside this network experience an intravoxel incoherent motion responsible for a decrease of the MR signal in DWI. From Le Bihan et al [1].

In IVIM imaging, one postulates that a DW sequence is sensitive to all kinds of intravoxel incoherent motions. It is not just able to measure the  $ADC$ , it can also evaluate the motion of spins in the capillary network. This type of motion is also different from free diffusion as it is produced by random orientations of the capillaries. It is called pseudo-diffusion to differentiate it from free diffusion.

To acquire images in IVIM imaging, a DW sequence is used, making the sequence easy to implement on clinical scanners. The difference with DWI rests on the number and values of the b-values acquired. In IVIM imaging, more b-values are acquired than in DWI. Also, a substantial number of b-values in the range of small b-values is added whereas a small number of b-values even none is usually used in that range for DWI. The apparent diffusion and pseudo-diffusion effects on the signal attenuation can be well separated as the  $ADC$  and the pseudo-diffusion coefficient are very different. Protons experiencing pseudo-diffusion are driven by blood displacement inside the capillaries so the associated pseudo-diffusion coefficient is much bigger than the  $ADC$  in tissue where diffusion is restricted by the presence of natural obstacles. IVIM imaging is thus able to extract at the same time the  $ADC$ , the pseudo-diffusion coefficient and also the volume fraction of the corresponding spin populations. Even if it is restricted diffusion, the phenomenon characterized by the  $ADC$  is usually simply called diffusion. The equation for

the signal attenuation in IVIM imaging is based on the one for DWI with an added component corresponding to the contribution of spins inside the capillaries,

$$S(b) = S_0 \left( (1 - f_{IVIM}) F_{Diff}(b) + f_{IVIM} F_{IVIM}(b) \right) \quad 2.27$$

where  $F_{Diff}(b)$  corresponds to the diffusion signal component allowing for the calculation of the  $ADC$ ,  $f_{IVIM}$  is the fractional volume occupied by spins flowing in the capillaries in a voxel and  $F_{IVIM}(b)$  the signal decay induced by isochromats in motion in the capillaries. This model neglects water exchanges between the capillaries and the tissue.

The model usually used to describe  $F_{IVIM}(b)$  in the literature is [1]

$$F_{IVIM}(b) = e^{-b(D^* + D_b)} \quad 2.28$$

where  $D^*$  is the pseudo-diffusion coefficient and  $D_b$  the diffusion coefficient of water in blood.

Efforts have been made to relate IVIM parameters,  $f_{IVIM}$  and  $D^*$ , to classical perfusion parameters, CBV and CBF, giving [109]

$$CBV = f_{IVIM} f_w \quad 2.29$$

and

$$CBF = \frac{6f_w}{\langle L \rangle L_T} f_{IVIM} D^* \quad 2.30$$

where  $f_w$  is the tissue NMR-visible water content fraction,  $\langle L \rangle$  the mean capillary length and  $L_T$  the total capillary length.

For a given tissue, the fraction in the expression of CBF in Eq. 2.30 is constant. CBF is thus directly proportional to the product  $f_{IVIM} \times D^*$ . However, the constant parameters in Eq. 2.29 and 2.30,  $f_w$ ,  $\langle L \rangle$  and  $L_T$ , are hard to estimate making the link between IVIM parameters and classical perfusion parameters still weak.

When it was first introduced by Le Bihan in the 1980s and 1990s, due to the lack of robust pulse sequences and relatively low available gradient strengths combined with the low CBV, IVIM imaging was less studied than other new emerging techniques like diffusion tensor imaging, for example. Now that these limitations have been overridden, IVIM imaging has many applications

in highly vascular organs like the kidneys [110], liver [111], etc. It also has potential applications in the brain for the identification of stroke regions [112], the classification of brain tumors [113] and also in neurodegenerative diseases such as Parkinson's disease [114].

Some drawbacks restrain IVIM imaging use in routine in clinics. The capillaries only represent 2-5 % of the total brain volume so IVIM imaging is only looking at a very small fraction of the total DWI signal giving a low SNR. Several averages and repetitions are thus needed to increase the SNR. A certain number of b-values also need to be acquired in order to adequately fit for both the diffusion and the IVIM signals. For these two purposes, the acquisition time is relatively long and IVIM imaging is very sensitive to motion.

Table 2.2 summarizes the main aspects of the MRI techniques of the microvasculature presented in the previous subsections and compares them to IVIM imaging.

	DSC	DCE	ASL	IVIM
<b>Contrast agent</b>	Gd-chelate	Gd-chelate	Without	Without
<b>Tracer</b>	Non-diffusible blood pool tracer	Diffusible tracer	Diffusible tracer	Non-diffusible blood pool tracer
<b>Effect</b>	Increased susceptibility effect	$T_1$ shortening effect	Blood magnetization inversion	Diffusion and pseudo-diffusion effect
<b>Signal behavior</b>	Decreased signal	Increased signal	Subtracted signal	Subtracted signal
<b>Quantitative parameters</b>	rCBF, rCBV, MTT, absolute CBF	Permeability-related parameters	CBF	$ADC$ , $f_{IVIM}$ , $D^*$ (related to CBF and CBV)
<b>Advantages</b>	-Widely used in clinics -Easy to post-process the data	-Quantitative assessment of microvascular permeability	-Non invasive -No need of contrast agent -Robust measure of CBF	-Non invasive -No need of contrast agent -Easy to post-process data
<b>Limitations</b>	-Invasive -No robust absolute quantification -Susceptibility artifacts	-Invasive -Complexity of kinetic modelling -Lack of widely used software to process the data	-Low SNR -Long acquisition times -Motion artifacts -Only measure of CBF -High SAR	-Low SNR -Long acquisition times -Motion artifacts -Hard to relate to CBF and CBV

Table 2.2. Comparison of the main characteristics of the MRI techniques of the microvasculature

IVIM imaging was chosen to be the focus of this thesis as it is a promising technique to study alterations of the capillary network non-invasively and without contrast agent injection in contrary to DSC and DCE MRI. It also has advantages over the ASL techniques as it is able to measure not only parameters related to the CBF but also to the CBV. The 180° RF pulses used for labeling in pCASL demand high power and produce heat (high specific absorption rate (SAR)). This technique is thus less suitable for children and weak patients than the IVIM technique for which this is not a problem. However, the IVIM technique still lacks of a more complete understanding of where the IVIM signal comes from. One assumption of the IVIM technique is that it is only able to probe the capillary network. Yet, many papers have challenged this hypothesis and stated that the IVIM technique is able to explore a larger part of the microvasculature. The next chapter, Chapter 3, will provide more information about how the IVIM signal can be modelled.

# Chapter 3: Impact of the diffusion encoding time on IVIM signal modelling

In this chapter, a review of the models of the IVIM signal is presented before showing that a bi-exponential model taking into account more than just the capillary network better describes the IVIM signal at shorter diffusion encoding time.

## 3.1 IVIM signal models

Since its first introduction by Le Bihan et al. in 1988 [1], IVIM signal modelling has been extensively studied. In this chapter we first present the two models introduced originally by Le Bihan et al. In the second subsection, a review of other proposed models is performed. Finally, the last subsection introduces a bi-exponential IVIM model valid at a wide range of diffusion times and accounting for more than just the capillary network.

### 3.1.1 Two models for two limit cases

Making the hypothesis that the microvascular network can be modeled by a series of straight tubes randomly oriented in space and uniformly distributed over the unit sphere in 3D, the expression for the IVIM signal,  $F_{IVIM}(b)$ , depends on the mean vessel length,  $L$ , the mean blood velocity,  $V$ , and the diffusion encoding time of the IVIM sequence. Two limit cases can be defined.

#### 3.1.1.1 The standard mono-exponential model

The original IVIM model [1] assumes that blood flow changes directions several times during the diffusion time like in Figure 3.1. In this case, the isochromat trajectories, which can be modeled as a random walk, add up to a process that resembles diffusion, which will be called “pseudo-diffusion” in this thesis.



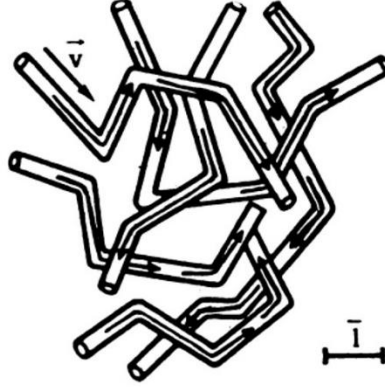


Figure 3.1. Representation of isochromats flowing in a capillary network. Each arrow corresponds to one isochromat trajectory in the network during the diffusion time. In this case, the arrows and thus trajectories consists of two or more segments. The isochromats see several vessel segments during the diffusion time. From Le Bihan et al [1].

Let  $D^*$  be the pseudo-diffusion coefficient, then the expression for  $F_{IVIM}(b)$  is an exponential:

$$F_{IVIM}(b) = e^{-b(D_b + D^*)} \quad 3.1$$

where  $D_b$  is the diffusion coefficient of water in blood. The expression for  $D^*$  can be found by going back to Einstein's equation (Eq. 2.21).

Supposing that an isochromat travels through  $N$  vessels during  $T_{Diff}$  and that the time to cross each vessel is  $T$ , for a 3D displacement the Einstein's equation becomes:

$$\langle R^2 \rangle = D^* 6NT \quad 3.2$$

In addition,  $\langle R^2 \rangle$  can also be written in terms of the number of vessels crossed,  $N$ , and the mean vessel length,  $L$ :

$$\langle R^2 \rangle = NL^2 \quad 3.3$$

By comparing the two equations above,  $D^*$  can be obtained:

$$D^* = \frac{LV}{6} \quad 3.4$$

where  $V = \frac{L}{T}$  is the mean blood velocity.

This model represents one of the two limit cases, namely, it is valid at the long time scale.

### 3.1.1.2 The sinc model

The other limit case is when vessels are long enough or the blood velocity small enough so that the isochromats stay in the same vessel during the diffusion time as shown in Figure 3.2.

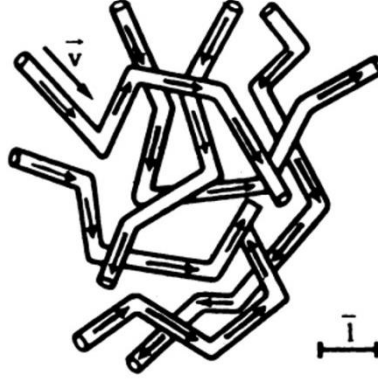


Figure 3.2. Representation of isochromats flowing in a capillary network. Each arrow corresponds to one isochromat trajectory in the network during the diffusion time. In this case, the arrows and thus trajectories stay in the same vessel segment. From Le Bihan et al [1].

In this regime and if the blood velocity is assumed to be constant, the expression for  $F_{IVIM}(b)$  becomes:

$$F_{IVIM}(c) = e^{-bD_b \text{sinc}(cV)} \quad 3.5$$

with

$$c = \gamma \left[ \int_0^{TE/2} -Gtdt + \int_{TE/2}^{TE} Gtdt \right] \quad 3.6$$

A  $D_{sinc}^*$  can also be defined in this regime by calculating the Taylor expansion of  $F_{IVIM}(c)$  [115]:

$$F_{IVIM}(c) \approx 1 - \frac{(cV)^2}{3!} \quad 3.7$$

and comparing it to the Taylor expansion of  $F_{IVIM}(b)$ :

$$F_{IVIM}(b) \approx 1 - bD^* \quad 3.8$$

This gives:

$$D_{sinc}^* = \frac{c^2 V^2}{6b} \quad 3.9$$

For a PGSE sequence,

$$c = \gamma \left[ \int_0^\delta -Gtdt + \int_\Delta^{\Delta+\delta} Gtdt \right] = \gamma G \delta \Delta \quad 3.10$$

In the short pulse approximation,  $\delta \ll \Delta$ ,  $b \cong \gamma^2 G^2 \delta^2 \Delta$ , and  $D_{sinc}^*$  simplifies to :

$$D_{sinc}^* = \frac{V^2 \Delta}{6} \quad 3.11$$

It can be noticed that  $D_{sinc}^*$  is independent of L as spins never get to probe the entire segment.

The sinc model is only valid at the very short time scale when the isochromats stay in the same vessel during the whole diffusion time.

The two limit models presented in this subsection are valid at very short and long diffusion times. To cover the intermediate regime between very short and long diffusion times, other models have been proposed.

### 3.1.2 Other models proposed in the literature

Besides the standard mono-exponential model and the sinc model, other models have been proposed to describe the IVIM signal. Two categories can be distinguished: models trying to include the intermediate regime and models obtained from using innovative strategies to directly suppress the signal from non-flowing isochromats in the tissue compartment.

#### 3.1.2.1 Models accounting for the intermediate regime

Kennan et al. [116] have proposed a model based on a velocity autocorrelation function to cover intermediate situations between the two extreme regimes, mono-exponential and sinc, but still only considering the capillaries. This model uses a velocity autocorrelation function to describe the isochromats' dynamics. The velocity autocorrelation function is a measure of velocity fluctuations in the network and is defined as the average of the scalar product of the velocity of an isochromat evaluated at different times  $t'$  and  $t''$ :  $\langle \overrightarrow{V(t'')} \cdot \overrightarrow{V(t')} \rangle$ . For a capillary network with a distribution of segments of different lengths, this product can be expressed as:

$$\langle \overrightarrow{V(t'')} \cdot \overrightarrow{V(t')} \rangle = \langle \bar{V}^2 \rangle e^{-\frac{|t''-t'|}{T_0}} \quad 3.12$$

where  $\langle \bar{V}^2 \rangle$  is the mean squared blood velocity and  $T_0$  the correlation time which corresponds to the average time the isochromats stay in a given segment.

After integrating the expression of the signal attenuation for the PGSE sequence and the assumed velocity autocorrelation function in Eq. 3.12, the IVIM signal becomes:

$$F_{IVIM}(b) = e^{-b\left(\frac{\langle \bar{V}^2 \rangle}{3} T_0 \Omega + D_b\right)} \quad 3.13$$

with  $\Omega = 1 - \frac{2T_0^2 \delta + T_0^3 m}{\delta^2 \left(\Delta - \frac{\delta}{3}\right)}$  and  $m = 2e^{-\frac{\delta}{T_0}} + 2e^{-\frac{\Delta}{T_0}} - e^{-\frac{\Delta+\delta}{T_0}} - e^{-\frac{\Delta-\delta}{T_0}} - 2$ .

The two parameters extracted from this model are  $\langle \bar{V}^2 \rangle$  and  $T_0$ . From them, morphological parameters can be extracted, the average flow velocity,  $\bar{V} = \sqrt{\langle \bar{V}^2 \rangle}$ , and the segment length,  $L = 2T_0 \sqrt{\langle \bar{V}^2 \rangle}$ .

This model converges toward the mono-exponential and the sinc regimes at long and very short diffusion times, respectively, and it is expected to also cover intermediate regimes. When comparing the expression of  $F_{IVIM}(b)$  in this model which we will call the Kennan model and the standard mono-exponential IVIM model, the models are very similar except that  $D^*$  has been replaced by  $\frac{\langle \bar{V}^2 \rangle}{3} T_0 \Omega$ .

Arguing that the Gaussian phase approximation assumed by Kennan et al. is invalid in some cases, Wetscherek et al. [117] introduced a model based on normalized phase distributions which only depend on the diffusion gradient waveform. According to the authors, this model is suitable for arbitrary choices of acquisition parameters. However, they state that a mono-exponential model can probably describe IVIM data equally well when non flow-compensated diffusion gradients are used but will most likely underestimate the pseudo-diffusion coefficient.

These two models assume that only flow in capillaries contributes to the signal attenuation. Some authors have contradicted this hypothesis and, by using other strategies to obtain the IVIM signal, they are taking into account a larger part of the microvascular network to model the IVIM signal.

### 3.1.2.2 Other strategies to directly obtain and model the IVIM signal

To overcome the difficulty to obtain the IVIM signal which represents only 5 % of the DW signal, Neil et al. developed a strategy to directly suppress the signal from non-flowing isochromats in

the extravascular space, i.e. the diffusion component [118]. They inject a contrast agent that decreases the  $T_1$  of flowing isochromats and selectively suppress the signal from non-flowing isochromats on the basis of  $T_1$ . This scheme artificially increases the blood volume fraction  $f_{IVIM}$  allowing for an easier measure of the IVIM signal. As the diffusion component was suppressed, one would think that the obtained IVIM signal would be fitted to a mono-exponential model (standard IVIM model). However, the IVIM signal they obtain is better fitted to a bi-exponential model. Their hypothesis for this second exponential in the IVIM signal is that it is associated with incompletely suppressed signal from non-flowing blood.

This problem of incompletely suppressed non-flowing water signal gave them the idea to completely replace blood with perfluorocarbon (PFC) blood substitute containing  $^{19}\text{F}$  (fluorine) [119]. When using this technique, it is sure that the signal observed only comes from the vascular compartment as the PFC does not cross the BBB and animals contain no naturally-occurring fluorine. A bi-exponential model is found to better describe the obtained IVIM signal. However, it is not clear what these two components represent. But comparing the pseudo-diffusion coefficients with the diffusion coefficient obtained from scanning the brain of a dead rat, they show that both pseudo-diffusion coefficients are at least one order of magnitude greater than the diffusion coefficient suggesting that the pseudo-diffusion coefficients are related to blood flow.

A few years later, coming back to proton experiments using the same technique of directly suppressing the contribution from non-flowing spins, Neil et al. performed a hypercapnia experiment increasing blood flow by adding  $\text{CO}_2$  to the anesthesia circuit and looked at the evolution of the two pseudo-diffusion coefficient with increasing  $\text{pCO}_2$  [120]. Both pseudo-diffusion coefficients correlate with the  $\text{pCO}_2$  which strongly suggests that both components are related to intravascular signal. However it is still most likely that the smallest  $D^*$  is subject to contamination from incompletely suppressed diffusion signal and stronger evidence needs to be gathered to be able to say that both  $D^*$  are related to vascular components.

Based on Neil et al.'s findings with the PFC experiments, Henkelman et al. have suggested an IVIM model which takes into account not only capillaries but all types of vessels [121]. Their

model is based on a distribution of vessel diameters and thus of blood flow velocities. They assume an isotropic orientation of the vessels and show that it is a good assumption for the whole brain except for the carotid arteries and the sagittal sinus. They are using laminar flow instead of plug flow as they are including larger vessels than capillaries. The mathematical equations related to laminar flow introduced by Ahn et al. will be described in details in the next chapter. Henkelman's model involves two pools associated with the arterial and venous trees. One diameter distribution represents the arterial or supply side of the vascular system and accounts for 80 % of the vascular volume of the brain whereas the other distribution describes the venous or drainage side and represents 20 % of the vascular volume of the brain. Diameters range from 5  $\mu\text{m}$  for the capillaries to 0.72 mm for the venous sinus, really incorporating all vessels in the brain. Henkelman et al. show that larger vessels than capillaries must be included in order to adequately model the IVIM signal. However, the perfusion estimated with their model is one order of magnitude lower than reported in the literature.

Duong et al. take inspiration from these PFC experiments and exploit the fact that the spin-lattice relaxation rate of the PFC correlates linearly with the dissolved oxygen concentration [122]. This allows them to link each of the pseudo-diffusion coefficients of the bi-exponential IVIM model to the arterial and venous trees and measure the associated regional arterial and venous blood volume fractions. However, this technique is invasive as the animals have to be euthanized at the end of the experiments. The process of replacing blood with PFC is not reversible.

These findings with PFC experiments suggest that the IVIM signal represents more than just the capillary network. However, it has not been possible to demonstrate this finding in proton experiments yet. Even with the non-flowing isochromats suppression technique, this could not be proven. As is shown in the next section, in this thesis, we establish that it is possible to describe the IVIM signal with a bi-exponential model in proton imaging in the case of short diffusion times.

### 3.1.3 The bi-exponential model

Here we introduce a bi-exponential IVIM model (not to be confused with the bi-exponential model used to separate diffusion and IVIM effects [123]), accounting for two different vascular pools, as an alternative to the mono-exponential model at short diffusion times:

$$F_{IVIM}(b) = e^{-bD_b} \left( f_{slow} e^{-bD_{slow}^*} + f_{fast} e^{-bD_{fast}^*} \right) \quad 3.14$$

with the constraints  $f_{slow} + f_{fast} = 1$  and  $D_{fast}^* > D_{slow}^*$ . We emphasize that, when fitting the bi-exponential model to experimental data, we always define the larger exponent as  $D_{fast}^*$ .

Our hypothesis about the physical meaning of the bi-exponential model is different from that of Henkelman and Duong. We hypothesize that the bi-exponential behavior reflects the contribution of flow in two distinct vascular pools: a slow and a fast flowing pool corresponding to capillaries and medium-sized vessels, respectively.  $T_2$  of venous blood being much smaller than  $T_2$  of arterial blood, the vessels contributing the most to the MR signal are mainly coming from the arterial part of the vascular tree.

Depending on the experimental parameters and the vascular properties, one can also consider models consisting of a combination of two sinc functions or one exponential and one sinc function. However, in agreement with the literature [117],[124], our simulations show that, when considering a Gaussian distribution of blood flow velocities, the IVIM signal plotted against the b-value “looks exponential” even when isochromats do not change direction many times (sinc regime). This transition is analyzed in more details in the next chapter section 4.2.5.

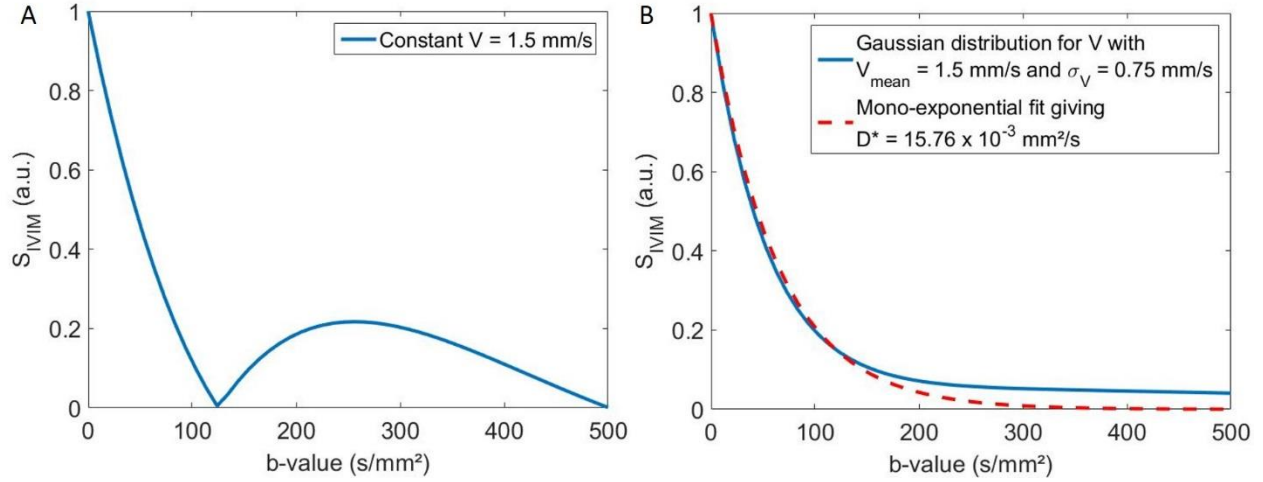


Figure 3.3. Plot of the IVIM signal in the sinc regime for  $\delta = 3$  ms,  $\Delta = 34$  ms and (A) a constant  $V = 1.5$  mm/s or (B) a Gaussian distribution for  $V$  with  $V_{mean} = 1.5$  mm/s,  $\sigma_V = 0.5 \times V_{mean}$  and 1000 samples of  $V$ . In Figure 3.3.B, a mono-exponential fit of the IVIM signal was added. It gives  $D^* = 15.76 \times 10^{-3}$  mm²/s.

So, if there is a Gaussian distribution of the blood velocity in the network of vessels, the signal does not look like a sinc function anymore rather like something closer to an exponential function. It is thus reasonable to consider a bi-exponential model to account for both the slow and the fast vascular pools.

If two pools can be observed, we should also consider the fact that three pools for example, could be observed too. This case can be modelled by a tri-exponential model:

$$F_{IVIM}(b) = e^{-bD_b} \left( f_{slow} e^{-bD_{slow}^*} + f_{fast} e^{-bD_{fast}^*} + f_{faster} e^{-bD_{faster}^*} \right) \quad 3.15$$

A third exponential component characterized by  $f_{faster}$  and  $D_{faster}^*$  has been added that represents the contribution from an even faster flowing pool than the fast pool introduced with the two-pool bi-exponential model. The condition  $f_{slow} + f_{fast} + f_{faster} = 1$  must be fulfilled. And naturally, we order the exponents by the property  $D_{faster}^* > D_{fast}^* > D_{slow}^*$ .



## 3.2 Evaluation of the best model for the IVIM signal at short diffusion encoding time

### 3.2.1 Material and methods

#### 3.2.1.1 Animal procedures

Dark Agouti male rats ( $N_R = 11$ , 240-360 g, 3-21 months, Janvier, Saint Isle, France) were used in this study. All animal experiments were conducted according to recommendations of the EU Directive 2010/63/EU for care and use of laboratory animals.

Throughout the experiments the animals, anesthetized with 1.5 - 2 % isoflurane in a 1:2 O<sub>2</sub>:air mixture, were monitored for respiration rate (30–50 breath per min) and temperature, maintained constant ( $36.5 \pm 0.5^\circ\text{C}$ ) using a heated air circuit device (SA Instruments, Inc, USA). To avoid motion-related artifacts, the head was immobilized using a bite bar and ear pins connected to the nose cone.

At first, plastic ear pins were used. However they are not convenient as they tend to bend if they are used too much and are too small to ensure that the rat's head will be well-fixed. Therefore, we use wood ear pins which are in fact small diameter cotton buds that can be easily cut by hand at the right length when the animal is in the right position in the nose cone. Movement should be avoided with the IVIM sequence as a small movement can introduce noise or ghosts in the images causing more difficult evaluation of the IVIM parameters. With the frequent changes of the head of the bed between the different scanner users, the head of the bed needs to be well fixed to the bed. The animal's head should not move at all with the rat's teeth well positioned in the bite bar and the nose cone well fixed.

#### 3.2.1.2 MRI experiments

Data were collected using a horizontally oriented 7T small animal MRI scanner (Biospec, Bruker Biospin, Etlingen, Germany) equipped with a 740 mT/m gradient coil system. A 3 x 3 cm<sup>2</sup> four-element phased-array receiver coil and a 7.2 cm (inside diameter) volume transmit coil (Bruker BioSpin, Etlingen, Germany) were used. After scout scans, the magnetic field homogeneity was ensured through the FASTMAP method (Paravision 5.1) followed by the MAPSHIM method to correct more specifically in the region of interest.

Coronal DW-MRI images were acquired using a standard pulsed-gradient EPI spin-echo sequence (PG-EPI-SE) with a GRAPPA reconstruction (acceleration factor 2) and 30 b-values (20 b-values ranging from 7 to 500 s/mm<sup>2</sup> and 10 b-values ranging from 500 to 2500 s/mm<sup>2</sup>). The acquisition parameters were set as follows: gradient directions [X=1, Y=1, Z=1], [X=0, Y=1, Z=0] and [X=0, Y=0, Z=1], diffusion gradient duration time  $\delta = 3$  ms, diffusion gradient separation times  $\Delta = 14, 24$  and 34 ms, in plane resolution 250 x 250  $\mu\text{m}^2$ , matrix size 80 x 80, field of view 20 x 20 mm<sup>2</sup>, slice thickness 1.5 mm, 1 segment, echo time TE = 45 ms, repetition time TR = 1000 ms, 6 averages, 6 repetitions, 2 slices. Data with strong motion artefacts were discarded and the acquisition repeated. For one rat, only 5 repetitions could be included.

### 3.2.1.3 Data processing

IVIM/diffusion MRI images were processed using MATLAB (MathWorks, Massachusetts, USA).

As diffusion is mostly isotropic in the gray matter with only some diffusion anisotropy visible at high resolution with MRI in the brain cortical gray matter [125], the signals from the different gradient diffusion directions were averaged to increase SNR. IVIM effects were also assumed to be isotropic.

Afterwards, ROIs were drawn manually on the cortical gray matter and on the thalamus of the left hemisphere and averaged over the two acquired slices. The two ROIs are shown in Figure 3.4. They consisted of approximately  $132 \pm 37$  and  $125 \pm 33$  pixels for each slice for the left cortex (LC), and  $90 \pm 18$  and  $88 \pm 15$  pixels for each slice for the left thalamus (LT), respectively.

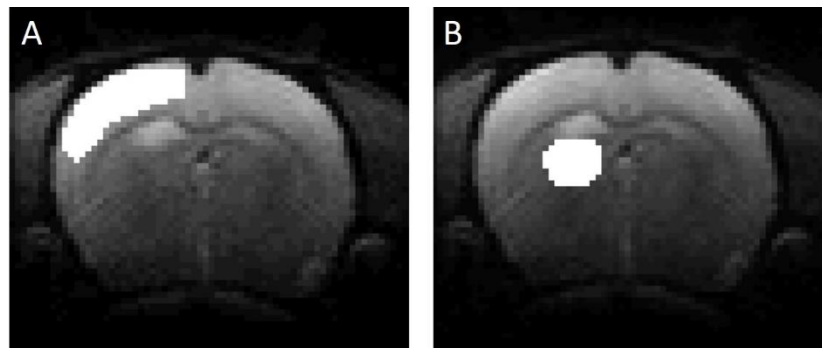


Figure 3.4. Example of the two ROIs drawn on the left cortex (A) and left thalamus (B).

The total MR signal obtained from the PG-EPI-SE sequence is:

$$S(b) = S_{0diff}F_{diff}(b) + S_{0IVIM}F_{IVIM}(b) \quad 3.16$$

where  $S_{0diff}$  and  $S_{0IVIM}$  are the fractions of diffusion and IVIM components, respectively, with  $S_{0diff} = S_0 \times (1 - f_{IVIM})$  and  $S_{0IVIM} = S_0 \times f_{IVIM}$ , where  $f_{IVIM}$  is the blood volume fraction and  $S_0$  is the overall signal when  $b = 0$  (it should be noted that tissue and blood contribute to  $S_0$  with different  $T_2$  and  $T_1$ -weightings).

IVIM parameters were obtained from the signal attenuation,  $S(b)$ , in two steps, first estimating the diffusion component,  $F_{diff}(b)$ , for  $b > 500 \text{ s/mm}^2$ , then estimating the IVIM component,  $F_{IVIM}(b)$ , from the residual signal, after the diffusion component has been removed for data corresponding to  $b < 500 \text{ s/mm}^2$ . This two-step approach was found to give better stability than direct fitting of the data which is more sensitive to noise in the image and outliers [126],[127].

The adequacy of the chosen  $b$  threshold value was confirmed after examination of many cases, as the residual signal taken after removing diffusion effects was found not to differ significantly from noise for  $b$ -values above  $500 \text{ s/mm}^2$ . This  $b$  threshold is higher than the one usually applied for the rat brain,  $300\text{-}400 \text{ s/mm}^2$  (ref. [128]). Due to the high SNR ( $\cong 44$  at  $b = 500 \text{ s/mm}^2$ ) made possible by the high field used and the many averages employed, we noticed that some IVIM signal was still present at  $b = 400 \text{ s/mm}^2$  and therefore increased the cut-off value.

An approach suggested by Wurning et al. could also have been used [129]. They developed an algorithm to adapt the  $b$ -value threshold for each set of data. The algorithm performs an iterative fitting of both diffusion and IVIM components for a varying number of  $b$ -values from the maximum number of  $b$ -values to two  $b$ -values, progressively decreasing the number of  $b$ -values taken into account for the diffusion fit. As we show that the cut-off  $b$ -value can be varied to improve accuracy of the fit, maybe this approach should be used at the beginning of a new study to find the adequate  $b$ -value threshold.

The most commonly used diffusion model in clinical studies [130],[131],[132] is the mono-exponential model which assumes that diffusion is Gaussian in tissues. Other popular models which account more accurately for the signal behavior at high  $b$ -values ( $> 1000 \text{ s/mm}^2$ ) are the bi-exponential diffusion model which assumes the presence of two slowly exchanging tissue

diffusion compartments and the polynomial, often referred to as the Kurtosis [133],[134] model which empirically handles the non-Gaussian nature of diffusion in tissues [123].

In this work, we used the Kurtosis model (Eq. 3.17) as it is more robust in the medium-range  $b$ -values ( $< 3000 \text{ s/mm}^2$  (ref. [135])):

$$F_{diff}(b) = e^{-bADC_0 + (bADC_0)^2 \frac{K}{6}} \quad 3.17$$

where  $ADC_0$  is the apparent diffusion coefficient obtained when  $b$  approaches 0 and  $K$  is the Kurtosis parameter which characterizes the deviation from the exponential decay.

The expression of the Kurtosis model goes to infinity for very high  $b$ -values. However, as stated by Jensen et al. [133], if we take typical values for  $ADC_0$  and  $K$  in the brain,  $ADC_0 = 1 \text{ } \mu\text{m}^2/\text{ms}$  and  $K = 1$ , the Kurtosis model should not be used to fit the diffusion component in the brain with  $b$ -values  $\geq 3000 \text{ s/mm}^2$ . Indeed, as shown in Figure 3.5, for  $b$ -values  $\leq 3000 \text{ s/mm}^2$ , the Kurtosis model is a monotonically decreasing function of the  $b$ -value.

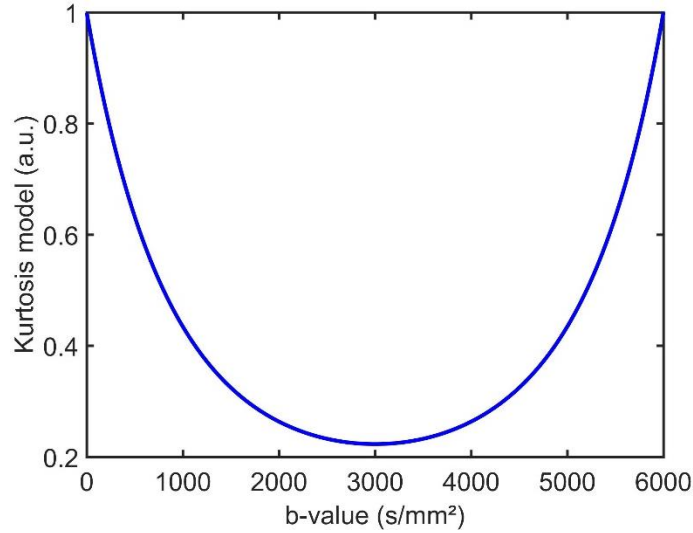


Figure 3.5. Plot of the Kurtosis model versus the  $b$ -value for  $ADC_0 = 1 \text{ } \mu\text{m}^2/\text{ms}$  and  $K = 1$ .

Not taking into account the non-Gaussian diffusion at high  $b$ -values with the Kurtosis model has a high impact on the value of  $f_{IVIM}$  [136]. As shown in Figure 3.6.A,  $f_{IVIM}$  is overestimated when fitting to a mono-exponential model. However, this does not change the results observed on the IVIM signal: the IVIM signal is still bi-exponential (Figure 3.6.B).

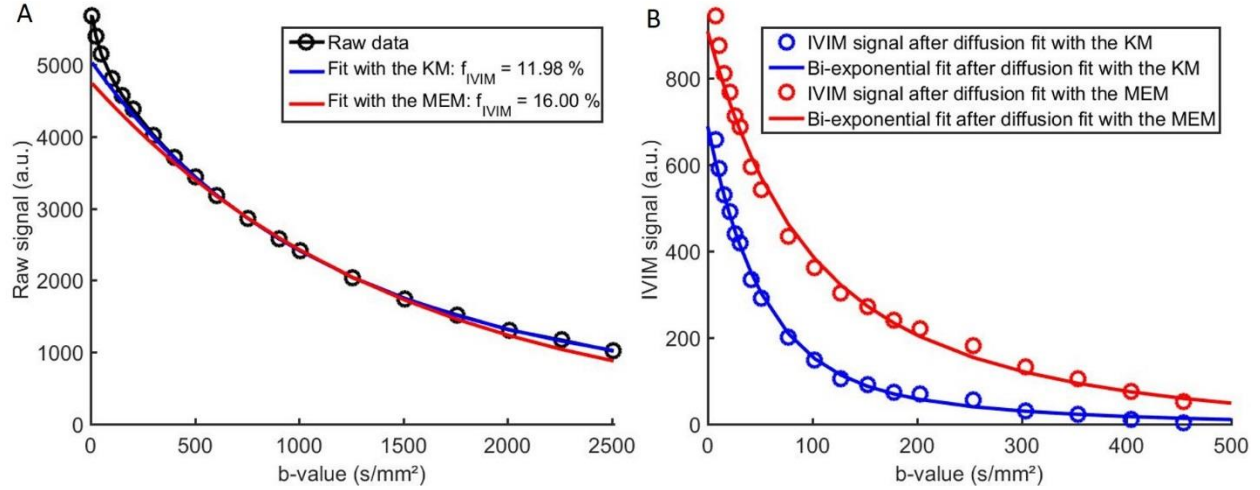


Figure 3.6. Differences between fitting the diffusion component to a Kurtosis model (KM) and a mono-exponential model (MEM). (A) Raw signal against the b-values superimposed to the diffusion fits to the KM for  $b = [500-2500] \text{ mm}^2/\text{s}$  and the MEM for  $b = [500-1500] \text{ mm}^2/\text{s}$ , in red and blue, respectively. (B) Bi-exponential fit of the residual IVIM signals after fitting to the KM and MEM, in red and blue, respectively. With the KM model, we get  $f_{slow} = 19.06 \%$ ,  $D_{slow}^* = 5.04 \times 10^{-3} \text{ mm}^2/\text{s}$  and  $D_{fast}^* = 19.91 \times 10^{-3} \text{ mm}^2/\text{s}$  and with the MEM model,  $f_{slow} = 48.50 \%$ ,  $D_{slow}^* = 4.43 \times 10^{-3} \text{ mm}^2/\text{s}$  and  $D_{fast}^* = 14.83 \times 10^{-3} \text{ mm}^2/\text{s}$ .

Then the IVIM component,  $F_{IVIM}(b)$ , was tested for the mono-, bi-, tri-exponential IVIM models and the Kennan model.

Several algorithms can be used to determine the best fit for each signal component. The most common are the non-linear least squares (NLLS) analysis and the Bayesian probability (BP) theory. The NLLS method, the sum of squared differences between the studied signal and the modelled signal is minimized. This analysis can be biased by inadequate starting values for the estimated parameters. In that case, a local minimum can be found instead of the global minimum, giving incorrect parameter estimates. On the other hand, BP algorithms uses probability density functions and thus does not require starting values of the parameter estimates. Quite a few papers show that the BP theory is performing better than the NLLS analysis [137], [138]. A dictionary-based approach has also been proposed by Lima et al. to bypass the NLLS problem of starting values [136]. This method compares the whole MRI signal to a dictionary of model signals with different values for the parameters of the diffusion and IVIM models also adding a noise correction factor to account for noise in the MR image. The dictionary only has to be generated once and then the algorithm runs quickly as it only has to

calculate the error between the studied signal and the signals of the dictionary and minimize it. It was found to behave better than the NLLS but was not compared to the BP algorithm. For this thesis, the NLLS algorithm was used, knowing its drawbacks. Care was taken to ensure that the minimum value found was indeed the global minimum and not a local minimum by varying the initial conditions of the parameters.

Another approach was also considered to test the Kennan model. As its equation takes into account  $\Delta$  and allows to directly obtain morphological parameters, i.e. the average flow velocity,  $\bar{V}$ , and the segment length,  $L$ , we put an additional constraint to the fit: the morphological parameters should be the same for all three diffusion encoding times. The experimental data were therefore compared to the Kennan model with a range of values for the two fit parameters: 200 values for  $\langle \bar{V}^2 \rangle = [0.01 - 100] \text{ mm}^2/\text{s}^2$  and 200 values for  $T_0 = [1 - 200] \text{ ms}$ .

#### 3.2.1.4 Statistical analysis

The statistical analysis for the comparison between the four models was performed using the corrected Akaike information criterion (AICc) for a small number of samples [139] ( $N_s < 30$ ):

$$AICc = N_b \ln(MSE) + \frac{2k(k+1)}{N_b - k - 1} \quad 3.18$$

with  $N_b$  the number of b-values used to fit the signals,  $MSE$  the mean squared error and  $k$  the number of parameters in the model, taking into account that the Gaussian noise hypothesis for the signal residuals counts as 1 parameter according to the AIC theory. Hence,  $k = 3, 4, 5$  and  $7$  for the mono-exponential ( $f_{IVIM}, D^* + 1$ ), Kennan ( $f_{IVIM}, \langle \bar{V}^2 \rangle, T_0 + 1$ ) bi- ( $f_{IVIM}, f_{slow}, D_{slow}^*, D_{fast}^* + 1$ ) and tri-exponential models ( $f_{IVIM}, f_{slow}, f_{slow}, D_{slow}^*, D_{fast}^*, D_{faster}^* + 1$ ), respectively.

For the comparison with the Kennan model with the constraint on the diffusion encoding times, the AICc was first calculated for each combination of  $\langle \bar{V}^2 \rangle$  and  $T_0$  in the ranges defined earlier. Then, the maximum AICc for each combination over the three  $\Delta$  was taken. Finally, the best fit was found by taking the minimum of the maximum AICc-values calculated.

The reported AICc-values have been calculated using only experimental and fitted signals corresponding to b-values  $< 500 \text{ s/mm}^2$  (residual IVIM component of the signal) (hence  $N_b =$

20). The Akaike weight [140],  $w_i(AICc)$ , was then calculated as the probability that model  $i$  is the best model given the data and the set of candidate models [141]:

$$w_i(AICc) = \frac{e^{-\frac{1}{2}\Delta_i(AICc)}}{\sum_{j=1}^{N_j} e^{-\frac{1}{2}\Delta_j(AICc)}} \quad 3.19$$

where

$$\Delta_i(AICc) = [AICc]_i - \min(AICc) \quad 3.20$$

where  $N_j$  is the number of compared models (here  $N_j = 4$ ). A weight  $> 0.90$  indicates that robust inferences can be made using the associated model.

The AICc calculations were done using MATLAB while the other statistical analyses were conducted using the R software [142]. First, the statistical significance of the difference between the AICc of the bi- and mono-exponential models was assessed using a Wilcoxon signed rank test. Then, to assess the existence of a dependence of the diffusion and bi-exponential models parameters on the diffusion time and/or ROI, we used the two-way ANOVA test. If the two-way ANOVA was statistically significant with regards to  $\Delta$ , the Tukey's Honest Significant Difference (HSD) post-hoc test was used, allowing the identification of the diffusion times for which the parameter means were significantly different. When one or both assumptions of the two-way ANOVA were not met, we used a non-parametric version of the two-way ANOVA, the Scheirer-Ray-Hare test. If the p-value of the Scheirer-Ray-Hare test was statistically significant with regards to  $\Delta$ , the Games-Howell post-hoc test was used, allowing the identification of the diffusion times for which the parameter means were significantly different.

### 3.2.2 Model comparison

For one diffusion time ( $\Delta = 24$  ms), examples of the IVIM signal versus the b-value along fitted signals for the bi-, mono-exponential, Kennan and tri-exponential models are given in Figure 3.7. The error bars come from averaging over the directions, repetitions and slices.

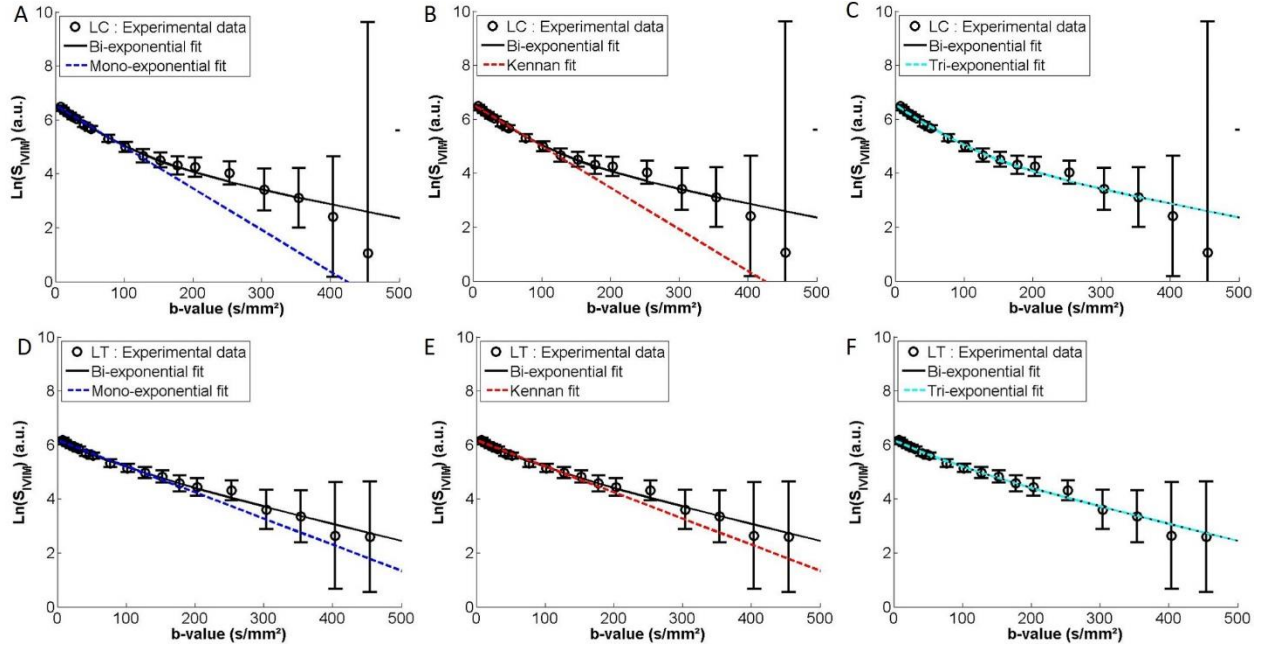


Figure 3.7. IVIM signal resulting from the subtraction of the diffusion component from the total MRI signal versus  $b$ -value for  $\Delta = 24$  ms and the two ROIs: (A-C) left cortex (LC) and (D-F) left thalamus (LT). The black circles represent the experimental data. The black, dark blue, red and light blue lines correspond to the four fitting models, the bi-, mono-exponential, Kennan and tri-exponential models, respectively. The curves were fit to the data with  $b$ -values ranging from 0 to 500  $\text{s/mm}^2$ . Error bars are  $\pm$  SD.

From the first two comparisons (Figure 3.7.A,B,D,E), it is clear that the bi-exponential better describes the IVIM signal than the mono-exponential and Kennan models. As shown in the previous section, the Kennan model is very close to the mono-exponential model except that  $D^*$  has been replaced by  $\frac{\langle \bar{v}^2 \rangle}{3} T_0 \Omega$ . The values found for the parameters in this fit show that we have  $D^* = \frac{\langle \bar{v}^2 \rangle}{3} T_0 \Omega$  for most of the fits. This is why the fitting curves with the mono-exponential and Kennan models look so alike in Figure 3.7.

In Figure 3.7.C and F, the tri- and bi-exponential models are superimposed. Indeed, when looking at the parameter estimates for the tri-exponential model, either one of the fraction is zero or two of the pseudo-diffusion coefficients are equal. These two cases bring back the tri-exponential to a simple bi-exponential model, explaining why the two fits are superimposed.



AICc for the mono-exponential ( $AIC_{CM}$ ), bi-exponential ( $AIC_{CB}$ ), tri-exponential ( $AIC_{CT}$ ) and Kennan ( $AIC_{CK}$ ) models are displayed for all the rat, diffusion and ROIs in Figure 3.8. The black circles highlight data for which  $AIC_{CM} < AIC_{CB}$ .

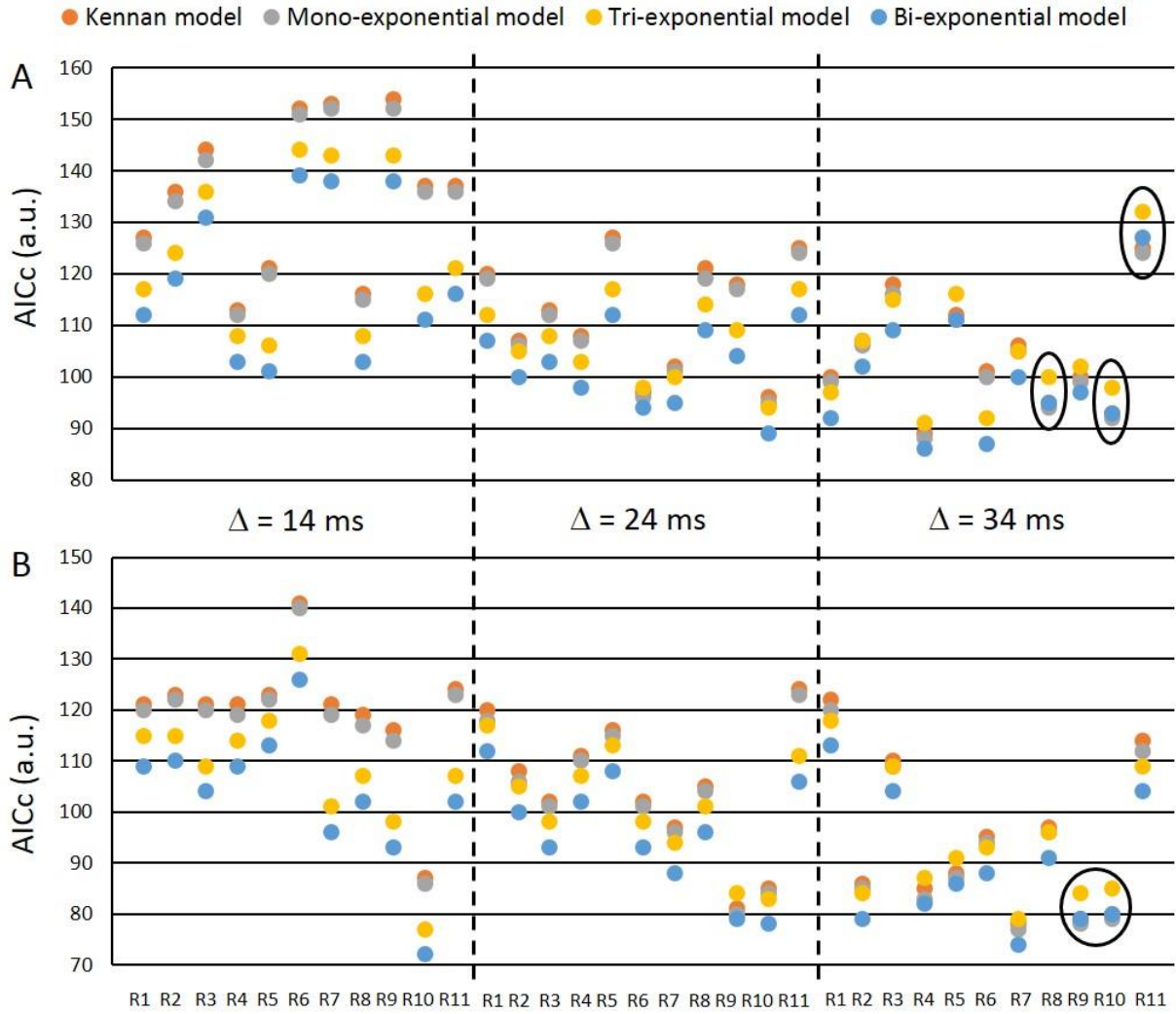


Figure 3.8. AICc for each model and ROI for 11 datasets: (A) LC, (B) LT. The black dotted lines separate the data between the diffusion times. The black circles highlight the cases for which  $AIC_{CM} < AIC_{CB}$ .

For every data set,  $AIC_{CM} < AIC_{CK}$ . This is coherent with the fact that the mono-exponential and Kennan model give the same fits. The Kennan model having more parameters to estimate, the correction factor in the AICc calculation is thus more important giving a higher AICc for the Kennan model compared to the mono-exponential model. We also have  $AIC_{CB} < AIC_{CT}$ . The same

principle applies for the tri- and bi-exponential models as for the Kennan and mono-exponential models.

The Kennan model was also constrained to have the fit parameters kept the same for all three diffusion encoding times. The separated AICc for each diffusion encoding time for the Kennan model are compared to the AICc of the bi-exponential model in Figure 3.9. There is no dataset for which all three AICc of the Kennan model are smaller than the AICcs of the bi-exponential model. Therefore, the Kennan model with this constraint on the diffusion encoding times was not further considered.

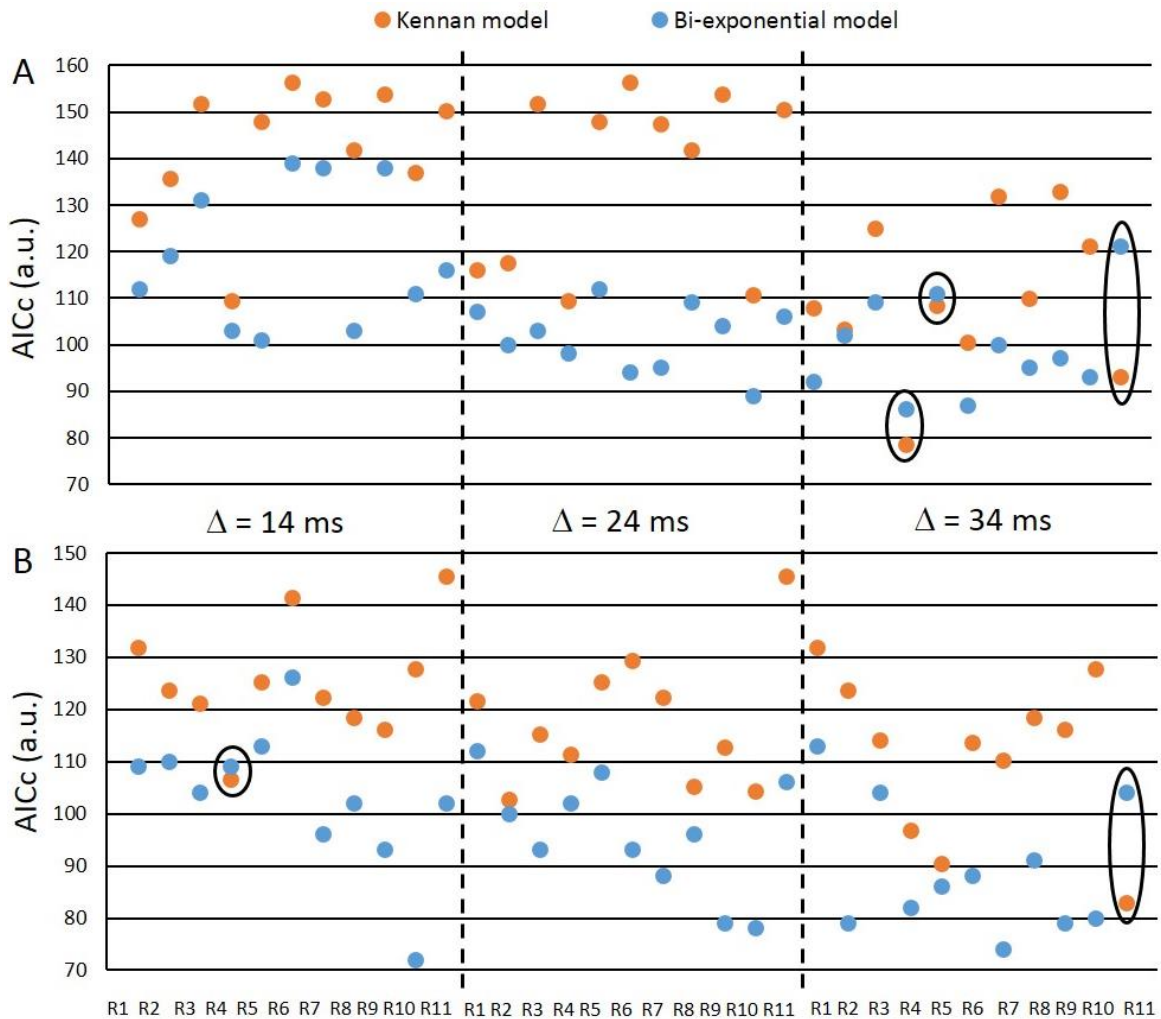


Figure 3.9. AICc for the bi-exponential and Kennan models while constraining the Kennan model to have the same fit parameters for every diffusion time for 11 datasets in the LC (A) and LT (B). The black dotted lines separate the data between the diffusion times. The black circles highlight the cases for which  $AICc_K < AICc_B$ .

Another way to look at the AICc is to calculate the Akaike weights (AW). They are shown in Figure 3.10 for the mono- ( $AW_M$ ), bi- ( $AW_B$ ), tri-exponential ( $AW_T$ ) and Kennan ( $AW_K$ ) models.

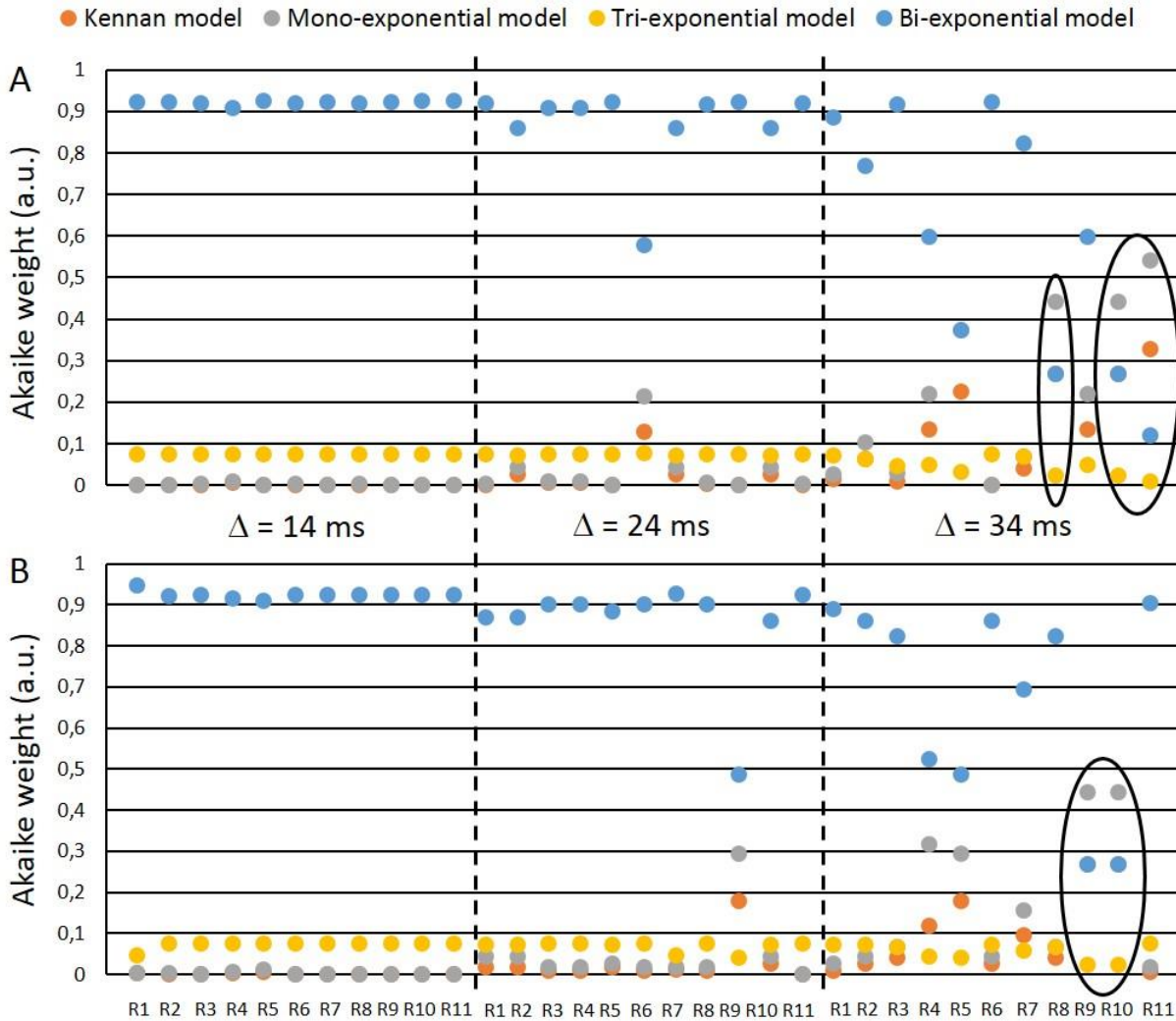


Figure 3.10. Akaike weights for each model and ROI for 11 datasets: (A) LC, (B) LT. The black dotted lines separate the data between the diffusion times. The black circles highlight the cases for which  $AW_B < AW_M$ .

We also observe that  $AW_K < AW_M$  and  $AW_B < AW_T$  for all ROIs and diffusion times. Given this, for the rest of the analysis, we only compare the bi- and mono-exponential models. For 61 out of 66 data points,  $AW_B > AW_M$ . A Wilcoxon signed rank test gives a p-value  $< 0.0001$  when comparing the AICc values, showing a significant difference between the AICc of the two models. This test assesses that the bi-exponential model is better to describe the IVIM data at these diffusion times than the mono-exponential model.

The black circles draw attention to the datasets for which  $AW_B$  is smaller than  $AW_M$ . One can notice that they are all observed for  $\Delta = 34$  ms, suggesting that the bi-exponential model is a better model to describe the IVIM signal than the standard mono-exponential model, especially at short diffusion times, but that the two models converge at longer diffusion times.

Figure 3.11.A displays the box-and-whisker plot for the difference in AICc between the mono- and bi-exponential models against the diffusion time for the two ROIs.

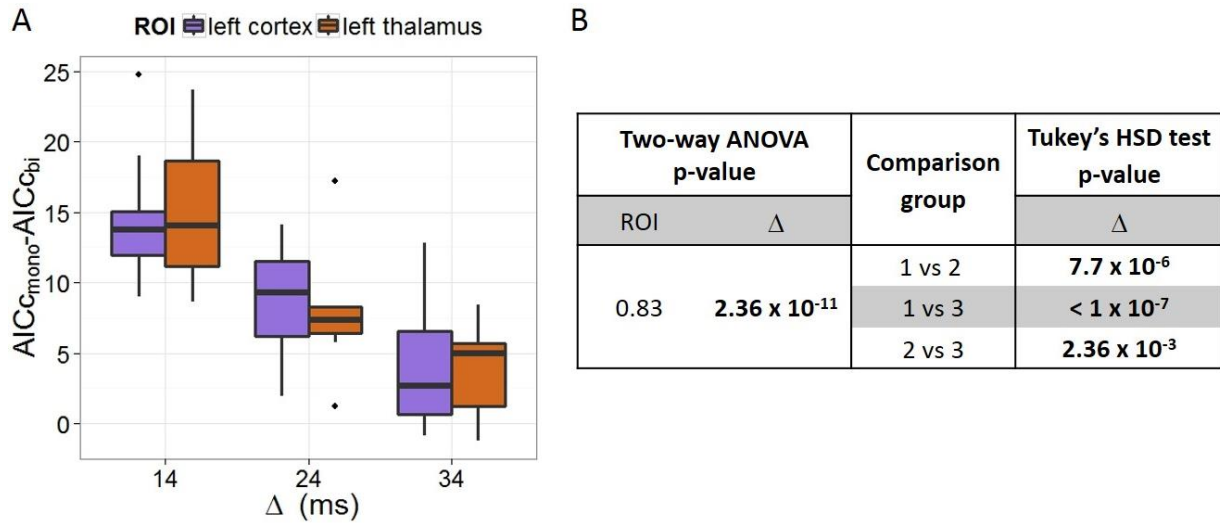


Figure 3.11. (A) Box-and-whisker plot of the difference in AICc between the mono- and bi-exponential models for the two ROIs against the diffusion time. (B) Table with the results of the two-way ANOVA and the Tukey's HSD post-hoc test for the difference in AICc between the mono- and bi-exponential models.

As shown in Figure 3.11.B, the two-way ANOVA test shows that the AICc is not different according to the ROI location, but is significantly different between diffusion times ( $p$ -value  $< 0.0001$ ). The Tukey's HSD post-hoc test indicates that the differences in AICc are significantly different between all diffusion times. Specifically, we see a decrease in the difference in AICc between the two models when the diffusion time increases. This corroborates the conclusion stated in the previous paragraph that the two models converge as the diffusion time increases.

### 3.2.3 Interpretation of the bi-exponential IVIM model

The physical interpretation behind the bi-exponential model is that, instead of reflecting only one vascular pool, i.e. the capillaries, the IVIM signal incorporates signals coming from two

different vascular components: a slow component, characterized by  $f_{slow}$  and  $D_{slow}^*$ , and a faster component, characterized by  $f_{fast}$  and  $D_{fast}^*$ .

Formerly, Neil et al. reported that the IVIM signal obtained by using a modified DW sequence in which the tissue component was directly suppressed can be better fit to a bi-exponential than a mono-exponential function [120]. The authors attributed this bi-exponential behavior to an incomplete saturation of the extravascular spins. In the analysis we performed, extra care was taken to insure that the tissue diffusion component has been completely removed, leaving the vascular component as the only possible contributor to the observed bi-exponential IVIM signal.

The two components could also correspond to two compartments inside one vascular compartment as for example water molecules inside RBCs and in the plasma. When the ratio between the RBC diameter (6-8  $\mu\text{m}$ ) and the vessel diameter is  $\leq 1$ , the mean velocity of the RBCs is about 40 % higher than the velocity of blood flow [57]. When this ratio is higher, this difference is less than 40 %. Even if the ratio is about 40 %, it does not match the difference we observe with our experimental data which is more a 400 % difference than a 40 % difference.

Now that incompletely suppressed diffusion and two compartments inside the vascular compartment have been ruled out, it leaves only the hypothesis of two different vascular components. Henkelman et al. and Duong et al. proposed two components corresponding to the arterial and venous trees to explain the results of their PFC experiments. However, we propose another explanation. Venules have a much shorter  $T_2$  value than arterioles, for example, at 7T,  $T_2$  for venules is 20 ms whereas it is 68 ms for the arterioles.  $f_{IVIM}$  being  $T_2$  dependent, if we estimate  $e^{-\frac{TE}{T_2}}$  for venules and arterioles at 7T for  $TE = 45$  ms, we get 0.11 for veins and 0.52 for arteries. Given this large difference in the  $f_{IVIM} T_2$ -weighting, we hypothesize that the IVIM signal that we see is mostly coming from water molecules inside capillaries and arterioles and less from venules. Therefore, we think that the bi-exponential behavior observed in this study comes from vascular components corresponding to the capillaries for the slow component and to larger vessels mostly from the arterial tree but also from the venous tree for the fast component.

This theory is supported by the variation of the bi-exponential model parameters with the diffusion time.

### 3.2.4 Evolution of the model parameters with the diffusion encoding time

The diffusion encoding time can be defined as  $\Delta + \delta$  [143].  $\delta$  was kept constant while three values were chosen for  $\Delta$ : 14, 30 and 60 ms. Table 3.1 gathers the means  $\pm$  SD and the results of the statistical tests for all parameters of the Kurtosis model,  $ADC_0$  and  $K$ , for diffusion, and the bi-exponential model,  $f_{IVIM}$ ,  $f_{fast}$ ,  $D_{slow}^*$  and  $D_{fast}^*$ , for IVIM.

Parameter	$\Delta = 14$ ms (1) (mean $\pm$ SD)		$\Delta = 24$ ms (2) (mean $\pm$ SD)		$\Delta = 34$ ms (3) (mean $\pm$ SD)		Two-way ANOVA or Scheirer-Ray-Hare test p-value		Comparison group	Tukey's HSD or Games-Howell post-hoc test p-value
	LC	LT	LC	LT	LC	LT	ROI	$\Delta$		
$ADC_0$ ( $10^{-4}$ mm <sup>2</sup> /s)	8.29 $\pm$ 0.43	8.57 $\pm$ 0.36	8.10 $\pm$ 0.24	8.47 $\pm$ 0.34	8.33 $\pm$ 0.48	8.77 $\pm$ 0.27	<b>1.30 <math>\times 10^{-6}</math></b>	<b>0.044</b>	1 vs 2 1 vs 3 2 vs 3	0.27 0.60 <b>0.036</b>
$K$	0.74 $\pm$ 0.02	0.94 $\pm$ 0.11	0.68 $\pm$ 0.05	0.92 $\pm$ 0.12	0.67 $\pm$ 0.05	0.91 $\pm$ 0.13	<b>4.08 <math>\times 10^{-9}</math></b>	0.62	-	-
$f_{IVIM}$ (%)	9.37 $\pm$ 1.84	11.08 $\pm$ 1.61	10.02 $\pm$ 2.05	12.44 $\pm$ 2.44	9.53 $\pm$ 1.85	12.08 $\pm$ 2.21	<b>5.74 <math>\times 10^{-5}</math></b>	0.17	-	-
$f_{fast}$ (%)	77.35 $\pm$ 11.54	78.16 $\pm$ 9.48	81.86 $\pm$ 6.32	70.12 $\pm$ 11.75	55.36 $\pm$ 26.79	48.52 $\pm$ 23.65	0.24	<b>1.61 <math>\times 10^{-5}</math></b>	1 vs 2 1 vs 3 2 vs 3	0.85 <b>3.2 <math>\times 10^{-4}</math></b> <b>7.7 <math>\times 10^{-4}</math></b>
$D_{slow}^*$ ( $10^{-3}$ mm <sup>2</sup> /s)	2.25 $\pm$ 1.58	1.53 $\pm$ 1.03	4.28 $\pm$ 2.25	4.10 $\pm$ 1.62	10.44 $\pm$ 5.91	6.48 $\pm$ 2.83	0.11	<b>6.83 <math>\times 10^{-7}</math></b>	1 vs 2 1 vs 3 2 vs 3	<b>1.4 <math>\times 10^{-4}</math></b> <b>9.7 <math>\times 10^{-6}</math></b> <b>2.2 <math>\times 10^{-3}</math></b>
$D_{fast}^*$ ( $10^{-3}$ mm <sup>2</sup> /s)	23.92 $\pm$ 6.09	21.32 $\pm$ 4.68	19.92 $\pm$ 2.30	16.52 $\pm$ 1.90	23.16 $\pm$ 6.45	18.23 $\pm$ 4.02	0.0039	<b>0.017</b>	1 vs 2 1 vs 3 2 vs 3	<b>0.0054</b> 0.50 0.18

Table 3.1. Diffusion and IVIM parameters for the three  $\Delta$  and two ROIs ( $N_R=11$ ) and results of the statistical tests on the dependence of the parameters against  $\Delta$  and the ROIs. The values reported here for  $D_{slow}^*$  and  $D_{fast}^*$  are obtained by removing the contribution from water diffusion in blood from those obtained by fitting the experimental data. The two-way ANOVA test was used as initial statistical test. When the assumptions of the two-way ANOVA test were not met, i.e. for all parameters except  $ADC_0$  and  $f_{IVIM}$ , the Scheirer-Ray-Hare test was used. The Tukey's HSD and Games-Howell post-hoc tests were used when a significant difference was found for  $\Delta$  with the two-way ANOVA or Scheirer-Ray-Hare tests, respectively; Groups 1, 2, 3 correspond to  $\Delta = 14$  ms, 24 ms and 34 ms, respectively. p-values  $< 0.05$ , highlighted in bold, were considered statistically significant.

Figure 3.12 displays the box-and-whisker plots for  $ADC_0$ ,  $K$ ,  $f_{IVIM}$ ,  $f_{fast}$ ,  $D_{slow}^*$  and  $D_{fast}^*$  against  $\Delta$  for the two ROIs.



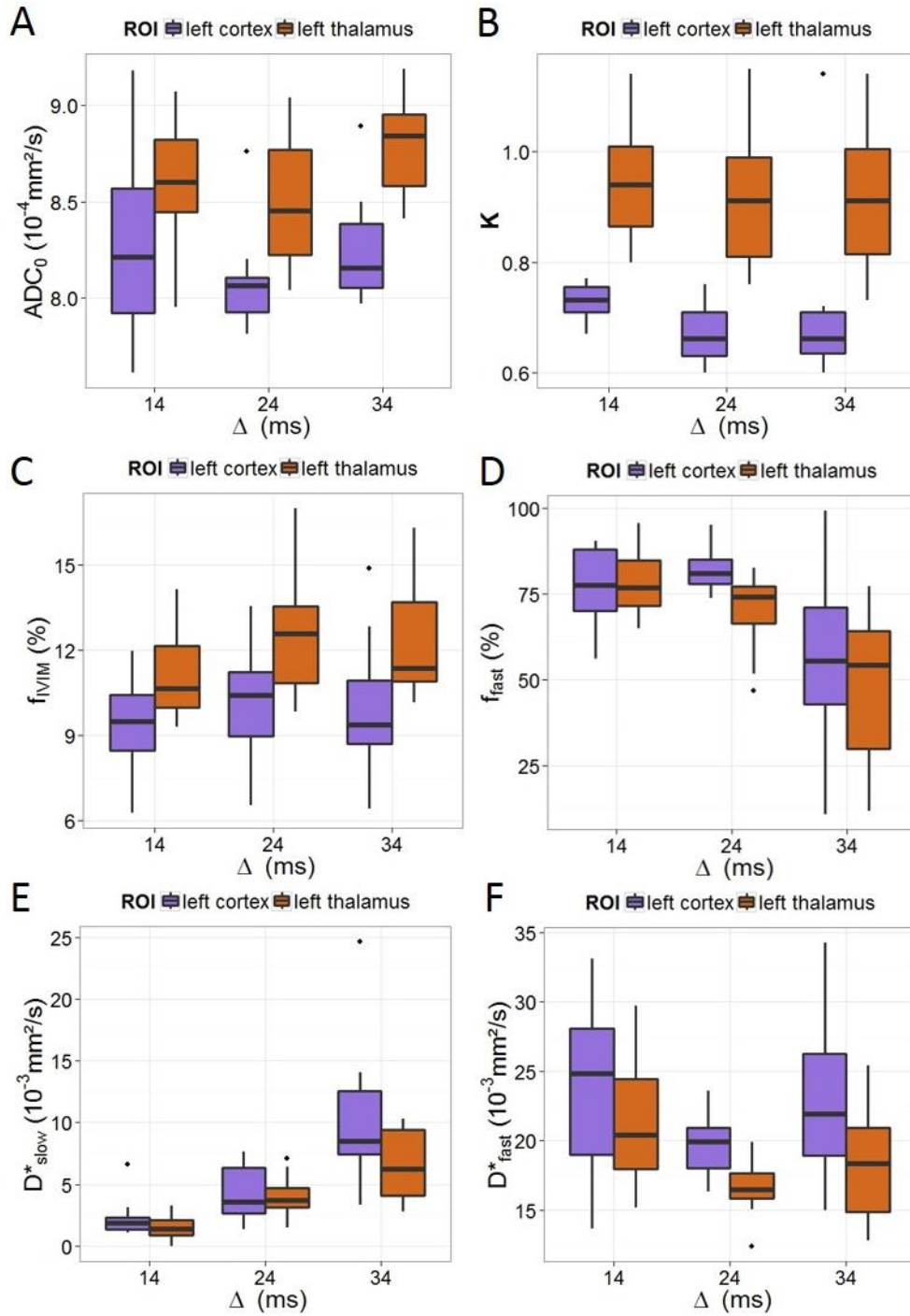


Figure 3.12. Box-and-whisker plots of the parameters of the Kurtosis and bi-exponential models against the diffusion time for the two ROIs: (A)  $ADC_0$ , (B)  $K$ , (C)  $f_{IVIM}$ , (D)  $f_{fast}$ , (E)  $D_{slow}^*$ , and (F)  $D_{fast}^*$ . Error bars represent SD ( $N_R=11$ ).

$ADC_0$  was found significantly different between  $\Delta = 24$  and 34 ms.  $K$  and  $f_{IVIM}$  were not significantly influenced by  $\Delta$  in the range used in this study. The trend for  $ADC_0$  is coherent with

previous results from Pyatigorskaya et al. [144] although no significant difference was found between all  $\Delta$ . We found a significant difference in  $ADC_0$ ,  $K$  and  $f_{IVIM}$  with the two ROIs studied, justified by the different composition and organization of the two structures.  $f_{IVIM}$  is higher than usually stated in the literature, around 5-6 % for healthy brain tissue [145]. This may be explained by the fact that more vessels than just the capillaries are seen at shorter diffusion encoding times. Also, TR being short, inflow effects could be present and artificially increase  $f_{IVIM}$ .

IVIM parameters,  $f_{fast}$  and  $D_{slow}^*$ , were not significantly different between the two ROIs while  $D_{fast}^*$  was found lower in the thalamus. These findings suggest similarities in the vascular organization of the slow pool between the two regions.

We found a  $f_{fast}$ -value smaller at  $\Delta = 34$  ms compared to  $\Delta = 24$  ms, in agreement with a transition to a mono-exponential behavior at the longest diffusion encoding time for  $\Delta = 34$  ms as indicated by the AICc analysis. Combined with the fact that  $f_{IVIM}$  is independent of the diffusion encoding time, this observation also implies that while both pools, slow and fast, are initially present at  $b = 0$  s/mm<sup>2</sup>, the decay of the IVIM signal corresponding to the fast pool is much faster as the diffusion encoding time increases, eventually becoming difficult or even impossible to estimate.

$D_{slow}^*$  significantly increased with the diffusion encoding time, suggesting a sinc (Eq. 3.5) or intermediate regime for the slow pool. Also in agreement with a sinc or intermediate regime,  $D_{fast}^*$  was higher at  $\Delta = 34$  ms than at  $\Delta = 24$  ms, although not statistically significant. Going from  $\Delta = 14$  to 24 ms, we see, however, a significant decrease in  $D_{fast}^*$ . This decrease could result from an additional dephasing effect present only at very short diffusion times. It is reasonable to consider that flow in the slow pool has a plug flow profile. However, if the fast pool corresponds to medium-sized vessels in between capillaries and pial arterioles (diameters ranging between 10 (ref. [146]) and 50  $\mu$ m (ref. [147]) and blood flow velocities ranging between 2 (ref. [55]) and 20 mm/s (ref. [148]) in rats), blood flow is expected to be laminar. In this case, an additional phase dispersion [149],  $D_{LF}$ , should be considered to the overall IVIM signal decay of the fast flow component:



$$F_{IVIM} = e^{-bD_b} \left( f_{slow} e^{-bD_{slow}^*} + f_{fast} e^{-b(D_{fast}^* + D_{LF})} \right) \quad 3.21$$

with  $D_{LF} = \frac{1}{6} \Delta \overline{u^2}$ , where  $\overline{u^2}$  is the variance in the laminar flow velocity field. This contribution is significant only for observation times on the order of the fluid element correlation time, defined as  $\tau_c = \frac{d}{\sqrt{\overline{u^2}}}$ , where  $d$  is the blood vessel diameter. A simple estimation, assuming  $d = 40 \mu\text{m}$  and a mean blood velocity of 5 mm/s (corresponding  $\overline{u^2} = 9 \text{ mm}^2/\text{s}$ ), leads to  $\tau_c \sim 13.33 \text{ ms}$ , implying that  $D_{LF}$  cannot be neglected when the diffusion time is 14 ms. At  $\Delta = 24 \text{ ms}$ , on the other hand,  $D_{LF}$  is negligible and, as a result, we witness a decrease in the measured  $D_{fast}^*$ .

The bi-exponential IVIM model being a new model, no literature with which to compare the present results is available. Additionally, as the two pools are likely to be in an intermediate regime between sinc and exponential regimes for which no equation for  $D^*$  can be found, it is not possible to directly extract morphological information from the experimental data. Similarly, as  $f_{slow}$  and  $D_{slow}^*$  vary with the diffusion time, it is not possible to relate them to values of CBF and CBV.

To further analyze the current datasets and overcome this difficulty, numerical simulations of the IVIM signal microvascular networks were performed to extract structural information from these datasets. The methodology for the numerical simulations is presented in Chapter 4 and the comparison between the simulations and the experimental data is detailed in Chapter 5.

## Chapter 4: Numerical simulations of the IVIM signal

This chapter first introduces the approach chosen in this thesis to obtain further information from the experimental signals. Then, the mathematical modelling and numerical simulations performed are described.

### 4.1 Introduction

In order to extract more information about the structure of the underlying vascular networks from the experimental signals, an approach involving numerical simulations is used. First, methods combining MR data acquisition with numerical simulations to extract this kind of parameters are presented. Then, the approach selected for our purpose is presented.

#### 4.1.1 Method combining perfusion MRI with simulations of the MR signal

The idea to combine simulations of the MR signal with experimental signals to extract parameters of the underlying structure is not new. Notably, we can cite the approach used by Yeh et al. who developed what they called a diffusion microscopist simulator [150]. However, for this introduction, we will focus on a technique which simulates perfusion MR signals.

For DCE MRI, Pannetier et al. have designed a simulation tool to model the MR signal [151]. These complex simulations include modelling of  $T_1$  and  $T_2$  relaxations, magnetic field perturbations induced by susceptibility interfaces (vessels and cells), diffusion of the water protons, blood flow, permeability of the vessel wall to the contrast agent and constrained diffusion of the contrast agent within the voxel. Based on these simulations, Christen et al. developed what they call MR vascular fingerprinting [152]. The principles of their technique is described in Figure 4.1. What they call fingerprint is the ratio of the DCE signal after and before contrast agent injection. They use the simulations to create a database of DCE MR signals to compare them with the fingerprint and extract measures of CBV, mean vessel radius and oxygenation maps of the brain.

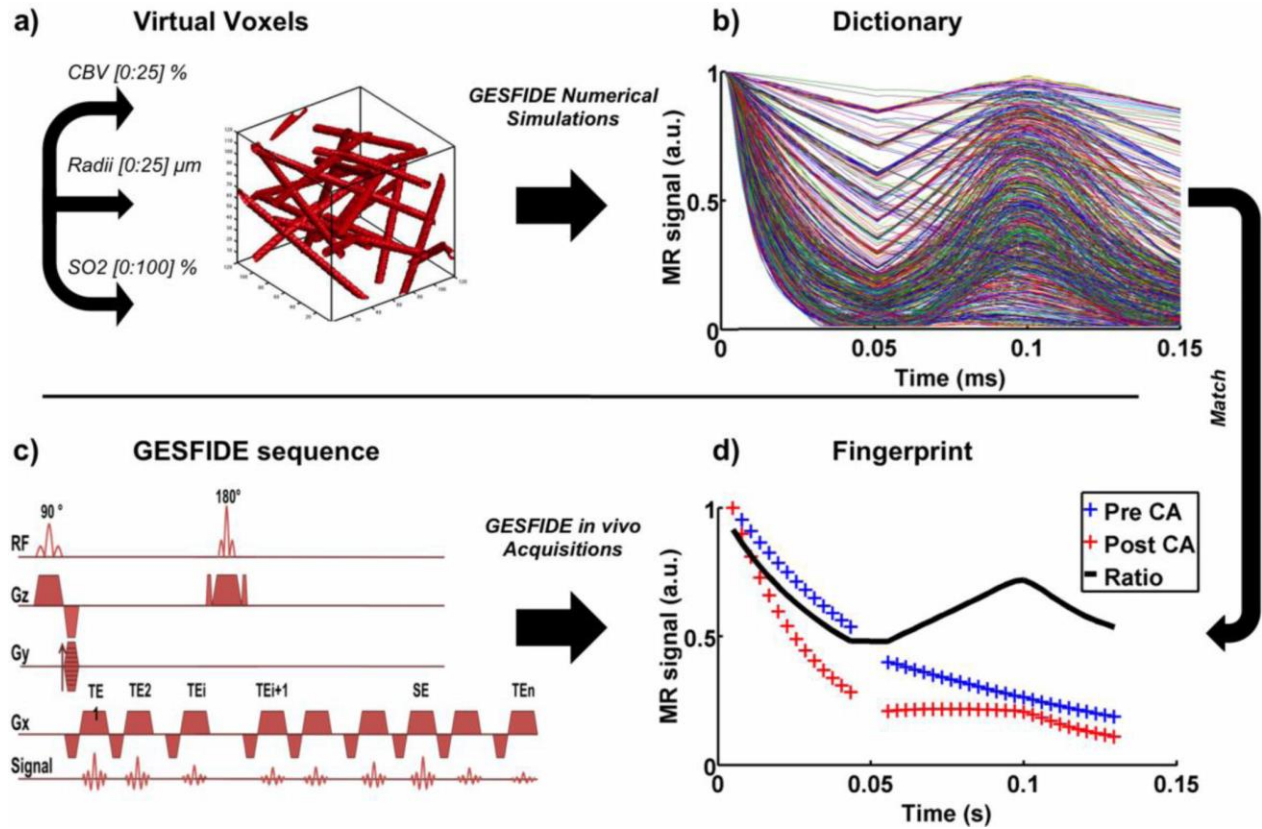


Figure 4.1. Summary of MR vascular fingerprinting. (a) A numerical simulation with different parameters for CBV, vessel size (Radius), and oxygen saturation (SO<sub>2</sub>) is used to create a family of curves (the dictionary) (b). (c,d) The actual fingerprint derived from DCE MRI (the GESFIDE sequence) is then compared to this dictionary to find the underlying parameters that make the best match. From Christen et al [152].

This approach opens the door to many possible applications as it can be adapted to other MRI sequences in order to foresee the results of a study or even predict the outcome of other perfusion techniques. However, no similar approach has yet been applied to IVIM imaging.

#### 4.1.2 Approach chosen for this thesis

The technique presented in the previous subsection was developed after the framework of this thesis had been defined. However, the approach chosen for this thesis is similar to theirs in the sense that we are comparing a dictionary of simulated MR signals to experimental signals in order to extract structural information about the microvascular network. We model the IVIM signal coming from microvascular networks by combining the simulated MR signals due to isochromats following different simplified trajectories with defined structural properties. More details are provided in the next subsections. The simulated MR signals are computed in a

separate step and saved to generate a dictionary. This dictionary is compared to IVIM signals acquired experimentally.

Unlike Christen et al., we compare directly the IVIM signal to the dictionary and not the ratio of signals coming from two different series of acquisitions as no contrast agent is needed to perform IVIM imaging.

## 4.2 Modelling of the IVIM signal in a microvascular network

In this chapter, we describe our chosen method to model the IVIM signal. One possible way to model the IVIM signal is to construct many realizations of (simulated) vascular networks. A realization of such a network defines the geometrical structure of the network and one then can follow the motion of the spins inside the network according to some appropriate laws of motion for blood motion. Even very simplistic rules such as imposed flow velocities in the vessels and fixed probability of flow into branching vessels at junctions would be very computationally intensive because of the large number of vessels in a micro-vascular network. Hence, in this thesis, we directly consider (simplified) spin trajectories, each with a fixed flow velocity, and we do not consider vessel branching effects. The IVIM signal is then defined as the total magnetization of the spins that follow a set of trajectories. A set of trajectory is defined by the probability distributions of vessel (segment) lengths, orientations, and flow velocity. All the spins that follow the same trajectory are called an isochromat.

### 4.2.1 Simplified spin trajectories and isochromat magnetization

Even though parts of vessels can be curved, for simplicity, we define an isochromat trajectory as a series of linked straight segments, connected head to tail, without any branching. Again for simplicity, the segment diameters are not taken into account. A typical trajectory is illustrated in Figure 4.2, along with the relevant notation, defined below.

A trajectory is made up of  $N$  segments. A segment  $k$  is characterized by:

- a starting point  $\overrightarrow{x_{k-1}}$  and an endpoint  $\overrightarrow{x_k}$
- the length of the segment, defined as  $L_k = ||\overrightarrow{x_k} - \overrightarrow{x_{k-1}}||$

- the orientation of the segment, defined as  $\vec{o}_k = \frac{(\vec{x}_k - \vec{x}_{k-1})}{L_k}$ , and in spherical coordinates it is  $\vec{o}_k = \cos(\theta_k) \sin(\varphi_k) \vec{e}_x + \sin(\theta_k) \sin(\varphi_k) \vec{e}_y + \cos(\theta_k) \vec{e}_z$
- a blood velocity vector  $\vec{V}_k = V_k \vec{o}_k$ , where its associated magnitude is  $V_k$
- the time to cross the segment  $T_k = \frac{L_k}{V_k}$
- the cumulative time to get to the end of the segment, defined as  $t_k = \sum_{m=0}^k T_m$

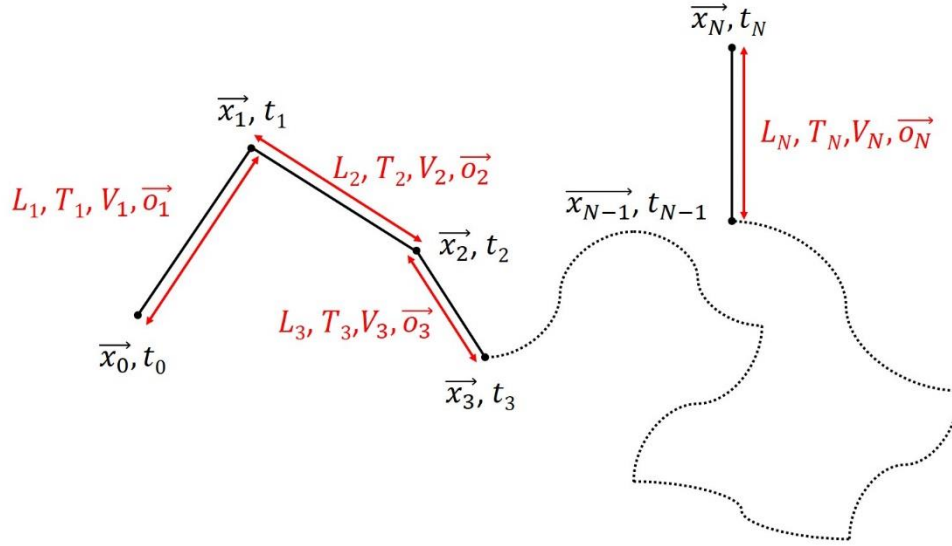


Figure 4.2. Schematic representation of an isochromat trajectory. There are  $N$  segments in this isochromat trajectory.

Considering an isochromat traveling along the trajectory defined above and calling its position vector  $\vec{x}(t)$ , to obtain the resulting magnetization of the isochromat, we solve the Bloch equation in the rotating frame while neglecting relaxation effects, water diffusion in blood and the effects of the imaging gradients. The expression of the phase accumulated by this isochromat from  $t = 0$  to  $TE$  can be written as:

$$\phi(\vec{x}, TE) = \gamma \int_0^{TE} \vec{x}(t) \cdot \vec{G}(t) dt \quad 4.1$$

We specify that  $\vec{G}(t) = f(t)G\vec{e}_G$ , with  $G$  the diffusion gradient amplitude,  $\vec{e}_G$  the diffusion gradient direction and  $\gamma$  is the gyromagnetic ratio. For a PGSE sequence with the time parameters defined as in Figure 4.3,  $f(t)$  is expressed as:

$$f(t) = \begin{cases} 0, & \text{for } 0 \leq t \leq t_{G1} \\ 1, & \text{for } t_{G1} \leq t \leq t_{G1} + \delta \\ 0, & \text{for } t_{G1} + \delta \leq t \leq t_{G2} \\ -1, & \text{for } t_{G2} \leq t \leq t_{G2} + \delta \\ 0, & \text{for } t_{G2} + \delta \leq t \leq TE \end{cases} \quad (\text{to reflect the effect of the } 180^\circ \text{ pulse}) \quad 4.2$$

where  $t_{G1}$  and  $t_{G2}$  correspond to the beginning of the first and second gradient pulses, respectively, and  $\Delta = t_{G2} - t_{G1}$ .

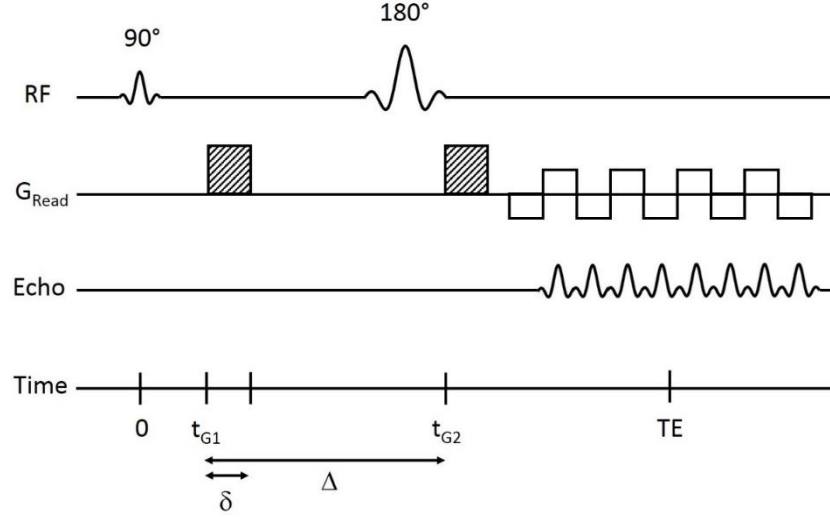


Figure 4.3. Part of the PGSE sequence diagram.  $t_{G1}$  and  $t_{G2}$  correspond to the times at the beginning of the first and second diffusion encoding gradients, respectively.

To compute the magnetization of the isochromat, we will fix the following values which do not limit the generality of our calculations:

- $t_0 = 0$
- $\vec{x}_0 = (0,0,0)$
- $\vec{e}_G = (0,0,1)$
- $TE = t_N$  with  $N$  the number of segments seen by the isochromat during TE.

Now we write out the position vector  $\vec{x}(t)$ :

$$\vec{x}(t) = \vec{x}_m(t) = \sum_{k=1}^{m-1} \vec{V}_k T_k + \vec{v}_m(t - t_{m-1}), \quad t_{m-1} < t < t_m, m \geq 1 \quad 4.3$$

Then, the accumulated phase is:

$$\begin{aligned} \phi &= \gamma \left( \int_0^{t_1} \vec{x}_1(t) \cdot \vec{G}(t) dt + \dots + \int_{t_{N-1}}^{t_N} \left( \sum_{k=1}^{N-1} \vec{V}_k T_k + \vec{V}_N(t - t_{N-1}) \right) \cdot \vec{G}(t) dt \right) \\ &= \gamma \sum_{m=0}^{N-1} \int_{t_m}^{t_{m+1}} \left( \sum_{k=1}^m \vec{V}_k T_k + \vec{V}_{m+1}(t - t_m) \right) \cdot \vec{G}(t) dt \end{aligned} \quad 4.4$$

$$= \gamma \sum_{m=1}^N \int_{t_{m-1}}^{t_m} (\sum_{k=1}^{m-1} \vec{V}_k T_k + \vec{V}_m (t - t_{m-1})) \cdot \vec{G}(t) dt$$

We can rewrite

$$\begin{aligned} \sum_{m=1}^N \int_{t_{m-1}}^{t_m} (\sum_{k=1}^{m-1} \vec{V}_k T_k) \cdot \vec{G}(t) dt &= \int_{t_1}^{t_2} \vec{V}_1 T_1 \cdot \vec{G}(t) dt + \int_{t_2}^{t_3} (\vec{V}_1 T_1 + \vec{V}_2 T_2) \cdot \vec{G}(t) dt \\ &+ \dots + \int_{t_{N-1}}^{t_N} (\vec{V}_1 T_1 + \dots + \vec{V}_{N-1} T_{N-1}) \cdot \vec{G}(t) dt \end{aligned} \quad 4.5$$

$$\begin{aligned} \sum_{m=1}^N \int_{t_{m-1}}^{t_m} (\sum_{k=1}^{m-1} \vec{V}_k T_k) \cdot \vec{G}(t) dt &= \vec{V}_1 T_1 \cdot \left( \int_{t_1}^{t_2} \vec{G}(t) dt + \int_{t_2}^{t_3} \vec{G}(t) dt + \dots + \int_{t_{N-1}}^{t_N} \vec{G}(t) dt \right) \\ &+ \vec{V}_2 T_2 \cdot \left( \int_{t_2}^{t_3} \vec{G}(t) dt + \int_{t_3}^{t_4} \vec{G}(t) dt + \dots + \int_{t_{N-1}}^{t_N} \vec{G}(t) dt \right) \\ &+ \dots + \vec{V}_{N-1} T_{N-1} \cdot \left( \int_{t_{N-1}}^{t_N} \vec{G}(t) dt \right) \end{aligned} \quad 4.6$$

Thus using the fact that

$$\sum_{m=1}^N \int_{t_{m-1}}^{t_m} (\sum_{k=1}^{m-1} \vec{V}_k T_k) \cdot \vec{G}(t) dt = \sum_{m=1}^{N-1} \vec{V}_m T_m \cdot \int_{t_m}^{TE} \vec{G}(t) dt \quad 4.7$$

we obtain

$$\begin{aligned} \phi &= \gamma \left( \sum_{m=1}^N \vec{V}_m \cdot \int_{t_{m-1}}^{t_m} (t - t_{m-1}) \vec{G}(t) dt + \sum_{m=1}^{N-1} \vec{V}_m T_m \cdot \int_{t_m}^{TE} \vec{G}(t) dt \right) \\ &= \gamma \sum_{m=1}^N \left( \vec{V}_m \cdot \int_{t_{m-1}}^{t_m} (t - t_{m-1}) \vec{G}(t) dt + \vec{V}_m T_m \cdot \int_{t_m}^{TE} \vec{G}(t) dt \right) \end{aligned} \quad 4.8$$

As  $\vec{V}_m \cdot \vec{G}(t) = V_m f(t) G \cos(\theta_m)$ , the equation above becomes:

$$\phi = \gamma G \sum_{m=1}^N V_m \cos(\theta_m) \left( \int_{t_{m-1}}^{t_m} (t - t_{m-1}) f(t) dt + T_m \int_{t_m}^{TE} f(t) dt \right) \quad 4.9$$

The magnetization of the isochromat is then  $e^{-i\phi}$ .

#### 4.2.2 Assumption 1: Uniform distribution of segment orientations

To proceed with our calculations, we will make an assumption about the distribution of the orientations of the segments in a trajectory. Namely, we will assume that for each segment  $k$ ,  $\vec{o}_k$  has equal probability of being anywhere on the unit sphere in 3D. Some of the possible trajectories with 3 segments are shown Figure 4.4 where for the simplicity of illustration, we drew 2D circles instead of 3D spheres.

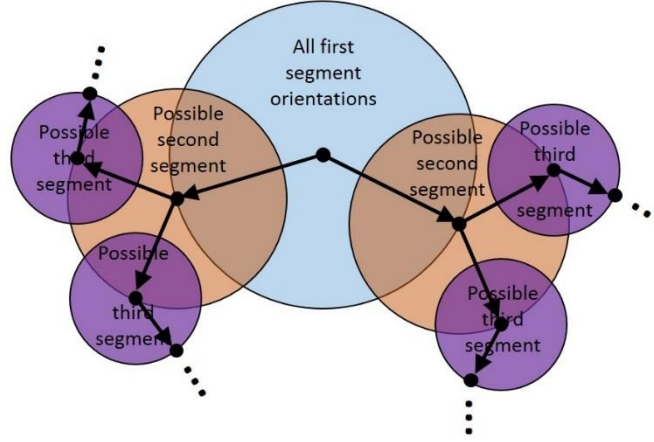


Figure 4.4. Possible trajectories containing three segments. Instead of 3D spheres, we draw 2D circles for the ease of illustration. The possible positions of the endpoint of the first segment lie on the first blue circle. The endpoints of the second and third segments of some trajectories lie on the orange and the violet circles, respectively.

The above assumption is physically reasonable and has the advantage of simplifying the calculations for the isochromat magnetization, as shown below.

By integrating over  $N$  unit spheres in 3D, we obtain the average magnetization for all the  $N$ -segment trajectories:

$$S_{IC} = \frac{1}{4\pi} \int_{\theta_1=0}^{\pi} \int_{\varphi_1=0}^{2\pi} \cdots \frac{1}{4\pi} \int_{\theta_N=0}^{\pi} \int_{\varphi_N=0}^{2\pi} e^{-i\gamma G \sum_{m=1}^N V_m \cos(\theta_m) \left( \int_{t_{m-1}}^{t_m} (t-t_{m-1}) f(t) dt + T_m \int_{t_m}^{T_E} f(t) dt \right)} \sin \theta_1 d\theta_1 d\varphi_1 \cdots \sin \theta_N d\theta_N d\varphi_N \quad 4.10$$

$$S_{IC} = \prod_{m=1}^N \left( \frac{1}{4\pi} \int_{\theta_m=0}^{\pi} \int_{\varphi_m=0}^{2\pi} e^{-i\gamma G V_m \cos(\theta_m) \left( \int_{t_{m-1}}^{t_m} (t-t_{m-1}) f(t) dt + T_m \int_{t_m}^{T_E} f(t) dt \right)} \sin \theta_j d\theta_j d\varphi_j \right) \quad 4.11$$

Thus, under the assumption that each segment of a trajectory has equal probability of being oriented in any direction in a unit sphere, the average magnetization of all the trajectories containing  $N$  segments (characterized by  $V_k$  and  $T_k$ ,  $k = 1 \dots N$ ) is

$$S_{IC} = \prod_{k=1}^N \text{sinc} \left( \gamma V_k G \left( \int_{t_{k-1}}^{t_k} (t - t_{k-1}) f(t) dt + T_k \int_{t_k}^{T_E} f(t) dt \right) \right) \quad 4.12$$

#### 4.2.3 Assumption 2: Gaussian distribution of segment lengths and flow velocity

Eq. 4.12 is an exact expression for the average magnetization of all  $N$ -segments trajectories that are characterized by the segment flow velocities  $V_1 \dots V_N$  and lengths  $L_1 = V_1 \times T_1 \dots L_N = V_N \times T_N$ . In a further attempt to reduce the number of freedom of the modeling of the IVIM signal,



we will assume that the segment velocities and the lengths follow probability distributions. The probability distribution that we will consider for both the lengths and the velocities of the segments is the Gaussian (normal) distribution.

#### 4.2.4 The average magnetization of trajectories in two limit cases

##### 4.2.4.1 Trajectories containing only one segment

For trajectories that contain only one segment of length  $L_1$  and blood velocity  $V_1$ , the end point of the segment has equal probability of being anywhere on a sphere of radius  $L_1$  (for illustration of the analogous 2D situation see Figure 4.5).

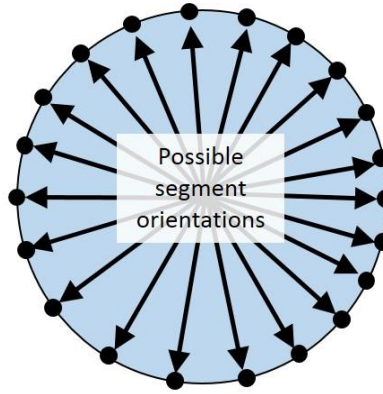


Figure 4.5. Representation of the uniform distribution of segment orientations. For simplicity, the illustration is made in a circle in 2D rather than a sphere in 3D.

The expression for  $\vec{x}(t)$  is

$$\vec{x}(t) = \vec{x}_0 + V_1 t \vec{o}_1, \text{ for } 0 \leq t \leq \delta \text{ and } \Delta \leq t \leq \Delta + \delta \quad 4.13$$

$\phi$  can then be calculated:

$$\begin{aligned} \phi &= \gamma G \left( \int_0^\delta V_1 t \cos(\theta_1) dt - \int_\Delta^{\Delta+\delta} V_1 t \cos(\theta_1) dt \right) \\ &= -\gamma G V_1 \cos(\theta_1) \delta \Delta \end{aligned} \quad 4.14$$

$S_{IC}$ , the resulting magnetization associated with all isochromats travelling at velocity  $V_1$  whose trajectory consists of only one segment is obtained by integrating over all possible segment orientations,  $\vec{o}_1$ :

$$S_{IC} = \frac{1}{4\pi(\Delta V_1)^2} \int_{\theta_1=0}^{\pi} \int_{\varphi_1=0}^{2\pi} e^{-i\gamma G V_1 \cos(\theta_1) \delta \Delta} (\Delta V_1)^2 \sin(\theta_1) d\theta_1 d\varphi_1 \quad 4.15$$

Using the fact that  $\frac{1}{4\pi} \int_{\theta=0}^{\pi} \int_{\varphi=0}^{2\pi} e^{-ix \cos \theta} \sin(\theta) d\theta d\varphi = \text{sinc}(x)$ , we obtain in this case:

$$S_{IC} = \text{sinc}(\gamma G V_1 \delta \Delta) \quad 4.16$$

This result confirms the expression for  $c$  in section 3.1.1.2 for a PGSE sequence:

$$c = \gamma \left[ \int_0^{T_{E/2}} -Gtdt + \int_{T_{E/2}}^{T_E} Gtdt \right] = \gamma G \left( -\frac{\delta^2}{2} + \frac{(\Delta+\delta)^2}{2} - \frac{\Delta^2}{2} \right) = \gamma G \delta \Delta \quad 4.17$$

#### 4.2.4.2 Trajectories containing many segments

As  $N$  becomes large, the isochromats change directions many times and we compute the limit of Eq. 4.12 as the segment length goes to 0, while the blood velocity and diffusion encoding sequence parameters ( $\delta$ ,  $\Delta$ ,  $G$ ) stay fixed. For simplicity, we show the calculation only for trajectories where all segments have the same length  $L$  and the same blood velocity  $V$ . Let  $N_1$  and  $N_2$  be the number of turns during the gradient pulses and between the pulses, respectively, so  $N = 2 \times N_1 + N_2 = \frac{V(\delta+\Delta)}{L}$  with  $N_1 = \frac{N\delta}{\delta+\Delta}$ ,  $N_2 = \frac{N(\Delta-\delta)}{\delta+\Delta}$  and  $T = \frac{L}{V} = \frac{\delta+\Delta}{N}$ . First, we separate  $S_{IC}$  into contributions during the pulses and between the pulses

$$S_{IC} = \prod_{k=1}^{N_1} \text{sinc} \left( \gamma V G T^2 \left( \frac{1}{2} - k \right) \right) \times (\text{sinc}(-\gamma V G T \delta))^{N_2} \quad 4.18$$

$$\times \prod_{k=1}^{N_1} \text{sinc} \left( \gamma V G \left( -\frac{T^2}{2} - (N_1 - k + 1) T^2 \right) \right)$$

We can see that the terms corresponding to the contributions during the two pulses are the same if we substitute  $k$  by  $-(N_1 - k + 1)$ , so we can rewrite the equation above as

$$S_{IC} = \left( \prod_{k=1}^{\frac{N\delta}{\delta+\Delta}} \text{sinc} \left( \gamma V G \left( \frac{1}{2} - k \right) \frac{(\delta+\Delta)^2}{N^2} \right) \right)^2 \times \left( \text{sinc} \left( -\gamma V G \delta \frac{\delta+\Delta}{N} \right) \right)^{\frac{N(\Delta-\delta)}{\delta+\Delta}} \quad 4.19$$

$$= (f_1(N))^2 \times f_2(N)$$

Using the Taylor expansion we have  $\log \left( \text{sinc} \left( \frac{w}{N^m} \right) \right) = -\frac{w^2}{6N^{2m}} + o \left( \frac{1}{N^{2m}} \right)$ , so the asymptotic values for the logarithms of  $f_1$  and  $f_2$  are

$$\log(f_2(N)) = \frac{N(\Delta-\delta)}{\delta+\Delta} \log \left( \text{sinc} \left( -\gamma V G \delta \frac{\delta+\Delta}{N} \right) \right) \approx -\frac{\gamma^2 V^2 G^2 \delta^2 (\Delta-\delta)(\delta+\Delta)}{6N} \quad 4.20$$

and

$$\log(f_1(N)) = \sum_{k=1}^{\frac{N\delta}{\delta+\Delta}} \log \left( \text{sinc} \left( \gamma V G \left( \frac{1}{2} - k \right) \frac{(\delta+\Delta)^2}{N^2} \right) \right) \approx - \frac{\gamma^2 V^2 G^2 (\delta+\Delta)^4}{6N^4} \sum_{k=1}^{\frac{N\delta}{\delta+\Delta}} \left( \frac{1}{2} - k \right)^2 \quad 4.21$$

Using the fact that  $\sum_{k=1}^m \left( \frac{1}{2} - k \right)^2 = \frac{1}{12} m(4m^2 - 1)$ , the term above becomes

$$\log(f_1(N)) \approx - \frac{\gamma^2 V^2 G^2 \delta^3 (\delta+\Delta)}{18N} \quad 4.22$$

In the end,

$$\lim_{N \rightarrow +\infty} S_{IC} = e^{-\frac{\gamma^2 V^2 G^2 \delta^3 (\delta+\Delta)}{9N}} e^{-\frac{\gamma^2 V^2 G^2 \delta^2 (\Delta-\delta)(\Delta+\delta)}{6N}} = e^{-\frac{\gamma^2 V^2 G^2 \delta^2 (\Delta+\delta)(3\Delta-\delta)}{18N}} = e^{-\frac{bLV}{6}} \quad 4.23$$

In other words,  $S_{IC}$  becomes a decaying exponential as  $N$  becomes large or equivalently,  $L$  becomes small.

#### 4.2.5 Influence of the Gaussian distribution of the blood velocity on the total magnetization

Because the experimental IVIM signal never has a sinc shape even when it is unlikely that the spins have changed directions several times during the measured diffusion time, we suspect that the Gaussian distribution of the spin velocity makes the magnetization curve smoother. Here we compute the magnetization of trajectories consisting of only one segment, averaged over a Gaussian distribution of velocities. The magnetization in this case becomes:

$$S_{IC} = \frac{1}{\sqrt{2\pi\sigma_V^2}} \int_{-\infty}^{+\infty} e^{-\frac{(V-V_{mean})^2}{2\sigma_V^2}} \text{sinc}(cV) dV \quad 4.24$$

To compute the slope with respect to the b-value of the above signal,  $D_{dis}^*$ , we replace  $\text{sinc}(cV)$  by its Taylor expansion  $1 - \frac{(cV)^2}{6}$

$$S_{IC} = 1 - \frac{c^2}{6} \frac{1}{\sqrt{2\pi\sigma_V^2}} \int_{-\infty}^{+\infty} v^2 e^{-\frac{(V-V_{mean})^2}{2\sigma_V^2}} dV + O(c^4) \quad 4.25$$

to get

$$S_{IC} = 1 - \frac{c^2}{6} (V_{mean}^2 + \sigma_V^2) + O(c^4) \quad 4.26$$

Given that  $c^2 = b \frac{\Delta^2}{(\Delta-\frac{\delta}{3})}$ , we obtain

$$D_{dis}^* = \frac{(V_{mean}^2 + \sigma_V^2)\Delta^2}{6\left(\Delta - \frac{\delta}{3}\right)} \quad 4.27$$

In Figure 4.6, the simulated signal (Eq. 4.24) is plotted against the b-value for  $\delta = 3$  ms,  $\Delta = 14$  ms and a Gaussian distribution for  $V$  with  $V_{mean} = 3$  mm/s while varying  $\sigma_V$ .

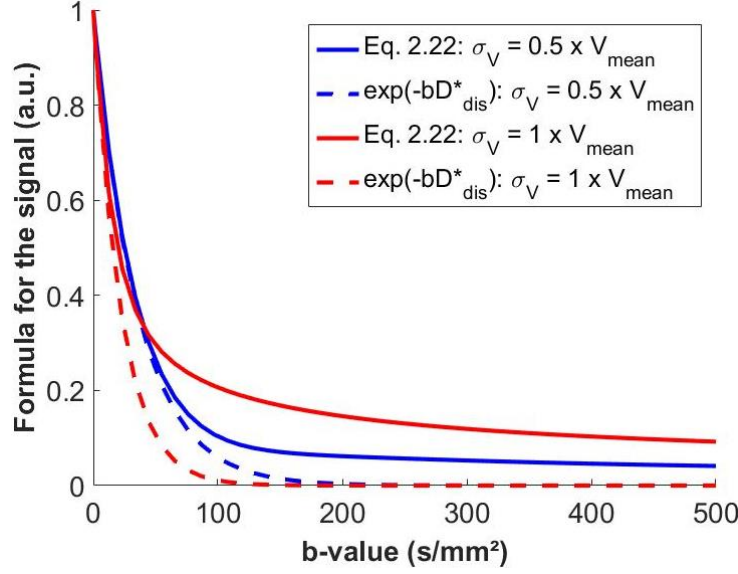


Figure 4.6. Evolution of the signal's shape with  $\delta = 3$  ms,  $\Delta = 14$  ms and a Gaussian distribution for  $V$  with  $V_{mean} = 3$  mm/s and varying  $\sigma_V$ .  $e^{-bD_{dis}^*}$  with  $D_{dis}^*$  given by Eq. 4.27 has been added for both values of  $\sigma_V$ .

As we suspected, for the values of  $\sigma_V$  shown, the sinc behavior disappears and the signal seems smoother. However, the signal is not exponential, as we can see by comparing the simulated signal with  $e^{-bD_{dis}^*}$ , where  $D_{dis}^*$  is given in Eq. 4.27. The decay is much slower than exponential at the higher b-values, with a larger  $\sigma_V$  associated with slower decay. Only at very small b-values can the decay be approximated by an exponential function.

#### 4.2.6 Taking into account starting position of spins in the trajectory

Given that spins can be anywhere in a vessel network at the start of a diffusion MRI experiment, we allow spins to start at various positions on the first segment of any  $N$ -segment trajectory. In essence, if the first segment has length  $L_1$ , then we will suppose the spins can start anywhere on the segment. This is equivalent to supposing that the first segment can be any length  $rL_1$ , where  $0 \leq r \leq 1$ . If  $r = 0$ , the isochromat starts at the beginning of the first segment while if

$r = 1$ , it starts at the beginning of the second segment. Figure 4.7 illustrates a system of two segments with their characteristics.

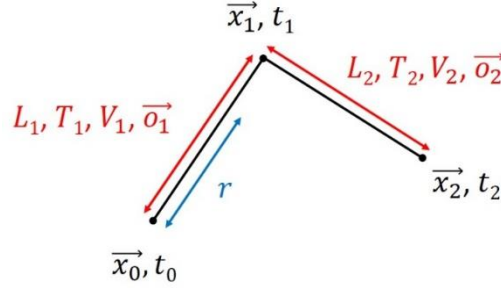


Figure 4.7. Representation of two segments with their characteristics.  $r$  has no unit and indicates where the isochromat is in the first segment at  $t = 0$ , i.e. the isochromat starts at the position  $\vec{x}_0 + rL_1\vec{o}_1$ .

### 4.3 Simulation results and discussion

The simulation protocol described in the previous section was implemented using MATLAB and in this section we describe and discuss our numerical simulation results.

#### 4.3.1 Simulation parameters

The goal of these simulations is to obtain the IVIM MRI signal coming from isochromats following different trajectories, with vessel segment lengths and blood flow velocities that correspond to real microvascular networks. A flowchart of the simulations is shown in Figure 4.8.

The first step is to generate a large number of trajectories, where each trajectory consists of no more than  $N_{SMAX}$  segments, characterized by the segment lengths,  $L_1 \dots L_{N_{SMAX}}$ , and blood flow velocities,  $V_1 \dots V_{N_{SMAX}}$ . Suppose  $N_T$  is the total number of trajectories we want, then we call a pseudorandom number generator to obtain  $N_T \times N_{SMAX}$  values for the segment lengths (with mean  $L_{mean}$  and standard deviation  $\sigma_L$ ) and  $N_T \times N_{SMAX}$  values for the blood flow velocities (with mean value  $V_{mean}$  and standard deviation  $\sigma_V$ ). In order to have reasonable values for  $L$  and  $V$  in accordance with estimates from the literature, segments for which  $L < 5 \mu m$  or  $V < 0.01 mm/s$  and  $V > 20 mm/s$  are removed. The constraint on  $V$  was set to take into account not only the capillaries but also larger segments,  $V = 20 mm/s$  representing the blood velocity in pial arterioles [153].

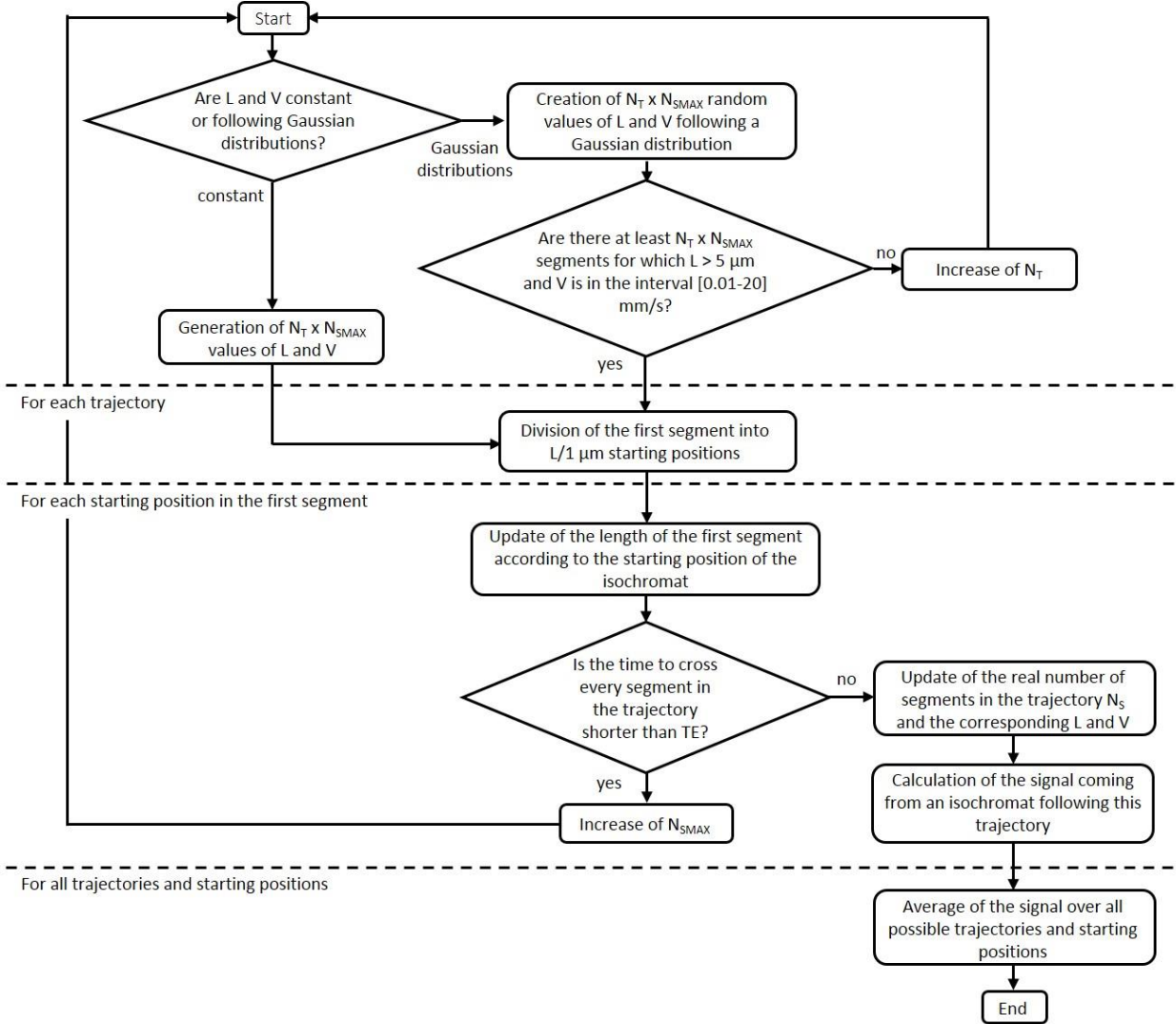


Figure 4.8. Flow diagram of the numerical simulations.  $N_T$  and  $N_S$  are the number of trajectories and segments, respectively, and  $N_{S_{MAX}}$  is the maximum number of segments in the trajectory set at the beginning of the simulations.

We note if  $\sigma_L = 0$  and  $\sigma_V = 0$ , then the signal can be obtained directly from Eq. 4.12. For the range of mean values and standard deviations relevant to IVIM signal modeling, we found that simulation results using 1000 trajectories were within 5 % of simulation results using 10 000 trajectories, hence from now on, so we set  $N_T = 1000$  (Figure 4.9).

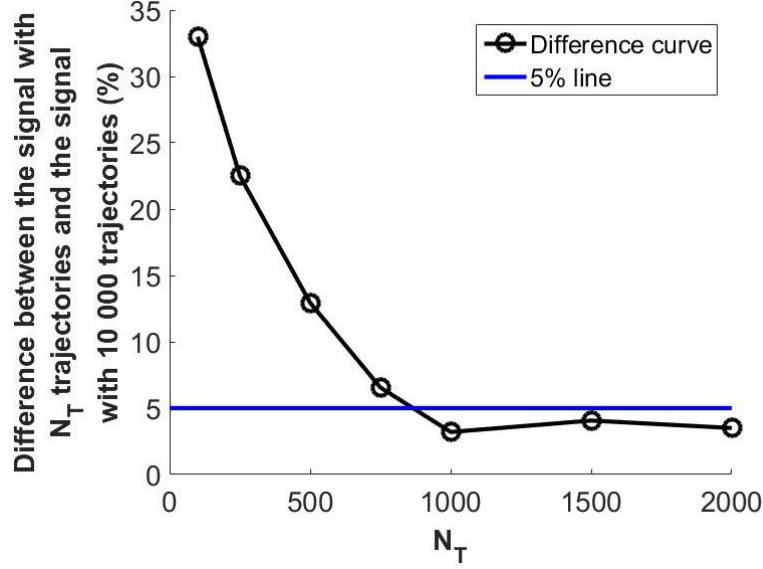


Figure 4.9. Plot of the difference between the simulated signal for  $N_T$  trajectories and the simulated signal for 10 000 trajectories. The solid black and blue represent the difference curve and the 5 % line, respectively. The simulations were performed with Gaussian distributions of  $L$  and  $V$  with  $L_{mean} = 61 \mu\text{m}$ ,  $\sigma_L = 0.5 \times L_{mean}$ ,  $V_{mean} = 2.2 \text{ mm/s}$ ,  $\sigma_V = 0.5 \times V_{mean}$ , 50 b-values linearly spaced between 2 and 500  $\text{s/mm}^2$ ,  $\delta = 3 \text{ ms}$  and  $\Delta = 14 \text{ ms}$ .

To vary the starting position of spins in the first segment, the starting positions were placed with  $1 \mu\text{m}$  spacing on the first segment. If the time to cross every segment in the trajectory is shorter than  $TE$ , then the number of segments in the trajectory will be increased by regenerating a set of lengths and velocities using a larger value of  $N_{SMAX}$ . Otherwise, the actual number of segments seen by the isochromat,  $N_S$ , is computed. The MRI signal coming from this trajectory containing  $N_S$  segments, with  $L_1 \dots L_{N_S}$  and  $V_1 \dots V_{N_S}$ , is calculated using Eq. 4.12. Finally, the total MRI signal is averaged over  $N_T$  trajectories.

The formula Eq. 4.12 was obtained by supposing that segment orientations are uniformly distributed on the unit sphere in 3D. This hypothesis may not be completely valid when there are relatively few vessels in a voxel. We note here that, in the case of trajectories consisting only one segment, having only 24 segments uniformly distributed on the unit sphere results in a magnetization that is within 10 % of the formula given in Eq. 4.12. In Figure 4.10 we show simulations where  $L_{mean} = 61 \mu\text{m}$ ,  $\sigma_L = 0$ , and  $V_{mean} = 2.2 \text{ mm/s}$ ,  $\sigma_V = 0$ , for 20 b-values linearly spaced between 0 and 500  $\text{s/mm}^2$ ,  $\delta = 3 \text{ ms}$  and  $\Delta = 14 \text{ ms}$ . The difference between the formula of Eq. 4.12 and the simulations is shown for several choices of  $N_o$ , the number of orientations.

The simulation results were obtained by generating large number realizations of a set of  $N_o$  orientations uniformly distributed in the unit sphere in 3D.

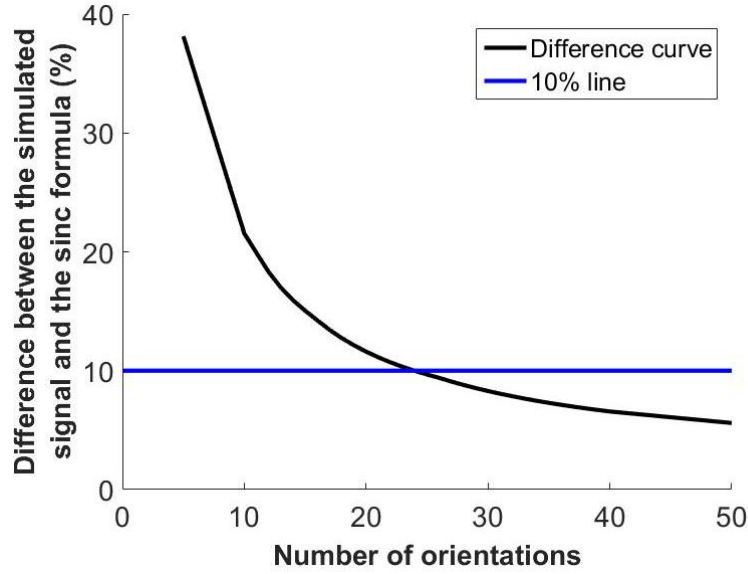


Figure 4.10. Plot of the difference between the simulated signal and the formula in Eq. 4.12 against the number of segment orientations. The solid black and blue lines represent the difference curve and the 10 % line, respectively. The difference was calculated for one segment with  $L = 61 \mu\text{m}$ ,  $V = 2.2 \text{ mm/s}$ ,  $b = [0-500] \text{ s/mm}^2$ ,  $\delta = 3 \text{ ms}$  and  $\Delta = 14 \text{ ms}$ . The two curves intersect at  $N_o = 24$ .

We note again that the choice to integrate the segment orientations over the unit sphere allows us to perform an analytical integration on the unit sphere and removes the need to sample the segment orientations in the numerical simulations, thus saving computing time.

#### 4.3.2 The transition from sinc to exponential regime

We have shown previously two limiting cases of Eq. 4.12:

- A. Averaging all trajectories with flow velocity  $V$  that consist of only one segment whose orientations are uniformly distributed in the unit sphere in 3D, the magnetization is a sinc function,
- B. Averaging all trajectories with flow velocity  $V$  that consist of  $N$  segments each of whose orientations are uniformly distributed in the unit sphere in 3D, the magnetization approaches an exponential function as  $N$  goes to infinity.



The present subsection aims to characterize this transition and define the minimum  $N$  larger than which the simulated signal can be considered exponential. To simplify the discussion, we consider for now  $\sigma_L = 0$  and  $\sigma_V = 0$  and that  $\delta \ll \Delta$ . In this case, we have

$$S_{IC} = \left( \text{sinc} \left( \frac{V\sqrt{b\Delta}}{N} \right) \right)^N \quad 4.28$$

where  $N = \frac{\Delta V}{L}$  is the number of segments seen by an isochromat during  $\Delta$ .  $N$  needs to be at least 1 in the formula above. When  $N \leq 1$ ,  $S_{IC}$  is given by Eq. 4.16 and can be rewritten with respect to the b-value,

$$S_{IC} = \text{sinc}(V\sqrt{b\Delta}) \quad 4.29$$

As  $N$  goes to infinity, the limit of  $S_{IC}$  is the exponential function

$$S_{IC} = e^{-\frac{bV^2\Delta}{6N}} \Rightarrow e^{-\frac{bVL}{6}} \quad 4.30$$

Figure 4.11 illustrates the transition to the exponential regime. This transition occurs for  $N = 5$  segments for the example shown.

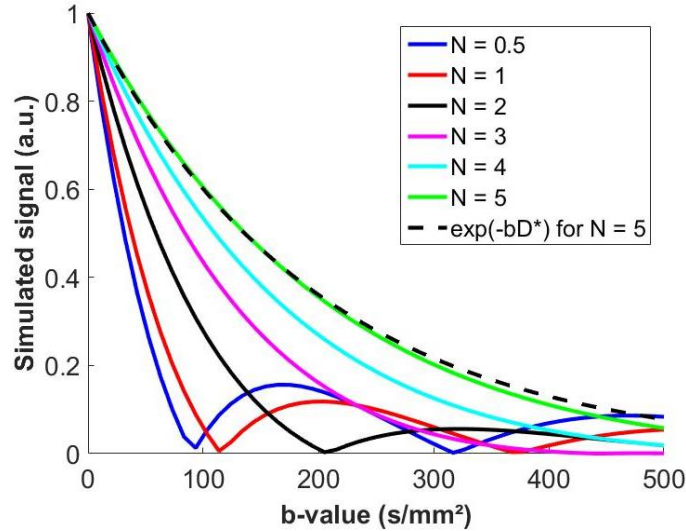


Figure 4.11. Evolution of the simulated signal with  $N = \frac{V(\Delta+\delta)}{L}$ , the number of segments seen by an isochromat during  $\Delta+\delta$ .  $N$  is varied by changing the segment length  $L$  and keeping the blood velocity  $V$  at 3 mm/s,  $\delta = 3$  ms and  $\Delta = 14$  ms. For  $N = 5$ ,  $e^{-bD^*}$  with  $D^* = \frac{LV}{6}$  has been added to show that the simulated signal becomes exponential for this  $N$ -value (difference between the two curves  $< 3\%$ ).

The evolution of the shape of the simulated signal with the segment length  $L$  is shown in Figure 4.12.A. Each simulated signal is calculated for a trajectory with one segment with the same  $V = 3$  mm/s but varying  $L$  in the range  $[10-150]$   $\mu\text{m}$ . The simulated signal has the shape of a sinc at long segment lengths which correspond to small  $N$ -values. For short segment lengths and thus big  $N$ -values, the shape of the simulated signal is smoothed and approaches an exponential shape.

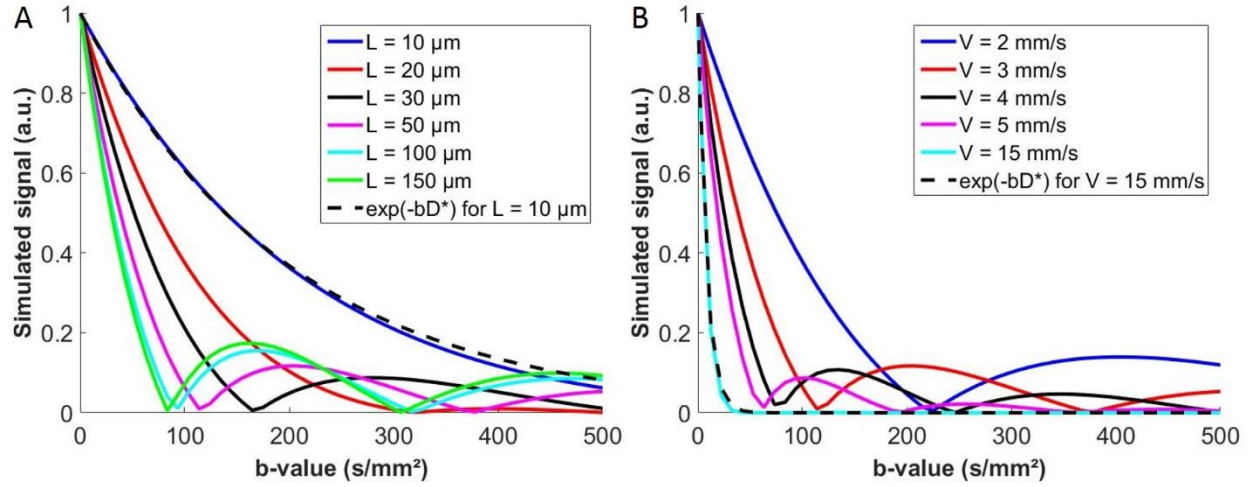


Figure 4.12. (A) Evolution of the shape of the simulated signal with increasing  $L$  with constant  $V = 3$  mm/s,  $\delta = 3$  ms and  $\Delta = 14$  ms.  $N = 5.1, 2.55, 1.7, 1.02, 0.51$  and  $0.34$  for each value of  $L$ .  $e^{-bD^*}$  with  $D^* = \frac{LV}{6}$  has been added for  $L = 10 \mu\text{m}$  as a black dotted line. (B) Evolution of the shape of the simulated signal with increasing  $V$  with constant  $L = 50 \mu\text{m}$ ,  $\delta = 3$  ms and  $\Delta = 14$  ms.  $N = 0.68, 1.02, 1.36, 1.7$  and  $5.1$  for each value of  $V$ .  $e^{-bD^*}$  with  $D^* = \frac{LV}{6}$  has been added for  $V = 15$  mm/s as a black dotted line.

For the blood velocity,  $V$ , the effect is the opposite. Indeed, as shown in Figure 4.12.B, for a constant  $L = 50 \mu\text{m}$ ,  $\delta = 3$  ms,  $\Delta = 14$  ms and increasing  $V$ , the signal has the shape of a sinc at low  $V$  and the shape of an exponential at high  $V$ . This pattern is also coherent with the evolution of the signal's shape with  $N$ .

#### 4.3.3 Influence of imposing a Gaussian distribution for the segment length and the blood velocity

The effect of having a Gaussian distribution for  $L$  and  $V$  on the simulated signal's shape is investigated in this subsection.

#### 4.3.3.1 Gaussian distribution for the segment length

For a constant  $V = 3$  mm/s, a Gaussian distribution is set for  $L$  with a mean segment length,  $L_{mean}$ , and standard deviation,  $\sigma_L$ . First, the effect of changing  $L_{mean}$  for a constant  $\sigma_L = 0.5 \times L_{mean}$  is shown in Figure 4.14.A.

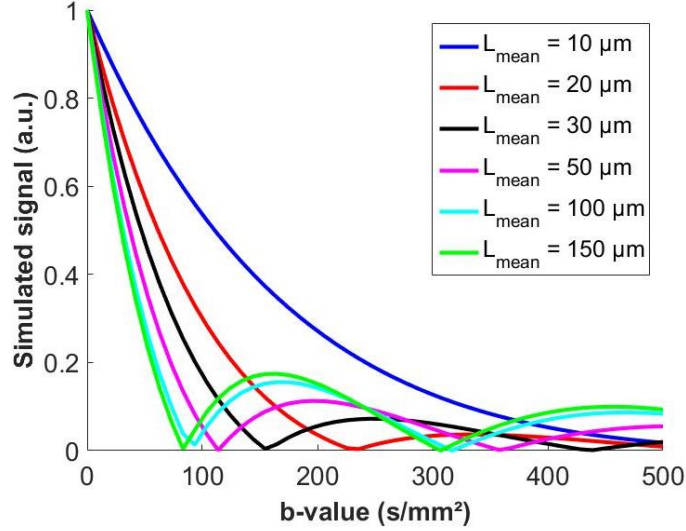


Figure 4.13 Evolution of the signal's shape with a constant  $V = 3$  mm/s,  $\delta = 3$  ms,  $\Delta = 14$  ms and a Gaussian distribution for  $L$  with  $\sigma_L = 0.5 \times L_{mean}$  and varying  $L_{mean}$ .  $N = 5.1, 2.55, 1.7, 1.02, 0.51$  and  $0.34$  for each value of  $L$ .

For  $N \leq 1$ , Figure 4.13 is not very different from Figure 4.12.A although a Gaussian distribution for  $L$  has been added. However, when  $N > 1$ , the curves are slightly different. This is confirmed by looking at Figure 4.14.A and B where  $\sigma_L$  changes while  $L_{mean}$  is kept constant at 100 and 20  $\mu\text{m}$ , respectively.

The effect of changing  $\sigma_L$  from  $[0-1] \times L_{mean}$  is very small for  $N \leq 1$ . Indeed, if a distribution for  $L$  is applied to the signal attenuation, as  $S_{IC}$  does not depend on  $L$  (Eq. 4.29), the distribution for  $L$  has no effect on the signal attenuation. However, we also integrate  $S_{IC}$  on the starting positions of the isochromats in the first segment. Adding a distribution for  $L$  changes the number of isochromats staying in the first segment during the experiment and the number of those that will be in a second segment at  $t = \Delta + \delta$ . This particularity of the simulations explains the small variation observed in Figure 4.14.A.

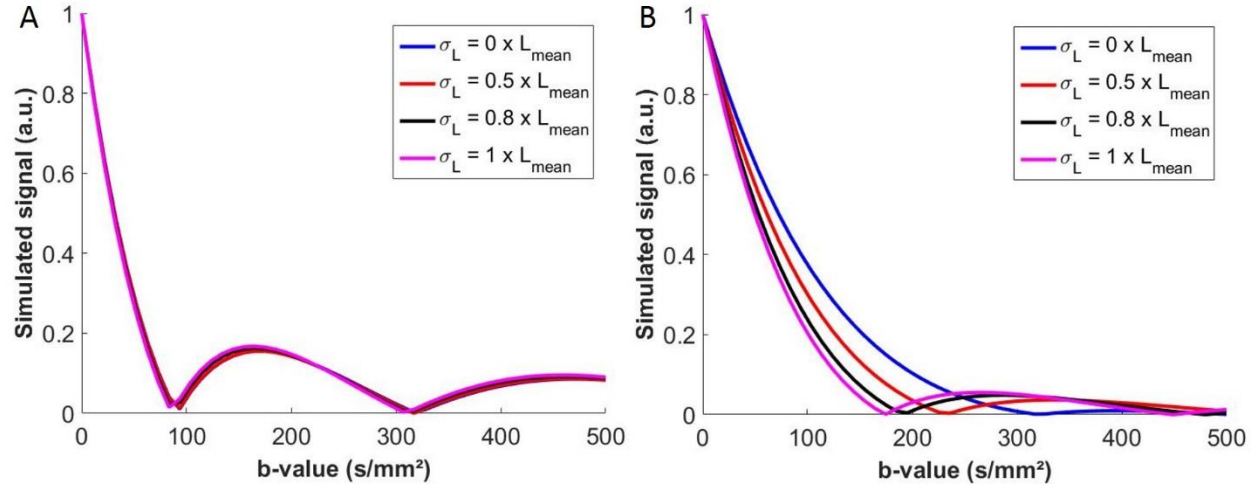


Figure 4.14. (A-B) Evolution of the signal's shape with a constant  $V = 3$  mm/s,  $\delta = 3$  ms,  $\Delta = 14$  ms and a Gaussian distribution for  $L$  varying  $\sigma_L$  with  $L_{mean} = 100$   $\mu\text{m}$  ( $N = 0.51$ ) and  $20$   $\mu\text{m}$  ( $N = 2.55$ ), respectively.

For  $N > 1$ , a larger difference is observed when varying  $\sigma_L$  from  $[0-1] \times L_{mean}$ . As such, the equation for  $S_{IC}$  is Eq. 4.28 in which  $L$  is present through  $N$ . Imposing a Gaussian distribution for  $L$  thus has a larger impact on the signal's shape. Taking into account the starting positions of the isochromats also adds to this effect.

#### 4.3.3.2 Gaussian distribution for the blood velocity

This time,  $L$  is kept constant and  $V$  is varied according to a Gaussian distribution with mean blood velocity,  $V_{mean}$ , and standard deviation,  $\sigma_V$ . Figure 4.15.A shows the evolution of the simulated signal while increasing  $V_{mean}$  with a constant  $\sigma_V = 0.5 \times V_{mean}$  and  $L = 50$   $\mu\text{m}$  for  $\delta = 3$  ms and  $\Delta = 14$  ms. The signal decays faster with increasing  $V_{mean}$ . Comparing Figure 4.15.A with Figure 4.12.B, we observe that the signal looks smoother for almost every  $V_{mean}$ -value when a Gaussian distribution is applied for  $V$ .

This is further confirmed by looking at Figure 4.15.B for which  $V_{mean}$  is kept constant at the value of  $3$  mm/s whereas  $\sigma_V$  is varied in the range  $[0-1] \times V_{mean}$ . For  $\sigma_V = 0$ , the signal is in the sinc regime. When  $\sigma_V$  increases, the signal is smoothed and the sinc behavior is not visible anymore.

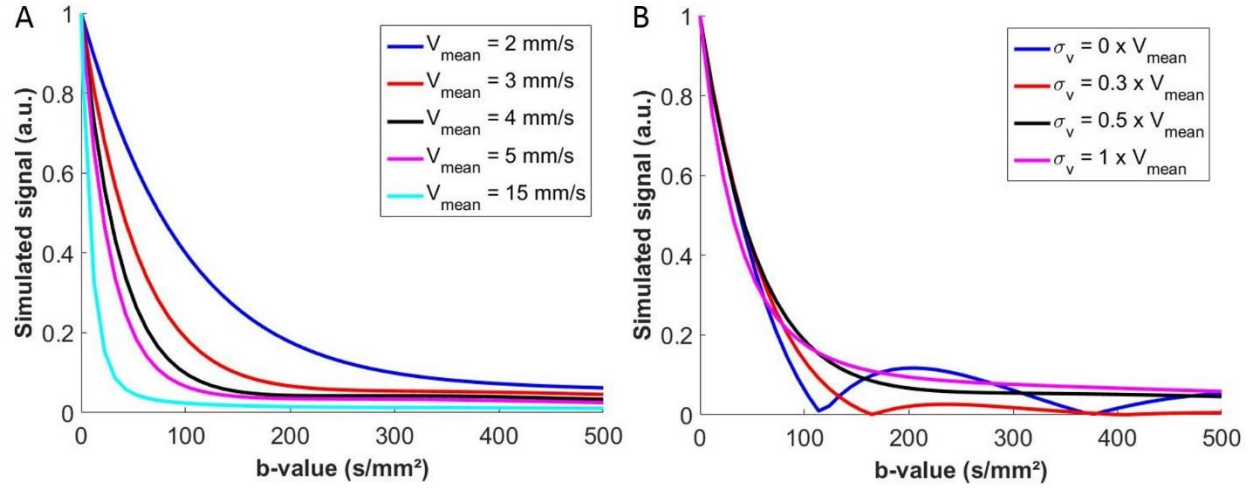


Figure 4.15. (A) Evolution of the signal's shape with a constant  $L = 50 \mu\text{m}$ ,  $\delta = 3 \text{ ms}$ ,  $\Delta = 14 \text{ ms}$  and a Gaussian distribution for  $V$  with  $\sigma_V = 0.5 \times V_{\text{mean}}$  and varying  $V_{\text{mean}}$ .  $N = 0.68, 1.02, 1.36, 1.7$  and  $5.1$  for each value of  $V$ . (B) Evolution of the signal's shape with a constant  $L = 50 \mu\text{m}$ ,  $\delta = 3 \text{ ms}$ ,  $\Delta = 14 \text{ ms}$  and a Gaussian distribution for  $V$  with  $V_{\text{mean}} = 3 \text{ mm/s}$  and varying  $\sigma_V$ .

Applying a Gaussian distribution to the segment length and most importantly to the blood velocity thus allows to get a closer match with the experimental data. The Gaussian distribution of the blood velocity has a larger impact on the signal's shape as  $V$  is present in the formula for  $S_{IC}$  at both  $N \leq 1$  and  $N > 1$ . As the generation of a dictionary of simulated signals is time consuming, we decided to give priority to the generation of numerous values of  $L_{\text{mean}}$  and  $V_{\text{mean}}$  while keeping  $\sigma_L$  and  $\sigma_V$  constant. To be coherent with the underlying vasculature, we did not set  $\sigma_L = \sigma_V = 0$  but  $\sigma_L = 0.5 \times L_{\text{mean}}$  and  $\sigma_V = 0.5 \times V_{\text{mean}}$ .

#### 4.3.4 Influence of the diffusion encoding time

The shape of the simulated signal is also influenced by another parameter in the definition of  $N$ :  $\Delta$ , the diffusion encoding time. Figure 4.16 illustrates the evolution of the simulated signal's shape with increasing  $\Delta$  in the range  $[3-100] \text{ ms}$  for Gaussian distributions of  $L$  and  $V$  with  $L_{\text{mean}} = 50 \mu\text{m}$ ,  $\sigma_L = 0.5 \times L_{\text{mean}}$ ,  $V_{\text{mean}} = 3 \text{ mm/s}$  and  $\sigma_V = 0.5 \times V_{\text{mean}}$ . When  $\Delta$  increases, the simulated signal decays faster.

For each diffusion time, the simulated signal can be fit to the mono-exponential model,  $e^{-bD^*}$ , and  $D^*$  called  $D_{\text{sim}}^*$  for the simulated signals plotted against the diffusion time in Figure 4.16.B.

This plot confirms the faster decay of the simulated signals by a steep increase of  $D^*$  as a function of  $\Delta$  for short  $\Delta$ -values.

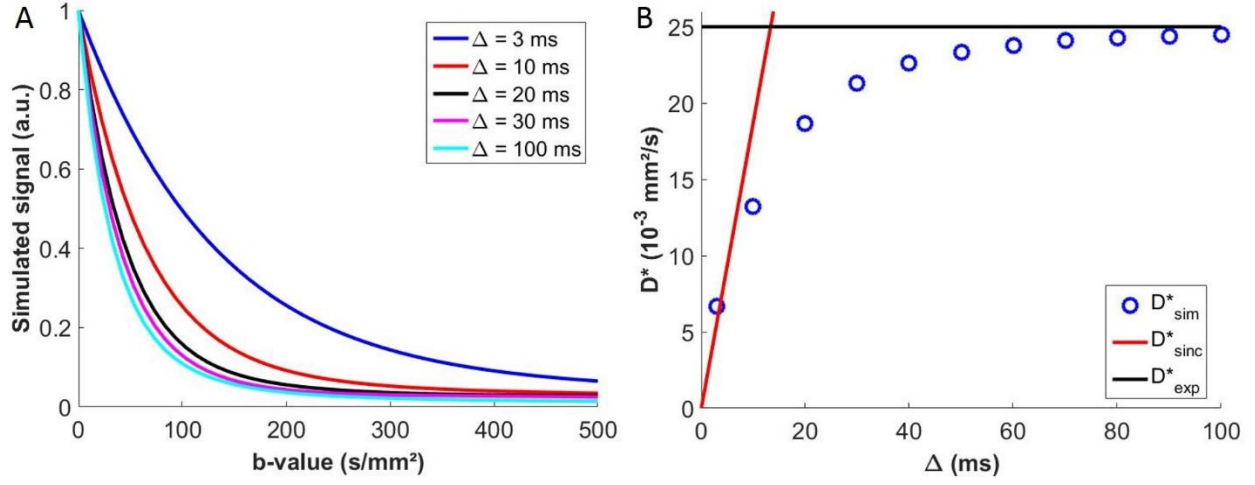


Figure 4.16. (A) Plot of the simulated signal for Gaussian distributions of  $L$  and  $V$  with  $L_{mean} = 50 \mu\text{m}$ ,  $\sigma_L = 0.5 \times L_{mean}$ ,  $V_{mean} = 3 \text{ mm/s}$  and  $\sigma_V = 0.5 \times V_{mean}$  while varying  $\Delta$ . (B) Plot of the obtained  $D^*$  value from fitting with an exponential model the simulated curves in Figure 4.16.A ( $D^*_{sim}$ ) against  $\Delta$ . The red and black lines correspond to  $D^*_{sinc} = \frac{(V_{mean}^2 + \sigma_V^2)\Delta}{6}$  and  $D^*_{exp} = \frac{L_{mean}V_{mean}}{6}$ , respectively.

At short diffusion times, we are in the sinc regime and the formula for  $D^*$  in this regime can be applied,  $D^*_{sinc} = \frac{(V_{mean}^2 + \sigma_V^2)\Delta}{6}$ . The equation for  $D^*_{sinc}$  has been corrected for a Gaussian distribution of  $V$ . Indeed, in Figure 4.16.B, for short  $\Delta$ ,  $D^*$  increases with the slope  $\frac{(V_{mean}^2 + \sigma_V^2)\Delta}{6}$ . At long diffusion times,  $D^*$  reaches a plateau which corresponds to the exponential regime. The maximum value of  $D^*$  in this regime is given by the exponential formula for  $D^*$ , i.e.  $D^*_{exp} = \frac{L_{mean}V_{mean}}{6}$ .

#### 4.3.5 The two pool hypothesis

It is possible to associate to each of the two pools defined in the previous chapter a simulated signal,  $F_{IVIM/Sim/slow \text{ or } fast}$ , characterized by different values of  $L_{mean}$  and  $V_{mean}$ . Using the simulations, we can predict the evolution of the signals of the two pools with  $\Delta$ . As seen in a previous subsection, the mean blood velocity is the most important parameter that determines the shape of the simulated signal. Thus, blood flow velocities characterizing small and larger



segments were chosen:  $V_{slow} = 1$  mm/s and  $V_{fast} = 4$  mm/s. The mean segment lengths were set to  $L_{slow} = 40$   $\mu$ m and  $L_{fast} = 50$   $\mu$ m. Figure 4.17.A-C shows the simulated signals for the two pools for different diffusion times: 3, 30 and 90 ms.

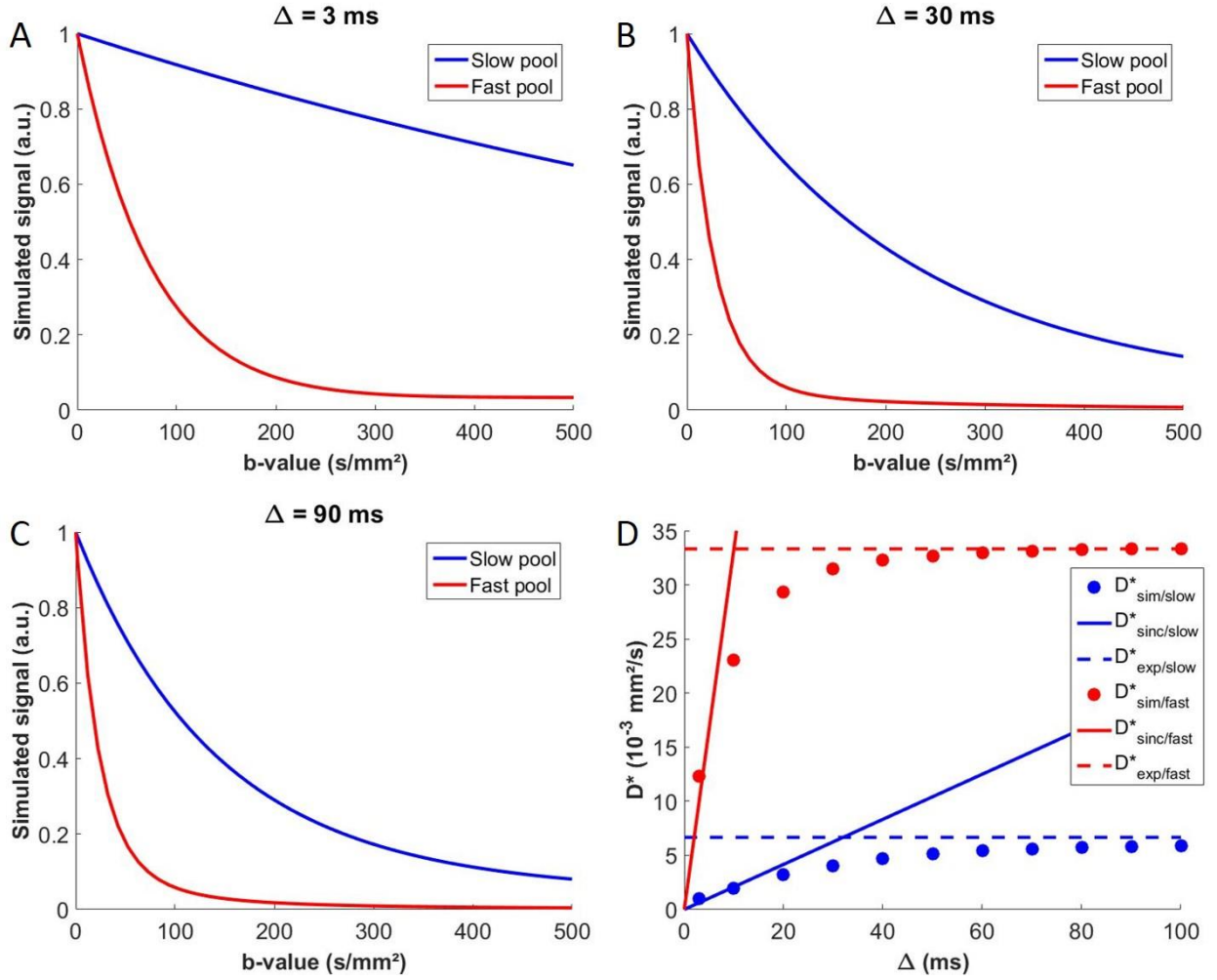


Figure 4.17. Influence of  $\Delta$  on the simulated signal for the two pools with Gaussian distributions of  $L$  and  $V$  with  $\sigma_L = 0.5 \times L_{mean}$  and  $\sigma_V = 0.5 \times V_{mean}$ ,  $L_{slow/mean} = 40$   $\mu$ m,  $V_{slow/mean} = 1$  mm/s,  $L_{fast/mean} = 50$   $\mu$ m,  $V_{fast/mean} = 4$  mm/s and  $\delta = 3$  ms. (A-C) Simulated signal for the two pools for different values of  $\Delta$ : 3, 30 and 90 ms. For the slow pool,  $N = 0.15, 0.83$  and  $2.33$  for each value of  $\Delta$ . For the fast pool,  $N = 0.48, 2.64$  and  $7.44$  for each value of  $\Delta$ . (D) Plot of  $D^*_{sim/slow}$ ,  $D^*_{sinc/slow}$ ,  $D^*_{exp/slow}$ ,  $D^*_{sim/fast}$ ,  $D^*_{sinc/fast}$  and  $D^*_{exp/fast}$  against  $\Delta$ .

With increasing diffusion time, the simulated signals decay faster with the space between the two pools' curves narrowing. The simulated signals for the two pools can be fit to the mono-exponential model,  $e^{-bD^*}$ , and  $D^*$  values obtained. The fitted  $D^*$  values are plotted in Figure 4.17.D for the two pools against  $\Delta$ . For the fast pool,  $D^*$  reaches a plateau at  $D^*_{exp/fast} = 33.33 \times$

$10^{-3} \text{ mm}^2/\text{s}$ . For  $\Delta = 100 \text{ ms}$ ,  $D^*$  of the slow pool is  $5.88 \times 10^{-3} \text{ mm}^2/\text{s}$  and has not reached its maximum,  $D_{exp/slow}^* = 6.67 \times 10^{-3} \text{ mm}^2/\text{s}$ , yet. For these choices of  $L_{mean}$  and  $V_{mean}$ , the predicted  $D^*$ -values from the simulations are well separated for every  $\Delta$  between the two pools. For the longest  $\Delta$  in the experimental data,  $\Delta = 34 \text{ ms}$ , the obtained  $D^*$ -values suggest that the two pools are in an intermediate regime between sinc and exponential regimes, which is coherent with the conclusions drawn in Chapter 3.

In this chapter, mathematical modelling and simulations of the IVIM signal have provided more insight into the different regimes and possible shapes of the IVIM signal. The next chapter, Chapter 5, uses the numerical simulations introduced in this chapter to extract structural information from the experimental data. The influence of acquisition parameters on the IVIM outputs is also investigated.



## Chapter 5: Extraction of vascular structural characteristics and influence of the acquisition parameters on the IVIM outputs

In the first section of this chapter we explain how the numerical simulations introduced in the previous chapter can be used to extract vascular structural information from the IVIM data already analyzed in Chapter 3. In the other sections of the chapter, the influence of the repetition time, the pulse sequence and the diffusion encoding time on the IVIM output parameters is studied.

### 5.1 Comparison of IVIM data with the numerical simulations

#### 5.1.1 Generation of a dictionary of simulated signals

In Chapter 4, we presented the mathematical formalism and the assumptions used to simulate the IVIM signal. The simulations are now used to generate a dictionary of simulated signals. We varied the chosen mean value of the Gaussian distributions for both blood flow velocities and segment lengths. The blood velocity is assumed to be constant within a trajectory but can be different between trajectories. For a given Gaussian distribution of lengths, with the mean value  $L_{mean}$  and the standard deviation  $\sigma_L = 0.5 \times L_{mean}$ , and a given Gaussian distribution of velocities, with the mean value  $V_{mean}$  and the standard deviation  $\sigma_V = 0.5 \times V_{mean}$ , we take 1000 samples of  $V$  and 1000 samples of 50 values of segment lengths:  $L_1, L_2, \dots, L_{50}$ . For each sample,  $N$  is the smallest value such that  $L_1 + L_2 \dots + L_N \geq V \times TE$ . To compute  $S_{IC}$  for this sample, we plug  $L_1, L_2, \dots, L_N$  and  $V$  into Eq. 4.12. The averaged  $S_{IC}$  over the 1000 samples is defined as the simulated signal  $F_{IVIM/Sim}$  for the distribution choice  $(L_{mean}, V_{mean})$ .

We computed  $F_{IVIM/Sim}$  for 72 values of  $L_{mean}$ , spanning the interval [8-150]  $\mu m$  with a 2  $\mu m$  step, and 100 values of  $v_{mean}$ , spanning the interval [0.1-10] mm/s with a 0.1 mm/s step. The simulated  $F_{IVIM/Sim}$  for each combination of  $L_{mean}$  and  $V_{mean}$  were assembled to build a dictionary of simulated signals.

As stated in Chapter 3, our hypothetical explanation for the bi-exponential shape of the IVIM signal is that IVIM imaging is sensitive to more than one vascular pool, i.e. to two different pools identified by two different diffusion coefficients. We insert this hypothesis into the simulations drawing an analogy with the bi-exponential model. Two simulated signals representing the two pools, one for the slow pool,  $F_{IVIM/Sim}(b, L_{slow}, V_{slow})$ , and another one for the fast pool,  $F_{IVIM/Sim}(b, L_{fast}, V_{fast})$ , are combined and compared to the experimental signals. This comparison aims to identify the mean values (lengths and blood flow velocities) best matching the experimental signals for the two pools. Very importantly, to simplify the data fitting problem, we fixed two of the free parameters, the fractions  $f_{slow}$  and  $f_{fast}$ , to be the values we found by fitting the experimental data (described in Chapter 3):

$$F_{IVIM/Sim}(b, L_{slow}, V_{slow}, L_{fast}, V_{fast}) = f_{slow}F_{IVIM/Sim}(b, L_{slow}, V_{slow}) + f_{fast}F_{IVIM/Sim}(b, L_{fast}, V_{fast}) \quad 5.1$$

As the self-diffusion of water molecules in the intravascular compartment was not taken into account in the simulations whereas it was included in the IVIM model, the simulated signals were not compared directly to the experimental signals but to  $\frac{F_{IVIM/data}(b)}{e^{-bD_b}}$  where  $D_b$  is the blood diffusion coefficient, set to  $1.75 \times 10^{-3} \text{ mm}^2/\text{s}$  [154].

### 5.1.2 Comparison of the experimental data with the dictionary of simulated signals

To evaluate the goodness of fit of the experimental data compared to the dictionary of simulated signals, the error  $\varepsilon$  between them was calculated using the normalized  $l^2$ -norm formula:

$$\varepsilon(L_{slow}, V_{slow}, L_{fast}, V_{fast}) = \sqrt{\frac{\sum_b \left( F_{IVIM/Sim}(b, L_{slow}, V_{slow}, L_{fast}, V_{fast}) - \frac{F_{IVIM/data}(b)}{e^{-bD_b}} \right)^2}{\sum_b \left( \frac{F_{IVIM/data}(b)}{e^{-bD_b}} \right)^2}} \quad 5.2$$

where  $F_{IVIM/Sim}$  and  $F_{IVIM/data}$  represent the simulated signals from the dictionary and the experimental signal, respectively. An  $\varepsilon$  less than 10 % was considered an acceptable match between the experimental data and a particular combination of simulated signals.

The comparison with the numerical simulations was performed for  $\Delta = 24$  ms only because at  $\Delta = 14$  ms,  $D_{fast}^*$  can be overestimated and at  $\Delta = 34$  ms, the signals from some datasets are better fitted to a mono-exponential than to a bi-exponential model.

Four parameters are allowed to change in the numerical simulations,  $L_{slow}$ ,  $V_{slow}$ ,  $L_{fast}$  and  $V_{fast}$ . As it is impossible to show in one figure all the possible combinations of the four parameters giving a value of  $\varepsilon$  less than 10%,  $\varepsilon$  isolines are displayed instead, where we fixed two of the parameters for one pool to show the possible values of  $L_{mean}$  and  $V_{mean}$  for the other pool.

In Figure 5.1, in red, we show the 10 %  $\varepsilon$  isolines for the slow pool obtained by fixing  $L_{fast}$  and  $V_{fast}$  to 50  $\mu\text{m}$  and 4 mm/s, respectively. The area between two isolines encompasses all acceptable combinations of  $L_{slow}$  and  $V_{slow}$  that match the experimental data for this particular set of  $L_{fast}$  and  $V_{fast}$ . Similarly, we obtain the 10 %  $\varepsilon$  isolines for the fast pool (in blue) by fixing  $L_{slow}$  and  $V_{slow}$  at  $L_{slow} = 40$   $\mu\text{m}$ ,  $V_{slow} = 1$  mm/s.

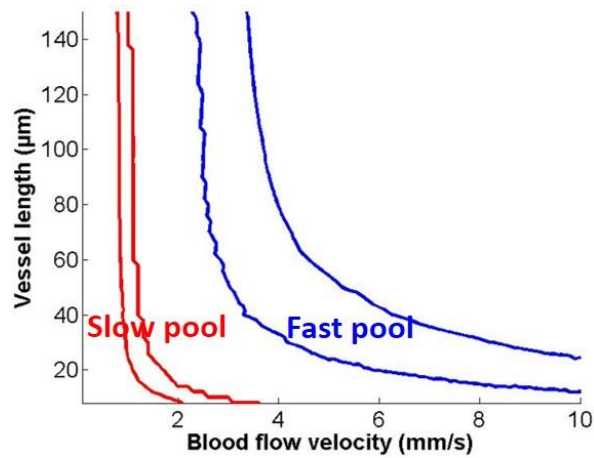


Figure 5.1. 10 %  $\varepsilon$  isolines for different combinations of vessel lengths and blood flow velocities. The red curves correspond to the slow pool for the fixed fast pool values of  $V_{fast} = 4$  mm/s,  $L_{fast} = 50$   $\mu\text{m}$  and the blue curves to the fast pool for the fixed slow pool values of  $V_{slow} = 1$  mm/s,  $L_{slow} = 40$   $\mu\text{m}$ .

The isolines' shapes are similar for both pools, with the slow pool thinner and shifted to the left compared to the fast pool, clearly demonstrating that the two pools are well separated with the slow pool associated with a smaller blood velocity than the fast pool. However, the vessel length is difficult to determine and Figure 5.1 shows that nearly all probed vessel lengths can

yield an acceptable match with the data. To better illustrate this, in Figure 5.2, we plot the experimental signal along with simulated signals with the same blood velocity,  $V_{fast} = 3$  mm/s, but with two different vessel lengths for the fast pool,  $L_{fast} = 70$  and  $150$   $\mu\text{m}$ , and with the same  $V_{slow} = 1$  mm/s and  $L_{slow} = 40$   $\mu\text{m}$  for the slow pool.

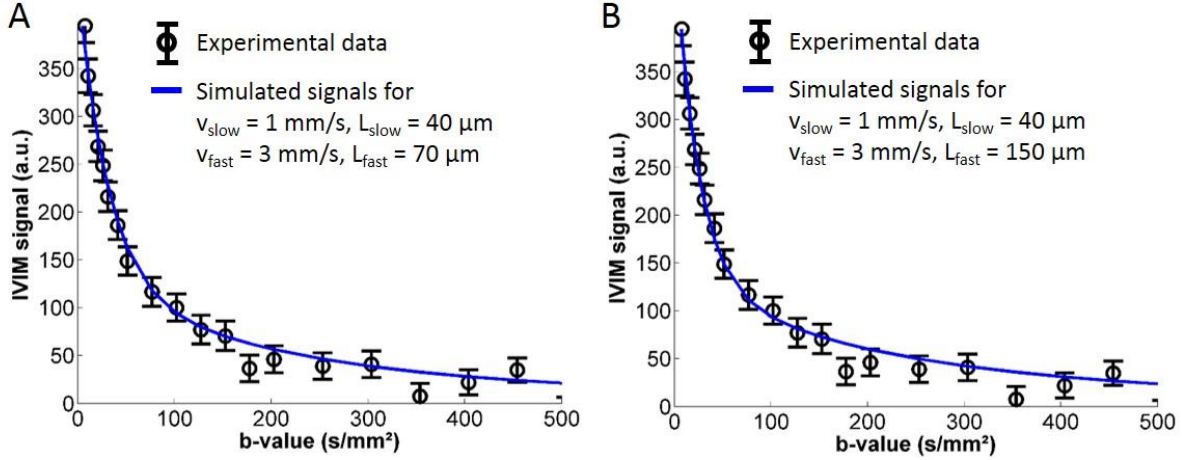


Figure 5.2. Examples of IVIM signal superimposed with simulated signals versus  $b$ -value for  $\Delta = 24$  ms in the LC. The black circles stand for the experimental data and the blue solid lines for the simulated signals with the same  $V_{slow} = 1$  mm/s,  $L_{slow} = 40$   $\mu\text{m}$  and  $V_{fast} = 3$  mm/s but with two different values for  $L_{fast}$ , (A)  $L_{fast} = 70$   $\mu\text{m}$ ,  $\varepsilon = 6.50$  % and (B)  $L_{fast} = 150$   $\mu\text{m}$ ,  $\varepsilon = 6.38$  % respectively. Error bars represent SD from the averaging step.

The two different lengths give a match with a similar quality confirming that the vessel length cannot be determined in this comparison ( $\varepsilon = 6.50$  % and  $6.38$  %, respectively). This incapability to determine the vessel lengths suggests that the two pools are closer to the sinc regime than to the exponential regime. To better understand the relation between the determination of the vessel length and the shape of the  $\varepsilon$  isolines, the contour plots are analyzed in more details.

### 5.1.3 Interpretation of the shape of the contour plots

To help understand the shape of the curves in Figure 5.1, we represent the regions corresponding to the sinc and exponential behaviors according to our experimental encoding times.

In Figure 5.3, the way the regions are obtained for the sinc regime for the fast pool is described highlighted by four circled numbers.

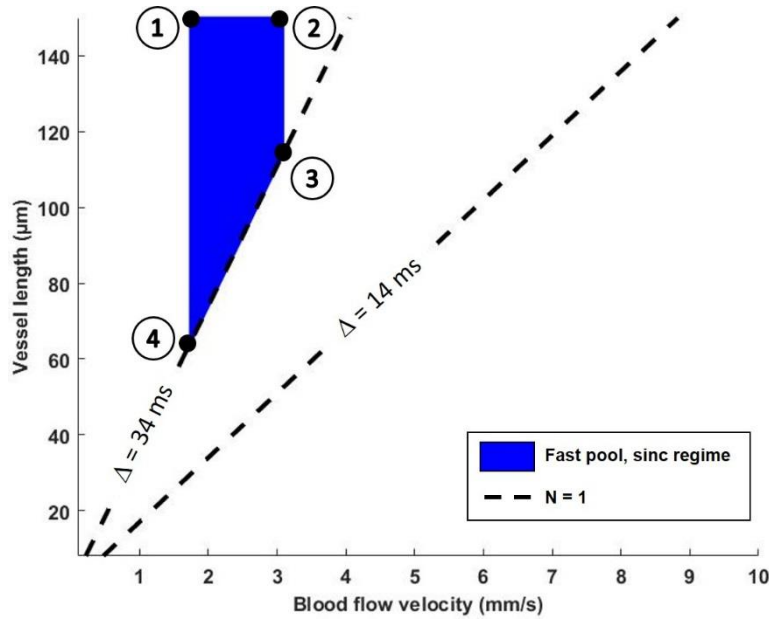


Figure 5.3. Description of the way the region corresponding to the sinc regime for the fast pool is obtained. Points 1 to 4 delimit the blue region corresponding to  $\Delta = 14$  to 34 ms. The dashed lines are drawn for a number of vessels seen during the encoding time,  $N = 1$ .

To represent the sinc regime, the equation of  $D^*$  in this regime is used. As a reminder of Eq. 3.11:

$$D_{sinc}^* = \frac{v^2 \Delta}{6} \quad 5.3$$

Also, the number of vessels,  $N$ , seen during the encoding time,  $\Delta + \delta$ , is less than 1 in this regime.

Therefore, the lines between points 1 and 4 as well as between points 2 and 3 are obtained from the equation of  $D^*$  in the sinc regime, Eq. 5.3, for the two  $\Delta$ , 34 and 14 ms, respectively:

$$V = \sqrt{\frac{6D_{fast}^*(\Delta)}{\Delta}} \quad 5.4$$

where  $D_{fast}^*(\Delta)$  is the value of  $D_{fast}^*$  for a certain  $\Delta$ .

The dashed lines are drawn for  $N = 1$  and  $\Delta = 14$  and 34 ms using:

$$L = \frac{V(\Delta + \delta)}{N} \quad 5.5$$

Points 1 and 2 are the points for which  $V$  is described by Eq. 5.4 and  $L = 150 \mu\text{m}$  for  $\Delta = 34$  and  $14 \text{ ms}$ , respectively. Points 3 and 4 are obtained by using Eq. 5.4 for  $V$ , with  $\Delta = 14$  and  $34 \text{ ms}$ , respectively, and calculating the intersection between Eq. 5.4, with  $\Delta = 14$  and  $34 \text{ ms}$ , respectively, and Eq. 5.5, with  $\Delta = 34 \text{ ms}$  and  $N = 1$ , for  $V$ . The blue region in Figure 5.3 is then obtained by linking the four points together. The same technique can be used to get the region corresponding to the slow pool by replacing  $D_{fast}^*(\Delta)$  by  $D_{slow}^*(\Delta)$  in Eq. 5.4.

The drawing of the region corresponding to the exponential regime for the fast pool and  $\Delta = 14$  to  $34 \text{ ms}$  is explained in Figure 5.4.

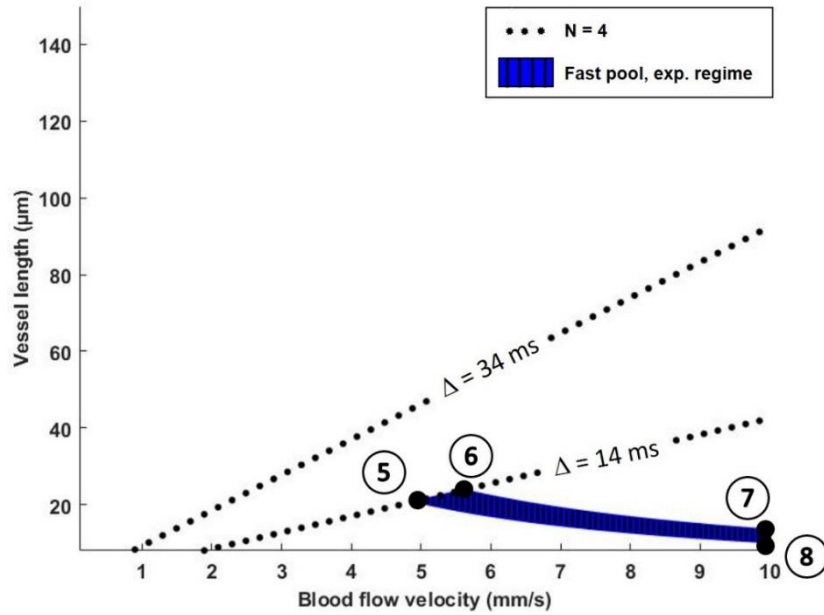


Figure 5.4. Plot of the hatched blue region corresponding to the fast pool in the exponential regime for  $\Delta = 14$  to  $34 \text{ ms}$ . Four points, 5, 6, 7 and 8 delimit the region. The dotted lines are drawn for a number of vessels seen during the encoding time,  $N = 4$ .

As for the sinc regime, four points, 5, 6, 7 and 8, have been added to delimit the region corresponding to the fast pool and the range of  $\Delta = 14$  to  $34 \text{ ms}$ . In the exponential regime, the expression for  $D^*$  in this regime is used. As a reminder of Eq. 3.4,

$$D_{exp}^* = \frac{LV}{6} \quad 5.6$$

The dotted lines are drawn for  $N = 4$  and  $\Delta = 14$  and  $34 \text{ ms}$  using Eq. 5.5 as  $N = 4$  is the limit value of  $N$  above which we are in the exponential regime.

The lines between points 6 and 7 as well as between points 5 and 8 are obtained from the equation of  $D^*$  in the exponential regime, Eq. 5.6, for the two  $\Delta$ , 14 and 34 ms, respectively:

$$L = \frac{6D_{fast}^*(\Delta)}{V} \quad 5.7$$

Points 7 and 8 are the points for which  $L$  is described by Eq. 5.7 and  $V = 10$  mm/s for  $\Delta = 14$  and 34 ms, respectively. Points 5 and 6 are obtained by using Eq. 5.7 for  $L$  for  $\Delta = 34$  and 14 ms, respectively, and calculating the intersection between Eq. 5.5, with  $\Delta = 14$  ms and  $N = 4$ , and Eq. 5.7, with  $\Delta = 34$  and 14 ms, respectively, for  $V$ . The hatched blue region in Figure 5.4 is finally obtained by linking the points 5, 6, 7 and 8 together. As for the regions in the sinc regime, to get the region corresponding to the slow pool in the exponential regime,  $D_{fast}^*(\Delta)$  needs to be replaced by  $D_{slow}^*(\Delta)$  in Eq. 5.7.

The four regions corresponding to the two pools, fast in blue and slow in red, and the two regimes, sinc with plain regions and exponential with hatched regions, are gathered in Figure 5.5.

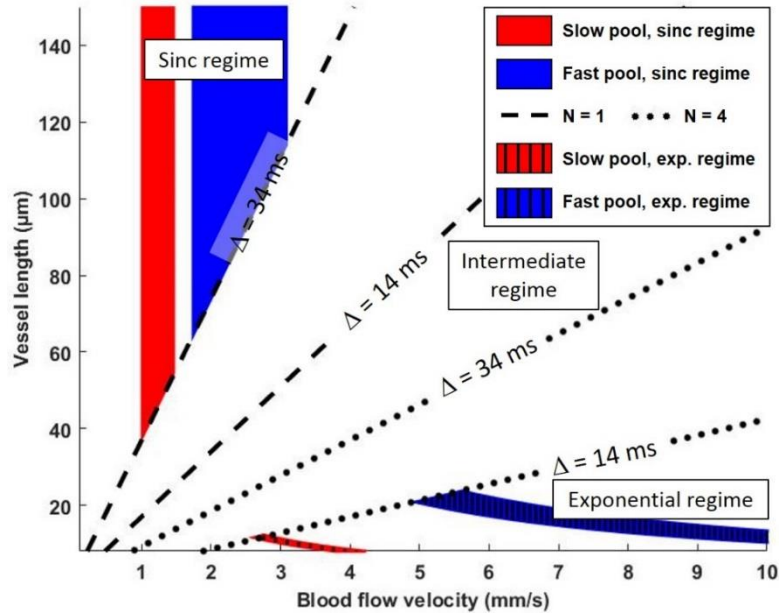


Figure 5.5. Plot showing the two regimes, sinc and exponential, corresponding to different combinations of mean vessel lengths and blood flow velocities, for the slow (red) and fast (blue) pools. The dashed and dotted lines, plotted for the two diffusion times ( $\Delta = 14$  and 34 ms), correspond to  $N = 1$  and 4, respectively.

In between the dashed  $N = 1$  line for  $\Delta = 14$  ms and the dotted  $N = 4$  line for  $\Delta = 34$  ms, we find the intermediate regime, which is not sinc anymore but no yet exponential. If we draw lines between the two red and two blue domains and connect them, we find again the shape of the red and blue isolines in Figure 5.1.

Considering a mean blood velocity for the slow pool of  $\cong 1.6$  mm/s, if the vessel length is small, below  $50 \mu\text{m}$ , we are mostly in an intermediate regime. If the vessel length is  $> 50 \mu\text{m}$ , we are in the sinc regime. Although only a small number of isochromats will experience the exponential regime, given the wide range of blood flow velocities and vessel lengths, the signal is smoothed and does not look like a sinc function. It can be approximated by an exponential function at very short b-values.

For the fast pool and  $V_{fast} \cong 4$  mm/s, for small vessel lengths, we observe the exponential regime. Increasing the length, we reach an intermediate regime and finally the sinc regime. Once again, the signal will not look like a product of a small number of sinc functions because of the length and velocity distributions which smooth the signal. This signal can thus also be approximated by an exponential function at very short b-values. However, when comparing with the slow pool, we can state that a larger proportion of isochromats will be in the exponential regime in the fast pool.

In conclusion, it is a reasonable approximation to fit the IVIM signal to a two pool bi-exponential model at short diffusion times; however, within each pool, the signal is not truly exponential but a combination of sinc, products of different numbers of sinc and exponential functions with different weights depending on the vascular pool.

#### 5.1.4 Extraction of structural parameters for the two pools

Even if it is not possible to determine the vessel length, to try to get an estimation of  $V_{slow}$  and  $V_{fast}$ , all possible combinations of parameters giving  $\varepsilon < 10$  % were averaged. The results of averaging on all possible combinations of  $[L_{slow}, V_{slow}, L_{fast}, V_{fast}]$  in all datasets with some constraints applied are gathered in Table 5.1.



		Constraints	
		$V_{slow} < V_{fast}$	$V_{slow} < V_{fast}$ and $L_{fast} \geq 30 \mu\text{m}$
$V_{slow}$ (mm/s)	LC	$1.76 \pm 1.23$	$1.30 \pm 0.46$
	LT	$1.44 \pm 0.87$	$1.20 \pm 0.43$
$V_{fast}$ (mm/s)	LC	$4.64 \pm 2.27$	$3.03 \pm 0.89$
	LT	$4.37 \pm 2.19$	$3.19 \pm 1.32$

Table 5.1. Mean  $\pm$  SD mean values of the segment length and blood velocity extracted from the comparison of experimental data with the dictionary of simulations ( $N_R=11$ ). The average was calculated on all possible solutions giving  $\varepsilon < 10\%$  without any constraint, with  $V_{slow} < V_{fast}$  or with  $V_{slow} < V_{fast}$  and  $L_{fast} \geq 30 \mu\text{m}$ . LC and LT refer to the left cortex and left thalamus ROIs, respectively.

Relatively to our hypothesis that the two pools are associated with different groups of vessels, one with a slow blood velocity and the other with a fast blood velocity, it is not coherent to have  $V_{slow} > V_{fast}$ . Therefore, we set the constraint that  $V_{slow} < V_{fast}$  and removed from the averaging all combinations for which  $V_{slow} > V_{fast}$ . This allows to get separated values of  $V_{slow}$  and  $V_{fast}$ .  $V_{slow}$  is particularly close to the blood velocity of capillaries found in the literature, around 1.6 mm/s. Another assumption can also be made for the fast pool. If it is related to vessels larger in diameter than capillaries, then their length should be at least larger than twice their minimum diameter. If we put this limit to  $30 \mu\text{m}$  and state that  $L_{fast} > 30 \mu\text{m}$  in addition to  $V_{slow} < V_{fast}$ , we obtain smaller values for both mean blood flow velocities. The validity of this second constraint is however questionable as it implies that the second pool of vessels corresponds to larger vessels and this assumption has not been validated yet. However, the first constraint allowed us to get reasonable estimations for  $V_{slow}$  and  $V_{fast}$  coherent with values from the literature for blood flow velocities inside the capillaries and somewhat larger vessels, possibly medium-size arterioles and venules.

## 5.2 Influence of the repetition time: inflow effect

Because the bi-exponential IVIM model includes a fast flow component, we checked for possible inflow effects by varying the repetition time. First, the inflow effect and the influence of varying the repetition time are described. Then, experimental results obtained for different repetition times are presented.

### 5.2.1 Explanation of the inflow effect

The inflow effect and its relation to the repetition time are illustrated in Figure 5.6. At short repetition times (compared to relaxation time  $T_1$ ), the longitudinal magnetization of spins in the tissue has not fully recovered from the slice radiofrequency excitation, while fresh flowing spins entering the voxel are fully magnetized. This difference between the magnetization of the two populations slightly enhances the contribution of the fresh flowing spins to the signal. Applied to our model, this effect, called inflow effect, depends on the fraction of fresh spins entering the slice, thus also on the blood velocity and can lead to an overestimation of  $f_{fast}$ . By increasing the repetition time, the spins inside the tissue have more time to recover their full magnetization and the difference with that of flowing spins vanishes, restoring the correct value for  $f_{fast}$ .

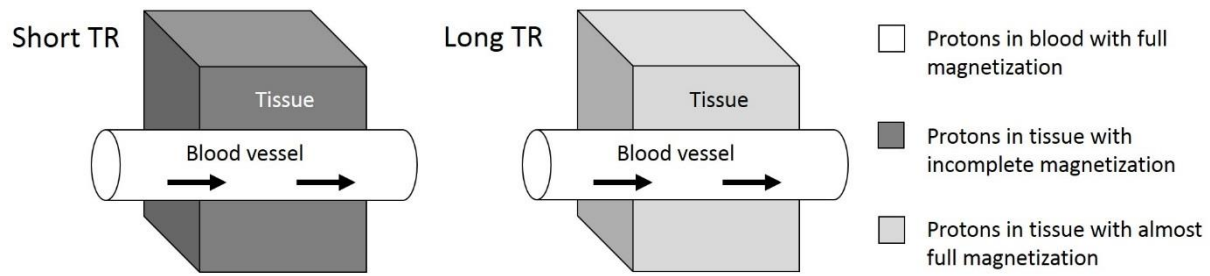


Figure 5.6. Scheme explaining the inflow effect at short and long repetition time. Protons in the blood vessels enter the voxels with their full magnetization (in white) whereas at short TR, protons present in the tissue do not have enough time to recover their full magnetization (dark grey). This enhances the signal contribution from the blood vessels compared to the tissue. On the contrary, at long TR, protons in the tissue have more time to recover their full magnetization (light grey) thus giving less difference with the signal coming from spins in blood vessels.

### 5.2.2 Impact on the IVIM outputs

For four rats, the influence of the repetition time was tested. A PGSE-EPI sequence was used with the following acquisition parameters: gradient direction  $[X=0, Y=1, Z=0]$ , TE = 45 ms, TR = 1000 and 3000 ms,  $\delta = 3$  ms,  $\Delta = 14$  ms, in-plane resolution  $250 \times 250 \mu\text{m}^2$ , matrix size  $80 \times 80$ , field of view  $2 \times 2 \text{ mm}^2$ , slice thickness 1.5 mm, 1 segment, 6 averages, 5 repetitions. We used 30 b-values (20 b-values ranging from 2 to 500  $\text{s/mm}^2$  and 10 b-values ranging from 500 to 2500  $\text{s/mm}^2$ ).

The data were analyzed similarly as in Chapter 3. After averaging on the repetitions and on an ROI on the LC, the signal obtained was first fitted for diffusion for  $b > 500 \text{ s/mm}^2$  with the Kurtosis model. This diffusion signal was then extrapolated and subtracted to the raw signal and fitted to the bi-exponential IVIM model for  $b < 500 \text{ s/mm}^2$ . The retrieved values of the IVIM parameters are gathered in Table 5.2. The AICc values corresponding to the fit of the IVIM signal to the bi-exponential and the mono-exponential IVIM models,  $\text{AICc}_{\text{bi}}$  and  $\text{AICc}_{\text{mono}}$ , respectively, were also calculated. The difference in AICc between the two models is also displayed in Table 5.2.

TR (ms)	1000	3000
$f_{\text{IVIM}}$ (%)	$13.41 \pm 0.55$	$6.36 \pm 1.06$
$f_{\text{slow}}$ (%)	$24.39 \pm 10.84$	$57.94 \pm 10.36$
$D_{\text{slow}}^*$ ( $10^{-3} \text{ mm}^2/\text{s}$ )	$2.21 \pm 0.33$	$2.16 \pm 0.70$
$D_{\text{fast}}^*$ ( $10^{-3} \text{ mm}^2/\text{s}$ )	$27.48 \pm 1.97$	$25.96 \pm 3.21$
$f_{\text{IVIM}} \times f_{\text{slow}}$ (%)	$3.25 \pm 1.45$	$3.76 \pm 0.92$
$f_{\text{IVIM}} \times f_{\text{fast}}$ (%)	$10.16 \pm 1.51$	$2.60 \pm 0.77$
$\text{AICc}_{\text{mono}} - \text{AICc}_{\text{bi}}$	$19.04 \pm 13.18$	$4.35 \pm 7.57$

Table 5.2. IVIM parameters for two different repetition times on an ROI on the LC and one slice ( $N_R = 4$ ).

A large decrease in  $\text{AICc}_{\text{mono}} - \text{AICc}_{\text{bi}}$  is observed when increasing TR from 1000 to 3000 ms. This decrease suggests that a further increase of TR might continue to reduce this difference resulting in the signal becoming mono-exponential at very long TRs.

With increasing TR, we observe a major decrease in  $f_{\text{IVIM}}$  and an increase in  $f_{\text{slow}}$  while  $D_{\text{slow}}^*$  and  $D_{\text{fast}}^*$  stay constant. As a result, even though the bi-exponential behavior was present for both repetition times,  $\text{AICc}_{\text{bi}}$  was on average lower for TR = 1000 ms. Interestingly, the product  $f_{\text{IVIM}} \times f_{\text{slow}}$  is similar with both TRs, suggesting that the slow flow component does not present inflow effects, while the contribution of the fast flow component to the overall IVIM effects,  $f_{\text{IVIM}} \times f_{\text{fast}}$ , increases when TR gets shorter. This is consistent with the fast pool signal coming from faster moving blood than for the slow pool. As a result, the volume fraction of the fast pool,  $f_{\text{fast}}$ , and therefore, the global  $f_{\text{IVIM}}$  fraction (or the  $f_{\text{IVIM}}$  value of the IVIM mono-exponential model), are most likely overestimated when inflow effects are present (small number of slices, short TRs).

### 5.3 Influence of the pulse sequence: spin echo versus stimulated echo

Both the SE and the STE pulse sequences can be used to acquire IVIM data. In this section, the differences between the two sequences are analyzed to understand their influence on the IVIM output parameters. As mentioned earlier, the STE sequence has the advantage to increase the diffusion encoding time without the need to increase TE and attenuate the signal because of increased  $T_2$ -relaxation. However, the baseline signal at  $t = 0$  is half that of the SE sequence so more repetitions are needed to keep the same SNR between the two sequences.

#### 5.3.1 Phantom experiment

To get an insight of the effect of the pulse sequence on the IVIM signal, a simple phantom experiment was designed. The phantom is a 15 mL falcon tube in which a thin pipe is inserted by piercing holes at both ends. As shown in Figure 5.7, the end without the cap is sealed with wax before adding agarose (2% agar) to fill the falcon and maintain the pipe straight inside of it. After solidification of the agarose, the hole in the cap was also sealed with wax. The phantom is then installed on a bed and inserted inside the MRI scanner. At one end of the pipe, a syringe pump pushes water inside the pipe at a controlled flow velocity towards a beaker located at the other end of the pipe outside of the MRI scanner.

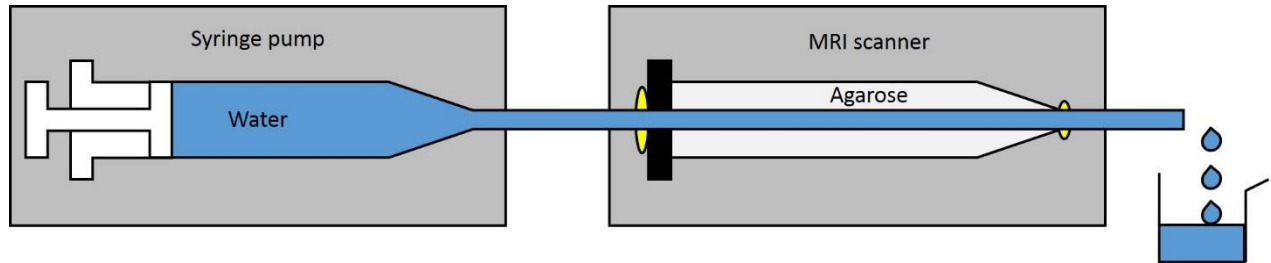


Figure 5.7. Scheme of the phantom experiment. The phantom consists of a thin pipe inserted inside a 15 mL falcon filled with agarose (2% agar). The holes performed in the falcon to insert the pipe are sealed with wax (in yellow). A syringe pump is used to control the blood velocity of the water flowing inside the phantom located inside the MRI scanner. A beaker is placed at the other end of the pipe to collect the water flowing inside the phantom.

The syringe pump was used to vary the flow velocity inside the pipe while scanning the phantom with the SE and the STE sequence and the following acquisition parameters: diffusion gradient direction  $[X=0, Y=1, Z=0]$ ,  $\delta = 3$  ms,  $\Delta = 14$  ms, in-plane resolution  $400 \times 400 \mu\text{m}^2$ , slice thickness 1.5 mm, 1 segment, TE/TR = 24/1500 ms, 4 averages, 1 and 4 repetitions for the SE

and STE sequences respectively, 1 slice, field of view 12.5 x 12.5 mm, matrix size 50 x 50, 26 b-values in the range [2-1500] s/mm<sup>2</sup>. The STE sequence was repeated four times and the signal averaged over these repetitions to increase the SNR and obtain similar signal level than with the SE sequence. Coronal images of the phantom with the two pulse sequences for  $V_{flow} = 0$  mm/s are displayed in Figure 5.8. Both sequences give similar signal inside the pipe which is clearly visible at the center of the phantom.

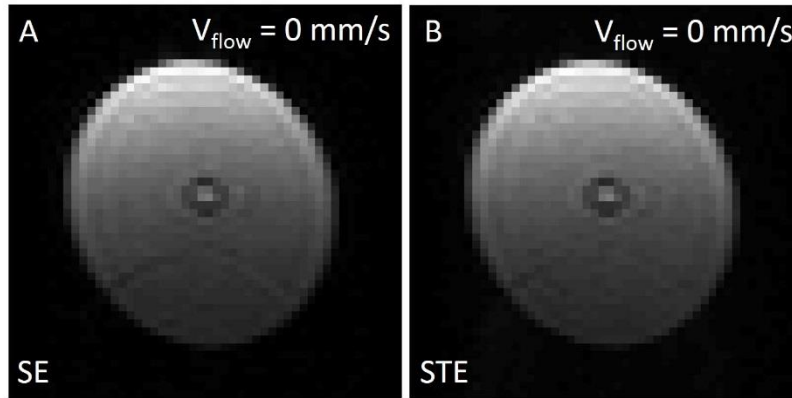


Figure 5.8. (A-B) Coronal images of the phantom for  $V_{flow} = 0$  mm/s and the SE and STE pulse sequences and the same acquisition parameters, respectively.

When turning on the syringe pump, the signal inside the tube becomes higher than the signal in the agarose due to inflow effects as illustrated in Figure 5.9.A and F. As the flow velocity increases, the signal intensity inside the tube does not change much for the SE sequence whereas it decreases substantially for the STE sequence.

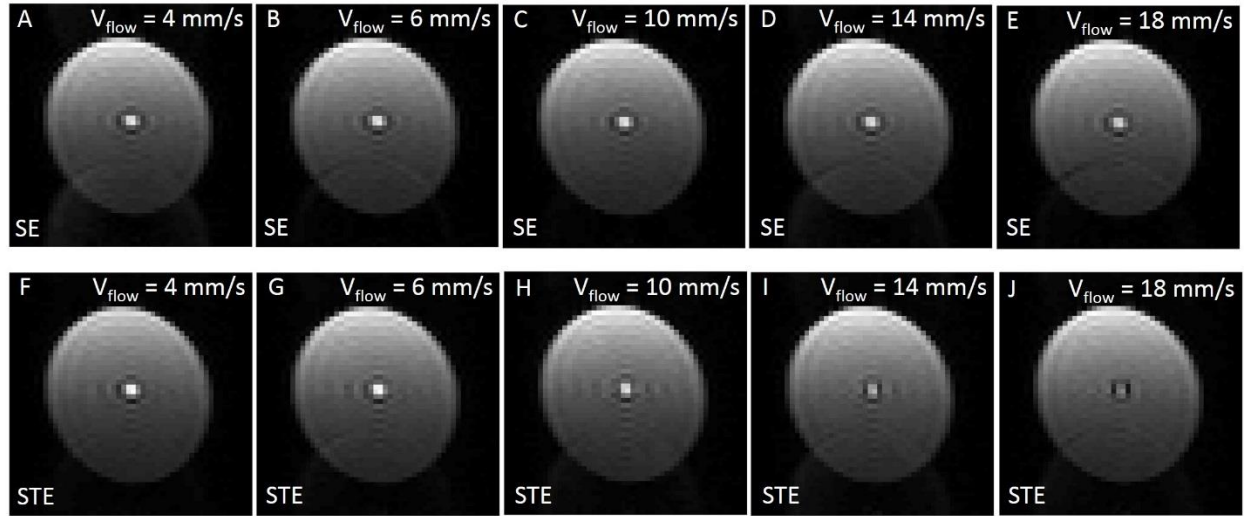


Figure 5.9. Evolution of the signal inside the pipe with increasing flow velocity,  $V_{flow} = 4, 6, 10, 14$  and  $18$  mm/s, for the two pulse sequences, SE (A-E) and STE (F-J).

Indeed, in Figure 5.10, when plotting the signal inside the tube normalized to the signal at  $V_{flow} = 4$  mm/s, this signal decreases by 10% and 50% when reaching  $V_{flow} = 18$  mm/s for the SE and STE sequences, respectively.

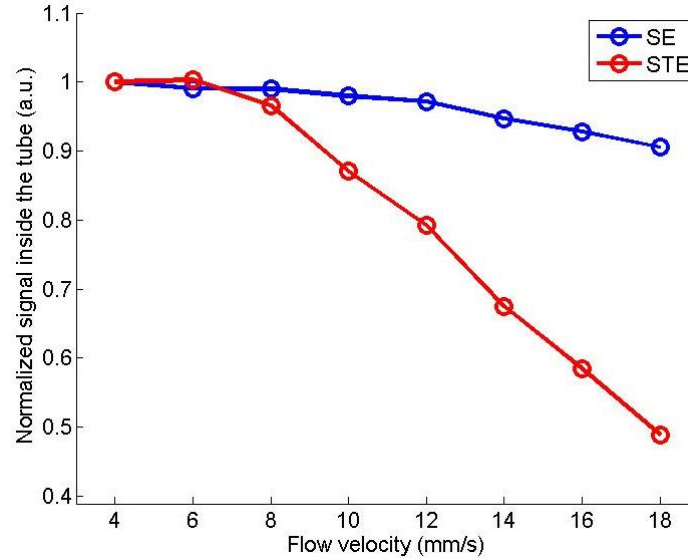


Figure 5.10. Normalized signal inside the tube against the flow velocity for the two sequences, SE and STE, in blue and red, respectively.

These experiments point to two differences between the STE and the SE pulse sequences:

- 1) The inflow effect is less important in the sequence STE than in the SE sequence.

- 2) The contribution to the signal of fast flowing spins is diminished in the STE compared to the SE sequence.

Both points suggest that the contribution of the fast pool is less important for the STE sequence than for the SE sequence. To understand why high flow velocities contribute less to the IVIM signal in the STE sequence, we propose the following physical explanation.

### 5.3.2 Physical explanation

The  $180^\circ$  pulse of the SE sequence is replaced by two  $90^\circ$  pulses in the STE sequence allowing for longer diffusion times [155]. It introduces a new time in which spins experience only  $T_1$ -relaxation, the mixing time, TM, between the two added  $90^\circ$  pulses. To explain why the STE sequence is less sensitive to high flow velocities than the SE sequence, the phase shifts accumulated during the  $180^\circ$  pulse, for the SE sequence, and between the two  $90^\circ$  pulses, for the STE sequence, are calculated. In this calculation, we do not take into consideration the diffusion encoding gradients, we consider only the slice selection gradients.

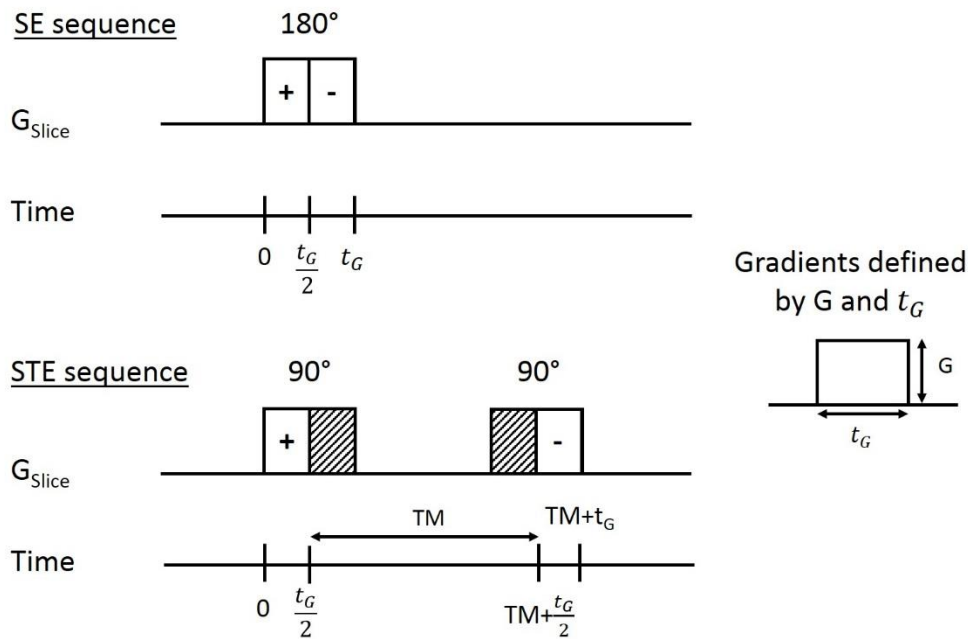


Figure 5.11. Representation of the slice gradients of the  $180^\circ$  and the second and third  $90^\circ$  pulses of the SE and STE sequences, respectively. The slice selection gradients are characterized by their gradient strength,  $G$ , and their duration  $t_G$ . The + and - signs refer to the sign of the gradients. After the  $180^\circ$  pulse, the gradient sign is reversed. For the STE sequence, the gradients are hatched during TM as spins are in the longitudinal plane and do not contribute to the gradient dephasing.

For the SE sequence, the expression for the position vector of an isochromat with blood velocity vector  $\vec{V}$  is:

$$\vec{x}(t) = \vec{V}t \text{ for } 0 < t < \frac{t_G}{2} \text{ and } \frac{t_G}{2} < t < t_G \quad 5.8$$

From Figure 5.11,

$$\vec{G}(t) = \begin{cases} G\vec{e}_G, & 0 < t < \frac{t_G}{2} \\ -G\vec{e}_G, & \frac{t_G}{2} < t < t_G \end{cases} \quad 5.9$$

with  $\vec{e}_G$  the gradient direction.

Making the hypothesis that  $\vec{V} \cdot \vec{e}_G = V \cos(\theta)$ , the phase shift accumulated during the 180° pulse of the SE sequence,  $\phi_{SE}$ , is then:

$$\begin{aligned} \phi_{SE} &= \gamma V G \cos(\theta) \left( \int_0^{\frac{t_G}{2}} t \, dt - \int_{\frac{t_G}{2}}^{t_G} t \, dt \right) \\ &= -\gamma V G \cos(\theta) \frac{t_G^2}{4} \end{aligned} \quad 5.10$$

For the STE sequence, only the contribution from gradients before and after  $TM$  need to be considered so the expression for  $\vec{x}(t)$  is:

$$\vec{x}(t) = \vec{V}t \text{ for } 0 < t < \frac{t_G}{2} \text{ and } TM + \frac{t_G}{2} < t < TM + t_G \quad 5.11$$

From Figure 5.11,

$$\vec{G}(t) = \begin{cases} G\vec{e}_G, & 0 < t < \frac{t_G}{2} \\ -G\vec{e}_G, & TM + \frac{t_G}{2} < t < TM + t_G \end{cases} \quad 5.12$$

The phase shift accumulated during the two 90° pulses of the STE sequence,  $\phi_{STE}$ , is then:

$$\begin{aligned} \phi_{STE} &= \gamma V G \cos(\theta) \left( \int_0^{\frac{t_G}{2}} t \, dt - \int_{TM + \frac{t_G}{2}}^{TM + t_G} t \, dt \right) \\ &= \phi_{SE} - \gamma V G \cos(\theta) \frac{t_G TM}{2} \end{aligned} \quad 5.13$$

With the STE sequence, a term is added to the phase shift of the SE sequence. So, for the same blood velocity, the absolute value of the phase shift is bigger with the STE than with the SE



sequence. The higher the blood velocity, the bigger this difference will be. This explains why the signal of the STE sequence is less sensitive to high blood flow velocities than the signal of the SE sequence. It implies that it is also less sensitive to inflow effects than the SE sequence.

The signal attenuation resulting from the dephasing calculated for the two sequences can be obtained by integrating over all possible segment orientation in a unit sphere giving:

$$S_{IC/SE} = \text{sinc}\left(\gamma V G \frac{t_G^2}{4}\right) \quad 5.14$$

And

$$S_{IC/STE} = \text{sinc}\left(\gamma V G \frac{t_G}{2}\left(TM + \frac{t_G}{2}\right)\right) \quad 5.15$$

These analytical signals are plotted in Figure 5.12 against the flow velocity  $V$  for  $TM = 6.2$  ms,  $t_G = 1.5$  ms and  $G = 7.12$  and  $11.24$  mT/m for the SE and STE sequences, respectively. They were normalized to the value for 4 mm/s to compare more easily with Figure 5.10.

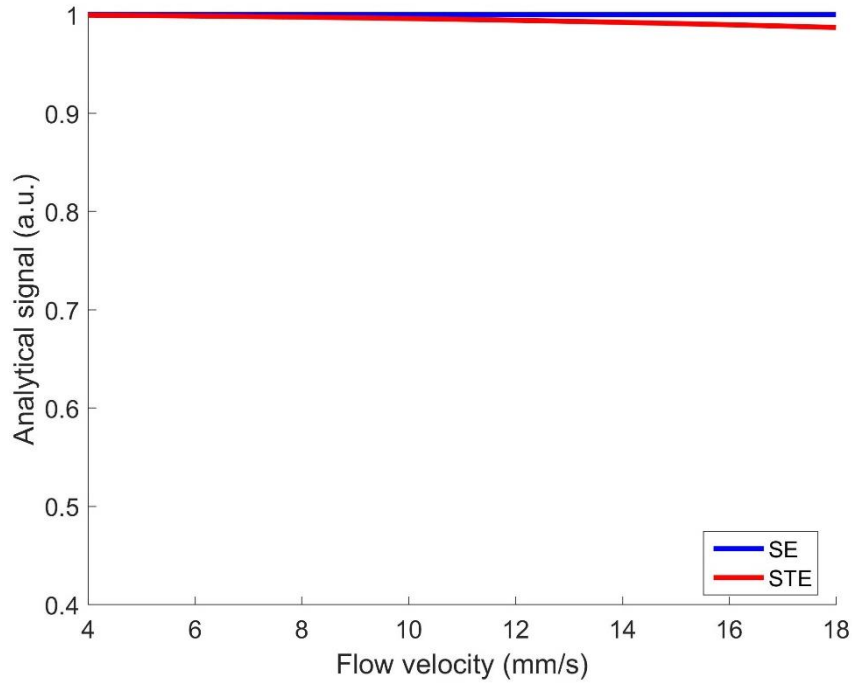


Figure 5.12. Normalized analytical signal against the flow velocity for the SE (Eq. 5.13) and STE (Eq. 5.14) sequences in blue and red, respectively to the signal at  $V = 4$  mm/s.

The trend of the curves in Figure 5.12 is similar to the one in Figure 5.10 but the decay of the two curves is much steeper in Figure 5.10, especially for the STE sequence. Indeed, the

theoretical curves in Figure 5.12 were plotted without considering inflow effects present in the phantom experiments as they were performed at short TRs.

To get rid of the inflow effects and only see the effect of the difference between the two pulse sequences, long TRs should be used. Thus, in the next subsection, the SE and STE sequences are compared both at short and long TRs.

### 5.3.3 Impact on the IVIM outputs

#### 5.3.3.1 At short repetition time

The two pulse sequences, SE and STE, were first compared on four rats at short repetition time, TR = 1000 ms, in the presence of inflow effects. The acquisition parameters for the two sequences are the same as used for the study of the influence of the repetition time except that 6 repetitions were performed, the in-plane resolution was 400 x 400  $\mu\text{m}^2$ , the matrix size 50 x 50 and TR = 1000 ms. The same data processing scheme was also used. The results of the fitting of the data with the bi-exponential IVIM model on a ROI on the LC are displayed in Table 5.3. The difference in AICc between the mono- and bi-exponential IVIM models is also shown in Table 5.3.

Sequence	SE	STE
$f_{IVIM}$ (%)	$11.21 \pm 0.91$	$6.21 \pm 1.93$
$f_{slow}$ (%)	$40.06 \pm 12.95$	$69.32 \pm 25.60$
$D^*_{slow}$ ( $10^{-3} \text{ mm}^2/\text{s}$ )	$1.79 \pm 0.16$	$2.33 \pm 0.14$
$D^*_{fast}$ ( $10^{-3} \text{ mm}^2/\text{s}$ )	$19.98 \pm 4.21$	$19.45 \pm 4.31$
$f_{IVIM} \times f_{slow}$ (%)	$4.45 \pm 1.29$	$4.66 \pm 2.37$
$f_{IVIM} \times f_{fast}$ (%)	$6.76 \pm 1.41$	$1.54 \pm 1.18$
$AICc_{mono} - AICc_{bi}$	$12.75 \pm 15.68$	$4.25 \pm 17.57$

Table 5.3. IVIM parameters for two pulse sequences, SE and STE, on an ROI on the LC for TR = 1000 ms ( $N_R = 4$ ).

For the same acquisition parameters but different pulse sequences,  $f_{IVIM}$  is divided by almost a factor of two between the SE and the STE sequences.  $f_{slow}$ ,  $D^*_{fast}$  and  $f_{IVIM} \times f_{slow}$  are not affected by the pulse sequence. However, student t-tests show a significant difference with  $p < 0.01$  for  $f_{IVIM}$ ,  $D^*_{slow}$  and  $f_{IVIM} \times f_{fast}$ . The difference in AICc is bigger for the SE sequence than

for the STE sequence suggesting that the two pools are harder to separate with the STE sequence when the other acquisition parameters are kept constant.

To study the difference between the two pulse sequences without the occurrence of inflow effects, experiments were also performed at long TRs.

### 5.3.3.2 At long repetition time

To decrease the inflow effects on both sequences, TR was increased to 3500 ms while keeping the same acquisition parameters as for TR = 1000 ms. Four rats were scanned with the SE and STE sequences with the longer TR. The obtained IVIM signals on an ROI on the LC were fitted to both the bi- and the mono-exponential models and the AICc was calculated to determine the best model to fit the data.

At TR = 3500 ms, for both sequences, the model best describing the data is the mono-exponential IVIM model. Therefore, only  $f_{IVIM}$ ,  $D^*$  and  $AICc_{mono}-AICc_{bi}$  are displayed in Table 5.4 for the two sequences.

Sequence	SE	STE
$f_{IVIM}$ (%)	$3.41 \pm 0.56$	$3.27 \pm 1.19$
$D^*$ ( $10^{-3} \text{ mm}^2/\text{s}$ )	$6.37 \pm 1.19$	$6.72 \pm 2.64$
$AICc_{mono}-AICc_{bi}$	$-0.92 \pm 22.47$	$-2.65 \pm 17.34$

Table 5.4. IVIM parameters for the two pulse sequences, SE and STE, on an ROI on the LC for TR = 3500 ms ( $N_R = 4$ ).

No significant difference was found for the two IVIM parameters,  $f_{IVIM}$  and  $D^*$ , between the pulse sequences when performing a Student's t-test.

### 5.3.3.3 Discussion

At the short TR-value, both sequences are also subject to inflow effects. They have no effects on the slow pool in the two sequences, as  $f_{IVIM} \times f_{slow}$  is not significantly different between the two sequences. However, we observe that  $f_{IVIM} \times f_{fast}$  is much smaller for the STE sequence than for the SE sequence. This decrease implies that the STE sequence is less affected by inflow effects than the SE sequence.  $D_{slow}^*$  was found higher in the STE compared to the SE sequence.

This parameter was not expected to vary with the pulse sequence. It is likely that this difference would disappear if more animals were scanned.

As  $f_{IVIM}$  is the ratio between the signal coming from the microvasculature against the total signal, its value depends on  $T_1$ . It is thus possible to estimate the variation of  $f_{IVIM}$  due to the change in TR. For the SE sequence (Eq. 2.19), the ratio of  $f_{IVIM}$  between TR = 1000 and TR = 3500 ms can be approximated by:

$$\frac{\left( \frac{1 - e^{-\frac{1000}{T_{1b}}}}{1 - e^{-\frac{1000}{T_{1b}}} + 1 - e^{-\frac{1000}{T_{1t}}}} \right)}{\left( \frac{1 - e^{-\frac{3500}{T_{1b}}}}{1 - e^{-\frac{3500}{T_{1b}}} + 1 - e^{-\frac{3500}{T_{1t}}}} \right)} \cong 94.51\%$$

with  $T_{1b} = 2200$  ms,  $T_1$  in blood, and  $T_{1t} = 1700$  ms,  $T_1$  in the tissue, here the cortex at 7T.

For the STE sequence (Eq. 2.20), the dependence of the signal upon  $T_1$  during the mixing time,  $TM$ , needs to be added. The ratio of  $f_{IVIM}$  between the two TRs then becomes:

$$\frac{\left( \frac{e^{-\frac{TM}{T_{1b}}} \left( 1 - e^{-\frac{1000}{T_{1b}}} \right)}{e^{-\frac{TM}{T_{1b}}} \left( 1 - e^{-\frac{1000}{T_{1b}}} \right) + e^{-\frac{TM}{T_{1t}}} \left( 1 - e^{-\frac{1000}{T_{1t}}} \right)} \right)}{\left( \frac{e^{-\frac{TM}{T_{1b}}} \left( 1 - e^{-\frac{3500}{T_{1b}}} \right)}{e^{-\frac{TM}{T_{1b}}} \left( 1 - e^{-\frac{3500}{T_{1b}}} \right) + e^{-\frac{TM}{T_{1t}}} \left( 1 - e^{-\frac{3500}{T_{1t}}} \right)} \right)} \cong 94.51\%$$

with  $TM = 6.17$  ms for  $\Delta = 14$  ms.

This ratio is almost the same for the two pulse sequences. Going from TR = 1000 to TR = 3500 ms, according to this calculation, without taking into account inflow effects,  $f_{IVIM}$  should decrease by 5.49 % for both sequences. A decrease is observed experimentally but it is much larger than expected by this calculation and different between the two sequences. This is another argument to say that inflow effects, present at short TR, impact more the SE than the STE sequence.

For  $TR = 3500$  ms,  $f_{IVIM}$  is similar for the two sequences, still slightly bigger for the SE compared to the STE sequence with a difference between  $f_{IVIM}$  of the two sequences less than 5 %. This difference is coherent with the order of magnitude of the calculations performed in section 5.3.2 to explain the difference between the two sequences. For  $V < 18$  mm/s, the difference observed between the signal of the two sequences only induced by the replacement of the  $180^\circ$  pulse in the SE sequence by two  $90^\circ$  pulses in the STE sequence is less than 5 %. However, no estimation of the blood velocity can be extracted from Figure 5.12 as the standard deviation of  $f_{IVIM}$  does not allow for a precise calculation of the ratio of  $f_{IVIM}$  between the two sequences.

At the long TR-value,  $AIC_{mono}-AIC_{bi}$  was found to be negative. In section 5.2.2, when comparing acquisitions performed with the SE sequence at  $TR = 1000$  and  $3000$  ms,  $AIC_{mono}-AIC_{bi}$  was already showing a large decrease. These negative values suggest that, at long TRs, only one pool is visible in the IVIM signal. The inflow effect, strong at short TRs, makes the two sequences more sensitive to fast flowing spins allowing for the separation of two distinct pools. At long TRs, the fast flowing spins become less visible and only one pool can be observed.

To summarize, the STE sequence is interesting to go to long diffusion times and get a more accurate estimation of  $f_{IVIM} \times f_{fast}$  without being affected by inflow effects. Yet,  $f_{fast}$  might be slightly underestimated as this sequence is less sensitive to fast flowing blood vessels. However, if the goal of a study is to analyze both pools and find a difference in the relative volume fractions of the two pools between two populations or conditions, it would be better to use the SE sequence at short TRs as the two pools can be more easily separated.

#### 5.4 Influence of the diffusion encoding time

We have seen in Chapter 3 that, when going from  $\Delta = 14$  to  $34$  ms, the IVIM signal tends to become mono-exponential at  $\Delta = 34$  ms. To confirm this trend, we decided to further increase the diffusion encoding time. To achieve a longer  $\Delta$  of  $60$  ms, we changed the pulse sequence, compared to Chapter 3, and used the STE sequence.

Six rats were imaged with the STE sequence and the following acquisition parameters: 30  $b$ -values in the range  $[2-2600]$  s/mm<sup>2</sup>, diffusion gradient direction  $[X=0, Y=1, Z=0]$ ,  $TE/TR = 18/1500$  ms,  $\delta = 3$  ms,  $\Delta = 14, 30$  and  $60$  ms, in-plane resolution  $400 \times 400$   $\mu\text{m}^2$ , matrix size  $50 \times$

50, field of view 2 x 2 mm<sup>2</sup>, slice thickness 1.5 mm, 1 segment, 6 averages, 5 repetitions. The data were then analyzed as in the previous sections of this chapter.

$\Delta$ (ms)	14	30	60
$f_{IVIM}$ (%)	$3.17 \pm 0.33$	$3.60 \pm 0.50$	$3.51 \pm 0.24$
$f_{slow}$ (%)	$58.65 \pm 23.19$	$49.01 \pm 13.95$	-
$D^*_{slow}$ (10 <sup>-3</sup> mm <sup>2</sup> /s)	$4.96 \pm 3.20$	$4.04 \pm 1.89$	-
$D^*_{fast}$ (10 <sup>-3</sup> mm <sup>2</sup> /s)	$25.60 \pm 10.95$	$14.86 \pm 4.07$	-
$AIC_{cm}-AIC_{cb}$	$4.67 \pm 9.66$	$3.33 \pm 11.07$	$0.5 \pm 9.21$

Table 5.5. IVIM parameters for the three values of  $\Delta$  on an ROI on the LC ( $N_R = 6$ ).

For 4 out of 6 datasets, the signal was better fit to the mono-exponential model for  $\Delta = 60$  ms. As a result,  $f_{slow}$ ,  $D^*_{slow}$  and  $D^*_{fast}$  were not calculated for  $\Delta = 60$  ms. No significant difference was observed between the different values of  $\Delta$  for any of the parameter in Table 5.5. However, the difference between the AICc of the two models decreases much between  $\Delta = 30$  and 60 ms. This implies that the IVIM signal tends to have a mono-exponential behavior at long diffusion encoding times, further validating what was shown in Chapter 3.

To conclude this chapter, we have shown that:

- It is possible to relate the two vascular pools of the bi-exponential IVIM model to the capillaries with a blood velocity around 1.6 mm/s and to larger vessels, possibly medium-size arterioles and venules, with a higher blood velocity around 4.5 mm/s.
- The mono- or bi-exponential behavior of the IVIM signal depends on TR and the diffusion encoding time.
- It is not always possible to separate the two pools at long TRs and diffusion encoding times.
- The STE sequence is less sensitive to inflow effects and fast flowing blood vessels than the SE sequence.
- The pulse sequence and TR greatly influence the values of  $f_{IVIM}$  and  $f_{fast}$ .

In the next chapter, the IVIM technique is applied to the study of a neurodegenerative disease involving deterioration of the microvessels in the early phases of the disease: Alzheimer's disease.

## **Chapter 6: Application of IVIM imaging to the study of Alzheimer's disease**

As early biological changes in Alzheimer's disease involve damages to the blood vessels, we investigated the potential of IVIM to study Alzheimer's disease. This chapter first introduces the disease in terms of clinical symptoms as well as underlying biological changes. Imaging techniques used for its diagnosis and follow-up are then described to show how IVIM imaging can contribute to its study. The experiments performed during this thesis using a mouse model of the disease are then presented and analyzed.

### **6.1 Alzheimer's disease**

This section first gives a description of the disease and exposes the advantages that IVIM could have in its study compared to other currently used imaging techniques.

#### **6.1.1 Description of the disease**

Alzheimer's disease (AD), named after Alois Alzheimer who first described it in 1906 [156], is a neurodegenerative disease particularly affecting elderly people over 65 years old. An earlier onset can also happen to people in their 40s or 50s. Symptoms are progressive and worsen over time. The first to appear are usually memory lapses due to damages to the hippocampus which plays a central role in day-to-day memory. The diseased gradually lose their ability to remember, think, learn and live independently. The disease is usually fatal between 4 to 8 years after diagnosis. Before these symptoms can be detected clinically, biological changes occur. Abnormal aggregates of proteins form amyloid plaques and tau tangles in the brain. Once-healthy neurons loose connections to their neuronal network and eventually die leading to shrinkage of brain tissue. Cerebral capillaries are also affected at early stages of the disease having their basement membrane thickening and intramural amyloid deposits [157]. These changes induce capillary lumen distortions and decreased microcirculation as shown in Figure 6.1.B.



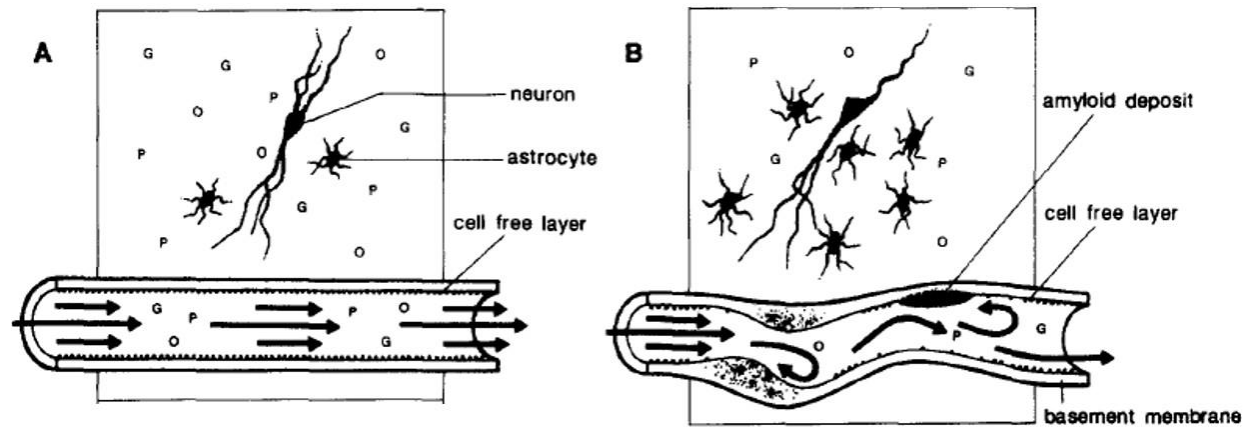


Figure 6.1. Sketch of a brain capillary surrounded by brain tissue in a normal brain and in case of AD. The drawing in (A) shows normal brain capillary with laminar flow (arrows) and optimal delivery of glucose (g), oxygen (o) and other proteins (p) to typical pyramidal neuron in CA1 sector of the hippocampus. A few astrocytes may be seen in the normal aged brain. (B) Brain capillary in AD shows basement membrane thickening, intramural deposits of amyloid fibrils and structural distortions causing variability in the luminal diameter. The segments of capillary distortions characterized by stenosis and dilation of the lumen, cause blood flow to become disturbed and to strip molecules of glucose, oxygen and proteins from the cell free layer, thus depriving neurons of optimal energy substrate delivery. Adapted from De la Torre et al [157].

There is currently no cure for AD but treatments exist to help with cognitive and behavioral symptoms. An early diagnosis of AD would give patients and their families a better chance to prepare for the future. In addition, it would give patients greater opportunities to participate in clinical trials testing possible new treatments or in other research studies.

### 6.1.2 Current imaging techniques used in clinics to diagnose and follow the disease

There is no single test to diagnose AD. The National Institute on Aging and the Alzheimer's Association published recommendations on diagnostic guidelines [158]. Initially, a clinical examination is performed including medical history screening, mental status testing, physical and neurological exams. Computed tomography or MRI can be used to rule out other causes of dementia. Then, only if the examination is conclusive are techniques measuring AD biomarkers used to confirm or infirm the diagnosis. But the institute does not advocate the use of these techniques for routine diagnosis because clinical criteria already offer good diagnostic accuracy and their too limited access. Imaging has the potential to play a major role in AD diagnose [159]. Structural MRI is able to measure brain atrophy which starts early and progresses with the disease [160]. Functional MRI is an indirect measure of neuronal activity and probes the

integrity of neuronal networks supporting memory and other cognitive domains which could be useful to evaluate a potential treatment of AD [161]. Fluorodeoxyglucose positron emission tomography (PET) is a biomarker of the overall brain metabolism [162]. Hypometabolism is observed when cognitive symptoms appear and can predict the rate of cognitive decline associated with AD. PET is also capable of imaging amyloid plaques [163]. ASL can measure brain atrophy along with regional cerebral hypoperfusion which was proven to be linked to glucose metabolism in AD patients [164],[165].

### 6.1.3 Potential of IVIM in the study of Alzheimer's disease

IVIM is already used in the study of many brain pathologies such as cancer [166] and stroke [112]. Its application to Parkinson's disease was recently proposed [114]. But IVIM has not yet been applied to the study of AD. IVIM benefits from all the advantages of MRI: its availability, safety because no ionizing radiation are used, etc. Economically, if we compare the costs of an imaging procedure with MRI (300 euros) against one with PET (1,200 euros including radiotracer), we cut down a lot the costs of the imaging sessions. PET also has limited availability and requires intravenous access and exposure to radioactivity. On the contrary, IVIM is completely non-invasive as no contrast agents are needed for its acquisitions. The closest competitor to IVIM is ASL. However, IVIM requires less RF power than ASL and is thus more adapted to repeated measurements (longitudinal studies). A key feature of IVIM diffusion MRI is that it does not involve contrast agents and it may serve as an interesting alternative to contrast-enhanced perfusion MRI in some patients with contraindications for contrast agents, such as patients with renal failure at risk for Nephrogenic Systemic Fibrosis (NSF) or patients requiring multiple MRI examinations, as gadolinium has been shown to accumulate in the brain. As seen in previous chapters, IVIM is also regionally specific and information rich as, within one acquisition, one can get diffusion and perfusion maps. Combining the information given by the evolution of the diffusion as well as the perfusion parameters, IVIM could be a valuable tool to detect and monitor AD evolution over time.

## 6.2 Material and methods

### 6.2.1 Animal model

The use of mouse models is beneficial in AD research as they are cheap to maintain, have short lifespans so symptoms appear faster and can target a single aspect of AD. Even if this aspect is not directly transferrable to humans, it is still useful to form a first hypothesis before expanding and testing it on more complicated models. They can also be used to test new treatments, using similar neuroimaging techniques that could be transferred to human studies in the future.

In this thesis, a transgenic mouse model of AD, APP/PS1, was used. The full name of this model is APP<sup>swe</sup>/PS1<sup>dE9</sup>. These mice overexpress the Swedish mutation of the amyloid precursor protein (APP) and presenilin 1 (PS1) deleted in exon 9 [167]. These animals develop amyloid plaques that can be observed as early as 4–6 months of age with abundant plaques in the hippocampus and cortex by 9 months. The plaques keep increasing up to around 12 months of age [168]. Activated microglia and astrocytes surround the ever growing deposits starting around six months. Tangles are not typical in these animals. Evidence of amyloid deposition in the vessel segments' membrane has been obtained for this model as early as 6 months of age [168]. An example of these deposits and the increase of their number over time in a representative vessel segment is shown in Figure 6.2.

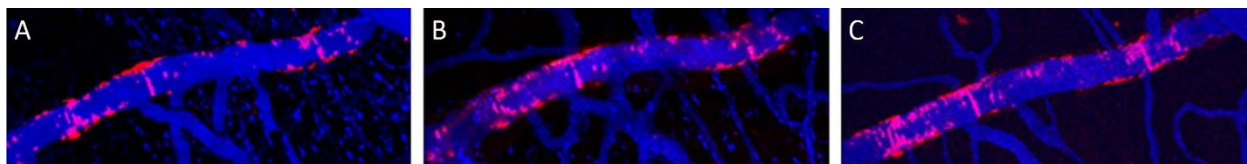


Figure 6.2. Illustrative example of amyloid angiopathy evolution, in a representative vessel segment of a 6-7-month old APP/PS1 mice. The imaging technique used is intravital multiphoton microscopy. Amyloid angiopathy deposits are shown in red and the angiogram in blue. The stains used are methoxy-XO4 and Texas Red dextran for amyloid plaques and vessel segments, respectively. (A) and (B) imaging sessions are separated by one week and the imaging session shown in (C) by 6 weeks from the one in (B). New senile plaques are observed in consecutive imaging sessions. Adapted from Garcia-Alloza et al [168].

APP/PS1 mice bred in the laboratory were used. As the breeding is quite recent, only 6-7-month mice could be scanned at the time the experiment was performed. The advantage of having an in-house breeding is that it is possible to follow the same mice longitudinally and monitor the

evolution of the disease. Additionally, as not all mice in the same litter are born with the disease, we have access to both APP/PS1 and control mice of the same age. Therefore six 6-7-month APP/PS1 and control mice were scanned.

To study the last stage of the disease, 21 to 24 months old APP/PS1 mice could be obtained from a collaboration with another research team and scanned as well. However, no control mice of the same age could be obtained.

### 6.2.2 MRI experiments and data processing

To take advantage of the cryoprobe available for the 11.7T MRI scanner in our laboratory, the experiments were performed on the 11.7T MRI scanner instead of the 7T MRI scanner. This cryoprobe dedicated to the study of the mice brain is a two-channel RF-coil cooled at 25 K which allows for a higher SNR compared to standard room temperature RF-coils allowing for higher spatial and temporal image resolution.

The mice were first anesthetized with 3 % inspired isoflurane in a 1:2 O<sub>2</sub>:air mixture during their installation on the bed. A catheter was inserted subcutaneously on the back of the mouse. A thin tubing was connected to the catheter and to a syringe pump with the syringe containing a 2 % medetomidine solution in NaCl. The isoflurane was then decreased to 2 %. After ensuring the animal was well positioned inside the scanner using scout scans, a bolus of medetomidine (Domitor, Pfizer, Karlsruhe, Germany) was injected to the animal using the syringe pump (0.092 mg/kg, s.c.). A continuous subcutaneous injection of medetomidine (0.13 mg/kg/h) was started right away. Isoflurane was progressively decreased and stopped 10 minutes later.

The design of this experiment is similar to the one already used in the previous chapters. To be able to distinguish well between the two vascular pools, a PGSE-EPI sequence with short TR was used. The acquisition parameters were set as follows: two diffusion gradient directions [X=1, Y=0, Z=0] and [X=0, Y=1, Z=0],  $\delta = 3$  ms,  $\Delta = 10$  and 20 ms, in-plane resolution 150 x 150  $\mu\text{m}^2$ , slice thickness 1 mm, 4 segments, TE/TR = 29/1000 ms, 2 averages, 6 repetitions, 9 slices, field of view 20 x 20 mm, matrix size 84 x 84, 29 b-values with 20 b-values in the range [2-500] s/mm<sup>2</sup> and 10 b-values in the range [600-2250] s/mm<sup>2</sup>. ROIs were drawn manually in a selection of slices in three different regions: the cortex (Ctx), the hippocampus (Hp) and the striatum (St).

They are displayed in Figure 6.3. The same data processing scheme used for the previous experiments was also applied to this experiment.

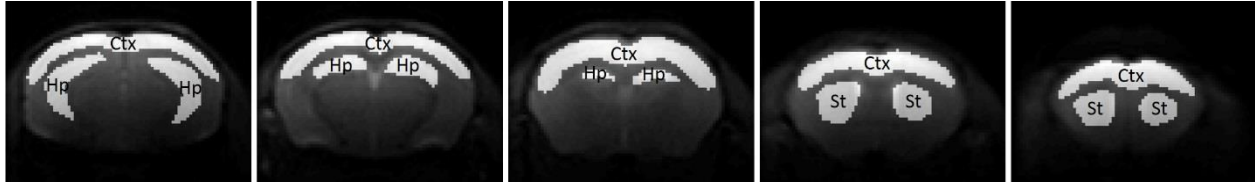


Figure 6.3. Example of the three ROIs drawn manually on the cortex (Ctx), the hippocampus (Hp) and the striatum (St). ROIs appear in white.

### 6.2.3 Statistical analysis

The statistical tests were performed using the R software [142]. To test if significant differences exist for the diffusion and IVIM parameters obtained for each ROI with the mouse type, control or APP/PS1 at the two different  $\Delta = 10$  and 20 ms, Student's t-tests were used. Before performing the Student's t-test, the assumptions of normality and homogeneity of variance were validated using Shapiro-Wilk and Bartlett's tests, respectively. If the normality assumption was not met, the Wilcoxon rank sum test was used instead of the Student's t-test. If the assumption of normality was met but not the one of homogeneity of variance, the Welch's t-test was performed. A p-value < 0.05 was considered statistically significant.

## 6.3 Results and discussion

### 6.3.1 Comparison of 6-month APP/PS1 and control mice

For each diffusion and IVIM parameter, the mean values  $\pm$  SD are gathered in Table 6.1 for each ROI,  $\Delta$  and mouse type, control or APP/PS1. Both mouse populations are 6 to 7 months old.

ROI	Parameter	Control mice		APP/PS1 mice	
		$\Delta = 10$ ms	$\Delta = 20$ ms	$\Delta = 10$ ms	$\Delta = 20$ ms
Ctx	$ADC_0$ ( $10^{-4}$ mm <sup>2</sup> /s)	$6.40 \pm 0.14$	$6.3 \pm 0.3$	$6.48 \pm 0.2$	$6.38 \pm 0.12$
	K	$0.68 \pm 0.02$	$0.53 \pm 0.08$	$0.67 \pm 0.03$	$0.53 \pm 0.05$
	$f_{IVIM}$ (%)	$5.14 \pm 0.37$	$5.4 \pm 0.34$	$5.27 \pm 0.63$	$5.59 \pm 0.76$
	$f_{fast}$ (%)	$73.76 \pm 4.37$	$62.38 \pm 21.19$	$78.32 \pm 3.57$	$69.89 \pm 10.45$
	$D^*_{slow}$ ( $10^{-3}$ mm <sup>2</sup> /s)	$4.79 \pm 0.88$	$6.35 \pm 4.1$	$7.28 \pm 5.34$	$6.26 \pm 2.55$
	$D^*_{fast}$ ( $10^{-3}$ mm <sup>2</sup> /s)	$29.14 \pm 4.3$	$23.85 \pm 7.03$	$34.53 \pm 8.11$	$24.07 \pm 5.08$

<b>Hp</b>	ADC <sub>0</sub> (10 <sup>-4</sup> mm <sup>2</sup> /s)	6.91 ± 0.14	6.78 ± 0.08	6.87 ± 0.13	6.83 ± 0.1
	K	0.75 ± 0.01	0.61 ± 0.04	0.72 ± 0.05	0.61 ± 0.03
	f <sub>IVIM</sub> (%)	5.92 ± 0.59	6.49 ± 0.66	5.61 ± 0.99	6.21 ± 1.15
	f <sub>fast</sub> (%)	40.55 ± 11.65	38.73 ± 11.05	42.45 ± 13.71	44.21 ± 18.86
	D* <sub>slow</sub> (10 <sup>-3</sup> mm <sup>2</sup> /s)	4.39 ± 0.36	4.91 ± 0.41	4.91 ± 0.99	5.46 ± 1.69
	D* <sub>fast</sub> (10 <sup>-3</sup> mm <sup>2</sup> /s)	19.5 ± 1.04	18.13 ± 1.16	22.32 ± 3.62	20.52 ± 5.23
<b>St</b>	ADC <sub>0</sub> (10 <sup>-4</sup> mm <sup>2</sup> /s)	6.37 ± 0.26	6.28 ± 0.36	6.63 ± 0.26	6.46 ± 0.38
	K	0.79 ± 0.06	0.67 ± 0.06	0.82 ± 0.08	0.68 ± 0.07
	f <sub>IVIM</sub> (%)	4.42 ± 0.84	4.8 ± 0.85	4.49 ± 1.33	5.5 ± 1.48
	f <sub>fast</sub> (%)	38.28 ± 12.59	47.24 ± 11.39	37.27 ± 17.6	44.94 ± 17.57
	D* <sub>slow</sub> (10 <sup>-3</sup> mm <sup>2</sup> /s)	4.19 ± 0.27	5.64 ± 3.12	4.32 ± 0.84	5.43 ± 2.89
	D* <sub>fast</sub> (10 <sup>-3</sup> mm <sup>2</sup> /s)	23.34 ± 1.94	23.51 ± 7.23	25.94 ± 4	25.16 ± 8.84

Table 6.1. Mean ± standard deviation of the diffusion and IVIM parameters for the three ROIs, cortex (Ctx), hippocampus (Hp) and striatum (St), the two  $\Delta = 10$  and 20 ms and the mouse type, control ( $N_M = 6$ ) or APP/PS1 ( $N_M = 6$ ).

No significant difference was found between the two mouse populations at any of the  $\Delta$ -values suggesting that neither diffusion nor IVIM parameters are able to distinguish between APP/PS1 and control mice at the age of 6 months. IVIM may not be able to detect a difference at 6 months of age but it would be interesting to scan these mice again at 9 months of age and also correlate the results with histology measurements to get information on the location of the amyloid plaques at that age.

Having the possibility to scan 21 to 24 months APP/PS1 mice, we also looked at the capability of IVIM imaging to monitor the evolution of the disease.

### 6.3.2 Comparison of young and old APP/PS1 mice

Five 21 to 24 months old APP/PS1 mice were imaged and compared to the six 6 to 7 months old APP/PS1 mice already presented in the previous subsection. Table 6.2 displays the mean ± standard deviation of the diffusion and IVIM parameters for the three ROIs, the two  $\Delta$  and the two ranges of age.

ROI	Parameter	Young APP/PS1 mice		Old APP/PS1 mice	
		$\Delta = 10$ ms	$\Delta = 20$ ms	$\Delta = 10$ ms	$\Delta = 20$ ms
Ctx	$ADC_0$ ( $10^{-4}$ mm <sup>2</sup> /s)	6.48 ± 0.2	6.38 ± 0.12	6.31 ± 0.12	6.07 ± 0.27
	K	0.67 ± 0.03	0.53 ± 0.05	0.74 ± 0.03	0.57 ± 0.03
	$f_{IVIM}$ (%)	5.27 ± 0.63	5.59 ± 0.76	4.63 ± 0.43	5.21 ± 0.42
	$f_{fast}$ (%)	78.32 ± 3.57	69.89 ± 10.45	79.54 ± 10.62	65.55 ± 18.95
	$D^*_{slow}$ ( $10^{-3}$ mm <sup>2</sup> /s)	7.28 ± 5.34	6.26 ± 2.55	4.39 ± 2.1	4.19 ± 1.5
	$D^*_{fast}$ ( $10^{-3}$ mm <sup>2</sup> /s)	34.53 ± 8.11	24.07 ± 5.08	35.31 ± 9.45	19.16 ± 3.62
Hp	$ADC_0$ ( $10^{-4}$ mm <sup>2</sup> /s)	6.87 ± 0.13	6.83 ± 0.1	6.94 ± 0.22	6.78 ± 0.28
	K	0.72 ± 0.05	0.61 ± 0.03	0.79 ± 0.04	0.64 ± 0.05
	$f_{IVIM}$ (%)	5.61 ± 0.99	6.21 ± 1.15	5.94 ± 1.3	7.55 ± 2.4
	$f_{fast}$ (%)	42.45 ± 13.71	44.21 ± 18.86	30.37 ± 3.57	39.55 ± 15.57
	$D^*_{slow}$ ( $10^{-3}$ mm <sup>2</sup> /s)	4.91 ± 0.99	5.46 ± 1.69	5.23 ± 0.6	5.05 ± 1.03
	$D^*_{fast}$ ( $10^{-3}$ mm <sup>2</sup> /s)	22.32 ± 3.62	20.52 ± 5.23	22.3 ± 2.93	17.33 ± 4.02
St	$ADC_0$ ( $10^{-4}$ mm <sup>2</sup> /s)	6.63 ± 0.26	6.46 ± 0.38	6.28 ± 0.16	6.23 ± 0.21
	K	0.82 ± 0.08	0.68 ± 0.07	0.84 ± 0.04	0.77 ± 0.08
	$f_{IVIM}$ (%)	4.49 ± 1.33	5.5 ± 1.48	3.75 ± 0.92	5.02 ± 1.38
	$f_{fast}$ (%)	37.27 ± 17.6	44.94 ± 17.57	40.56 ± 20.35	56.14 ± 20.56
	$D^*_{slow}$ ( $10^{-3}$ mm <sup>2</sup> /s)	4.32 ± 0.84	5.43 ± 2.89	4.66 ± 1.03	6.97 ± 3.52
	$D^*_{fast}$ ( $10^{-3}$ mm <sup>2</sup> /s)	25.94 ± 4	25.16 ± 8.84	27.56 ± 6.04	24.96 ± 9.57

Table 6.2. Mean ± standard deviation of the diffusion and IVIM parameters for the three ROIs, cortex (Ctx), hippocampus (Hp) and striatum (St), the two  $\Delta = 10$  and 20 ms and the APP/PS1 mouse age, young between 6 and 7 months ( $N_M = 6$ ) and old between 21 and 24 months ( $N_M = 5$ ).

Significant differences with the mouse age were found only for  $ADC_0$  and  $K$ . The p-values of the statistical tests are displayed in Table 6.3.

ROI	$ADC_0$		K	
	$\Delta = 10$ ms	$\Delta = 20$ ms	$\Delta = 10$ ms	$\Delta = 20$ ms
Ctx	0.15	0.035	0.010†	0.16†
Hp	0.53	0.75†	0.048	0.18
St	0.026	0.23	0.58	0.090

Table 6.3. P-values of Student's t-test corresponding to  $ADC_0$  and  $K$  for the two  $\Delta$ -values, 10 and 20 ms and the three ROIs, cortex (Ctx), hippocampus (Hp) and striatum (St). † indicates that the Wilcoxon rank sum test was used instead of Student's t-test. P-values < 0.05 are highlighted in red.

A significant difference can be found in  $ADC_0$  with the mouse age in the cortex for  $\Delta = 20$  ms and in the striatum for  $\Delta = 10$  ms but not in the hippocampus. In these regions,  $ADC_0$  decreases with increasing mouse age.

$ADC_0$  is expected to increase in AD patients compared to controls because of loss of myelin and damage to cell membranes consequently increasing the extracellular spaces available for the water molecules to diffuse in [169]. Significant increases in  $ADC_0$  have been observed in AD patients compared to controls in many different brain regions including the hippocampus and the frontal and parietal GM [170]. However, comparing young and old APP/PS1 mice, our study shows a decrease in  $ADC_0$  in aged mice. The studies found in the literature always compare APP/PS1 mice with control mice of the same age, maybe there is a trend at the late stages of the disease of  $ADC_0$  to decrease. This trend would have to be confirmed by scanning more animals in the two populations and control animals of the same age.

$K$  is also significantly different with the mouse age in the cortex and the hippocampus for  $\Delta = 10$  ms. It increases with the mouse age. Reports from the literature using diffusion kurtosis imaging (DKI) had observed such an increase in the cortex comparing 16-month old APP/PS1 and control mice but no significant difference in the hippocampus [171].

However, no significant difference is observed with the IVIM parameters with the mouse age. The best way to analyze the data would have been to compare the 21-24 month-APP/PS1 mice to control mice of the same age. Unfortunately, we could not scan control mice of that age. Maybe, if this comparison had been performed, differences in IVIM parameters would have been seen between APP/PS1 and control mice. Nevertheless, more animals would need to be scanned to confirm the results obtained here by comparing diffusion parameters as some of them are in disagreement with the literature.



## 6.4 Conclusion

IVIM has the potential to help in the diagnosis and monitoring of the evolution of AD because it is able to extract diffusion as well as perfusion parameters from the imaged tissues. The study performed here was not able to detect a difference in IVIM/diffusion parameters with the APP/PS1 mouse model used at 6 months of age. Control mice of 21 to 24 months old would have to be scanned and compared to the 21 to 24-month APP/PS1 mice to confirm the findings presented in this chapter on the diffusion parameters. This study would also benefit from a larger number of scanned animals. Other parameters such as fractional anisotropy or even perfusion anisotropy could also be studied to better characterize the disease. They can both be measured using IVIM. IVIM still has much to offer and the application of this technique to diseases involving impairments of the microcirculation should be continued.

## Chapter 7: Summary and conclusion

The final chapter of this thesis gives a summary, discusses some of the limitations of this work and possible improvements before exposing leads for future work and ending with a general conclusion.

### 7.1 Summary

Throughout this thesis, we have sought to give a better understanding of the origins of the IVIM signal using mathematical modelling, numerical simulations and experimental validation. In summary, we have demonstrated that the IVIM technique is sensitive to more than just water protons flowing in the capillary network. The IVIM signal is better described by a bi-exponential model representing the combination of two vascular pools. One of them, the slow pool, corresponds to the capillary network and is characterized by a slower blood velocity than the other pool, the fast pool, which is thought to be related to larger vessels, possibly medium-size arterioles and venules. The influence of acquisition parameters on the IVIM signal model parameters was also studied. At short repetition times compared to the  $T_1$  of blood, the contribution of the fast flowing blood vessels to the signal attenuation is increased due to inflow effects. Therefore,  $f_{IVIM}$  and  $f_{fast}$  tend to be overestimated at short TRs. Using the STE instead of the SE pulse sequence allows to go to longer diffusion times and be less sensitive to inflow effects. However,  $f_{fast}$  might be underestimated using the STE sequence. As the bi-exponential IVIM model converges into the mono-exponential IVIM model at long diffusion times, one should use short diffusion times in order to measure  $f_{fast}$ ,  $D_{slow}^*$  and  $D_{fast}^*$ . Finally, the IVIM technique with the proposed bi-exponential model was applied to the study of AD in an APP/PS1 mouse model. No significant difference in the diffusion or IVIM parameters was obtained between 6-month control and APP/PS1 mice. When comparing young and old APP/PS1 mice, significant differences were obtained for the diffusion parameters,  $ADC_0$  and  $K$ . In accordance with previous reports from the literature,  $K$  increases with the APP/PS1 mouse age in the cortex and the hippocampus, although not reported in the literature for the latter. However, in our study,  $ADC_0$  decreases whereas it has been shown to increase in the literature. No significant difference has been shown in the IVIM parameters with the mouse age. These

results need further confirmation and a follow-up of the same mice at different ages along with control mice of the same age would maybe reveal the potential of the IVIM technique to study the appearance and follow-up of this disease.

## 7.2 Limitations and possible improvements

This work is subject to several limitations. Some of them are detailed in this section and ways to deal with them are suggested.

### 7.2.1 Experimental protocol: anesthesia

One major variable directly impacting the blood flow which was not discussed before in this thesis is the anesthesia. All actions and impacts of anesthetics are still not completely well understood. However, their effect on the cerebral blood flow has been extensively studied. Anesthetics have different effects depending on their type.

During this thesis, two different anesthetics were used: isoflurane and medetomidine. Like the other inhaled anesthetics, isoflurane allows for a better control over the length and depth of the anesthesia, as opposed to injectable anesthetics [172]. It is believed to be safe and easy to maintain with a quick and uneventful recovery. However, inhaled anesthetics produce a dose-dependent increase in CBF [173]. This effect is more pronounced with isoflurane than with other inhaled anesthetics. On the contrary, medetomidine is an injectable anesthetic which requires intravenous or subcutaneous access. It causes vasoconstriction of the cerebral arteries which leads to reduced CBF [174]. These effects of the two anesthetics have also been observed during this thesis as TOF-MRA images under both anesthetics could be acquired on a mouse on the 11.7T.

Two examples of the maximum intensity projection rendering of a 3D-TOF MRA sequence of a mouse brain are given in Figure 7.1. For the left image, the sequence was acquired with the mouse under isoflurane anesthesia while it was under medetomidine anesthesia for the right image. We observe that the vessels are less visible in the image on the right compared to the image on the left.

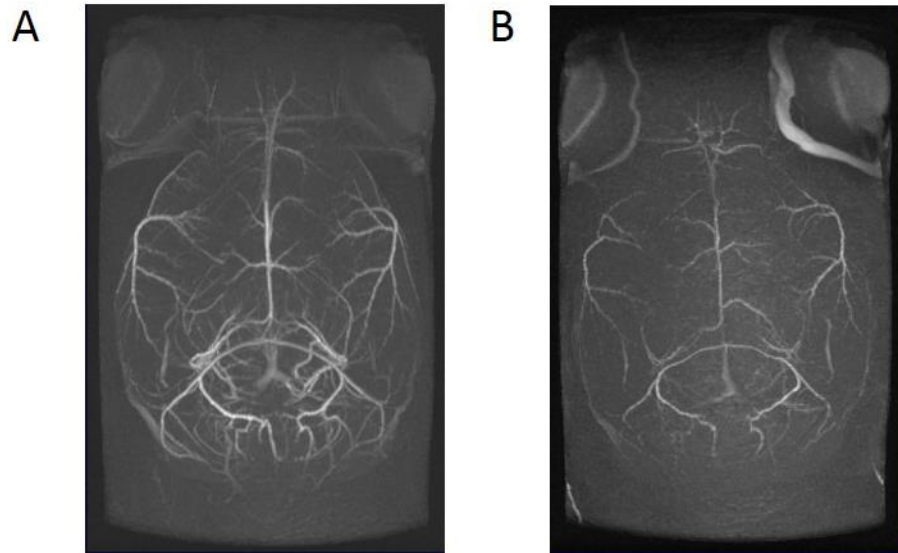


Figure 7.1. Maximum intensity projection of a 3D-TOF MRA sequence of a mouse brain acquired on the 11.7T scanner with two different anesthesia conditions: (A) isoflurane and (B) medetomidine.

Differences between these two anesthetics have already been observed by Ciobanu et al [175]. They show that changes in physiological parameters such as CBF, tissue oxygenation and vasodilation cause differences in the vessel-tissue contrast in  $T_2^*$ -weighted images. In TOF images, as vessels with higher blood flow and thus larger lumen diameter generate higher vessel-tissue contrast, the difference between our two images is most likely due to the dilation and constriction effects of isoflurane and medetomidine, respectively. Additionally, as the CBF is altered, the oxygen level is likely to change as well. As a result, the  $T_2$  value of the vessel pool varies and this can be another explanation for the difference observed between the two images.

As such, one has to keep in mind that, for animal experiments, the anesthetic used can influence the results obtained. During this thesis, the rat experiments were performed under isoflurane anesthesia. Most of the results obtained did not need an absolute quantification of the perfusion parameters so the choice of anesthetic was not essential. However, the values obtained for the blood flow velocities of the two pools after the comparison with the dictionary of simulated signals might be overestimated due to the vasodilation effect of isoflurane. As the goal of the mouse study was to observe a significant difference in the perfusion parameters and the vasoconstrictor effect of medetomidine is less pronounced than the vasodilatory effect of

isoflurane, isoflurane was replaced by medetomidine anesthesia for these series of experiments.

Recently, another intravenous anesthetic has been proposed: etomidate [176]. It acts rapidly and basal CBF values were found to be substantially lower when compared to isoflurane. This anesthetic has been shown to be compatible for use in more mouse strains than medetomidine. Etomidate could also be a good alternative to isoflurane and be used on more mouse strains than medetomidine.

### 7.2.2 Data analysis: diffusion coefficient of water in blood

In this work, a constant value for the coefficient of water in blood,  $D_b$ , has been assumed. However, its value varies with  $\Delta$  and the size of the vessels [154].

In blood, water can be located inside the plasma, the RBCs and the macromolecules. However, the movement of the macromolecules is slow so the diffusion of the macromolecules can be neglected. Depending on the value of  $\Delta$  and the vessel diameter,  $d$ , water exchanges between the RBCs and the plasma need to be considered or can be neglected. The one-dimensional diffusion distance can be expressed as  $\sqrt{2D\Delta}$  with  $D$  the diffusion coefficient along this dimension. When  $\sqrt{2D\Delta} < d$ , exchanges can be neglected as only a small number of molecules hit the cell walls. On the contrary when  $\sqrt{2D\Delta} > d$ , many molecules hit the cell walls and the exchange rate between the RBCs and the plasma needs to be taken into consideration. The exchange rate is most likely different between vessels of the two pools as the difference in blood flow velocities and shape of the RBCs are likely to impact its value. The value for  $D_b$  can influence both  $D_{slow}^*$  and  $D_{fast}^*$  values and it would be interesting to measure it properly.

### 7.2.3 Improvements of the numerical simulations

Branching of vessels was not considered in the simulations but it is important to really describe the complexity of microvascular networks. Hierarchical structures as presented in section 1.3.4.2 could be used as a first approximation to model the branching of vessels.

As our bi-exponential IVIM model also includes a fast flowing pool, a laminar flow velocity profile should be used when modelling the IVIM signal of the fast pool. A way to mathematically

model flow with a laminar velocity profile has already been proposed [177]. It would be relatively straightforward to add this change in flow velocity profile to the simulations. Also, plasma viscosities and RBC folding effects could be taken into account when laminar flow is considered.

Additionally, the vessel lumen diameter could be added as a structural parameter in the simulations. A relationship between the vessel lumen diameter and the blood velocity would be needed to keep coherence with a real vascular network. For example, a model inspired from the network models of flow impedance for cardiovascular applications could be used [178]. A laminar flow profile could be imposed from a certain diameter value. All vessels with a diameter above this threshold diameter would be associated with a laminar flow profile.

Section 1.3.4.2 highlighted the importance of diffusive transport for a vascular network to be fully functional. Although in IVIM, exchanges with the extravascular space are neglected, it could be relevant to take them into account and simulate them in pathologies for which the BBB is impaired, i.e. in cancers.

### 7.3 Future work

Advances in the understanding of the origins of the IVIM signal have opened the door to more possible applications for the IVIM technique. Being sensitive to the capillaries and larger vessels smaller than arteries gives IVIM advantages over techniques such as MRA which are only sensitive to large vessels. Imaging techniques usually study either the capillaries or the very large vessels and not the medium-size vessels. It can be interesting for example to follow a disease which first affects the capillaries and then spreads to medium-size vessels and diagnose the disease with some kind of grading. IVIM could help diagnose for the right type of vasculitis which can affect small as well as large vessels. The proposed bi-exponential model could provide additional information about diseases already studied with IVIM such as for cancer and stroke.

Animal experiments would clearly benefit from a study on the effects of anesthetics on the values of the IVIM parameters. It would help choose the right anesthesia best matching to each study.

Now that we have established that the IVIM technique consists of two pools with different vascular characteristics, it would be interesting to better model the IVIM signal by applying the improvements suggested in the previous section to the numerical simulations. This would allow for a better description of the second vascular pool and help monitor changes in the blood velocity of this second pool as well. With the current simulations and acquisition parameters, we have not been able to give precise estimations of the segment length. Other strategies could be considered, such as combining the data acquisition from multiple diffusion times in a model like Kennan's or acquire data with long diffusion encoding times and compare them to simulated data. To get further information from the networks, joint IVIM and ASL acquisitions could be considered [179] or the use of flow-compensated and non-flow-compensated gradients [117]. These different acquisitions schemes could also be simulated.

Finally, the results obtained in the study of APP/PS1 mice need confirmation and a longitudinal study of the disease would help understand the changes operating in the aging AD model. At each step, comparison with control mice would be needed to assess that the changes observed are not the result of normal aging.

#### 7.4 General conclusion

The IVIM technique has a great potential to help diagnose and monitor diseases involving disruption of the microvascular network. The many advantages of the IVIM technique make it fit to image patients with contraindications for contrast agents or requiring repeated MRI examinations. The goal of this thesis has been to improve our understanding of the technique and take a few more steps toward the realization of this potential. The application of IVIM to the study of AD needs further investigation to really determine its potential. But the proposed bi-exponential model for the IVIM signal raises interest for the more complete study of numerous diseases such as cancer, stroke and other neurodegenerative diseases with IVIM.

# Bibliography

1. Le Bihan D, Breton E, Lallemand D, Aubin ML, Vignaud J, Laval-Jeantet M. Separation of diffusion and perfusion in intravoxel incoherent motion MR imaging. *Radiology*, 1988; 168: 497-505.
2. Leningher A. Principles of Biochemistry 3rd Edition. Worth Publishers (Ed.). 2000.
3. Clarke E, O'Malley C. The Human Brain and Spinal Cord, a Histological Study Illustrated by Writings from Antiquity to the Twentieth Century. San Francisco: Norman (Ed.). 1996.
4. Fields RD. White matter matters. *Sci. Am.*, 2008; 298: 42-49.
5. Sokoloff L. The physiological and biochemical bases of functional brain imaging. *Cogn Neurodyn*, 2008; 2: 1-5.
6. Zlokovic BV, Apuzzo ML. Strategies to circumvent vascular barriers of the central nervous system. *Neurosurgery*, 1998; 43: 877-878.
7. Bickler PE, Donohoe PH. Adaptive responses of vertebrate neurons to hypoxia. *J. Exp. Biol.*, 2002; 205: 3579-3586.
8. Liu Z, Tian R, An W, Zhuge Y, Li Y, Shao H et al. Identification of E-selectin as a novel target for the regulation of postnatal neovascularization: implications for diabetic wound healing. *Ann. Surg.*, 2010; 252: 625-634.
9. Hur J, Yoon C, Lee C, Kim T, Oh I, Park K et al. Akt is a key modulator of endothelial progenitor cell trafficking in ischemic muscle. *Stem Cells*, 2007; 25: 1769-1778.
10. Ding D, Shyu W, Lin S, Li H. The role of endothelial progenitor cells in ischemic cerebral and heart diseases. *Cell Transplant*, 2007; 16: 273-284.
11. Laschke MW, Giebels C, Menger MD. Vasculogenesis: a new piece of the endometriosis puzzle. *Hum. Reprod. Update*, 2011; 17: 628-636.
12. Carmeliet P, Tessier-Lavigne M. Common mechanisms of nerve and blood vessel wiring. *Nature*, 2005; 436: 193-200.
13. Zheng D, LaMantia AS, Purves D. Specialized vascularization of the primate visual cortex. *J. Neurosci.*, 1991; 11: 2622-2629.
14. Hirschi KK, Skalak TC, Peirce SM, Little CD. Vascular assembly in natural and engineered tissues. *Ann. N. Y. Acad. Sci.*, 2002; 961: 223-242.
15. Iqbal S. A comprehensive study of the anatomical variations of the circle of willis in adult human brains. *J Clin Diagn Res*, 2013; 7: 2423-2427.
16. Ezzatian-Ahar S, Amin FM, Obaid HG, Arngrim N, Hougaard A, Larsson HBW et al. Migraine without aura is not associated with incomplete circle of Willis: a case-control study using high-resolution magnetic resonance angiography. *J Headache Pain*, 2014; 15: 27.



17. Cucchiara B, Detre J. Migraine and circle of Willis anomalies. *Med. Hypotheses*, 2008; 70: 860-865.
18. Shih AY, Driscoll JD, Drew PJ, Nishimura N, Schaffer CB, Kleinfeld D. Two-photon microscopy as a tool to study blood flow and neurovascular coupling in the rodent brain. *J. Cereb. Blood Flow Metab.*, 2012; 32: 1277-1309.
19. Freitas Jr. R. *Nanomedicine, Volume I: Basic Capabilities*. Landes Bioscience, Georgetown, TX (Ed.). 1999.
20. Schoonover C. *Portraits of the mind: visualizing the brain from antiquity to the 21st century*. Abrams (Ed.). 2010.
21. Duvernoy HM, Delon S, Vannson JL. Cortical blood vessels of the human brain. *Brain Res. Bull.*, 1981; 7: 519-579.
22. Tata DA, Anderson BJ. A new method for the investigation of capillary structure. *J. Neurosci. Methods*, 2002; 113: 199-206.
23. Tsai PS, Kaufhold JP, Blinder P, Friedman B, Drew PJ, Karten HJ et al. Correlations of neuronal and microvascular densities in murine cortex revealed by direct counting and colocalization of nuclei and vessels. *J. Neurosci.*, 2009; 29: 14553-14570.
24. Lu H, Clingman C, Golay X, van Zijl PCM. Determining the longitudinal relaxation time (T<sub>1</sub>) of blood at 3.0 Tesla. *Magn Reson Med*, 2004; 52: 679-682.
25. Laursen H, Diemer NH. Capillary size and density in the cerebral cortex of rats with a porto-caval anastomosis. *Acta Neuropathol*, 1977; 40: 117-122.
26. Bannister RG, Romanul FC. The localization of alkaline phosphatase activity in cerebral blood vessels. *J. Neurol. Neurosurg. Psychiatr.*, 1963; 26: 333-340.
27. Glaser EM, Van der Loos H. Analysis of thick brain sections by obverse-reverse computer microscopy: application of a new, high clarity Golgi-Nissl stain. *J. Neurosci. Methods*, 1981; 4: 117-125.
28. Miguel-Hidalgo JJ, Jiang W, Konick L, Overholser JC, Jurjus GJ, Stockmeier CA et al. Morphometric analysis of vascular pathology in the orbitofrontal cortex of older subjects with major depression. *Int J Geriatr Psychiatry*, 2013; 28: 959-970.
29. Li Y, Song Y, Zhao L, Gaidosh G, Laties AM, Wen R. Direct labeling and visualization of blood vessels with lipophilic carbocyanine dye DiI. *Nat Protoc*, 2008; 3: 1703-1708.
30. Weiss HR, Buchweitz E, Murtha TJ, Auletta M. Quantitative regional determination of morphometric indices of the total and perfused capillary network in the rat brain. *Circ. Res.*, 1982; 51: 494-503.
31. Blinder P, Tsai PS, Kaufhold JP, Knutsen PM, Suhl H, Kleinfeld D. The cortical angiome: an interconnected vascular network with noncolumnar patterns of blood flow. *Nat. Neurosci.*, 2013; 16: 889-897.

32. Moy AJ, Wiersma MP, Choi B. Optical histology: a method to visualize microvasculature in thick tissue sections of mouse brain. *PLoS One*, 2013; 8: e53753.
33. Hashimoto H, Kusakabe M, Ishikawa H. A novel method for three-dimensional observation of the vascular networks in the whole mouse brain. *Microsc. Res. Tech.*, 2008; 71: 51-59.
34. Li A, Gong H, Zhang B, Wang Q, Yan C, Wu J et al. Micro-optical sectioning tomography to obtain a high-resolution atlas of the mouse brain. *Science*, 2010; 330: 1404-1408.
35. Wu J, He Y, Yang Z, Guo C, Luo Q, Zhou W et al. 3D BrainCV: simultaneous visualization and analysis of cells and capillaries in a whole mouse brain with one-micron voxel resolution. *Neuroimage*, 2014; 87: 199-208.
36. Xue S, Gong H, Jiang T, Luo W, Meng Y, Liu Q et al. Indian-ink perfusion based method for reconstructing continuous vascular networks in whole mouse brain. *PLoS One*, 2014; 9: e88067.
37. Mayerich D, Abbott L, McCormick B. Knife-edge scanning microscopy for imaging and reconstruction of three-dimensional anatomical structures of the mouse brain. *J Microsc*, 2008; 231: 134-143.
38. Mayerich D, Kwon J, Sung C, Abbott L, Keyser J, Choe Y. Fast macro-scale transmission imaging of microvascular networks using KESM. *Biomed Opt Express*, 2011; 2: 2888-2896.
39. Minnich B, Lametschwandtner A. Scanning electron microscopy and vascular corrosion casting for the characterization of microvascular networks in human and animal tissues. *Microscopy: Science, Technology, Applications and Education*, A. Méndes-Vilas and J.Díaz Alvarez (Eds), 2011; 1: 29-39.
40. Dorr A, Sled JG, Kabani N. Three-dimensional cerebral vasculature of the CBA mouse brain: a magnetic resonance imaging and micro computed tomography study. *Neuroimage*, 2007; 35: 1409-1423.
41. Pathak AP, Kim E, Zhang J, Jones MV. Three-dimensional imaging of the mouse neurovasculature with magnetic resonance microscopy. *PLoS One*, 2011; 6: e22643.
42. Cassot F, Lauwers F, Fouard C, Prohaska S, Lauwers-Cances V. A novel three-dimensional computer-assisted method for a quantitative study of microvascular networks of the human cerebral cortex. *Microcirculation*, 2006; 13: 1-18.
43. Pawlik G, Rackl A, Bing RJ. Quantitative capillary topography and blood flow in the cerebral cortex of cats: an in vivo microscopic study. *Brain Res.*, 1981; 208: 35-58.
44. Lauwers F, Cassot F, Lauwers-Cances V, Puwanarajah P, Duvernoy H. Morphometry of the human cerebral cortex microcirculation: general characteristics and space-related profiles. *Neuroimage*, 2008; 39: 936-948.
45. Craigie E. The vascular supply of the archicortex of the rat IV. Inbred albino rats. *Journal of Comparative Neurology*, 1932; 55: 443-451.

46. Hunziker O, Emmenegger H, Frey H, Schulz U, Meier-Ruge W. Morphometric characterization of the capillary network in the cat's brain cortex: a comparison of the physiological state and hypovolemic conditions. *Acta Neuropathol*, 1974; 29: 57-63.
47. Meier-Ruge W, Hunziker O, Schulz U, Tobler HJ, Schweizer A. Stereological changes in the capillary network and nerve cells of the aging human brain. *Mech. Ageing Dev.*, 1980; 14: 233-243.
48. Ivanov KP, Kalinina MK, Levkovich Yul. Blood flow velocity in capillaries of brain and muscles and its physiological significance. *Microvasc. Res.*, 1981; 22: 143-155.
49. Ben Hamida C, Bisconte JC, Margules S. Postnatal maturation of the vascularisation of the suprasylvian gyrus of the cat. *J. Anat.*, 1983; 137 (Pt 2): 371-385.
50. Villringer A, Them A, Lindauer U, Einhupl K, Dirnagl U. Capillary perfusion of the rat brain cortex. An in vivo confocal microscopy study. *Circ. Res.*, 1994; 75: 55-62.
51. Lu M, Zhang ZG, Chopp M. Analysis of cerebral microvascular architecture--application to cortical and subcortical vessels in rat brain. *J. Neurosci. Methods*, 2004; 138: 81-87.
52. Hauck EF, Apostel S, Hoffmann JF, Heimann A, Kempfski O. Capillary flow and diameter changes during reperfusion after global cerebral ischemia studied by intravital video microscopy. *J. Cereb. Blood Flow Metab.*, 2004; 24: 383-391.
53. Michaloudi H, Batzios C, Grivas I, Chiotelli M, Papadopoulos GC. Developmental changes in the vascular network of the rat visual areas 17, 18 and 18a. *Brain Res.*, 2006; 1103: 1-12.
54. Hudetz AG. Blood flow in the cerebral capillary network: a review emphasizing observations with intravital microscopy. *Microcirculation*, 1997; 4: 233-252.
55. Unekawa M, Tomita M, Takashi O, Tomita Y, Toriumu H, Tatarishvili J et al. Frequency distribution function of red blood cell velocities in single capillaries of the rat cerebral cortex using intravital laser-scanning confocal microscopy with highspeed camera. *Asian Biomed*, 2008; 2: 203-218.
56. Wang T, Xing Z. Characterization of blood flow in capillaries by numerical simulation. *Journal of modern physics*, 2010; 1: 349-356.
57. Suter SP, Seshadri V, Croce PA, Hochmuth RM. Capillary blood flow. II. Deformable model cells in tube flow. *Microvasc. Res.*, 1970; 2: 420-433.
58. Fernandez-Klett F, Offenhauser N, Dirnagl U, Priller J, Lindauer U. Pericytes in capillaries are contractile in vivo, but arterioles mediate functional hyperemia in the mouse brain. *Proc. Natl. Acad. Sci. U.S.A.*, 2010; 107: 22290-22295.
59. Vennemann P, Kiger KT, Lindken R, Groenendijk BCW, Stekelenburg-de Vos S, ten Hagen TLM et al. In vivo micro particle image velocimetry measurements of blood-plasma in the embryonic avian heart. *J Biomech*, 2006; 39: 1191-1200.

60. Stücker M, Baier V, Reuther T, Hoffmann K, Kellam K, Altmeyer P. Capillary blood cell velocity in human skin capillaries located perpendicularly to the skin surface: measured by a new laser Doppler anemometer. *Microvasc. Res.*, 1996; 52: 188-192.
61. Demené C, Tiran E, Sieu L, Bergel A, Gennisson JL, Pernot M et al. 4D microvascular imaging based on ultrafast Doppler tomography. *Neuroimage*, 2016; 127: 472-483.
62. Fedosov D, Caswell B, Popel A, Karniadakis G. Blood flow and cell-free layer in microvessels. *Microcirculation*, 2010; 17: 615-628.
63. Stokes G. On the effect of the internal friction of fluids on the motion of pendulums. *Transactions of the cambridge philosophical society*, 1851; 9: 8-106.
64. Reynolds O. An experimental investigation of the circumstances which determine whether the motion of water shall be direct or sinuous, and of the law of resistance in parallel channels. *Phil. Trans. R. Soc. Lond.*, 1883; 174: 935-982.
65. Lorthois S, Cassot F. Fractal analysis of vascular networks: insights from morphogenesis. *J. Theor. Biol.*, 2010; 262: 614-633.
66. Linninger AA, Gould IG, Marinnan T, Hsu C, Chojecki M, Alaraj A. Cerebral microcirculation and oxygen tension in the human secondary cortex. *Ann Biomed Eng*, 2013; 41: 2264-2284.
67. Pries AR, Secomb TW. Making microvascular networks work: angiogenesis, remodeling, and pruning. *Physiology (Bethesda)*, 2014; 29: 446-455.
68. Boas DA, Jones SR, Devor A, Huppert TJ, Dale AM. A vascular anatomical network model of the spatio-temporal response to brain activation. *Neuroimage*, 2008; 40: 1116-1129.
69. Zagzoule M, Marc-Vergnes JP. A global mathematical model of the cerebral circulation in man. *J Biomech*, 1986; 19: 1015-1022.
70. Su S, Catherall M, Payne S. The influence of network structure on the transport of blood in the human cerebral microvasculature. *Microcirculation*, 2012; 19: 175-187.
71. Prim R. Shortest connection networks and some generalizations. *Bell System Technical Journal*, 1957; 36: 1389-1401.
72. Rabi I, Millman S, Kusch P, Zacharias J. The Molecular Beam Resonance Method for Measuring Nuclear Magnetic Moments. The Magnetic Moments of  $^3\text{Li}6$ ,  $^3\text{Li}7$  and  $^9\text{F}19$ . *Physical Review*, 1939; 55: 526-535.
73. Purcell E, Torrey H, Pound R. Resonance Absorption by Nuclear Magnetic Moments in a Solid. *Phys Rev*, 1946; 69: 37-38.
74. Bloch F, Hansen W, Packard M. Nuclear Induction. *Phys Rev*, 1946; 69: 127.
75. Lauterbur P. Image Formation by Induced Local Interactions - Examples Employing Nuclear Magnetic-Resonance. *Nature*, 1973; 242: 553-576.

76. Mansfield P. Proton Spin Imaging by Nuclear Magnetic-Resonance. *Contemp Phys*, 1976; 17: 553-576.
77. Haacke E, Brown R, Thompson M, Venkatesan R. Magnetic resonance imaging: physical principles and sequence design. Wiley (Ed.). 1999.
78. Dobre MC, Uğurbil K, Marjanska M. Determination of blood longitudinal relaxation time (T1) at high magnetic field strengths. *Magn Reson Imaging*, 2007; 25: 733-735.
79. Lin A, Qin Q, Zhao X, Duong TQ. Blood longitudinal (T1) and transverse (T2) relaxation time constants at 11.7 Tesla. *MAGMA*, 2012; 25: 245-249.
80. Zhao JM, Clingman CS, Närväinen MJ, Kauppinen RA, van Zijl PCM. Oxygenation and hematocrit dependence of transverse relaxation rates of blood at 3T. *Magn Reson Med*, 2007; 58: 592-597.
81. Atalay MK, Reeder SB, Zerhouni EA, Forder JR. Blood oxygenation dependence of T1 and T2 in the isolated, perfused rabbit heart at 4.7T. *Magn Reson Med*, 1995; 34: 623-627.
82. Krishnamurthy LC, Liu P, Xu F, Uh J, Dimitrov I, Lu H. Dependence of blood T(2) on oxygenation at 7 T: in vitro calibration and in vivo application. *Magn Reson Med*, 2014; 71: 2035-2042.
83. Lee SP, Silva AC, Ugurbil K, Kim SG. Diffusion-weighted spin-echo fMRI at 9.4 T: microvascular/tissue contribution to BOLD signal changes. *Magn Reson Med*, 1999; 42: 919-928.
84. de Graaf RA, Brown PB, McIntyre S, Nixon TW, Behar KL, Rothman DL. High magnetic field water and metabolite proton T1 and T2 relaxation in rat brain in vivo. *Magn Reson Med*, 2006; 56: 386-394.
85. Hahn E. Spin Echoes. *Physical Review*, 1950; 80: 580-594.
86. Kingsley P. Product Operators, Coherence Pathways, and Phase Cycling. Part II. Coherence Pathways in Multipulse Sequences: Spin Echoes, Stimulated Echoes, and Multiple-Quantum Coherences. *Concepts in Magnetic Resonance*, 1995; 7: 115-136.
87. Fauth J, Schweiger A, Braunschweiler L, Forrer J, Ernst R. Elimination of Unwanted Echoes and Reduction of Dead Time in Three-Pulse Electron Spin-Echo Spectroscopy. *Journal of magnetic resonance*, 1986; 66: 74-85.
88. Sattin W, Mareci T, Scott K. Exploiting the Stimulated Echo in Nuclear Magnetic Resonance Imaging. I. Method. *Journal of Magnetic Resonance*, 1985; 64: 177-182.
89. Mansfield P. Multi-planar image formation using NMR spin echoes. *J Phys C: Solid State Phys*, 1977; 10: L55-L58.
90. Brown R. A brief account of microscopical observations made in the months of June, July and August, 1827, on the particles contained in the pollen of plants; and on the general existence of active molecules in organic and inorganic bodies. *Phil. Mag.*, 1828; 4: 161.

91. Einstein A. Investigations on the Theory of the Brownian Movement. edited with notes by R. Fürth, Dover publications, 1956.
92. Stejskal R, Tanner J. Spin Diffusion Measurements: Spin Echoes in the Presence of a Time Dependent Field Gradient. J. Chem. Phys., 1965; 42: 288-292.
93. Fick A. Ueber Diffusion. Annalen der Physik, 1855; 170: 59-86.
94. Torrey H. Bloch Equations with Diffusion Terms. Physical Review, 1956; 104: 563-565.
95. Le Bihan D, Breton E. Imagerie de Diffusion In Vivo par Résonance Magnétique Nucléaire. C. R. Acad. Sc. Paris, 1985; 301: 1109-1112.
96. Turner R, Le Bihan D, Maier J, Vavrek R, Hedges LK, Pekar J. Echo-planar imaging of intravoxel incoherent motion. Radiology, 1990; 177: 407-414.
97. Lohan D, Saleh R, Nael K, Krishnam M, Finn J. Contrast-enhanced MRA versus nonenhanced MRA: Pros and cons. Applied radiology, Journal of Practical medical imaging and Management. Supplement to May, 2007.
98. Cashen TA, Carr JC, Shin W, Walker MT, Futterer SF, Shaibani A et al. Intracranial time-resolved contrast-enhanced MR angiography at 3T. AJNR Am J Neuroradiol, 2006; 27: 822-829.
99. Haller S, Pereira VM, Lazeyras F, Vargas MI, Lövblad K. Magnetic resonance imaging techniques in white matter disease: potentials and limitations. Top Magn Reson Imaging, 2009; 20: 301-312.
100. Calamante F. Arterial input function in perfusion MRI: a comprehensive review. Prog Nucl Magn Reson Spectrosc, 2013; 74: 1-32.
101. Tofts PS, Brix G, Buckley DL, Evelhoch JL, Henderson E, Knopp MV et al. Estimating kinetic parameters from dynamic contrast-enhanced T<sub>1</sub>-weighted MRI of a diffusable tracer: standardized quantities and symbols. J Magn Reson Imaging, 1999; 10: 223-232.
102. Barnes SL, Whisenant JG, Loveless ME, Yankeelov TE. Practical dynamic contrast enhanced MRI in small animal models of cancer: data acquisition, data analysis, and interpretation. Pharmaceutics, 2012; 4: 442-478.
103. Wong EC. An introduction to ASL labeling techniques. J Magn Reson Imaging, 2014; 40: 1-10.
104. Williams DS, Detre JA, Leigh JS, Koretsky AP. Magnetic resonance imaging of perfusion using spin inversion of arterial water. Proc. Natl. Acad. Sci. U.S.A., 1992; 89: 212-216.
105. Wu W, Fernandez-Seara M, Detre J, Wehrli F, Wang J. A theoretical and experimental investigation of the tagging efficiency of pseudocontinuous arterial spin labeling. Magnetic Resonance in Medicine, 2007; 58: 1020-1027.
106. Dai W, Garcia D, de Bazelaire C, Alsop DC. Continuous flow-driven inversion for arterial spin labeling using pulsed radio frequency and gradient fields. Magn Reson Med, 2008; 60: 1488-1497.

107. Kwong KK, Belliveau JW, Chesler DA, Goldberg IE, Weisskoff RM, Poncelet BP et al. Dynamic magnetic resonance imaging of human brain activity during primary sensory stimulation. *Proc. Natl. Acad. Sci. U.S.A.*, 1992; 89: 5675-5679.
108. Alsop DC, Detre JA, Golay X, Günther M, Hendrikse J, Hernandez-Garcia L et al. Recommended implementation of arterial spin-labeled perfusion MRI for clinical applications: A consensus of the ISMRM perfusion study group and the European consortium for ASL in dementia. *Magn Reson Med*, 2014; 73: 102-116.
109. Le Bihan D, Turner R. The capillary network: a link between IVIM and classical perfusion. *Magn Reson Med*, 1992; 27: 171-178.
110. Chandarana H, Kang SK, Wong S, Rusinek H, Zhang JL, Arizono S et al. Diffusion-weighted intravoxel incoherent motion imaging of renal tumors with histopathologic correlation. *Invest Radiol*, 2012; 47: 688-696.
111. Yoon JH, Lee JM, Baek JH, Shin C, Kiefer B, Han JK et al. Evaluation of hepatic fibrosis using intravoxel incoherent motion in diffusion-weighted liver MRI. *J Comput Assist Tomogr*, 2014; 38: 110-116.
112. Hu L, Hong N, Zhu W. Quantitative Measurement of Cerebral Perfusion with Intravoxel Incoherent Motion in Acute Ischemia Stroke: Initial Clinical Experience. *Chin. Med. J.*, 2015; 128: 2565-2569.
113. Hu Y, Yan L, Wu L, Du P, Chen B, Wang L et al. Intravoxel incoherent motion diffusion-weighted MR imaging of gliomas: efficacy in preoperative grading. *Sci Rep*, 2014; 4: 7208.
114. Cruz G, Nie S, Wang L. Potential application of IVIM and DWI imaging in Parkinson's disease. *Revista Tecnura*, 2014; 18: 80-89.
115. Le Bihan D. Magnetic resonance imaging of perfusion. *Magn Reson Med*, 1990; 14: 283-292.
116. Kennan RP, Gao JH, Zhong J, Gore JC. A general model of microcirculatory blood flow effects in gradient sensitized MRI. *Med Phys*, 1994; 21: 539-545.
117. Wetscherek A, Stieltjes B, Laun FB. Flow-compensated intravoxel incoherent motion diffusion imaging. *Magn Reson Med*, 2015; 74: 410-419.
118. Neil J, Scherrer L, Ackerman J. An approach to solving the dynamic range problem in measurement of the pseudodiffusion coefficient in vivo with spin echoes. *Journal of magnetic resonance*, 1991; 95: 607-614.
119. Neil J, Ackerman J. Detection of pseudodiffusion in rat brain following blood substitution with perfluorocarbon. *Journal of magnetic resonance*, 1992; 97: 194-201.
120. Neil JJ, Bosch CS, Ackerman JJ. An evaluation of the sensitivity of the intravoxel incoherent motion (IVIM) method of blood flow measurement to changes in cerebral blood flow. *Magn Reson Med*, 1994; 32: 60-65.

121. Henkelman RM, Neil JJ, Xiang QS. A quantitative interpretation of IVIM measurements of vascular perfusion in the rat brain. *Magn Reson Med*, 1994; 32: 464-469.
122. Duong TQ, Kim SG. In vivo MR measurements of regional arterial and venous blood volume fractions in intact rat brain. *Magn Reson Med*, 2000; 43: 393-402.
123. Iima M, Le Bihan D. Clinical Intravoxel Incoherent Motion and Diffusion MR Imaging: Past, Present, and Future. *Radiology*, 2016; 278: 13-32.
124. Nevo U, Ozarslan E, Komlosh ME, Koay CG, Sarlls JE, Basser PJ. A system and mathematical framework to model shear flow effects in biomedical DW-imaging and spectroscopy. *NMR Biomed*, 2010; 23: 734-744.
125. McNab JA, Polimeni JR, Wang R, Augustinack JC, Fujimoto K, Stevens A et al. Surface based analysis of diffusion orientation for identifying architectonic domains in the in vivo human cortex. *Neuroimage*, 2013; 69: 87-100.
126. Fujima N, Yoshida D, Sakashita T, Homma A, Tsukahara A, Tha KK et al. Intravoxel incoherent motion diffusion-weighted imaging in head and neck squamous cell carcinoma: assessment of perfusion-related parameters compared to dynamic contrast-enhanced MRI. *Magn Reson Imaging*, 2014; 32: 1206-1213.
127. Suo S, Lin N, Wang H, Zhang L, Wang R, Zhang S et al. Intravoxel incoherent motion diffusion-weighted MR imaging of breast cancer at 3.0 tesla: Comparison of different curve-fitting methods. *J Magn Reson Imaging*, 2015; 42: 362-370.
128. Iima M, Reynaud O, Tsurugizawa T, Ciobanu L, Li J, Geffroy F et al. Characterization of glioma microcirculation and tissue features using intravoxel incoherent motion magnetic resonance imaging in a rat brain model. *Invest Radiol*, 2014; 49: 485-490.
129. Wurnig MC, Donati OF, Ulbrich E, Filli L, Kenkel D, Thoeny HC et al. Systematic analysis of the intravoxel incoherent motion threshold separating perfusion and diffusion effects: Proposal of a standardized algorithm. *Magn Reson Med*, 2015; 74: 1414-1422.
130. Sigmund EE, Cho GY, Kim S, Finn M, Moccaldi M, Jensen JH et al. Intravoxel incoherent motion imaging of tumor microenvironment in locally advanced breast cancer. *Magn Reson Med*, 2011; 65: 1437-1447.
131. Ichikawa S, Motosugi U, Ichikawa T, Sano K, Morisaka H, Araki T. Intravoxel incoherent motion imaging of focal hepatic lesions. *J Magn Reson Imaging*, 2013; 37: 1371-1376.
132. Andreou A, Koh DM, Collins DJ, Blackledge M, Wallace T, Leach MO et al. Measurement reproducibility of perfusion fraction and pseudodiffusion coefficient derived by intravoxel incoherent motion diffusion-weighted MR imaging in normal liver and metastases. *Eur Radiol*, 2013; 23: 428-434.
133. Jensen JH, Helpert JA. MRI quantification of non-Gaussian water diffusion by kurtosis analysis. *NMR Biomed*, 2010; 23: 698-710.



134. Chabert S, Meca C, Le Bihan D. Relevance of the information about the diffusion distribution in vivo given by kurtosis in q-space imaging. *Proc. Intl. Soc. Mag. Reson. Med.*, 2004; 11: 1238.
135. Iima M, Kataoka M, Nakanishi Y, Umehana M, Ito T, Yano K et al. EPOS: Computer-aided IVIM/Kurtosis Diffusion MRI for breast lesions: comparison with BI-RADS MRI categories. *Proceedings of the European Congress of Radiology*, 2014.
136. Iima M, Yano K, Kataoka M, Umehana M, Murata K, Kanao S et al. Quantitative non-Gaussian diffusion and intravoxel incoherent motion magnetic resonance imaging: differentiation of malignant and benign breast lesions. *Invest Radiol*, 2015; 50: 205-211.
137. Neil JJ, Bretthorst GL. On the use of Bayesian probability theory for analysis of exponential decay data: an example taken from intravoxel incoherent motion experiments. *Magn Reson Med*, 1993; 29: 642-647.
138. Barbieri S, Donati OF, Froehlich JM, Thoeny HC. Impact of the calculation algorithm on biexponential fitting of diffusion-weighted MRI in upper abdominal organs. *Magn Reson Med*, 2016; 75: 2175-2184.
139. Akaike H. Information theory and an extension of the maximum likelihood principle. *Second international symposium on information theory*, 1973.
140. Wagenmakers E, Farrell S. AIC model selection using Akaike weights. *Psychon Bull Rev*, 2004; 11: 192-196.
141. Burnham KP, Anderson DR. Kullback-Leibler information as a basis for strong inference in ecological studies. *Wildlife Research*, 2001; 28: 111-119.
142. <https://www.R-project.org/>.
143. Lori NF, Conturo TE, Le Bihan D. Definition of displacement probability and diffusion time in q-space magnetic resonance measurements that use finite-duration diffusion-encoding gradients. *J. Magn. Reson.*, 2003; 165: 185-195.
144. Pyatigorskaya N, Le Bihan D, Reynaud O, Ciobanu L. Relationship between the diffusion time and the diffusion MRI signal observed at 17.2 Tesla in the healthy rat brain cortex. *Magn Reson Med*, 2014; 72: 492-500.
145. Federau C, Maeder P, O'Brien K, Browaeys P, Meuli R, Hagmann P. Quantitative measurement of brain perfusion with intravoxel incoherent motion MR imaging. *Radiology*, 2012; 265: 874-881.
146. Stefanovic B, Hutchinson E, Yakovleva V, Schram V, Russell JT, Belluscio L et al. Functional reactivity of cerebral capillaries. *J. Cereb. Blood Flow Metab.*, 2008; 28: 961-972.
147. Régrigny O, Delagrangé P, Scalbert E, Lartaud-Idjouadiene I, Atkinson J, Chillon JM. Effects of melatonin on rat pial arteriolar diameter in vivo. *Br. J. Pharmacol.*, 1999; 127: 1666-1670.

148. Ngai AC, Winn HR. Modulation of cerebral arteriolar diameter by intraluminal flow and pressure. *Circ. Res.*, 1995; 77: 832-840.
149. Callaghan P. Principles of nuclear magnetic resonance microscopy. Oxford Science Publications (Ed.). 1991.
150. Yeh C, Schmitt B, Le Bihan D, Li-Schlittgen J, Lin C, Poupon C. Diffusion microscopist simulator: a general Monte Carlo simulation system for diffusion magnetic resonance imaging. *PLoS One*, 2013; 8: e76626.
151. Pannetier NA, Debacker CS, Mauconduit F, Christen T, Barbier EL. A simulation tool for dynamic contrast enhanced MRI. *PLoS One*, 2013; 8: e57636.
152. Christen T, Pannetier NA, Ni WW, Qiu D, Moseley ME, Schuff N et al. MR vascular fingerprinting: A new approach to compute cerebral blood volume, mean vessel radius, and oxygenation maps in the human brain. *Neuroimage*, 2014; 89: 262-270.
153. Ma YP, Koo A, Kwan HC, Cheng KK. On-line measurement of the dynamic velocity of erythrocytes in the cerebral microvessels in the rat. *Microvasc. Res.*, 1974; 8: 1-13.
154. Li JG, Stanisz GJ, Henkelman RM. Integrated analysis of diffusion and relaxation of water in blood. *Magn Reson Med*, 1998; 40: 79-88.
155. Burstein D. Stimulated Echoes: Description, Applications, Practical Hints. *Concepts in Magnetic Resonance*, 1996; 8: 269-278.
156. Berchtold NC, Cotman CW. Evolution in the conceptualization of dementia and Alzheimer's disease: Greco-Roman period to the 1960s. *Neurobiol. Aging*, 1998; 19: 173-189.
157. de la Torre JC. Impaired brain microcirculation may trigger Alzheimer's disease. *Neurosci Biobehav Rev*, 1994; 18: 397-401.
158. McKhann GM, Knopman DS, Chertkow H, Hyman BT, Jack CRJ, Kawas CH et al. The diagnosis of dementia due to Alzheimer's disease: recommendations from the National Institute on Aging-Alzheimer's Association workgroups on diagnostic guidelines for Alzheimer's disease. *Alzheimers Dement*, 2011.
159. Johnson K, Fox N, Sperling R, Klunk W. Brain Imaging in Alzheimer Disease. *Cold Spring Harb Persp Med*, 2012; 2: 1-23.
160. de Jong LW, van der Hiele K, Veer IM, Houwing JJ, Westendorp RGJ, Bollen ELEM et al. Strongly reduced volumes of putamen and thalamus in Alzheimer's disease: an MRI study. *Brain*, 2008; 131: 3277-3285.
161. Sperling R. Potential of functional MRI as a biomarker in early Alzheimer's disease. *Neurobiol. Aging*, 2011; 32 Suppl 1: S37-43.
162. Mosconi L, Berti V, Glodzik L, Pupi A, De Santi S, de Leon MJ. Pre-clinical detection of Alzheimer's disease using FDG-PET, with or without amyloid imaging. *J. Alzheimers Dis.*, 2010; 20: 843-854.

163. Vlassenko AG, Benzinger TLS, Morris JC. PET amyloid-beta imaging in preclinical Alzheimer's disease. *Biochim. Biophys. Acta*, 2012; 1822: 370-379.
164. Hébert F, Grand'maison M, Ho M, Lerch JP, Hamel E, Bedell BJ. Cortical atrophy and hypoperfusion in a transgenic mouse model of Alzheimer's disease. *Neurobiol. Aging*, 2013; 34: 1644-1652.
165. Wolk DA, Detre JA. Arterial spin labeling MRI: an emerging biomarker for Alzheimer's disease and other neurodegenerative conditions. *Curr. Opin. Neurol.*, 2012; 25: 421-428.
166. Federau C, Meuli R, O'Brien K, Maeder P, Hagmann P. Perfusion measurement in brain gliomas with intravoxel incoherent motion MRI. *AJNR Am J Neuroradiol*, 2014; 35: 256-262.
167. Jankowsky JL, Fadale DJ, Anderson J, Xu GM, Gonzales V, Jenkins NA et al. Mutant presenilins specifically elevate the levels of the 42 residue beta-amyloid peptide in vivo: evidence for augmentation of a 42-specific gamma secretase. *Hum. Mol. Genet.*, 2004; 13: 159-170.
168. Garcia-Alloza M, Robbins EM, Zhang-Nunes SX, Purcell SM, Betensky RA, Raju S et al. Characterization of amyloid deposition in the APPswe/PS1dE9 mouse model of Alzheimer disease. *Neurobiol. Dis.*, 2006; 24: 516-524.
169. Schwartz RB. Apparent diffusion coefficient mapping in patients with Alzheimer disease or mild cognitive impairment and in normally aging control subjects: present and future. *Radiology*, 2001; 219: 8-9.
170. Ramani A, Jensen JH, Helpert JA. Quantitative MR imaging in Alzheimer disease. *Radiology*, 2006; 241: 26-44.
171. Vanhoutte G, Pereson S, Delgado Y, Palacios R, Guns P, Asselbergh B, Veraart J et al. Diffusion kurtosis imaging to detect amyloidosis in an APP/PS1 mouse model for Alzheimer's disease. *Magn Reson Med*, 2013; 69: 1115-1121.
172. Liu X, Li R, Yang Z, Hudetz AG, Li S. Differential effect of isoflurane, medetomidine, and urethane on BOLD responses to acute levo-tetrahydropalmatine in the rat. *Magn Reson Med*, 2012; 68: 552-559.
173. Matta BF, Heath KJ, Tipping K, Summors AC. Direct cerebral vasodilatory effects of sevoflurane and isoflurane. *Anesthesiology*, 1999; 91: 677-680.
174. Sinclair MD. A review of the physiological effects of alpha2-agonists related to the clinical use of medetomidine in small animal practice. *Can. Vet. J.*, 2003; 44: 885-897.
175. Ciobanu L, Reynaud O, Uhrig L, Jarraya B, Le Bihan D. Effects of anesthetic agents on brain blood oxygenation level revealed with ultra-high field MRI. *PLoS One*, 2012; 7: e32645.
176. Petrinovic MM, Hankov G, Schroeter A, Bruns A, Rudin M, von Kienlin M et al. A novel anesthesia regime enables neurofunctional studies and imaging genetics across mouse strains. *Sci Rep*, 2016; 6: 24523.

177. Ahn CB, Lee SY, Nalcioğlu O, Cho ZH. The effects of random directional distributed flow in nuclear magnetic resonance imaging. *Med Phys*, 1987; 14: 43-48.
178. Shi Y, Lawford P, Hose R. Review of zero-D and 1-D models of blood flow in the cardiovascular system. *Biomed Eng Online*, 2011; 10: 33.
179. Wang J, Fernández-Seara MA, Wang S, St Lawrence KS. When perfusion meets diffusion: in vivo measurement of water permeability in human brain. *J. Cereb. Blood Flow Metab.*, 2007; 27: 839-849.

## List of relevant publications

### Peer-reviewed journals

**G. Fournet**, J.R. Li, A. Cerjanic, B. Sutton, L. Ciobanu and D. Le Bihan. A two pool model to describe the IVIM cerebral perfusion. In press at JCBFM, doi: 10.1177/0271678X16681310.

**G. Fournet**, J.R. Li, D. Le Bihan, L. Ciobanu. Influence of acquisition parameters on the IVIM metrics. In preparation.

### Conference proceedings

**G. Fournet**, J.R. Li, D. Le Bihan and L. Ciobanu. The dependence of IVIM outputs on experimental parameters. Proc. of the ESMRMB 2016 – e-poster.

**G. Fournet**, L. Ciobanu, J.R. Li, A. Cerjanic, B. Sutton and D. Le Bihan. The IVIM signal: a combination of two vascular pools. Proc. of the ISMRM 2016 – e-poster.

**G. Fournet**, L. Ciobanu, J.R. Li, A. Cerjanic, B. Sutton and D. Le Bihan. A new two pool model for the IVIM signal. Proc. of the NeWS 2016 – poster.

**G. Fournet**, J.R. Li, A. Cerjanic, B. Sutton, D. Le Bihan and L. Ciobanu. A new insight into the origins of the IVIM signal. Proc. of the ESMRMB 2015 – e-poster.

**Titre :** IVIM : Modélisation, validation expérimentale et application à des modèles animaux

**Mots clés :** IRM, perfusion, rat, microcirculation, cerveau, flux sanguin cérébral

**Résumé :** Cette thèse porte sur l'étude de la séquence d'imagerie IRM IVIM (« Intravoxel incoherent motion »). Cette séquence permet l'étude des microvaisseaux sanguins tels que les capillaires, artérioles et veinules. Pour être sensible seulement aux groupes de spins non statiques dans les tissus, des gradients de diffusion sont ajoutés avant et après l'impulsion  $180^\circ$  d'une séquence d'écho de spin. La composante du signal correspondant aux spins qui diffusent dans le tissu peut être séparée de celle des spins en mouvement dans les vaisseaux sanguins qui est appelée signal IVIM. Ces deux composantes sont pondérées par  $f_{IVIM}$  qui représente la fraction volumique du sang à l'intérieur du tissu. Le signal IVIM est en général modélisé par une fonction mono-exponentielle (ME) caractérisée par un

coefficient de pseudo-diffusion  $D^*$ . Nous proposons un modèle IVIM bi-exponentiel formé d'une composante lente caractérisée par  $f_{slow}$  et  $D_{slow}^*$  qui correspondrait aux capillaires comme dans le modèle ME, et d'une composante rapide caractérisée par  $f_{fast}$  et  $D_{fast}^*$  qui correspondrait à des vaisseaux plus gros comme des artérioles et veinules. Ce modèle a été validé expérimentalement et des informations supplémentaires ont été obtenues en comparant les signaux expérimentaux avec un dictionnaire de signaux IVIM simulés numériquement. L'influence de la séquence d'impulsions, du temps de répétition et du temps d'encodage de diffusion a également été étudiée. Enfin, la séquence IVIM a été appliquée à l'étude d'un modèle animal de la maladie d'Alzheimer.

**Title:** IVIM: Modeling, experimental validation and application to animal models

**Keywords:** MRI, perfusion, rat, microcirculation, brain, cerebral blood flow

**Abstract:** This PhD thesis is centered on the study of the IVIM ("Intravoxel Incoherent Motion") MRI sequence. This sequence allows for the study of the blood microvasculature such as the capillaries, arterioles and venules. To be sensitive only to moving groups of spins, diffusion gradients are added before and after the  $180^\circ$  pulse of a spin echo (SE) sequence. The signal component corresponding to spins diffusing in the tissue can be separated from the one related to spins travelling in the blood vessels which is called the IVIM signal. These two components are weighted by  $f_{IVIM}$  which represents the volume fraction of blood inside the tissue. The IVIM signal is usually modelled by a mono-exponential (ME) function and

characterized by a pseudo-diffusion coefficient,  $D^*$ . We propose instead a bi-exponential IVIM model consisting of a slow pool, characterized by  $f_{slow}$  and  $D_{slow}^*$ , corresponding to the capillaries as in the ME model, and a fast pool, characterized by  $f_{fast}$  and  $D_{fast}^*$ , related to larger vessels such as medium-size arterioles and venules. This model was validated experimentally and more information was retrieved by comparing the experimental signals to a dictionary of simulated IVIM signals. The influence of the pulse sequence, the repetition time and the diffusion encoding time was also studied. Finally, the IVIM sequence was applied to the study of an animal model of Alzheimer's disease.

